


Spring 1-1-2015

Representation of Unknown and Unmodeled Space Events for Satellites : Characteristics and Applications

Hyun Chul Ko

University of Colorado Boulder, untildie74@gmail.com

Follow this and additional works at: https://scholar.colorado.edu/asen_gradetds

 Part of the [Mechanical Engineering Commons](#), [Navigation, Guidance, Control and Dynamics Commons](#), [Space Vehicles Commons](#), and the [Systems Engineering Commons](#)

Recommended Citation

Ko, Hyun Chul, "Representation of Unknown and Unmodeled Space Events for Satellites : Characteristics and Applications" (2015). *Aerospace Engineering Sciences Graduate Theses & Dissertations*. 120.
https://scholar.colorado.edu/asen_gradetds/120

This Dissertation is brought to you for free and open access by Aerospace Engineering Sciences at CU Scholar. It has been accepted for inclusion in Aerospace Engineering Sciences Graduate Theses & Dissertations by an authorized administrator of CU Scholar. For more information, please contact cuscholaradmin@colorado.edu.

**Representation of Unknown and Unmodeled Space Events
for Satellites : Characteristics and Applications**

by

“Ddard” Hyun Chul Ko

B.A., U.S. Air Force Academy, 1998

M.S., The University of Science & Technology at South Korea, 2010

A thesis submitted to the
Faculty of the Graduate School of the
University of Colorado in partial fulfillment
of the requirements for the degree of
Doctor of Philosophy
Department of Aerospace Engineering

2015

This thesis entitled:
Representation of Unknown and Unmodeled Space Events for Satellites : Characteristics and
Applications
written by “Ddard” Hyun Chul Ko
has been approved for the Department of Aerospace Engineering

Daniel J. Scheeres

Prof. George H. Born

Prof. John Hauser

Prof. Jay McMahon

Prof. Jeffrey S. Parker

Date _____

The final copy of this thesis has been examined by the signatories, and we find that both the content and the form meet acceptable presentation standards of scholarly work in the above mentioned discipline.

Ko, “Ddard” Hyun Chul (Ph.D., Aerospace Engineering)

Representation of Unknown and Unmodeled Space Events for Satellites : Characteristics and Applications

Thesis directed by Prof. Daniel J. Scheeres

A new way of representing unknown and unmodeled space events (USEs) with Thrust-Fourier-Coefficients (TFCs) is introduced and its applications to satellite orbit determination (OD) and event detection are studied. A USE is regarded as an event due to unknown changes of force model caused by unplanned maneuvers, unknown deployment, collision, or some other drastic change in space environment. A satellite’s motion under USEs, transitioning between two arbitrary orbit states, can be represented as an equivalent orbital maneuver connecting those two states by applying the Fourier series representation of perturbing accelerations. This event representation with TFCs rigorously provides a unique control law that can generate the given secular behavior of a satellite due to a USE. This technique enables us to facilitate the analytical propagation of orbit information across a USE, which allows for the usage of an existing pre-event orbit solution to compute a post-event orbit solution. By directly appending TFCs and the represented event dynamics to a regular OD filter, the modified filter using TFCs is able to blend post-event tracking data to improve a post-event orbit solution in the absence of a dynamics model of USE. Case studies with simulated tracking data show that the event representation using TFCs helps to maintain OD across a period of USEs. In addition, when there is measurement data available during USEs, a modified sequential filter with TFCs is able to detect the onset and the termination time of an event. This event representation-based OD and event detection distinguishes itself from other approaches in that it does not rely on any assumption or *a priori* information of a USE. This generic approach enables us to fit tracking data in real time and therefore to maintain a satellite tracking in the presence of USEs. This method has the advantage of avoiding the difficulty of manual parameter tuning and, thus, is able to provide more accurate post-event OD solution with a single OD filter.

Dedication

To my mom, AnSun, and dad, IlHwan, for guiding me how to live

&

To my wife, 'Grace' NaYoung, and two sons, 'Joey' Geonhee and 'Ray' Kanghee, for showing me
how to love

Acknowledgements

First and foremost, I am heartily grateful to my advisor, Dan Scheeres, for supporting me throughout my PhD program with his patience and knowledge while allowing me the freedom to pursue my interest. Without him, this thesis would not have been completed. Sincere gratitude to George Born, Jay McMahon, Jeff Parker, and John Hauser for agreeing to be members of the thesis committee and for providing constructive comments and valuable suggestions on this dissertation. I have learned a great deal from their wealth of knowledge and attention to detail.

In my daily work, I have been blessed with a friendly and cheerful group of fellow CSML members from all over the world. All you folks have inspired me in my research and life through our interactions during my time at the University of Colorado at Boulder. In particular, it has been four wonderful years of ‘suffering’ together with InKwan, David, Antonella and Dan.

Furthermore, I would like to thank R.O.K. Air Force for allowing me to pursue my degree abroad with their generous support. I will show that it has been a worthy investment. Above all, I would like to thank my family, whose ongoing support has led me to where I am today. Special thanks to my dad for his unconditional love and support. Words fail to express my appreciation to my wife ‘Grace’ NaYoung for her patience, love and persistent confidence in me. Many thanks to my two sons, ‘Joey’ Geonhee and ‘Ray’ Kanghee, who continue to inspire and motivate me everyday to go further.

Go as far as you can see; when you get there, you will be able to see further. - Thomas Carlyle

Contents

Chapter	
1 Introduction	1
1.1 Motivation	1
1.2 Organization	4
1.3 Contributions and Publications	6
1.3.1 Contributions	6
1.3.2 Publications	8
2 Finding Essential Thrust-Fourier-Coefficient Set for Event Representation	10
2.1 Orbital averaging method	11
2.2 Relationship between TFCs and time rates of change in mean orbital elements . . .	15
2.2.1 Controlling semi-major axis and eccentricity : a, e	16
2.2.2 Controlling argument of perigee and epoch of periapsis passage : ω, σ	17
2.2.3 Controlling inclination and longitude of ascending node : i, Ω	19
2.2.4 Controlling 4 orbital elements : $i, \Omega, \omega, \sigma$	22
2.3 Finding the essential TFC set	22
2.3.1 Essential TFC candidate sets	22
2.3.2 Minimum norm solution using 14 TFCs	28
2.3.3 Cost analysis	28
2.3.4 Essential TFC set	29

2.4	Different solutions for the essential TFC set to represent an event	31
2.4.1	Averaged solution	31
2.4.2	Non-averaged solution	33
2.4.3	Numerically updated solution	35
2.5	Summary	41
3	Event Representation Based Orbit Determination Across Unmodeled Space Events Using Thrust-Fourier-Coefficients	43
3.1	Uncertainty propagation via event representation	45
3.1.1	Analytical study	45
3.1.2	Numerical study	50
3.2	Orbit determination across unmodeled space events via event representation	58
3.2.1	Modified Batch filter with the essential TFC set	58
3.2.2	Modified Batch filter with different TFC sets	74
3.3	Summary	82
4	Event Detection and Maneuvering Satellite Tracking Using Event Representation with 14 Thrust-Fourier-Coefficients	84
4.1	Event representation with 14 TFCs	85
4.2	Event detection with event representation using 14 TFCs	87
4.2.1	Event detection algorithm using the modified sequential filter	89
4.2.2	Simulations and results	93
4.3	Tracking a maneuvering satellite with event representation using TFCs	107
4.3.1	Modified extended Kalman filter with 14 TFCs	111
4.3.2	Simulations and results using 14 TFCs	114
4.3.3	Simulations and results using the essential TFC set	123
4.4	Summary	124

5	Conclusion and Future Works	129
5.1	Conclusion	129
5.2	Future Works	131
	Bibliography	133
	Appendix	
A	Computation of \mathcal{G}_{ess} Matrix for Non-averaged Solution	139
B	Contribution of Adding TFCs on State Uncertainty Estimation	141
C	Orbit Determination Across Unmodeled Space Events via Event Representation Using Different TFC Sets	146
D	Simulation Result of Modifying Orbit Determination Toolbox (ODTBX) with the TFC event representation	153

Tables

Table

1.1	Comparing Different Event Representation Methods	3
2.1	Separability of a and e using different TFC sets	16
2.2	Separability of ω and σ using different TFC sets	19
2.3	Initial and desired final state of orbital elements for different cases	26
2.4	Cost of changing mean orbital elements by using different TFC sets	29
2.5	Final position and velocity errors by using different TFC solutions	38
3.1	Initial state of orbital elements	50
3.2	Different space event cases (P : orbital period, 1.8 hr)	50
3.3	Averaged uncertainty realism test result	57
3.4	Estimated Vs True ΔV in circumferential direction	71
3.5	Different unmodeled event cases	76
3.6	Initial orbit state of LEO satellite	76
3.7	True vs Estimated ΔV for different cases (m/s)	78
4.1	Initial state of LEO satellite	93
4.2	Simulation cases with different USEs	94
4.3	Simulation cases with different maneuvers	114
C.1	Different unmodeled event cases	146

D.1 Initial state of LEO satellite	153
D.2 Perturbations for different USE cases	153
D.3 Estimated ΔV from the filter	159

Figures

Figure

2.1	Controlling a and e using different TFC set	18
2.2	Controlling ω and σ using different TFC set	20
2.3	Controlling i and Ω with $[\alpha_1^W \beta_1^W]$	21
2.4	Controlling orbital elements with $[\alpha_0^R \beta_1^S \alpha_1^W \beta_1^W]$	23
2.5	Controlling orbital elements using an invalid set	24
2.6	Controlling 6 orbital elements using different TFC sets for case 1	27
2.7	Essential TFC set	30
2.8	Averaged/Minimum norm solutions vs short period corrected solution for case 1	32
2.9	Controlling 6 orbital elements using different TFC solutions for Case 3	37
2.10	Trajectory estimation in different orbit space for a high thrust maneuver ($\Delta V 200m/s$)	39
3.1	True vs interpolated trajectories	46
3.2	Uncertainty propagation without modeling the unknown event for case 3	52
3.3	Uncertainty propagation with event representation for case 1	54
3.4	Uncertainty propagation with event representation for case 2	54
3.5	Uncertainty propagation with event representation for case 3	55
3.6	Uncertainty propagation with event representation for case 4	55
3.7	Uncertainty propagation with event representation for case 5	56
3.8	Uncertainty propagation with event representation for case 6	56

3.9	Flow chart for the modified Batch algorithm (blue : modified part)	61
3.10	State estimation error & 3σ boundary without modeling an unknown event for case 1	63
3.11	State estimation error with 3σ uncertainty boundary for case 1	64
3.12	State estimation error with 3σ uncertainty boundary for case 2	65
3.13	State estimation error with 3σ uncertainty boundary for case 4	67
3.14	State estimation error with 3σ uncertainty boundary with IOD for case 4	68
3.15	State estimation error with 3σ uncertainty boundary for case 6	69
3.16	Represented vs True acceleration components in body frame	72
3.17	Batch result for case 1 with range, azimuth, elevation measurement	73
3.18	Event representation for case 4	77
3.19	Post-event OD solution from different batch filters for case 4 with one hour tracking data	80
3.20	OD solution with different sizes of tracking data for case 4	81
4.1	Event acceleration representation using 14 TFCs	86
4.2	EKF_{TFC} results with pre-event tracking data in step 1 for case 1	96
4.3	Generalized norm value of TFCs from EKF_{TFC} in step 2-8 for case 1	96
4.4	OD solution with estimated perturbation in step 9 for case 1	97
4.5	Unknown acceleration representation with estimated TFCs in step 10	99
4.6	OD solution with estimated perturbation for case 2	100
4.7	OD solution with estimated perturbation for case 3	100
4.8	OD solution with estimated perturbation for case 3 after two iterations	101
4.9	unmodeled event representation for case 3	102
4.10	OD solution with estimated perturbation for case 4	103
4.11	OD solution with estimated perturbation for case 5	104
4.12	unmodeled event representation	104
4.13	Measurement residuals and TFC estimates from forward EKF_{TFC} for case 6	105

4.14	Un-modeled drag representation for case 6	106
4.15	OD solution with estimated perturbation for case 6	107
4.16	Flow chart for the modified EKF	115
4.17	OD solution from the modified EKF for case 1	116
4.18	Measurement residuals from the modified EKF for case 1	116
4.19	OD solution from the modified EKF for case 2	118
4.20	OD solution from the modified EKF for case 3	119
4.21	OD solution from the modified EKF for case 4	120
4.22	OD solution from the modified EKF for case 5	121
4.23	OD solution from the modified EKF for case 6	122
4.24	OD solution from the modified EKF with the essential TFC set for case 1	125
4.25	OD solution from the modified EKF with the essential TFC set for case 3	126
4.26	OD solution from the modified EKF with the essential TFC set for case 6	127
C.1	Event representation for case 1	147
C.2	OD solution with different sizes of tracking data for case 1	148
C.3	Event representation for case 2	149
C.4	OD solution with different sizes of tracking data for case 2	150
C.5	Event representation for case 3	151
C.6	OD solution with different sizes of tracking data for case 3	152
D.1	OD result (state errors) with the unmodified filter on case 1	154
D.2	OD result (state, measurement errors) with modified filter on case 1	156
D.3	OD result (state, measurement errors) with modified filter on case 6	157
D.4	OD results from 30 Monte Carlo runs on case 1	158
D.5	Represented vs True acceleration components in body frame	160

Chapter 1

Introduction

1.1 Motivation

Understanding and analyzing the changes in an orbit under perturbing acceleration is a fundamental problem of orbital mechanics, with the prediction and description of a perturbed satellite's orbit remaining an important concern in achieving space situational awareness (SSA). However, predicting future behaviors of a satellite is often limited by unknown perturbations acting on it. Various unknown perturbations, such as unannounced or unplanned maneuvers, unmodeled structural deployment, thrust malfunction, explosions, collision with space objects, or some other drastic change in space environment, cause acceleration changes on a spacecraft in time, which is regarded as a space event [1]. Without information about such events, it is difficult to maintain SSA across the period of an unknown and unmodeled space event (USE), which may cause a lost track of satellite due to abrupt changes of orbit states. At this stage, a post-event analysis tries to recover a lost satellite due to a USE using post-event tracking data. Generally, it is a time-consuming task that requires a significant amount of training on the matter [2]. Therefore, developing an efficient way to represent a USE could play an essential role in analyzing space events or estimating the post-event trajectory of a satellite.

Generally, the event representation is usually done by determining the thrust acceleration required to link the pre-event orbit to the post-event orbit estimate, and there have been different ways of estimating such an unknown acceleration. A simple and conventional approach to estimate a perturbing acceleration is based on the idea of connecting an initial state to a post-event orbital

state by applying ΔV [3]. It computes the velocity difference at the closest point of a pre-event orbit to a post-event orbit. While this ΔV approach is easy to implement and is computationally time-efficient, its orbit estimation becomes inaccurate when there is an event with a long duration or with multiple firings since this case can not be represented as an instantaneous event. A more common method of representing an event is to model a target event based on the Gauss-Markov process by adding stochastic acceleration terms to the orbit determination filter in order to compensate for unknown perturbations [4, p. 230]. Orbit determination (OD) filters, such as state noise compensation (SNC [4, p. 501]), dynamic model compensation (DMC [4, p. 505]), or an optimal sequential filter (e.g., the Analytical Graphics Inc. orbit determination tool kit [5][6]) use a process noise as the acceleration term to account for unmodeled dynamics [7]. Even though this method is not limited to a certain type of USEs, it still requires coefficient tuning for a filter to have a converged solution, which is usually a manual task that requires time and experience. In addition, the Gauss-Markov process approach provides neither a dynamical insight of unknown perturbations nor the uncertainty information about the estimated control law. In recent research, the optimal control concept is applied to the unknown event detection and characterization [8][9][10]. This optimal control based event representation assumes that the event is fuel optimal and therefore provides an optimal solution of thrust acceleration that accounts for unknown dynamics. These recovered optimal dynamics facilitate the propagation of state uncertainty across a USE. However, this optimal control based approach is limited to an event related to optimal maneuvers and finding the initial values of the adjoint parameters could present difficulty.

In a different vein, Hudson and Scheeres developed a new method to represent trajectory dynamics by applying orbital averaging and control law parameterization using the Fourier series representation of thrust components [11][12]. Applying the fact that every physical form of thrust acceleration could be represented by the Fourier series, they isolated the secular behavior of a satellite under perturbations. Due to the orthogonality of the Fourier series representation, the averaged dynamics equations were found to be a function of 14 thrust-Fourier-coefficients (TFCs) [11]. We further investigated this approach and introduced a simple way to effectively represent unknown

space events with a selected minimum set of six TFCs [13]. This allows us to construct a control profile with a reduced set of 6 TFCs instead of 14 parameters. Although this event representation with TFCs does not recover the actual perturbing acceleration for a given event, it rigorously provides a unique solution of control law that produces the apparent secular behavior induced by a USE. Unlike other representation techniques, this generic approach is not restricted to a certain type of USE; such as an event with constant-acceleration, low-thrust maneuver, or optimal control maneuver. It presents a very simple and quick way of computing the fundamental elements of perturbing accelerations acting on a satellite. Table. 1.1 compares the restrictions and capabilities of different event representation approaches. Since it provides us with a basic understanding of

Table 1.1: Comparing Different Event Representation Methods

	Direct Del V Computation	Gauss-Markov Process	Optimal Control Matrix	TFC Event Representation
implementation difficulty	easy	moderate	complicated	moderate
computation time	low	medium	medium	low
uncertainty estimation	unavailable	unavailable	available	available
dynamics interpretation	no	no	yes	yes
application restriction	short-duration event	none	optimal maneuver	none

unknown dynamics, the event representation with TFCs can be utilized to improve SSA in the presence of a USE.

The importance of attaining reliable SSA is the essential component of safe space operation. Improving SSA capability means to provide valuable information that can be used to determine space object status, ongoing mission tasks, present and future position, or estimated behaviors [14]. However, achieving SSA with respect to a spacecraft with USEs is quite difficult, particularly when it is operated by uncooperative parties [15]. It is also a very challenging task to maintain SSA across a USE solely based on a few discrete observations. Since the TFC event

representation provides the fundamental basis of the unknown dynamics of a given USE, it can be applied to improve SSA of the satellite under USEs. The represented dynamics model with the TFCs allows us to analytically propagate pre-event OD solutions through a USE period. The strength of this approach is its ability to maintain OD solutions of a satellite during the unknown event period and be able to blend post-event observations to minimize the OD solution errors after the event given a few measurement. Therefore, this methodology can help us to maintain SSA in a data-sparse space environment, in where tracking a maneuvering satellite along with the timely detection of a USE is an important task since the number of maneuvering satellites has been increasing [16]. Applying the TFC event representation method in SSA supports safe and effective space operation and motivates the following thesis statement of this dissertation.

Thesis Statement

Event representation with thrust-Fourier-coefficients can be utilized to enhance space situational awareness capability in the area of uncertainty propagation, event detection, and maneuvering satellite tracking in the presence of an unknown and unmodeled space event.

1.2 Organization

The main section, chapter 2-4, of this dissertation is organized as follows: first, we present how to represent a USE using different TFC sets obtained from the averaged Gauss equations. In the following chapter, before utilizing this TFC event representation technique to solve OD problems with USEs, the orbit uncertainty propagation through the represented dynamics is evaluated analytically and the characteristics are verified with numerical study. Then, the last two main chapters introduce several applications of the event representation approach using TFCs in the area of uncertainty propagation, event detection, and maneuvering satellite tracking. Each main chapter begins with its own introduction and a brief review of previous related works, and ends the

chapter with a summary.

In chapter 2, the previous work developed by Hudson and Scheeres is reviewed first, where the averaged dynamic equations are found to be a function of only 14 TFCs [11]. Then, we analyze the relationship between the time rates of change of orbital elements and 14 TFCs to identify minimal sets of six TFCs that can effectively represent the secular effect of perturbing acceleration. The controllability and the sensitivity of the TFCs are analyzed and a cost analysis is also performed by employing different combinations of 14 TFCs in order to compare varying representations of a given secular motion. In addition, three different ways to compute TFC values for a given orbital change are presented and their performances are compared with the minimum norm solution of 14-TFC set. Furthermore, we show that this TFC representation approach can be extended to compute non-averaged control acceleration between Cartesian positions and velocities, indicating a certain level of universality.

Chapter 3 consists of two main sections. The first section is devoted to a theoretical proof that enables us to apply the event representation to uncertainty propagation. It summarizes analytical aspects of uncertainty propagation using a dynamics representation of an unknown event, and verifies that the covariance propagation using an event representation is valid in the linear region. This fundamental finding serves as the basis for this dissertation and is applied to OD problems using the representation technique with different TFC sets. The second section presents the development of the Batch filter using the event representation with the essential TFCs and demonstrates the proposed filter's OD performance across a USE. In addition, different TFC sets are used to represent a USE in the modified Batch filter to investigate how different event representations with different combinations of TFCs affect OD solutions across USEs. Both main sections include simulation studies of different space event scenarios to verify our approach.

In chapter 4, we apply the event representation technique using TFCs to develop a new event detection algorithm and a maneuvering satellite tracking method. Chapter 4.1 provides a brief explanation of how to represent a USE with 14 TFCs. The subsequent chapter, chapter 4.2, explains how the sequential filter is modified to identify a change-point of unknown perturbation

acting on a satellite. With this modified sequential filter, a new event detection algorithm is introduced and is tested across different USEs to check its performance in OD process. The level of veracity of detecting an event and the accuracy of post-event OD solutions are examined in the simulation study. In chapter 4.3. the extended Kalman filter (EKF) is modified to maintain tracking of a maneuvering satellite by applying the event representation method with TFCs. Since a satellite's motion under USEs can be represented as an equivalent orbital maneuver connecting two arbitrary states, USEs can be regarded as unknown maneuvers throughout this dissertation. The performance of the modified filter is verified by applying the filter to different types of USEs. In addition, the EKF is modified with the essential TFC set instead of the 14-TFC set and their OD solutions across a USE are compared in the simulation study.

1.3 Contributions and Publications

1.3.1 Contributions

The primary contributions of this dissertations are:

- To develop a new way of rigorously describing an unknown and unmodeled space event (USE) using the event representation technique with Thrust-Fourier-Coefficients (TFCs).
 - * The implication of the TFC event representation technique is fundamental: Any orbital change, transitioning between two arbitrary orbit states, can be represented as an equivalent maneuver using a represented control law with TFCs.
 - * It provides a very simple and efficient way of representing the fundamental elements of a sequence of control laws for a given USE, which significantly reduces computational requirements.
 - * This preliminary analysis of a control law can provide us with a basic understanding of the perturbing accelerations, which can be used to bound the control effort necessary for linking two separate states across a USE.

- To provide analytic and numerical proof that the covariance propagation in the linear region is independent of orbit dynamics that connect two separate states via different paths.
 - * It contributes an analytical framework of uncertainty propagation using an event representation in implementing an OD filter across USEs. It allows for the usage of existing pre-event orbit estimation to compute the post-event orbit solution using represented dynamics.
 - * It enables us to modify a Batch filter using the event representation with TFCs in order to process OD across a USE in data sparse environments.
 - The modified Batch filter using TFCs is a fully automated process and avoids the difficulty of manually tuning thrust coefficients . Also, it provides a faster convergence, better orbit solution, and more flexibility with the initial estimate than those in the regular Batch filter.
 - The proposed OD filter is particularly valuable for the case with no measurement available during a USE period and could allow ground station operators to obtain a valid orbit trajectory immediately following an unknown event.
- To develop new methods to detect a USE and to maintain tracking of a satellite under unknown perturbations.
 - * Unlike other methods, these methods are knowledge-free schemes that do not require pre-defined models of unknown accelerations nor assumptions about a USE.
 - * The proposed detection algorithm using the TFC representation is able to detect various types of USEs and to directly estimate the onset and the termination time of a USE from observation data.
 - * Using a single modified EKF with TFCs, the new satellite tracking method is able to track a wide range of maneuvering satellites in real-time, ranging from an impulsive burn to a continuous low-thrust burn.

1.3.2 Publications

The following publications are related to this dissertation (most recent to oldest).

Journals

- Ko, H. C., and Scheeres, D. J., “Real-Time Maneuvering Satellite Tracking with Event Representation Using Thrust-Fourier-Coefficients,” To be submitted to the *Journal of Guidance, Control, and Dynamics*.
- Ko, H. C., and Scheeres, D. J., “Maneuver Detection with Event Representation using Thrust-Fourier-Coefficients,” Manuscript submitted to the *Journal of Guidance, Control, and Dynamics*, (2015/5).
- Ko, H. C., and Scheeres, D. J., “Orbit determination Across Unknown Maneuvers Using the Essential Thrust-Fourier-Coefficients,” *Acta Astronautica*. Vol. 118, January–February 2016, pp. 90–95. doi:10.1016/j.actaastro.2015.10.002
- Ko, H. C., and Scheeres, D. J., “Event Representation Based Orbit Determination Across Unknown Space Events,” *Journal of Guidance, Control, and Dynamics*, In press (2015), accessed 20 May 2015. <http://arc.aiaa.org/doi/abs/10.2514/1.G001050>
- Ko, H. C., and Scheeres, D. J., “Essential Thrust-Fourier-Coefficient Set of Averaged Gauss Equations for Orbital Mechanics,” *Journal of Guidance, Control, and Dynamics*, Vol. 37, No. 4, 2014, pp. 1236–1249. doi: 10.2514/1.62407

Conference papers

- Ko, H. C., and Scheeres, D. J., “Orbit determination and Maneuver Detection Using Event Representation with Thrust-Fourier-Coefficients,” Proceedings of the Advanced Maui Optical and Space Surveillance Technologies Conference, Maui, Hawaii, September, 2015.

- Ko, H. C., and Scheeres, D. J., “Maneuver Detection with Event Representation using Thrust-Fourier-Coefficients,” AAS 15-375, 2015 AAS/AIAA Astrodynamics Specialist Conference, Vail, Colorado, August, 2015.
- Ko, H. C., and Scheeres, D. J., “Spacecraft Orbit Anomaly Representation Using Thrust-Fourier-Coefficients with Orbit Determination Toolbox,” Proceedings of the Advanced Maui Optical and Space Surveillance Technologies Conference, Maui, Hawaii, September, 2014, p. 63.
- Ko, H. C., and Scheeres, D. J., “Orbit Determination Across Unknown Maneuvers Using the Essential Thrust Fourier Coefficients,” IAC 14-C1.5.1, 65th International Astronautical Congress, Toronto, Canada, October, 2014.
- Ko, H. C., and Scheeres, D. J., “Unobserved Maneuver Representation and Covariance Propagation Using the Essential Thrust Fourier Coefficients,” IAC 13-C1.4.2, 64th International Astronautical Congress, Beijing, China, September, 2013.
- Ko, H. C., and Scheeres, D. J., “Essential Thrust Fourier Coefficient Set of Averaged Gauss Equations for Orbital Mechanics,” AAS 13-375, 23rd AAS/AIAA Space Flight Mechanics Meeting, Kauai, Hawaii, February, 2013.

Chapter 2

Finding Essential Thrust-Fourier-Coefficient Set for Event Representation

Finding a proper representation of control law to generate a desired change in orbit state remains as a fundamental and unsolved problem. Within this problem, the use of orbital averaging is a useful technique since the mean orbital elements describe the secular behavior of perturbative effects on a satellite, providing dynamical insight into the secular variations. Over the last few decades, various methods have been developed to solve orbital transfer problems using averaging methods. Kluever developed a guidance scheme based on inverse dynamics using averaged state equations [17][18], and trajectory tracking guidance using orbital averaging and a predictive tracking method [19]. Ferrier and Epenoy presented optimal low-thrust transfer solutions for electro-ionic propulsion with averaging technique and a smoothing method [20]. Petropoulos formed analytic integrals of the averaged variational equations for a thrusting spacecraft [21]. Bonnard solved an energy minimization problem of single input orbit transfer by averaging and continuation techniques [22]. Gao proposed near-optimal low-thrust transfers and nonlinear guidance by using the orbital averaging method [23][24]. All these works have proved that the orbital averaging is an effective method to obtain a control law for a desired orbital transfer.

Most recently, Hudson and Scheeres applied averaging techniques to thrusting motion, using the Fourier series representation of the control law [11][12]. In their works, the perturbing acceleration components were represented as the Fourier series in eccentric anomaly and the averaged dynamic equations were found to be a function of only 14 Thrust-Fourier-Coefficients (TFCs). In this chapter, we analyze the relationship between the time rates of change of orbital elements and

these TFCs, and identify minimal sets of 6 TFCs in order to represent the secular effect of perturbing acceleration effectively, instead of the full 14 TFCs. Given the initial and desired final orbital state of a spacecraft, an essential set of 6 TFCs values can be computed analytically and the required control accelerations can be constructed to achieve any orbital transfer. The emphasis in this chapter is on how to obtain different TFC sets to uniquely represent any desired change in orbit.

2.1 Orbital averaging method

The following Gauss equations describe the time rates of change of the classical orbital elements of a body subject to perturbations which can be broken down into the radial, circumferential and normal components ($\vec{F} = F_R \hat{r} + F_S \hat{w} \times \hat{r} + F_W \hat{w}$ [25]).

$$\begin{aligned}
 \frac{da}{dt} &= 2\sqrt{\frac{a}{\mu}} \left[F_R \frac{ae}{\sqrt{1-e^2}} \sin \nu + F_S \frac{a\sqrt{1-e^2}}{1-e \cos E} \right] \\
 \frac{de}{dt} &= \sqrt{\frac{a}{\mu}} \sqrt{1-e^2} [F_R \sin \nu + F_S (\cos \nu + \cos E)] \\
 \frac{di}{dt} &= \sqrt{\frac{a}{\mu}} \frac{1-e \cos E}{\sqrt{1-e^2}} F_W \cos(\nu + \omega) \\
 \frac{d\Omega}{dt} &= \sqrt{\frac{a}{\mu}} \frac{1-e \cos E}{\sqrt{1-e^2}} F_W \frac{\sin(\nu + \omega)}{\sin i} \\
 \frac{d\omega}{dt} &= \sqrt{\frac{a}{\mu}} \frac{\sqrt{1-e^2}}{e} \left[-F_R \cos \nu + F_S \left(1 + \frac{1-e \cos E}{1-e^2} \right) \sin \nu \right] - \cos i \frac{d\Omega}{dt} \\
 \frac{d\sigma}{dt} &= -\sqrt{\frac{a}{\mu}} \left[2(1-e \cos E) - \frac{1-e^2}{e} \cos \nu \right] F_R - \sqrt{\frac{a}{\mu}} \left[\frac{2-e^2-e \cos E}{e} \right] \sin \nu F_S
 \end{aligned} \tag{2.1}$$

where σ is the epoch of periapsis passage that can be obtained by $\sigma = -nt_0 = (M - M_0) - nt$ and M, n are the mean anomaly and the mean motion respectively. Using the decomposed perturbing accelerations represented as the Fourier series expansion in eccentric anomaly (E), the perturbation

component in each direction can be expressed in terms of TFCs (α_k, β_k) [26] :

$$\begin{aligned} F_R &= \sum_{k=0}^{\infty} [\alpha_k^R \cos kE + \beta_k^R \sin kE] \\ F_S &= \sum_{k=0}^{\infty} [\alpha_k^S \cos kE + \beta_k^S \sin kE] \\ F_W &= \sum_{k=0}^{\infty} [\alpha_k^W \cos kE + \beta_k^W \sin kE] \end{aligned} \quad (2.2)$$

As explained in Reference [11], the use of eccentric anomaly as the basis for the Fourier series expansion is essential if the number of thrust coefficients is to be made finite. Substituting the Fourier series for the thrust vector components into the Gauss equations, the osculating orbital elements at a future time can be expressed as:

$$\begin{aligned} \vec{\alpha\epsilon}(t) &= \vec{\alpha\epsilon}_0 + \int_0^t \dot{\vec{\alpha\epsilon}}(\tau) d\tau \\ &= \vec{\alpha\epsilon}_0 + \int_0^t [G(\vec{\alpha\epsilon}, \tau) \cdot \vec{\alpha\beta}] d\tau \end{aligned} \quad (2.3)$$

where $\vec{\alpha\epsilon}$ is the state vector of osculating orbital elements, and $G(\vec{\alpha\epsilon}, \tau)$ and $\vec{\alpha\beta}$ are defined as:

$$\begin{aligned} \vec{\alpha\epsilon} &= \begin{bmatrix} a & e & i & \Omega & \omega & \sigma \end{bmatrix}^T \\ G(\vec{\alpha\epsilon}, \tau) &= \sqrt{\frac{a}{\mu}} \begin{bmatrix} 2\frac{ae}{\sqrt{1-e^2}} \sin \nu & 2\frac{a\sqrt{1-e^2}}{1-e \cos E} & 0 \\ \sqrt{1-e^2} \sin \nu & \sqrt{1-e^2}(\cos \nu + \cos E) & 0 \\ 0 & 0 & \frac{1-e \cos E}{\sqrt{1-e^2}} \cos(\nu + \omega) \\ 0 & 0 & \frac{1-e \cos E}{\sqrt{1-e^2}} \frac{\sin(\nu + \omega)}{\sin i} \\ -\frac{\sqrt{1-e^2}}{e} \cos \nu & \frac{\sqrt{1-e^2}}{e} \left(1 + \frac{1-e \cos E}{1-e^2}\right) \sin \nu & -\cos i \frac{1-e \cos E}{\sqrt{1-e^2}} \frac{\sin(\nu + \omega)}{\sin i} \\ -2(1-e \cos E) + \frac{1-e^2}{e} \cos \nu & -\left(\frac{2-e^2-e \cos E}{e}\right) \sin \nu & 0 \end{bmatrix} \begin{bmatrix} A & \text{zeros} & \text{zeros} \\ \text{zeros} & A & \text{zeros} \\ \text{zeros} & \text{zeros} & A \end{bmatrix} \\ A &= \begin{bmatrix} 1 & \cos E & \cos 2E & \cdots & \sin E & \sin 2E & \cdots \end{bmatrix} \\ \vec{\alpha\beta} &= \begin{bmatrix} \alpha_0^R & \alpha_1^R & \alpha_2^R & \cdots & \beta_1^R & \beta_2^R & \cdots & \alpha_0^S & \alpha_1^S & \alpha_2^S & \cdots & \beta_1^S & \beta_2^S & \cdots & \alpha_0^W & \alpha_1^W & \alpha_2^W & \cdots & \beta_1^W & \beta_2^W & \cdots \end{bmatrix}^T \end{aligned}$$

By defining $\Delta\vec{\alpha\epsilon} = \vec{\alpha\epsilon}(t) - \vec{\alpha\epsilon}_0$ and $\mathcal{G} = \int_0^t G(\vec{\alpha\epsilon}, \tau) d\tau$, Eq. (2.3) can be simplified as:

$$\Delta\vec{\alpha\epsilon} = \mathcal{G} \cdot \vec{\alpha\beta} \quad (2.4)$$

The Gauss equations in general form can also be derived from Eq. (2.3) as functions of TFCs:

$$\dot{\vec{\alpha}}(t) = G(\vec{\alpha}, t) \cdot \vec{\alpha}\beta \quad (2.5)$$

where $G(\vec{\alpha}, t)$ is a $6 \times \infty$ nonlinear function matrix of $\vec{\alpha}$.

If a perturbing acceleration is relatively small, then the orbital elements will not change dramatically and the change in orbital elements over one orbit period can be computed independent of an initial point in an orbit. Therefore, these averaged equations capture the secular evolution of the system. The first-order averaging is carried out with eccentric anomaly [11] :

$$\begin{aligned} \overline{\dot{\vec{\alpha}}} &= \frac{1}{2\pi} \int_0^{2\pi} \dot{\vec{\alpha}} dM \\ &= \frac{1}{2\pi} \int_0^{2\pi} G(\vec{\alpha}, t)(1 - e \cos E) dE \cdot \vec{\alpha}\beta \end{aligned} \quad (2.6)$$

By integrating $G(\vec{\alpha}, t)$ over one orbital period with keeping the orbit elements constant, the “average” of $G(\vec{\alpha}, t)$ is computed as:

$$\overline{G(\vec{\alpha})}_{6 \times \infty} = \frac{1}{2\pi} \int_0^{2\pi} G(\vec{\alpha}, t)(1 - e \cos E) dE \quad (2.7)$$

By eliminating columns consisting of only zeros in $\overline{G}_{6 \times \infty}$ and defining this column reduced 6×14 matrix as \overline{G} and its corresponding TFC vector as $\vec{\tau}$, the averaged orbit dynamic equation, Eq. (2.6), can be simplified to:

$$\begin{aligned} \overline{\dot{\vec{\alpha}}} &= \overline{G(\vec{\alpha})}_{6 \times \infty} \cdot \vec{\alpha}\beta = \overline{G(\vec{\alpha})} \cdot \vec{\tau} \\ \vec{\alpha} &= \left[\bar{a} \quad \bar{e} \quad \bar{i} \quad \bar{\Omega} \quad \bar{\omega} \quad \bar{\sigma} \right]^T \\ \vec{\tau} &= \left[\alpha_0^R \quad \alpha_1^R \quad \alpha_2^R \quad \beta_1^R \quad \alpha_0^S \quad \alpha_1^S \quad \alpha_2^S \quad \beta_1^S \quad \beta_2^S \quad \alpha_0^W \quad \alpha_1^W \quad \alpha_2^W \quad \beta_1^W \quad \beta_2^W \right]^T \end{aligned} \quad (2.8)$$

where $\vec{\tau}$ is the vector of 14 TFCs for the averaged dynamics. From now, the bar sign over orbital elements will be omitted for clarity since we are focusing only on mean orbital elements in this

chapter. The 6×14 \bar{G} -matrix is obtained from the averaged equation is as follows:

$$\bar{G} = \begin{bmatrix} 0 & 0 & 0 & G_{1,4} & G_{1,5} & 0 & 0 & 0 & 0 & 0 & 0 & 0 & 0 & 0 \\ 0 & 0 & 0 & G_{2,4} & G_{2,5} & G_{2,6} & G_{2,7} & 0 & 0 & 0 & 0 & 0 & 0 & 0 \\ 0 & 0 & 0 & 0 & 0 & 0 & 0 & 0 & 0 & G_{3,10} & G_{3,11} & G_{3,12} & G_{3,13} & G_{3,14} \\ 0 & 0 & 0 & 0 & 0 & 0 & 0 & 0 & 0 & G_{4,10} & G_{4,11} & G_{4,12} & G_{4,13} & G_{4,14} \\ G_{5,1} & G_{5,2} & 0 & 0 & 0 & 0 & 0 & G_{5,8} & G_{5,9} & G_{5,10} & G_{5,11} & G_{5,12} & G_{5,13} & G_{5,14} \\ G_{6,1} & G_{6,2} & G_{6,3} & 0 & 0 & 0 & 0 & G_{6,8} & G_{6,9} & 0 & 0 & 0 & 0 & 0 \end{bmatrix} \quad (2.9)$$

$$G_{1,4} = \sqrt{\frac{a}{\mu}} a e$$

$$G_{1,5} = 2\sqrt{\frac{a}{\mu}} a \sqrt{1-e^2}$$

$$G_{2,4} = \sqrt{\frac{a}{\mu}} \frac{1}{2} (1-e^2)$$

$$G_{2,5} = \sqrt{\frac{a}{\mu}} \frac{-3}{2} e \sqrt{1-e^2}$$

$$G_{2,6} = \sqrt{\frac{a}{\mu}} \sqrt{1-e^2}$$

$$G_{2,7} = \sqrt{\frac{a}{\mu}} \frac{-1}{4} e \sqrt{1-e^2}$$

$$G_{3,10} = \sqrt{\frac{a}{\mu}} \frac{1}{\sqrt{1-e^2}} \frac{-3}{2} e \cos w$$

$$G_{3,11} = \sqrt{\frac{a}{\mu}} \frac{1}{\sqrt{1-e^2}} \frac{1}{2} (1+e^2) \cos w$$

$$G_{3,12} = \sqrt{\frac{a}{\mu}} \frac{1}{\sqrt{1-e^2}} \frac{-1}{4} e \cos w$$

$$G_{3,13} = \sqrt{\frac{a}{\mu}} \frac{1}{\sqrt{1-e^2}} \frac{-1}{2} \sqrt{1-e^2} \sin w$$

$$G_{3,14} = \sqrt{\frac{a}{\mu}} \frac{1}{\sqrt{1-e^2}} \frac{1}{4} e \sqrt{1-e^2} \sin w$$

$$G_{4,10} = \sqrt{\frac{a}{\mu}} \csc i \frac{1}{\sqrt{1-e^2}} \frac{-3}{2} e \sin w$$

$$G_{4,11} = \sqrt{\frac{a}{\mu}} \csc i \frac{1}{\sqrt{1-e^2}} \frac{1}{2} (1+e^2) \sin w$$

$$G_{4,12} = \sqrt{\frac{a}{\mu}} \csc i \frac{1}{\sqrt{1-e^2}} \frac{-1}{4} e \sin w$$

$$G_{4,13} = \sqrt{\frac{a}{\mu}} \csc i \frac{1}{\sqrt{1-e^2}} \frac{1}{2} \sqrt{1-e^2} \cos w$$

$$G_{4,14} = \sqrt{\frac{a}{\mu}} \csc i \frac{1}{\sqrt{1-e^2}} \frac{-1}{4} e \sqrt{1-e^2} \cos w$$

$$G_{5,1} = \sqrt{\frac{a}{\mu}} \sqrt{1-e^2}$$

$$G_{5,2} = \sqrt{\frac{a}{\mu}} \frac{1}{e} \frac{-1}{2} \sqrt{1-e^2}$$

$$G_{5,8} = \sqrt{\frac{a}{\mu}} \frac{1}{e} \frac{1}{2} (2-e^2)$$

$$G_{5,9} = \sqrt{\frac{a}{\mu}} \frac{1}{e} \frac{-1}{4} e$$

$$G_{5,10} = -\cos i \sqrt{\frac{a}{\mu}} \csc i \frac{1}{\sqrt{1-e^2}} \frac{-3}{2} e \sin w$$

$$G_{5,11} = -\cos i \sqrt{\frac{a}{\mu}} \csc i \frac{1}{\sqrt{1-e^2}} \frac{1}{2} (1+e^2) \sin w$$

$$G_{5,12} = -\cos i \sqrt{\frac{a}{\mu}} \csc i \frac{1}{\sqrt{1-e^2}} \frac{-1}{4} e \sin w$$

$$G_{5,13} = -\cos i \sqrt{\frac{a}{\mu}} \csc i \frac{1}{\sqrt{1-e^2}} \frac{1}{2} \sqrt{1-e^2} \cos w$$

$$G_{5,14} = -\cos i \sqrt{\frac{a}{\mu}} \csc i \frac{1}{\sqrt{1-e^2}} \frac{-1}{4} e \sqrt{1-e^2} \cos w$$

$$G_{6,1} = -3\sqrt{\frac{a}{\mu}}$$

$$G_{6,2} = \frac{1}{2} \sqrt{\frac{a}{\mu}} (4e + \frac{1-e^2}{e})$$

$$G_{6,3} = -\frac{1}{2} \sqrt{\frac{a}{\mu}} e^2$$

$$G_{6,8} = -\frac{1}{2} \sqrt{\frac{a}{\mu}} \frac{\sqrt{1-e^2}}{e} (2-e^2)$$

$$G_{6,9} = \sqrt{\frac{a}{\mu}} \frac{1}{4} \sqrt{1-e^2}$$

The averaged Gauss equations have singularity problems in the case of $i = 0$, $e = 0$ or $e = 1$, however Hudson and Scheeres have shown that using nonsingular variables can avoid this issue [11]. It is not an issue for our research since the TFC event representation is utilized in Cartesian space. In the following chapters, the secular behavior of each mean orbital element with respect to corresponding TFCs will be analyzed in terms of sensitivity. Also, different combinations of TFCs will be tested to determine whether they enable control of the orbital elements separately.

2.2 Relationship between TFCs and time rates of change in mean orbital elements

To achieve a given orbital transfer in 6-dimensional orbit element space, we may select fewer than 14 TFCs to represent the control law. To recognize a minimal set of TFCs that represents a finite basis for any perturbing event or sequence of maneuvers, the time rates of change of the mean orbital elements related to the TFCs need to be analyzed. The G -matrix has a noticeable structure where certain sets of coupled orbital elements like $[a e]$, $[i \Omega]$, and $[\omega \sigma]$ are affected by certain TFC combinations. Analyzing the representation of TFCs as a function of change in orbit state, we study the controllability and the separability of the orbital elements and the impact of the TFC on each orbital element. In control problems, “controllability” is known as the ability of a control input to drive the state of a system from any initial state to any final state in a finite time interval [27]. We define “separability” as “the ability to separately control each orbital element while keeping all others constant on average”. To determine the separability we use numerical simulations to find valid TFC combinations that do not induce undesired secular drifts in other elements. The application of different TFC sets to various orbital transfers is shown in Fig. 2.1-2.5. Initial conditions for these transfers are all the same (case 1 in Table D.1) and a normalized gravitational parameter ($\mu = 1$) is used. Assuming that the orbit is elliptic ($0 < e < 1$) and non-equatorial ($i \neq 0$), singularity checks are also conducted on blocks within the G -matrix to verify valid sets of TFCs that allow the controllability of the orbital elements. To find out the impact of each TFC on different mean orbital elements, sensitivity checks are performed by calculating the

impacting factors on each mean orbital element. By doing this analysis, several efficient sets of 6 TFCs are obtained and they become the essential TFC candidate sets.

2.2.1 Controlling semi-major axis and eccentricity : a, e

The time rate of change in $[a e]$ is related to the following 4 TFCs, including one from the radial component and three from the circumferential component of a perturbing acceleration:

$$\begin{bmatrix} \dot{a} \\ \dot{e} \end{bmatrix} = \frac{1}{2} \sqrt{\frac{a}{\mu}} \sqrt{1-e^2} \begin{bmatrix} 2\frac{ae}{\sqrt{1-e^2}} & 4a & 0 & 0 \\ \sqrt{1-e^2} & -3e & 2 & \frac{-e}{2} \end{bmatrix} \begin{bmatrix} \beta_1^R \\ \alpha_0^S \\ \alpha_1^S \\ \alpha_2^S \end{bmatrix} \quad (2.10)$$

Only β_1^R and α_0^S control the time rate change of the semi-major axis. For the eccentricity, α_1^S has the biggest impact on \dot{e} followed by β_1^R , α_0^S and α_2^S . A singularity problem exists when \dot{a} and \dot{e} are controlled by just using α_1^S and α_2^S . Therefore, five different sets of TFCs are available to control $[a e]$ which are $[\beta_1^R \alpha_0^S]$, $[\alpha_0^S \alpha_1^S]$, $[\alpha_0^S \alpha_2^S]$, $[\beta_1^R \alpha_1^S]$, $[\beta_1^R \alpha_2^S]$. Table 2.1 summarizes how these different TFC sets can control $[a e]$ without affecting the other orbital elements. For instance, a set consisting of α_0^S from the circumferential direction and β_1^R from radial direction can be used to control \dot{a} and \dot{e} . Those two TFC values are calculated by using an initial value, a desired final value and a required time of completing the transfer, then $[a e]$ are obtained by integrating Eq. 2.10. Figure 2.1 shows that the integration result of mean orbital elements from the averaged equations

Table 2.1: Separability of a and e using different TFC sets

	$[\beta_1^R \alpha_0^S]$	$[\alpha_0^S \alpha_1^S]$	$[\alpha_0^S \alpha_2^S]$	$[\beta_1^R \alpha_1^S]$	$[\beta_1^R \alpha_2^S]$
Separability	Yes	Yes	No	No	No

using this TFC set agrees well with the secular motion of osculating orbital elements from the integration of the full dynamics equations. The 6th subplot describes how the σ term is changing due to the fact that the position of perigee shifts slowly and the average angular speed (mean motion) varies when semi-major axis is changing. As a result, only 2 of the 5 controllable TFC

sets are able to control the orbital elements separately. The remaining sets show undesired secular drifts in ω and σ , especially when e has a second order frequency in one of its thrust coefficients. A synchronized effect between the second order frequency of e and the Fourier series of a perturbing force acting on ω and σ is making the actual mean values of those two orbital elements drift from the desired mean values, which are shown at subplot (c) and (d) of Fig. 2.1.

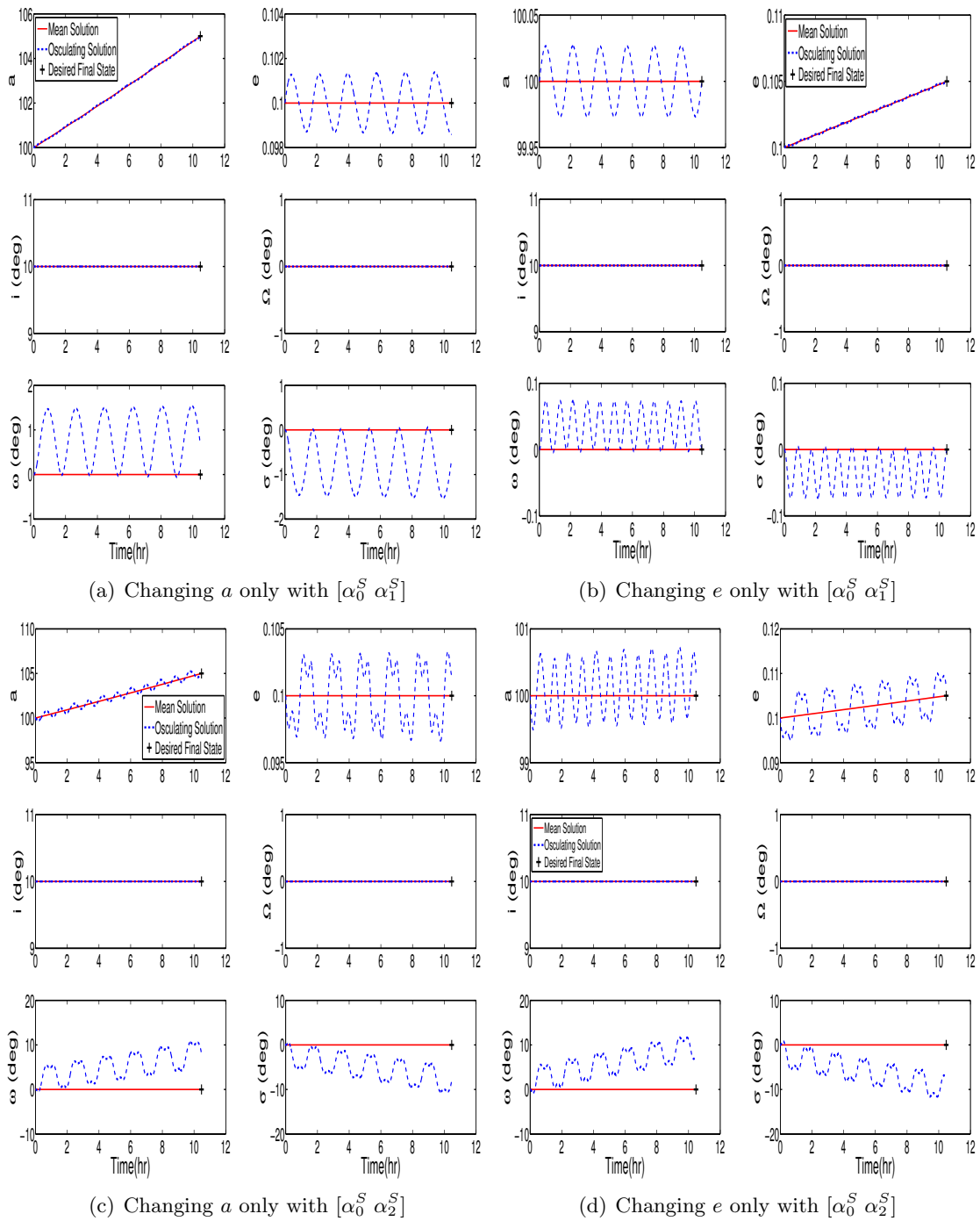
2.2.2 Controlling argument of perigee and epoch of periapsis passage : ω, σ

The time rate of change in $[\omega \ \sigma]$ is related to 5 TFCs from the radial and circumferential components of perturbation, while $\dot{\omega}$ is also affected by 5 TFCs from the normal component of perturbation:

$$\begin{bmatrix} \dot{\omega} \\ \dot{\sigma} \end{bmatrix} = \frac{1}{2} \sqrt{\frac{a}{\mu}} \begin{bmatrix} 2\sqrt{1-e^2} & -\frac{\sqrt{1-e^2}}{e} & 0 & \frac{2-e^2}{e} & -\frac{1}{2} \\ -6 & \frac{3e^2+1}{e} & -e^2 & -\frac{2-e^2}{e}\sqrt{1-e^2} & \frac{\sqrt{1-e^2}}{2} \end{bmatrix} \begin{bmatrix} \alpha_0^R \\ \alpha_1^R \\ \alpha_2^R \\ \beta_1^S \\ \beta_2^S \end{bmatrix} \quad (2.11)$$

$$+ \frac{\cos i}{4 \sin i} \sqrt{\frac{a}{\mu(1-e^2)}} \begin{bmatrix} 6e \sin w & -2(1+e^2) \sin w & e \sin w & -2\sqrt{1-e^2} \cos w & e\sqrt{1-e^2} \cos w \\ 0 & 0 & 0 & 0 & 0 \end{bmatrix} \begin{bmatrix} \alpha_0^W \\ \alpha_1^W \\ \alpha_2^W \\ \beta_1^W \\ \beta_2^W \end{bmatrix}$$

By setting the 5 TFCs in the normal direction to zero, $[\omega \ \sigma]$ can be controlled by using 5 TFCs in radial and circumferential directions. Since the sensitivity of these TFCs on $[\omega \ \sigma]$ is a function of a and e , the order of impact can be found : $\beta_1^S > \alpha_1^R > \alpha_0^R > \beta_2^S > \alpha_2^R$ for small eccentricity. A singularity exists when $\dot{\omega}$ and $\dot{\sigma}$ are evaluated by just using β_1^S and β_2^S . Therefore, 9 different sets of TFCs are available to control $[\omega \ \sigma]$, when there is no perturbation in normal direction. Table 2.2 summarizes how the selected TFC set can control $[\omega \ \sigma]$ without affecting the other orbital elements. Figure 2.2 shows how each TFC set can control the mean orbital elements by comparing them with the osculating orbital elements from integration of the full dynamics equations. We find that 3

Figure 2.1: Controlling a and e using different TFC set

out of the 9 TFC sets are able to control $[\omega \ \sigma]$ separately and those valid sets consist of only zero- and first-order frequency terms. However, $[\omega \ \sigma]$ cannot be controlled separately if there is a perturbation in normal direction which will change ω through the 5 TFCs in the normal direction. Since there is a coupling effect among \dot{i} , $\dot{\Omega}$, $\dot{\omega}$ and $\dot{\sigma}$, a valid TFC set to control those 4 orbital elements with separability has to be considered together. This will be discussed in the following chapter.

Table 2.2: Separability of ω and σ using different TFC sets

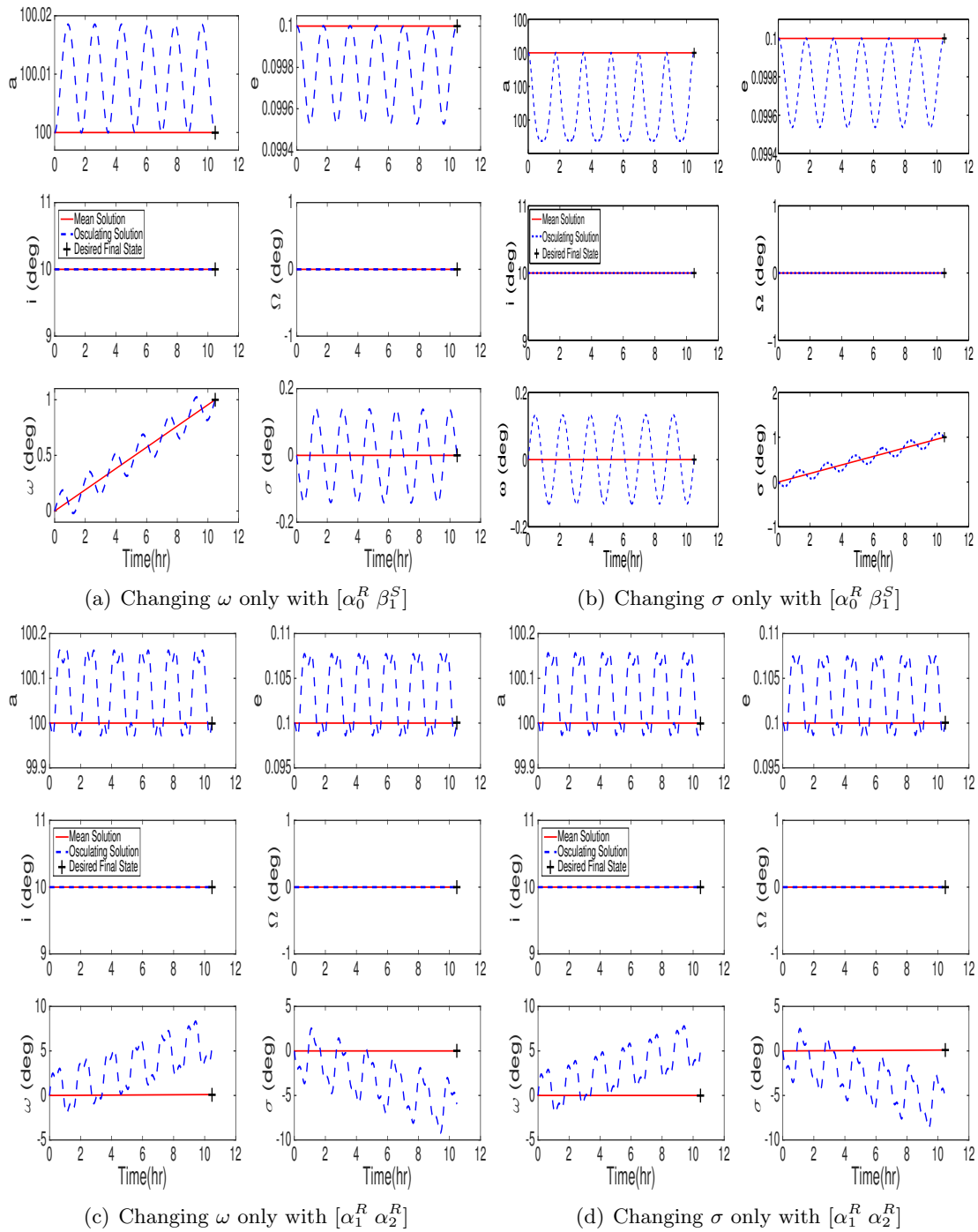
	$[\alpha_0^R \ \alpha_1^R]$	$[\alpha_0^R \ \alpha_2^R]$	$[\alpha_0^R \ \beta_1^S]$	$[\alpha_0^R \ \beta_2^S]$	$[\alpha_1^R \ \alpha_2^R]$	$[\alpha_1^R \ \beta_1^S]$	$[\alpha_1^R \ \beta_2^S]$	$[\alpha_2^R \ \beta_1^S]$	$[\alpha_2^R \ \beta_2^S]$
Separability	Yes	No	Yes	No	No	Yes	No	No	No

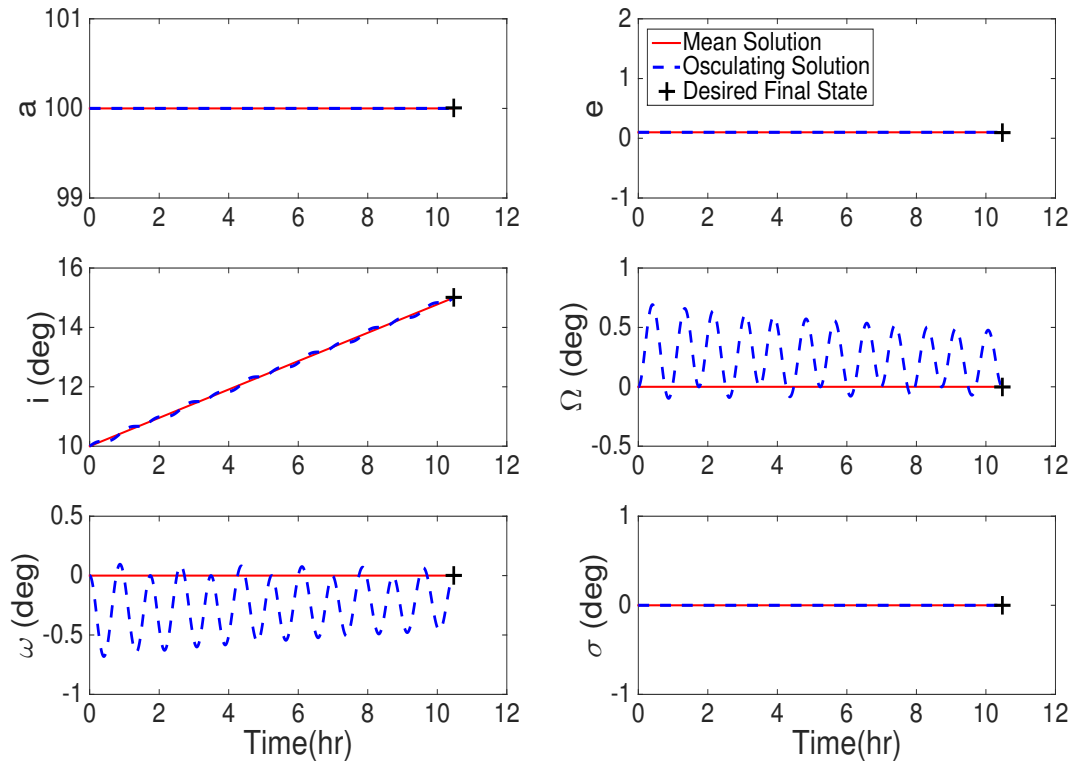
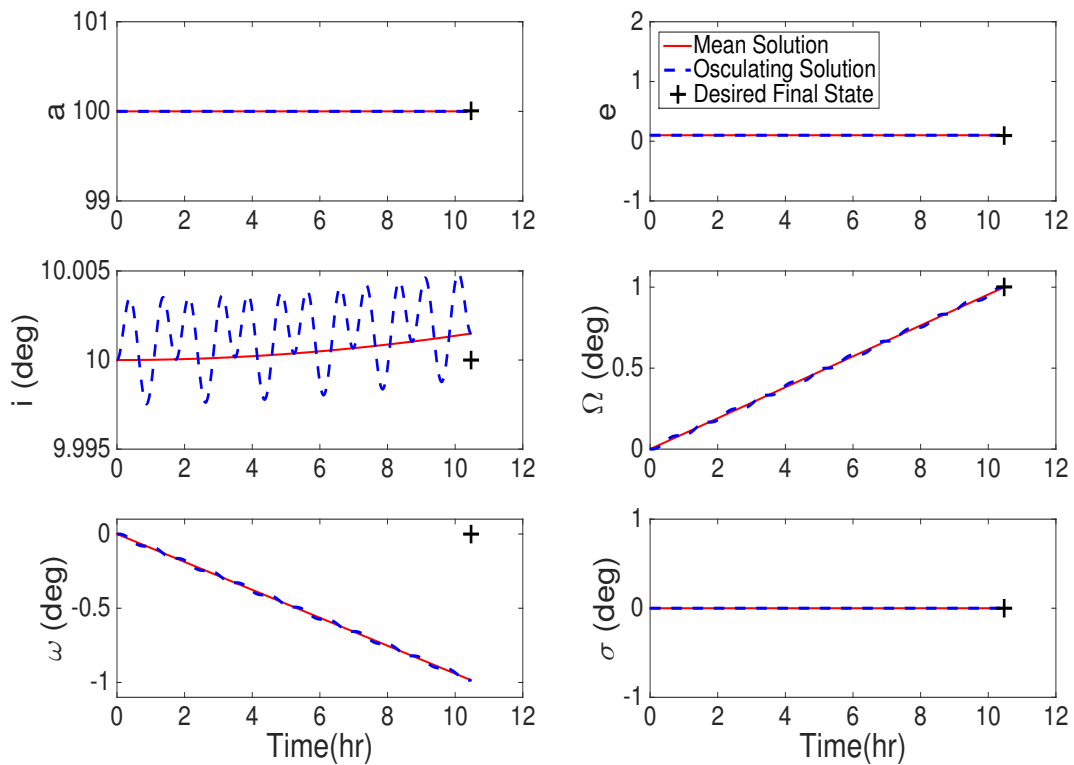
2.2.3 Controlling inclination and longitude of ascending node : i, Ω

The time rate change in $[i \ \Omega]$ are related to 5 TFCs from the normal component of perturbation:

$$\begin{bmatrix} \dot{i} \\ \dot{\Omega} \end{bmatrix} = -\frac{1}{4} \sqrt{\frac{a}{\mu(1-e^2)}} \begin{bmatrix} 6e \cos w & -2(1+e^2) \cos w & e \cos w & 2\sqrt{1-e^2} \sin w & -e\sqrt{1-e^2} \sin w \\ 6e \frac{\sin w}{\sin i} & -2(1+e^2) \frac{\sin w}{\sin i} & e \frac{\sin w}{\sin i} & -2\sqrt{1-e^2} \frac{\cos w}{\sin i} & e\sqrt{1-e^2} \frac{\cos w}{\sin i} \end{bmatrix} \begin{bmatrix} \alpha_0^W \\ \alpha_1^W \\ \alpha_2^W \\ \beta_1^W \\ \beta_2^W \end{bmatrix} \quad (2.12)$$

Following the previous sensitivity analysis, α_0^W , α_1^W and β_1^W are found to have more impact on \dot{i} and $\dot{\Omega}$. Singularity problems exist when \dot{i} and $\dot{\Omega}$ are calculated by just using α_0^W , α_1^W and α_2^W or just using β_1^W and β_2^W . Therefore, 6 TFC sets are available for controlling $[i \ \Omega]$. However, different from the other orbital elements, $[i \ \Omega]$ cannot be controlled separately by these TFC sets because their effect on ω will also affect i eventually. For instance, Fig. 2.3 shows how one of those TFC sets affects ω as well as $[i \ \Omega]$. To control this coupling effect, $[i \ \Omega]$ and $[\omega \ \sigma]$ have to be considered together. The following chapter shows how to find the valid TFC sets for these orbital elements.

Figure 2.2: Controlling ω and σ using different TFC set

(a) Changing i only(b) Changing Ω onlyFigure 2.3: Controlling i and Ω with $[\alpha_1^W \beta_1^W]$

2.2.4 Controlling 4 orbital elements : $i, \Omega, \omega, \sigma$

Combining the previously selected 9 TFC sets for $[\omega \sigma]$ with 6 available TFC sets for $[i \Omega]$, 54 candidate sets can be constructed to control i, Ω, ω and σ independently. For example, a TFC set consisting of $\alpha_0^R, \beta_1^S, \alpha_1^W, \beta_1^W$ can be used to calculate the time rate of $[i \Omega \omega \sigma]$:

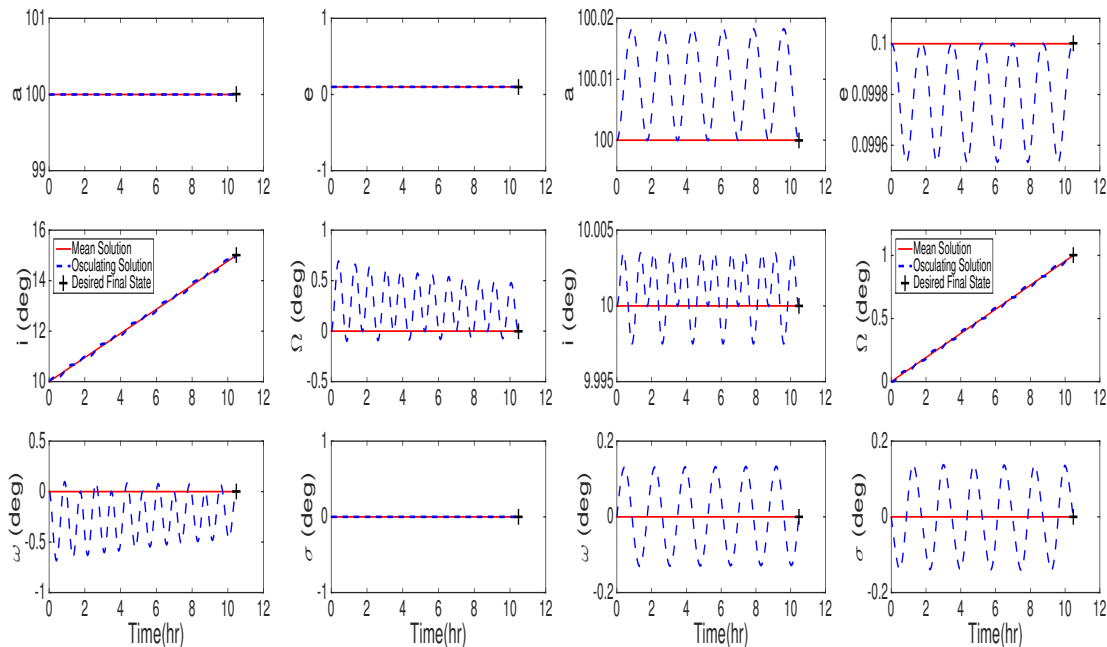
$$\begin{bmatrix} \dot{i} \\ \dot{\Omega} \\ \dot{\omega} \\ \dot{\sigma} \end{bmatrix} = \frac{1}{2} \sqrt{\frac{a}{\mu}} \begin{bmatrix} 0 & 0 & \sqrt{\frac{1}{1-e^2}}(1+e^2) \cos w & -\sin w \\ 0 & 0 & \sqrt{\frac{1}{1-e^2}}(1+e^2) \frac{\sin w}{\sin i} & \frac{\cos w}{\sin i} \\ 2\sqrt{1-e^2} & \frac{2-e^2}{e} & -\frac{\cos i}{\sin i} \frac{(1+e^2)}{\sqrt{1-e^2}} \sin w & -\frac{\cos i}{\sin i} \cos w \\ -6 & -\frac{2-e^2}{e} \sqrt{1-e^2} & 0 & 0 \end{bmatrix} \begin{bmatrix} \alpha_0^R \\ \beta_1^S \\ \alpha_1^W \\ \beta_1^W \end{bmatrix} \quad (2.13)$$

The 4×4 matrix in Eq. (2.13) has a determinant of $\frac{a^2(4-e^2)(e^2+1)}{8\mu^2 \sin i e \sqrt{1-e^2}}$ that becomes 0 only when $e^2 = 2$ or $a = 0$. Therefore, this equation does not have any singularity problem and provides an adequate TFC set to control those orbital elements. Simulation results show that 18 out of those 54 candidate sets are valid to control those orbital elements separately and those 18 sets all consists of zero- and first-order terms: combinations of $\{[\alpha_0^R \ \alpha_1^R], [\alpha_0^R \ \beta_1^S], \text{ or } [\alpha_1^R \ \beta_1^S]\}$ and $\{[\alpha_0^W \ \beta_1^W], [\alpha_0^W \ \beta_2^W], [\alpha_1^W \ \beta_1^W], [\alpha_1^W \ \beta_2^W], [\alpha_2^W \ \beta_1^W], \text{ or } [\alpha_2^W \ \beta_2^W]\}$. Figure 2.4 shows that a valid set is able to control $[i \ \Omega]$ and $[\omega \ \sigma]$ separately to generate a required secular motion. On the contrary, Fig. 2.5 shows how invalid sets fail to control orbital elements separately. The integration results of orbital elements neither match with the osculating orbital elements nor control the secular motion of osculating orbital elements separately.

2.3 Finding the essential TFC set

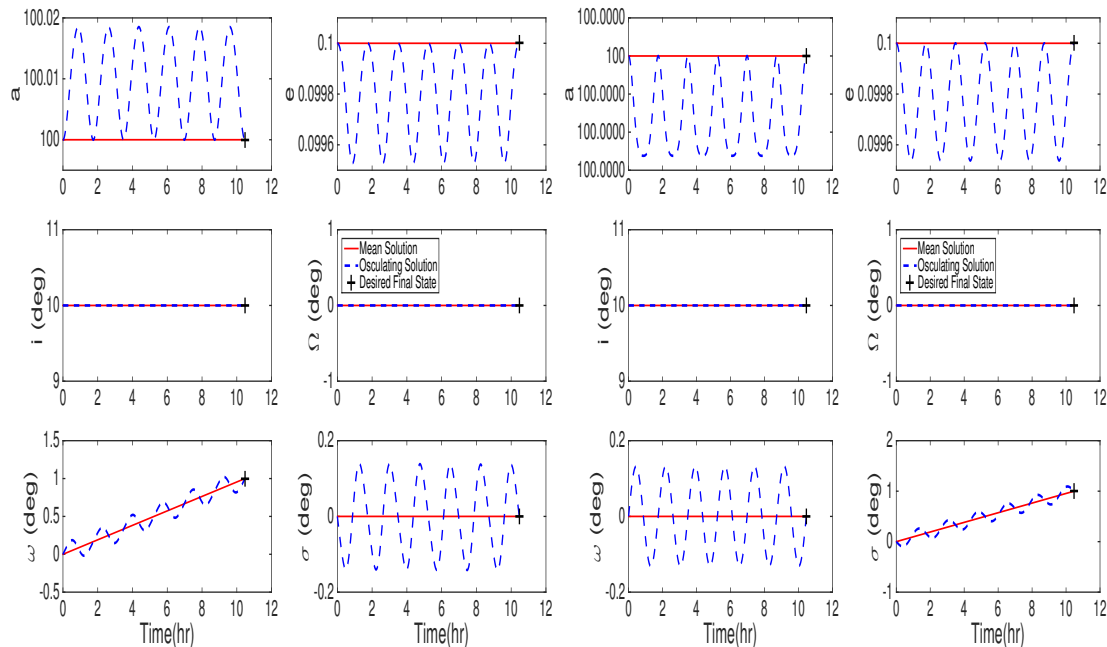
2.3.1 Essential TFC candidate sets

From the analysis in the previous chapter, we can derive 270 different controllable sets that combine 6 out of the 14 TFCs such that they do not have singularity problems for controlling the orbital elements. Out of these 270 sets, there are 36 valid sets that are able to control each orbital element separately. Among those 36 sets, it is possible to find the most efficient sets for controlling the secular motion of orbital elements. To do this we consider the sensitivity of each orbital element



(a) Changing i only

(b) Changing Ω only



(c) Changing ω only

(d) Changing σ only

Figure 2.4: Controlling orbital elements with $[\alpha_0^R, \beta_1^S, \alpha_1^W, \beta_1^W]$

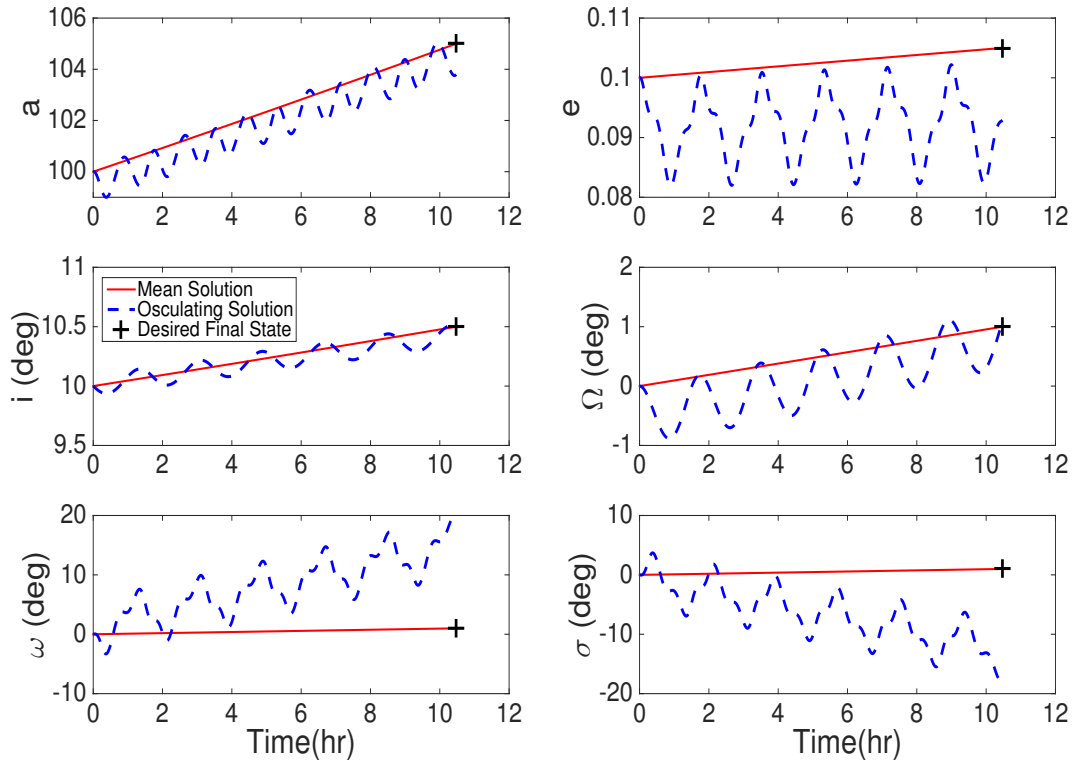
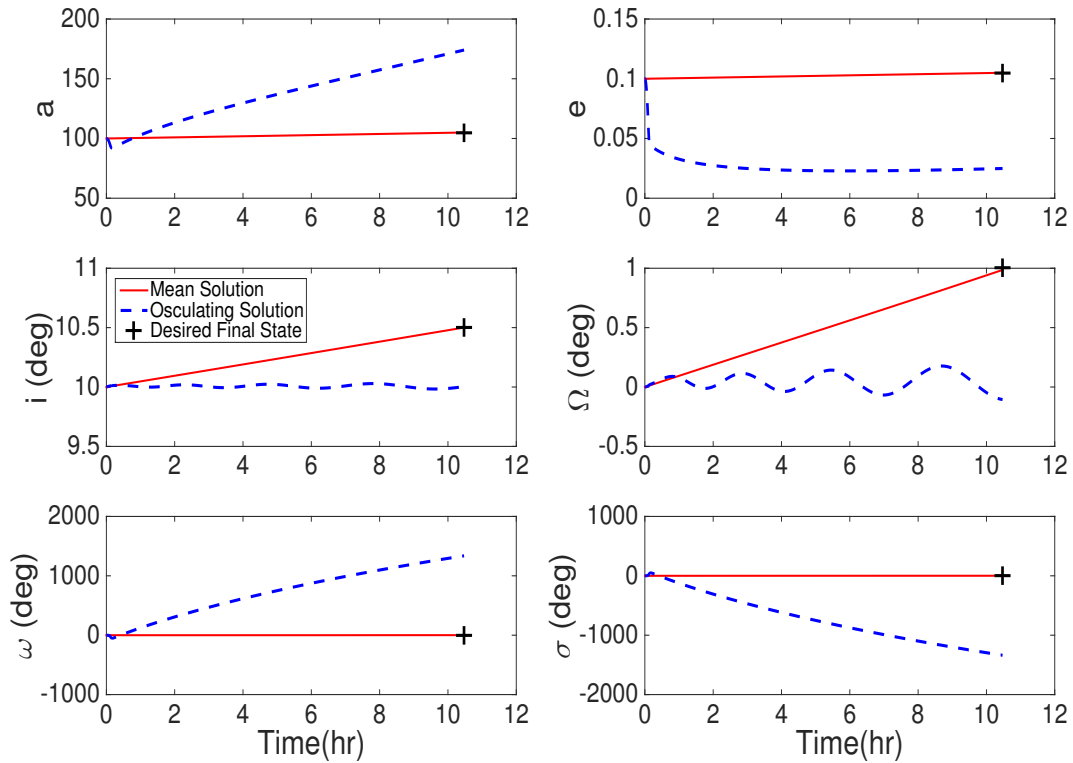
(a) Changing orbital elements with $[\alpha_0^R \beta_2^S \alpha_0^W \beta_1^W]$ (b) Changing orbital elements with $[\alpha_1^R \beta_2^S \alpha_1^W \beta_1^W]$

Figure 2.5: Controlling orbital elements using an invalid set

on the candidate TFCs and the separability of the orbital elements. We find that α_0^S , α_1^S or β_1^R have larger impacts on \dot{a} and \dot{e} , that α_0^R , α_1^R and β_1^S have larger impacts on $[\omega \ \sigma]$, and that $(\alpha_1^W \ \beta_1^W)$ have the largest impact on \dot{i} and $\dot{\Omega}$. Therefore, the essential TFC candidate sets we settle on are:

$$\begin{aligned}\vec{c}_{ess1} &= \left[\alpha_0^R \ \alpha_0^S \ \alpha_1^S \ \beta_1^S \ \alpha_1^W, \beta_1^W \right] \\ \vec{c}_{ess2} &= \left[\alpha_0^R \ \beta_1^R \ \alpha_0^S \ \beta_1^S \ \alpha_1^W, \beta_1^W \right] \\ \vec{c}_{ess3} &= \left[\alpha_0^R \ \alpha_1^R \ \alpha_0^S \ \alpha_1^S \ \alpha_1^W, \beta_1^W \right] \\ \vec{c}_{ess4} &= \left[\alpha_0^R \ \alpha_1^R \ \beta_1^R \ \alpha_0^S \ \alpha_1^W, \beta_1^W \right] \\ \vec{c}_{ess5} &= \left[\alpha_1^R \ \alpha_0^S \ \alpha_1^S \ \beta_1^S \ \alpha_1^W, \beta_1^W \right] \\ \vec{c}_{ess6} &= \left[\alpha_1^R \ \beta_1^R \ \alpha_0^S \ \beta_1^S \ \alpha_1^W, \beta_1^W \right]\end{aligned}$$

Note that none of these candidate sets have an order-2 frequency component. If the candidate set 6, for instance, is used to control orbital elements, their corresponding \vec{G}_{ess6} matrix could be obtained from Eq. (2.8):

$$\dot{\vec{\alpha}}(t) = \vec{G}_{ess6}(\vec{\alpha}) \cdot \vec{c}_{ess6} \quad (2.14)$$

$$\vec{G}_{ess6} = \frac{1}{2} \sqrt{\frac{a}{\mu}} \begin{bmatrix} 0 & 2ae & 4a\sqrt{1-e^2} & 0 & 0 & 0 \\ 0 & 1-e^2 & -3e\sqrt{1-e^2} & 0 & 0 & 0 \\ 0 & 0 & 0 & 0 & \sqrt{\frac{1}{1-e^2}}(1+e^2)\cos w & -\sin w \\ 0 & 0 & 0 & 0 & \sqrt{\frac{1}{1-e^2}}(1+e^2)\frac{\sin w}{\sin i} & \frac{\cos w}{\sin i} \\ -\frac{1}{e}\sqrt{1-e^2} & 0 & 0 & \frac{2-e^2}{e} & -\frac{\cos i}{\sin i} \frac{(1+e^2)}{\sqrt{1-e^2}} \sin w & -\frac{\cos i}{\sin i} \cos w \\ \frac{3e^2+1}{e} & 0 & 0 & -\frac{2-e^2}{e}\sqrt{1-e^2} & 0 & 0 \end{bmatrix} \quad (2.15)$$

Using the inverse of \vec{G}_{ess6} matrix with initial and final states of orbital elements and the transferring

time, the TFC set 6 can be obtained to control the time rate of orbital elements:

$$\begin{bmatrix} \alpha_1^R & \beta_1^R & \alpha_0^S & \beta_1^S & \alpha_1^W & \beta_1^W \end{bmatrix}^T = \vec{G}_{ess6}(\vec{\alpha\epsilon})^{-1} \begin{bmatrix} \dot{a} & \dot{e} & \dot{i} & \dot{\Omega} & \dot{\omega} & \dot{\sigma} \end{bmatrix}^T \quad (2.16)$$

$$\begin{aligned} \vec{c}_{ess6} &= \vec{G}_{ess6}(\vec{\alpha\epsilon})^{-1} \cdot \dot{\vec{\alpha\epsilon}}(t) \\ &= \vec{G}_{ess6}(\vec{\alpha\epsilon})^{-1} \cdot \left[\frac{\vec{\alpha\epsilon}(t_f) - \vec{\alpha\epsilon}(t_0)}{t_f - t_0} \right] \end{aligned} \quad (2.17)$$

In order to find the superior set among those candidate sets, numerical simulations are performed and each candidate set of TFCs is applied to different cases of orbital transfers. Initial and final states for different orbital transfer cases are shown in Table. D.1. There are cases for which the time rates of change in orbital elements are either positive (case 1) or negative (case 2) with different initial eccentricities. The required orbital transfer time for all cases is 6 orbital periods. Case 1 and 2 are simulated by using the normalized gravitational parameter ($\mu = 1$) while case 3 is simulated with a unnormalized gravitational parameter. All simulations performed in this paper used MATLAB's ode45 function as a numerical scheme. Figure 2.6 shows how each TFC

Table 2.3: Initial and desired final state of orbital elements for different cases

Case #	State	a	e	i, deg	Ω, deg	ω, deg	σ, deg
1 (normalized)	initial	100	0.1	10	0	0	0
	final	105	0.105	10.5	1	1	1
2 (normalized)	initial	100	0.9	10	10	10	0
	final	95	0.855	9.5	9	9	-1
3 (real unit)	initial	7500(km)	0.5	20	20	20	0
	final	7700(km)	0.55	25	25	25	5

set controls the mean orbital elements separately for case 1. Even though the averaged trajectories obtained from each TFC set confirm the secular behaviors of osculating orbital elements quite well, some sets cannot control the mean orbital elements precisely. Subplot (e) and (f) in Fig. 2.6 show that set 5 and 6 induce slight secular drifts from the true mean values due to interfering effects between selected TFCs and the dynamics. For all the cases, set 1 and 2 perform best to control the orbital elements to reach the desired state at the given time.

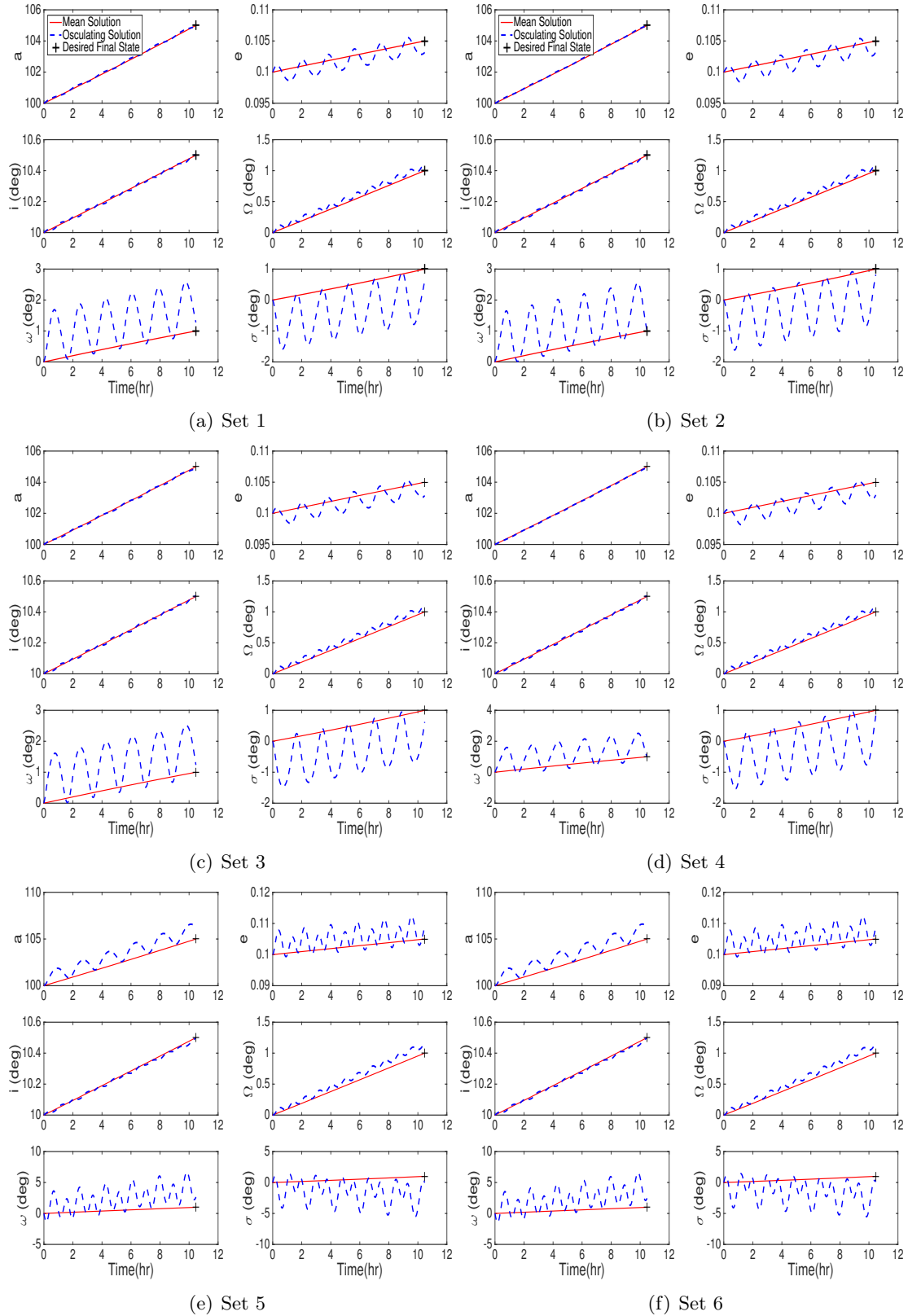


Figure 2.6: Controlling 6 orbital elements using different TFC sets for case 1

2.3.2 Minimum norm solution using 14 TFCs

For a given change in the orbital elements, there are an infinite number of solutions for the 14 TFCs that could induce the specific secular behavior. To obtain a unique solution for the 14 TFC set, the minimum norm criterion can be applied. The minimum norm criterion chooses \vec{c} to minimize $\vec{c}^T \cdot \vec{c}$, which is also subject to Eq. (2.8). Hence, the following cost function is obtained:

$$J(\vec{c}) = \frac{1}{2} \vec{c}^T \cdot \vec{c} + \vec{\lambda}^T \left[\dot{\vec{\alpha}}(t) - \overline{G}(\vec{\alpha}) \cdot \vec{c} \right] \quad (2.18)$$

Using the pseudo-inverse of $\overline{G}(\vec{\alpha})$ -matrix with initial and final states of orbital elements and a transfer time between two states, a minimum norm solution of those 14 TFCs can be obtained analytically which will control the secular motion of trajectory to reach the given final state.

$$\vec{c} = \overline{G}(\vec{\alpha})^T \cdot \left[\overline{G}(\vec{\alpha}) \cdot \overline{G}(\vec{\alpha})^T \right]^{-1} \cdot \left[\frac{\vec{\alpha}(t_f) - \vec{\alpha}(t_0)}{t_f - t_0} \right] \quad (2.19)$$

A numerical example of the minimum norm solution for case 1 is shown in Fig. 2.8, where the mean orbital element with the minimum norm solution is almost identical to the mean orbital element of an averaged solution computed from the essential TFC set.

2.3.3 Cost analysis

A cost analysis has been performed on these essential TFC candidate sets to find which is the most effective one for minimizing the control effort. A cost function is defined to attain a minimum energy solution over one orbit period which will eventually provide the minimized control solution to manage the secular behavior of orbital elements over a long time span:

$$J(\vec{c}) = \frac{1}{2\pi} \int_0^{2\pi} (F_R^2 + F_S^2 + F_W^2)(1 - e \cos E) dE \quad (2.20)$$

By substituting the Fourier series expansion of perturbing force components, which are made up of the 14 TFCs, into Eq. (2.20), the cost function can be simplified due to orthogonality conditions:

$$\begin{aligned}
J(\vec{c}) &= \frac{1}{2\pi} \int_0^{2\pi} (\alpha_0^R + \alpha_1^R \cos E + \beta_1^R \sin E + \alpha_2^R \cos 2E)^2 (1 - e \cos E) dE \\
&\quad + \frac{1}{2\pi} \int_0^{2\pi} (\alpha_0^S + \alpha_1^S \cos E + \beta_1^S \sin E + \alpha_2^S \cos 2E + \beta_2^S \sin 2E)^2 (1 - e \cos E) dE \\
&\quad + \frac{1}{2\pi} \int_0^{2\pi} (\alpha_0^W + \alpha_1^W \cos E + \beta_1^W \sin E + \alpha_2^W \cos 2E + \beta_2^W \sin 2E)^2 (1 - e \cos E) dE \\
&= \frac{1}{2} \left(\vec{c}^T \cdot \vec{c} + (\alpha_0^R)^2 + (\alpha_0^S)^2 + (\alpha_0^W)^2 \right) \\
&\quad - \frac{e}{2} \left(2\alpha_0^R \alpha_1^R + \alpha_1^R \alpha_2^R + 2\alpha_0^S \alpha_1^S + \alpha_1^S \alpha_2^S + \beta_1^S \beta_2^S + 2\alpha_0^W \alpha_1^W + \alpha_1^W \alpha_2^W + \beta_1^W \beta_2^W \right)
\end{aligned} \tag{2.21}$$

Applying this simplified equation to the essential TFC candidate sets that control each orbital element for different cases, the energy costs are computed in Table. 2.4. Overall, set 1 requires the least control effort to reach the desired final state for all three cases. Table. 2.4 also includes the cost of changing mean orbital elements by using minimum norm solution which uses 14 TFCs to control the orbital elements. Note that the event representation with 14-TFC set provides more

Table 2.4: Cost of changing mean orbital elements by using different TFC sets

Case #	Set 1	Set 2	Set 3	Set 4	Set 5	Set 6	Minimum Norm
1	0.1009×10^{-13}	0.1072×10^{-13}	0.1074×10^{-13}	0.1137×10^{-13}	2.8351×10^{-13}	2.8414×10^{-13}	0.10002×10^{-13}
2	0.7562×10^{-13}	0.7841×10^{-13}	44.0102×10^{-13}	44.0381×10^{-13}	0.7554×10^{-13}	0.7833×10^{-13}	0.53213×10^{-13}
3	11.2084×10^{-4}	12.5153×10^{-4}	76.1862×10^{-4}	77.4931×10^{-4}	19.5678×10^{-4}	20.8748×10^{-4}	10.2434×10^{-4}

cost efficient control law than the sets with 6 TFCs. Therefore, it can represents a USE more accurately when the event is related to optimal thrusting.

2.3.4 Essential TFC set

Considering the separability of the orbital elements' secular behavior as well as the cost of control effort, set 1 appears to be the most efficient 6-TFC set to represent a sequence of unmodeled events acting on a satellite:

$$\vec{c}_{ess} = \{\alpha_0^R, \alpha_0^S, \alpha_1^S, \beta_1^S, \alpha_1^W, \beta_1^W\} \tag{2.22}$$

Any orbit transfer can be accomplished by this essential TFC set that defines how the control law needs to be constructed. The selected essential set consists of six TFCs, which are zero- or first-order terms: one from the radial direction, two from the normal direction, and three from the circumferential direction of perturbation as described in Fig. 2.7. The zero-order terms give a base

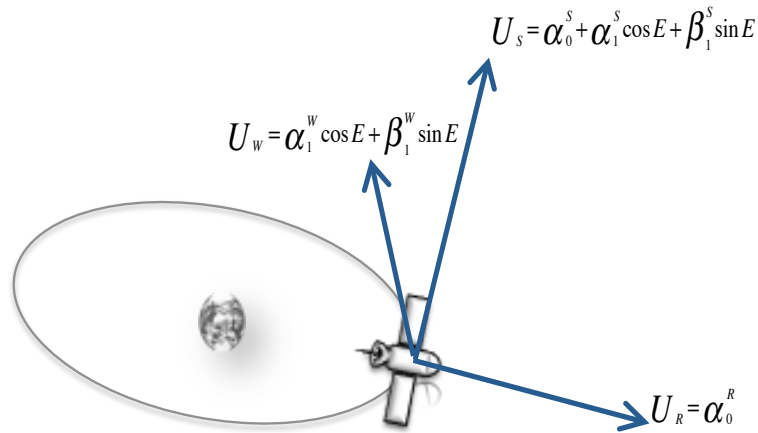


Figure 2.7: Essential TFC set

value which the first-order sinusoidal components oscillate around. Since this set has only a zero-order term in radial component, the perturbing force component in radial direction will be fixed at a certain value. The circumferential components represent periodic effects of the perturbation using the sine and cosine components as well as a fixed term. This set is useful because it is usually optimal to have a controlling force on a circumferential direction rather than the radial direction. The normal component in this set is able to represent a periodic effect of a perturbation on the normal direction. Using this essential TFC set, an efficient control law can be obtained to satisfy the given orbital transfer.

2.4 Different solutions for the essential TFC set to represent an event

2.4.1 Averaged solution

Using the essential TFC set instead of using the full set of 14 TFCs, a control law is obtained from the averaged equation:

$$\vec{\alpha}(t) = \bar{G}_{ess}(\vec{\alpha}) \cdot \vec{c}_{ess} \quad (2.23)$$

where the \bar{G}_{ess} matrix corresponding to the essential TFC set:

$$\bar{G}_{ess} = \frac{1}{2} \sqrt{\frac{a}{\mu}} \begin{bmatrix} 0 & 4a\sqrt{1-e^2} & 0 & 0 & 0 & 0 \\ 0 & -3e\sqrt{1-e^2} & 2\sqrt{1-e^2} & 0 & 0 & 0 \\ 0 & 0 & 0 & 0 & \sqrt{\frac{1}{1-e^2}}(1+e^2)\cos w & -\sin w \\ 0 & 0 & 0 & 0 & \sqrt{\frac{1}{1-e^2}}(1+e^2)\frac{\sin w}{\sin i} & \frac{\cos w}{\sin i} \\ 2\sqrt{1-e^2} & 0 & 0 & \frac{2-e^2}{e} & -\frac{\cos i}{\sin i} \frac{(1+e^2)}{\sqrt{(1-e^2)}} \sin w & -\frac{\cos i}{\sin i} \cos w \\ -6 & 0 & 0 & -\frac{2-e^2}{e}\sqrt{1-e^2} & 0 & 0 \end{bmatrix}$$

Following the same procedure of deriving Eqs. 2.16, 2.17 with the inverse of \bar{G}_{ess} matrix, the averaged solution can be obtained to make mean orbital elements to reach the desired final state.

$$\begin{bmatrix} \alpha_0^R & \alpha_0^S & \alpha_1^S & \beta_1^S & \alpha_1^W & \beta_1^W \end{bmatrix}^T = \bar{G}_{ess}(\vec{\alpha})^{-1} \begin{bmatrix} \dot{a} & \dot{e} & \dot{i} & \dot{\Omega} & \dot{\omega} & \dot{\sigma} \end{bmatrix}^T \quad (2.24)$$

$$\vec{c}_{ess} = \bar{G}_{ess}(\vec{\alpha})^{-1} \cdot \begin{bmatrix} \vec{\alpha}(t_f) - \vec{\alpha}(t_0) \\ t_f - t_0 \end{bmatrix} \quad (2.25)$$

Figure 2.8 shows that mean orbital elements successfully represent the secular behavior of the orbit trajectory, but there is an offset from the true averaged values of osculating orbital elements since the average values of the short period oscillations are not zero. To make a short period correction, the averaged values of short period oscillation have to be added to the mean orbital elements. Using Eqs. 2.3, 2.8 with the essential TFC set, the osculating orbital elements as well as the mean orbital elements at any time t can be calculated:

$$\vec{\alpha}(t) = \vec{\alpha}_0 + \int_0^t [G(\vec{\alpha}, \tau) \cdot \vec{c}_{ess}] d\tau \quad (2.26)$$

$$\vec{\alpha}(t) = \vec{\alpha}_0 + \int_0^t [\bar{G}(\vec{\alpha})_{ess} \cdot \vec{c}_{ess}] d\tau \quad (2.27)$$

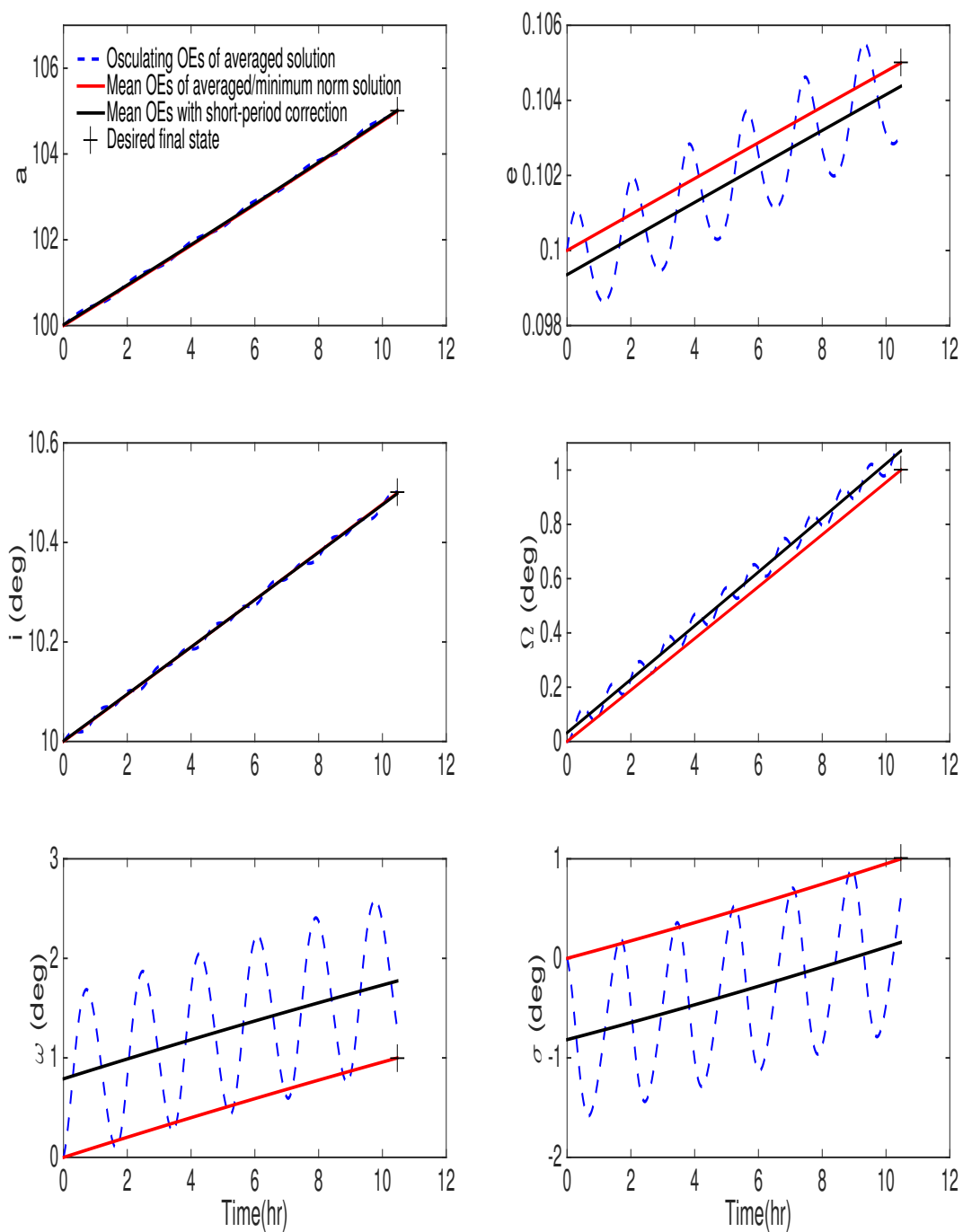


Figure 2.8: Averaged/Minimum norm solutions vs short period corrected solution for case 1

The short period correction term then can be computed by averaging their difference over one orbit period [36]. Since the averaged components, $G(\vec{\alpha\bar{\alpha}})_{ess} \cdot \vec{c}_{ess}$, is constant over one orbit period, it can be simplified:

$$\begin{aligned}\bar{\delta\alpha\bar{\alpha}} &= \frac{1}{T} \int_0^T \int_0^\tau \left[G(\vec{\alpha\bar{\alpha}}, \tau) \cdot \vec{\alpha\bar{\beta}} - \overline{G(\vec{\alpha\bar{\alpha}})_{ess}} \cdot \vec{c}_{ess} \right] d\tau' d\tau \\ &= \frac{1}{T} \int_0^T \int_0^\tau \left[G(\vec{\alpha\bar{\alpha}}, \tau) \cdot \vec{\alpha\bar{\beta}} \right] d\tau' d\tau - \frac{T}{2} \overline{G(\vec{\alpha\bar{\alpha}})_{ess}} \cdot \vec{c}_{ess}\end{aligned}\quad (2.28)$$

This short period correction is compatible with the initial offset correction term used in [11]. This correction term can be added to the original averaged dynamics equation, Eq. (2.27), and forces the mean orbital elements to capture the true mean behavior of an orbit:

$$\vec{\alpha\bar{\alpha}}(t) = \vec{\alpha\bar{\alpha}}_0 + \bar{\delta\alpha\bar{\alpha}} + \left[\overline{G(\vec{\alpha\bar{\alpha}})_{ess}} \cdot \vec{c}_{ess} \right] t \quad (2.29)$$

By using Eq. (2.25), the corrected averaged trajectories obtained from an essential TFC set can be expressed as:

$$\begin{aligned}\vec{\alpha\bar{\alpha}}(t) &= \vec{\alpha\bar{\alpha}}_0 + \bar{\delta\alpha\bar{\alpha}} + \left(\overline{G_{ess}(\vec{\alpha\bar{\alpha}})} \cdot \overline{G_{ess}(\vec{\alpha\bar{\alpha}})}^{-1} \cdot \left(\frac{\vec{\alpha\bar{\alpha}}(t_f) - \vec{\alpha\bar{\alpha}}_0}{t_f} \right) \right) t \\ &= \vec{\alpha\bar{\alpha}}_0 + \bar{\delta\alpha\bar{\alpha}} + \left(\frac{\vec{\alpha\bar{\alpha}}(t_f) - \vec{\alpha\bar{\alpha}}_0}{t_f} \right) t\end{aligned}\quad (2.30)$$

Figure 2.8 shows how the short period correction term, Eq. (2.28), yields more reliable mean values of orbital elements compared to the mean orbital elements from the averaged solution, Eq. (2.25), or the minimum norm solution, Eq. (2.19), without the correction term.

2.4.2 Non-averaged solution

The averaged solution is focusing on orbital mechanics over long-duration while excluding short-periodic behavior which only reflects local dynamics of orbital elements within each transfer revolution. Due to this fact, the osculating orbital elements driven by the averaged solution show large errors in final state after a long transfer time. Therefore, it is necessary to obtain short-period information to reach our desired final state using the essential TFC set. To match the final state

requirement, we need to extract the osculating orbital elements from the orbital dynamics using the essential TFC set. The osculating orbital elements at a future time, which consist of short periodic variations as well as the secular variations, could be obtained from Eq. (2.3):

$$\begin{aligned}\vec{\alpha}(t) &= \vec{\alpha}_0 + \int_0^t G(\vec{\alpha}, \tau)_{ess} d\tau \cdot \vec{c}_{ess} \\ &= \vec{\alpha}_0 + \mathcal{G}_{ess} \cdot \vec{c}_{ess}\end{aligned}\quad (2.31)$$

where $G(\vec{\alpha}, \tau)_{ess}$ is a 6×6 block matrix of $G(\vec{\alpha}, \tau)$ that contains the frequency terms that correspond to the selected TFCs of the essential set. Integrating this $G(\vec{\alpha}, \tau)_{ess}$ over time using eccentric anomaly, their corresponding \mathcal{G}_{ess} matrix is obtained:

$$\begin{aligned}\mathcal{G}_{ess} &= \int_0^t G(\vec{\alpha}, \tau)_{ess} d\tau \\ &= \frac{1}{n} \int_0^E G(\vec{\alpha}, \tau)_{ess} (1 - e \cos E) dE\end{aligned}\quad (2.32)$$

The matrix expression for Eq. (2.32) is shown in the Appendix A. When computing the integration of $G(\vec{\alpha}, \tau)_{ess}$ over time, the orbital elements are assumed to be constant. This \mathcal{G}_{ess} matrix with Eq. (2.31) gives a non-averaged solution. Using the inverse of \mathcal{G}_{ess} matrix with initial and final states of orbital elements and the transfer time, the essential TFC solution can be obtained to control the time rate of osculating orbital elements.

$$\vec{c}_{ess} = \mathcal{G}_{ess}^{-1} [\vec{\alpha}(t) - \vec{\alpha}_0] \quad (2.33)$$

The osculating orbital elements solution computed with the essential TFC set matches the secular behavior of the mean orbital elements obtained by averaged equations. As expected, the final state obtained from the osculating orbital elements solution is closer to the desired final state, which is shown in Table 2.5 and Fig. 2.9.

2.4.3 Numerically updated solution

In orbital element space : So far, the approximate values of the essential TFC set are obtained analytically by using either mean orbital elements or osculating orbital elements.

$$\text{Averaged solution : } \vec{c}_{ess} = \left[\frac{1}{2\pi} \int_0^{2\pi} G_{ess}(\vec{\alpha}, t)(1 - e \cos E) dE \right]^{-1} \cdot \left[\frac{\vec{\alpha}(t_f) - \vec{\alpha}(t_0)}{t_f - t_0} \right] \quad (2.34)$$

$$\text{Non-averaged solution : } \vec{c}_{ess} = \left[\frac{1}{n} \int_0^E G_{ess}(\vec{\alpha}, t)(1 - e \cos E) dE \right]^{-1} [\vec{\alpha}(t_f) - \vec{\alpha}(t_0)] \quad (2.35)$$

The above two solutions are obtained by assuming that the orbital elements stay constant over an orbital transfer during integration. This assumption makes errors in the TFC calculations, which eventually induces noticeable position and velocity errors at the final states especially when there is large difference between the two states. Those errors can be corrected by using a numerical iteration method to update the TFC values. Either the averaged or non-averaged solutions can serve as a good initial estimate to initiate the numerical computation. Using this initial estimate as a starting point, the two-point boundary value problem between the states and epochs can be solved using the Newton iteration [28] and using the numerically integrated Gauss equations with the updated TFC values. The following section describes how to update TFC values in the iteration process.

Equation 2.3 can be rewritten by using the essential coefficient set in the Gaussian equation:

$$\begin{aligned} \vec{\alpha}(t) &= \vec{\alpha}_0 + \int_0^t [G_{ess}(\vec{\alpha}, \tau) \cdot \vec{c}_{ess}] d\tau \\ &= \vec{\alpha}_0 + \mathcal{G}_{ess}(\vec{\alpha}, t) \cdot \vec{c}_{ess} \end{aligned} \quad (2.36)$$

By defining $\psi(t_0, t_f, \vec{\alpha}_0, \vec{c}_{ess}) = \vec{\alpha}_0 + \mathcal{G}_{ess}(\vec{\alpha}, t) \cdot \vec{c}_{ess}$ and using the Taylor expansion, an updated solution flow can be expressed:

$$\psi(t_0, t_f, \vec{\alpha}_0, \vec{c}_{ess} + \delta \vec{c}) = \psi(t_0, t_f, \vec{\alpha}_0, \vec{c}_{ess}) + \frac{\partial \psi}{\partial \vec{c}_{ess}} \cdot \delta \vec{c}_{ess} + H.O.T \quad (2.37)$$

To drive $\psi(t_0, t_f, \vec{\alpha}_0, \vec{c}_{ess} + \delta \vec{c})$ very close to the desired final state values ($\vec{\alpha}_{desired}$), the following

condition has to be satisfied:

$$\vec{\alpha}_{desired} - \psi(t_0, t_f, \vec{\alpha}_0, \vec{c}_{ess}) - \frac{\partial \vec{\psi}}{\partial \vec{c}_{ess}} \cdot \delta \vec{c}_{ess} - H.O.T = 0 \quad (2.38)$$

Ignoring the high order terms in the Taylor's series and defining $\Phi_c(t, t_0) = \frac{\partial \vec{\psi}}{\partial \vec{c}_{ess}}$, a proper \vec{c} can be obtained by updating $\delta \vec{c}$ numerically :

$$\delta \vec{c} = \Phi_c^{-1}(t_f, t_0) [\vec{\alpha}_{desired} - \psi(t_0, t_f, \vec{\alpha}_0, \vec{c}_{ess})] \quad (2.39)$$

$$\Phi_c(t, t_0) = \frac{\partial \vec{\psi}}{\partial \vec{c}_{ess}} = \mathcal{G}_{ess}(\vec{\alpha}, t), \quad \Phi_c(0, 0) = 0 \quad (2.40)$$

$$\begin{aligned} \dot{\Phi}_c(t, t_0) &= \frac{d}{dt} \left[\frac{\partial \vec{\psi}}{\partial \vec{c}_{ess}} \right] = \frac{\partial}{\partial \vec{c}_{ess}} \left[\frac{d\vec{\psi}}{dt} \right] \\ &= \frac{\partial (G_{ess}(\vec{\alpha}, t) \cdot \vec{c}_{ess})}{\partial \vec{c}_{ess}} \\ &= \frac{\partial (G_{ess}(\vec{\alpha}, t) \cdot \vec{c}_{ess})}{\partial \vec{\alpha}} \cdot \Phi_c + G_{ess}(\vec{\alpha}, t) \end{aligned} \quad (2.41)$$

Numerical simulations are performed on the previous three different cases with the different solutions which also includes the minimum norm solution for comparison purposes. The resulting final position and velocity errors are shown in Table 2.5. It clearly shows that the numerically updated solution provides the most precise solution of the essential TFC values that control the orbital elements to meet the desired final state. The minimum norm solution which uses 14 TFCs works better than the averaged solution, but is less efficient than non-averaged solutions which uses 6 TFCs. Using the numerical iteration method, the essential TFC set is able to provide a precise control law to meet the final condition. Figure 2.9 shows different trajectories obtained by numerical integrations of the orbital elements using the Gauss equations with different solutions for case 3. They all have similar secular behaviors, but the numerically updated solution gives a more precise solution. So far, the maneuver cases have been relevant for orbit elements under an assumption that the thrust magnitude is relatively small. However, a difficulty arises to get a converged solution when the orbit is perturbed by a large thrust maneuvers. If a thrust acceleration is relatively large, then the orbital elements change significantly within one orbit period and the

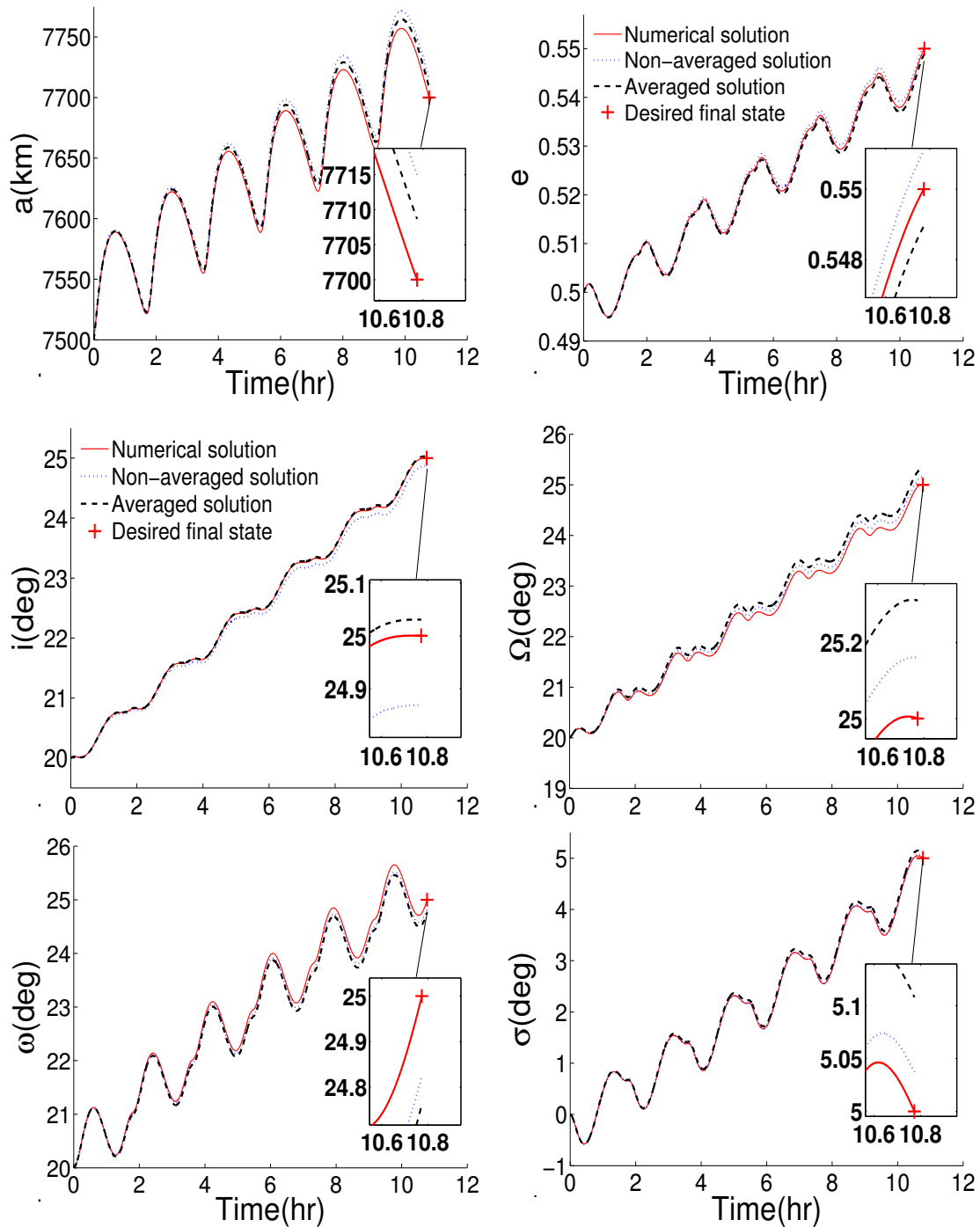


Figure 2.9: Controlling 6 orbital elements using different TFC solutions for Case 3

Table 2.5: Final position and velocity errors by using different TFC solutions

Case #		Averaged	Non-averaged	Numerically Updated	Minimum Norm
1 normalized	Pos	2.0293	0.3801	1.3492×10^{-13}	1.5306
	Vel	1.5846×10^{-3}	3.1838×10^{-4}	1.2471×10^{-16}	1.1690×10^{-3}
2 normalized	Pos	24.8329	18.3023	9.8100×10^{-12}	19.6567
	Vel	0.0291	0.0214	1.0356×10^{-14}	0.0226
3 real unit	Pos(m)	5.8951×10^9	3.8949×10^9	0.2007	4.3542×10^9
	Vel(m/s)	427.5610	297.5106	0.1515×10^{-3}	331.2419

numerically updated solution fails or takes longer to be converged. Figure 2.10(b) shows that neither the averaged nor the non-averaged solution can be used as a good initial estimate to obtain a converged numerical solution. To avoid this problem, the numerically updated solution can be obtained in the Cartesian space where the state of position and velocity does not change dramatically even with larger maneuvers.

In Cartesian space : The TFC event representation can be extended to non-averaged thrusting between Cartesian positions and velocities, which indicates a certain level of universality. In the Cartesian coordinate, the equation of motion for a satellite can be rewritten by using the essential coefficient set :

$$\dot{\vec{X}}(t) = F(\vec{X}, t) + B \cdot T(\vec{X}, t) \cdot S \cdot c_{ess} \quad (2.42)$$

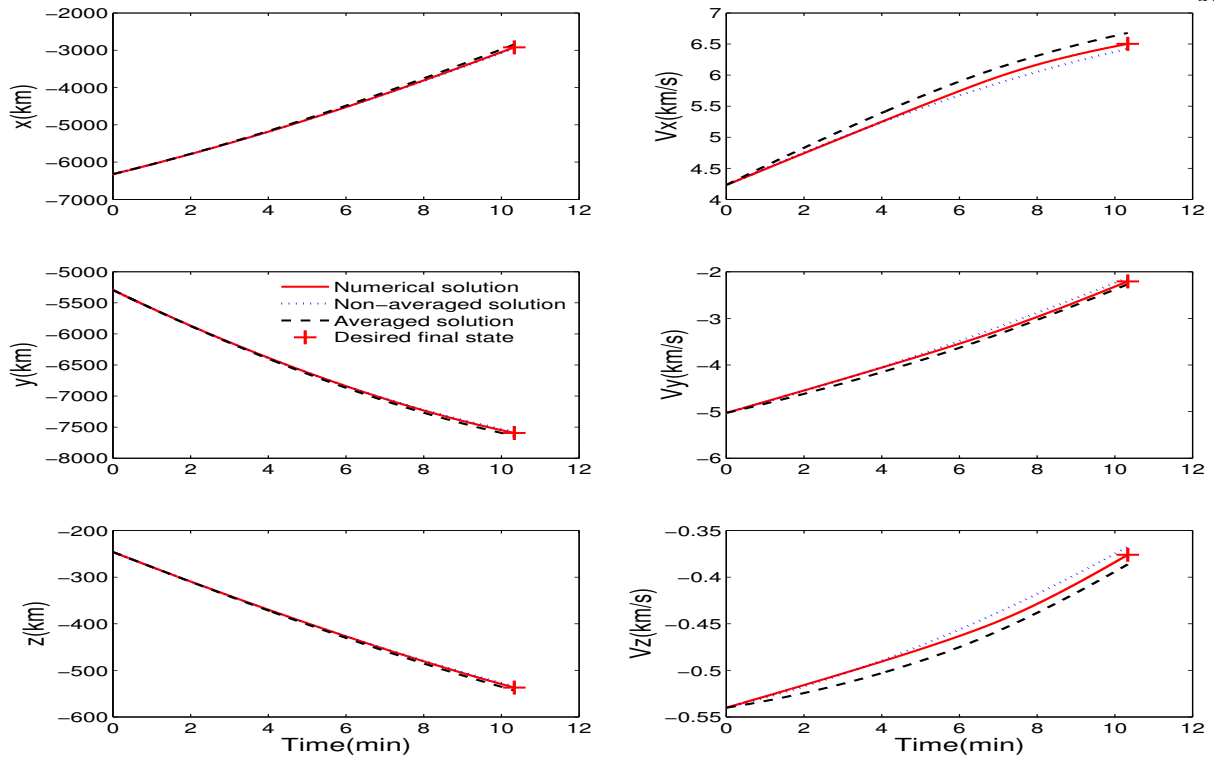
in which \vec{X} is the state vector containing the position and the velocity elements :

$$\vec{X} = \begin{bmatrix} \vec{r} \\ \dot{\vec{r}} \end{bmatrix}, F(\vec{X}) = \begin{bmatrix} \vec{r} \\ -\frac{\mu \vec{r}}{|\vec{r}|^3} \end{bmatrix}, B = \begin{bmatrix} 0_{3 \times 3} \\ I_{3 \times 3} \end{bmatrix}$$

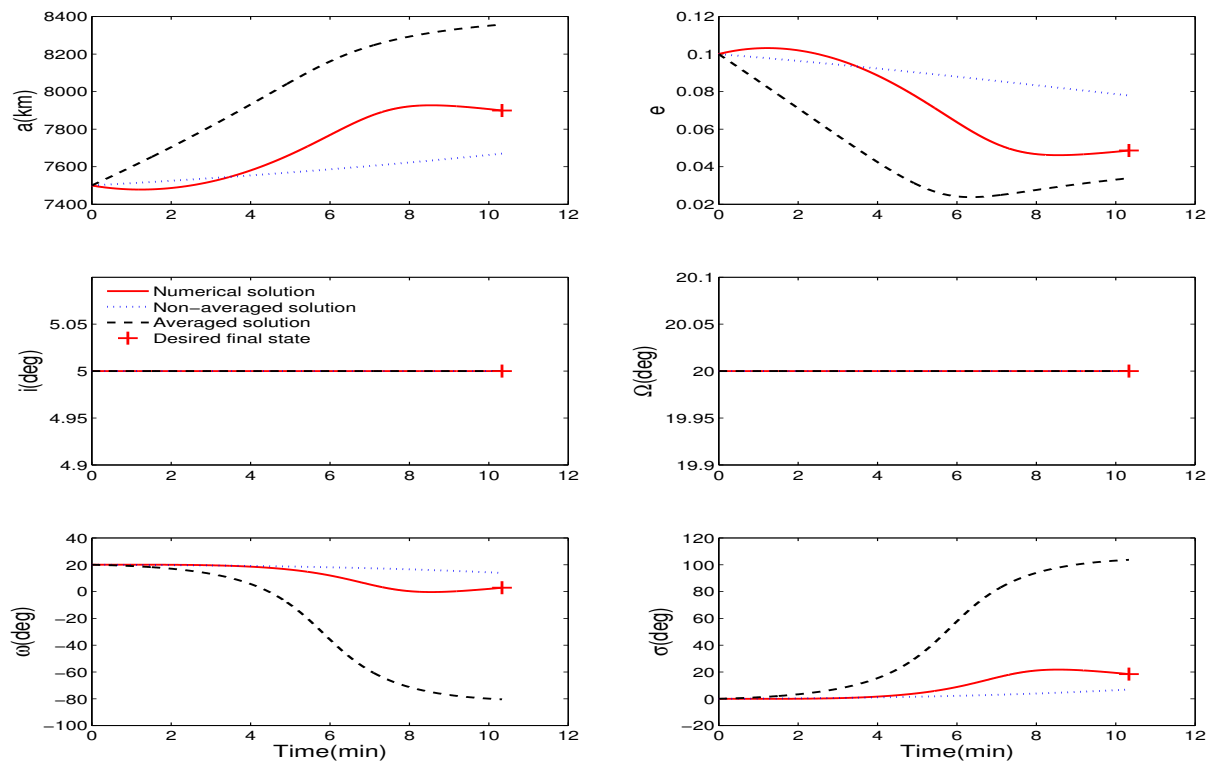
$$T = \begin{bmatrix} \hat{r} & \hat{s} & \hat{w} \end{bmatrix}$$

$$S = \begin{bmatrix} 1 & 0 & 0 & 0 & 0 & 0 \\ 0 & 1 & \cos E & \sin E & 0 & 0 \\ 0 & 0 & 0 & 0 & \cos E & \sin E \end{bmatrix}$$

By defining $\psi(t; \vec{X}_0, t_0, c_{ess}) = \vec{X}(t)$ and using the Taylor expansion, an updated solution flow can



(a) Cartesian Space



(b) Orbital Element Space

Figure 2.10: Trajectory estimation in different orbit space for a high thrust maneuver ($\Delta V 200 m/s$)(Initial Condition : $a(7500\text{km})$, $e(0.1)$, $i(5^\circ)$, $\Omega(20^\circ)$, $\omega(20^\circ)$, $\nu(180^\circ)$)

be expressed:

$$\begin{aligned} & \psi(t; \vec{X}_0, t_0, c_{ess} + \delta c_{ess}) \\ &= \psi(t; \vec{X}_0, t_0, c_{ess}) + \frac{\partial \psi}{\partial c_{ess}} \cdot \delta c_{ess} + H.O.T \end{aligned} \quad (2.43)$$

The goal is to find a proper δc_{ess} to make $\psi(t_f; \vec{X}_0, t_0, c_{ess} + \delta c_{ess})$ be close to the desired final state (\vec{X}_f) :

$$\begin{aligned} & \vec{X}_f - \psi(t_f; \vec{X}_0, t_0, c_{ess}) \\ &= \frac{\partial \psi}{\partial c_{ess}} \cdot \delta c_{ess} + H.O.T = 0 \end{aligned} \quad (2.44)$$

Ignoring the H.O.T in the Taylor's series and defining $\Gamma(t, t_0) = \frac{\partial \psi}{\partial c_{ess}}$, δc_{ess} can be updated in the Cartesian space :

$$\delta c_{ess} = \Gamma^{-1}(t_f, t_0) \left[\vec{X}_f - \psi(t_f; \vec{X}_0, t_0, c_{ess}) \right] \quad (2.45)$$

$$\Gamma(t, t_0) = \frac{\partial \psi}{\partial c_{ess}}, \quad \Gamma(0, 0) = 0 \quad (2.46)$$

$$\dot{\Gamma}(t, t_0) = \frac{d}{dt} \left[\frac{\partial \psi}{\partial c_{ess}} \right] \quad (2.47)$$

$$\begin{aligned} &= \frac{\partial}{\partial c_{ess}} \left(F(\vec{X}) + B \cdot T(\vec{X}) \cdot S \cdot c_{ess} \right) \\ &= \frac{\partial F(\vec{X})}{\partial \vec{X}} \cdot \frac{\partial \vec{X}}{\partial c_{ess}} + B \cdot T(\vec{X}) \cdot S \\ &\quad + B \cdot \frac{\partial T(\vec{X})}{\partial \vec{X}} \cdot \frac{\partial \vec{X}}{\partial c_{ess}} \cdot S \cdot c_{ess} \end{aligned}$$

Assuming that the change of the transformation matrix with respect to the changes of the state is so small, $\frac{\partial T(\vec{X})}{\partial \vec{X}}$ can be ignored and Eq. 2.47 is simplified :

$$\dot{\Gamma}(t, t_0) = \frac{\partial F(\vec{X})}{\partial \vec{X}} \cdot \Gamma(t, t_0) + B \cdot T(\vec{X}) \cdot S \quad (2.48)$$

With updated δc_{ess} , the numerically updated solution, $c_{essN} = c_{ess} + \delta c_{ess}$, of the essential TFC values can be computed in the Cartesian space.

Numerical simulations are performed for a high thrust ($\Delta V : 200 \text{ m/s}$) maneuver case. The maneuver is performed 5 minutes after the initial time with 10 m/s^2 thrust acceleration for 20 seconds. The numerically updated solution is easily converged in the Cartesian space and the converged solution of the essential TFCs drives the orbital trajectory to the desired state at a given time, which is shown at Fig. 2.10(a). After obtaining the numerically updated solution from the Cartesian space, it can be applied into the orbit element space. Figure 2.10(b) shows that the essential TFC values obtained in the Cartesian space also work well in the orbital element space. It verifies that the essential TFC set provides a finite basis representation of arbitrary thrust acceleration in any coordinate frame.

2.5 Summary

By applying an averaging method to the Gauss equations, the perturbing accelerations acting on a satellite can be represented as a function of 14 constant thrust-Fourier-coefficients (TFCs). Time rates of change of mean orbital elements due to these TFCs are analyzed and the representation of these thrust coefficients as a function of the change in orbit states is studied. Among all sets of 6 TFCs, some exhibit superior control of the elements while others induce undesired secular drifts in other orbital elements and require more thrust expenditure to control the secular motion. To determine which sets of TFCs allow us to efficiently control the secular behavior of the orbital elements, the controllability and the separability of the orbital elements under these controls, and the sensitivity of the TFCs are analyzed. We also perform a cost analysis of the various minimal TFC sets that we find. A selected minimum set of 6 TFCs is able to provide a finite basis representation of arbitrary orbital maneuvers that allow us to dynamically interpolate between orbital states. It uniquely represents an efficient control law to achieve a desired final state and reduces computational requirements significantly. For a given essential TFC set, we describe 3 different solution techniques to compute TFC values; an averaged solution, a non-averaged solution and a numerically updated solution. Simulation results show that all three solutions drive an orbit trajectory to reach a desired final state with some errors, with the numerically updated solution yielding

the least position/velocity errors at a final time. Besides, the minimum norm solution of 14-TFC set is also derived and its performance is compared. In the end, the TFC event representation approach is extended to non-averaged Cartesian space to show its applicability.

The TFC event representation technique has potential applications to various problems of interest. It provides a very simple way of reconstructing the fundamental elements of a sequence of control laws. Given a non-ballistic trajectory between two epochs due to a USE (or due to a maneuver), it is possible to ‘interpolate’ between these states using a unique control law using TFCs. Mission designers could apply the essential TFC set to efficiently compute the control acceleration to reach a desired destination. This preliminary analyses of a canonical control law can provide us with a basic understanding of the perturbing effects of thrust on a nominal trajectory. For space situational awareness (SSA), the TFC event representation can be applied for orbit determination problems to estimate the perturbing elements of a USE with sparse observations. By interpolating dynamically between states across a USE, we can propagate orbit uncertainty through the reconstructed dynamics using various TFC sets. It allows us to make use of *a priori* orbit information and map it to a specific epoch after an event. In addition, the represented orbit dynamics using TFCs can be used to improve the quality of orbit fits through an unknown event period.

Chapter 3

Event Representation Based Orbit Determination Across Unmodeled Space Events Using Thrust-Fourier-Coefficients

A limiting factor for space catalog maintenance is the modeling and estimation of unknown perturbations acting on orbiting satellites. Tracking Earth orbiting satellites in the catalog is made difficult when these objects go through an unknown and unmodeled space event (USE). Without accounting for unknown perturbations, the accuracy of state estimation across the event will be degraded, which causes them to either be refit from scratch or “lost”. At this stage, a post-event analysis tries to recover the subsequent orbit based on the latest orbit solution and tracking data in order to assess possible risks and take appropriate actions [29]. However, when there is no measurement available during the event, maintaining orbit determination (OD) across USEs and obtaining reliable post-event orbit estimations will be a challenging task. In order to update state and uncertainty information across unknown events, the pre-event OD estimation has to be tied together with the post-event observation by representing an unknown event solely based on orbital state changes.

A conventional method used at the time of encountering an unknown event is to use the least square filter over a span following the event [30]. However, OD across any space event is generally not performed in the least square method due to its complexities introduced in a computation of the inverse of the information matrix [4, p. 229]. One of the common methods to perform OD across an unknown event is to add process noises to the sequential estimation filter in order to compensate for unknown perturbations [31][32][33]. This approach is usually a time-consuming

process to find valid parameters to compensate for unknown dynamics of a USE. Even if the OD filter with process noise can estimate an unknown acceleration, this approach does not provide any dynamical insight of the unknown orbit dynamics for a given event. Moreover, this method requires observation throughout the USE period, which often cannot be achieved in a data-starved space surveillance environment. To deal with a USE in data sparse environments, new approaches have been introduced to reconstruct unknown space events by using minimum fuel cost functions [9], or applying optimal control performance metrics [8][10]. However, the perturbing acceleration related to a space event may not be always optimal, specially for a USE caused by structural deployment, thrust malfunction, explosions, or collision with space objects.

Achieving reliable post-event state estimation given a small number of post-event measurements is a difficult problem. By applying the event representation technique using thrust-Fourier-Coefficients (TFCs), we present an alternative way to maintain OD across a USE in data sparse environments. Since the orbital motion has to follow its dynamic law, it is possible to model the unknown dynamics by representing a space event as an equivalent orbit maneuver using TFCs. This chapter aims to show how to use a TFC set to represent an unknown space event and to adapt it into OD filter formulations capable of state and uncertainty estimation across unknown events. To accomplish this goal, it is necessary to answer the fundamental question of how the propagated covariance matrices are different if they take different paths to reach a given final state from the same initial state. After verifying that the covariance propagation in the linear region is independent of orbit dynamics that connect two separate states via different paths, the event representation can be used in the development of different OD filters with TFCs. Therefore, this chapter consists of two main chapters. Chapter 3.1 is devoted to theoretical proof to enable us to apply the event representation in uncertainty propagation. It summarizes analytical aspects of uncertainty propagation using a dynamics representation of an unknown event, and verifies that the covariance propagation using an event representation is valid in a linear region. Chapter 3.2 presents the development of a batch filter using the event representation with different TFC sets and demonstrates the proposed filter's OD performance across an unknown space event.

3.1 Uncertainty propagation via event representation

While there have been various ways to represent a USE, relatively little attention has been paid to an analytical framework of uncertainty propagation using an event representation. This chapter provides a theoretical proof to enable to use the event representation in implementing an OD filter across unknown events. This analytic study verifies that a reconstructed dynamics model with an event representation allows us to map the *a priori* covariance matrix to a specific epoch even through an unknown event. This method is also validated by numerical simulations and provides a basic principle from which to develop a batch algorithm for the uncertainty estimation in chapter 3.2.

3.1.1 Analytical study

Given an initial orbital state (\vec{X}_0) and a final orbital state (\vec{X}_f), the true trajectory connecting these two states is said to be \vec{X}_T . In general, the true dynamics for satellite motion under unknown space events can be described with the perturbing thrust acceleration arising linearly in the equations [34]:

$$\dot{\vec{X}}_T = \vec{F}(\vec{X}_T, t) + B \cdot \vec{U}_T(t) \quad (3.1)$$

$$\frac{d}{dt} \begin{bmatrix} \vec{r}_T(t) \\ \vec{v}_T(t) \end{bmatrix}_{6 \times 1} = \begin{bmatrix} \dot{\vec{r}}_T(t) \\ \dot{\vec{v}}_T(t) \end{bmatrix}_{6 \times 1} + \begin{bmatrix} 0_{3 \times 3} \\ I_{3 \times 3} \end{bmatrix}_{6 \times 3} \cdot \vec{U}_T(t)_{3 \times 1} \quad (3.2)$$

where \vec{X}_T is the true satellite position and velocity state, $\vec{F}(\vec{X}_T, t)$ are the known dynamics, B is the projection matrix of perturbing acceleration onto orbital state, and $\vec{U}_T(t)$ is the true perturbing acceleration for an unknown event. By representing an unknown space event with a modeled thrust acceleration, an interpolated trajectory, $\vec{X}_I(t)$, connecting \vec{X}_0 and \vec{X}_f can be written in the form :

$$\dot{\vec{X}}_I = \vec{F}(\vec{X}_I, t) + B \cdot \vec{U}_I(t) \quad (3.3)$$

in which $\vec{U}_I(t)$ is a modeled unknown acceleration that drives the initial state to a given final state at a given time ($\vec{X}_I(t_f) = \vec{X}_T(t_f)$). Figure 3.1 illustrates the relationship between the true

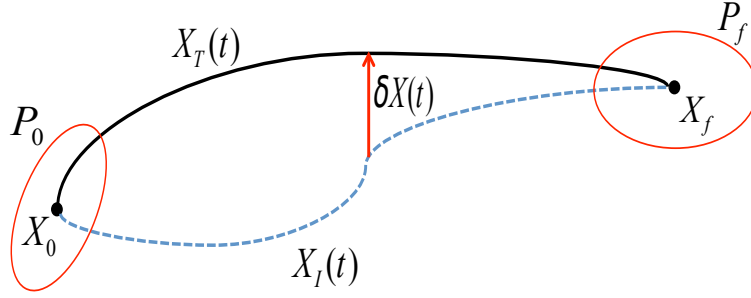


Figure 3.1: True vs interpolated trajectories

trajectory and the interpolated trajectory. The difference between the true and the interpolated trajectories and the difference between the true and the modeled unknown accelerations are defined as :

$$\delta \vec{X}(t) = \vec{X}_T(t) - \vec{X}_I(t) \quad (3.4)$$

$$\delta \vec{U}(t) = \vec{U}_T(t) - \vec{U}_I(t) \quad (3.5)$$

By expanding the true dynamics equation in Taylor's series and neglecting the terms of order higher than the first, Eq. (3.1) can be rewritten as :

$$\dot{\vec{X}}_T = \vec{F}(\vec{X}_T, t) + B \cdot \vec{U}_T(t) \quad (3.6)$$

$$= \vec{F}(\vec{X}_I(t) + \delta \vec{X}(t)) + B \cdot [\vec{U}_I(t) + \delta \vec{U}(t)] \quad (3.7)$$

$$= \vec{F}(\vec{X}_I, t) + B \cdot \vec{U}_I(t) + \frac{\partial \vec{F}}{\partial \vec{X}} \Big|_{\vec{X}_I} \cdot \delta \vec{X}(t) + B \cdot \delta \vec{U}(t) \quad (3.8)$$

$$= \dot{\vec{X}}_I + \frac{\partial \vec{F}}{\partial \vec{X}} \Big|_{\vec{X}_I} \cdot \delta \vec{X}(t) + B \cdot \delta \vec{U}(t) \quad (3.9)$$

Defining $A_I(t) = \frac{\partial \vec{F}}{\partial \vec{X}} \Big|_{\vec{X}_I(t)}$, the linearized dynamics equation of state difference can be obtained :

$$\dot{\delta \vec{X}} = A_I(t) \cdot \delta \vec{X}(t) + B \cdot \delta \vec{U}(t) \quad (3.10)$$

where the first term propagates the state difference through the known dynamics and the second term indicates the difference due to the acceleration modeling error. The complete solution of this linear differential equation has the following form [35] :

$$\delta \vec{X}(t) = \Phi_d(t, t_0) \delta \vec{X}_0 + \Phi_d(t, t_0) \int_{t_0}^t \left[\Phi_d^{-1}(\tau, t_0) B \cdot \delta \vec{U}(\tau) \right] d\tau \quad (3.11)$$

in which $\Phi_d(t, t_0)$ is the State Transition Matrix (STM) that maps the initial state difference between the true and the interpolated trajectories from t_0 to t :

$$\Phi_d(t, t_0) = \frac{\partial(\delta\vec{X}(t))}{\partial(\delta\vec{X}(t_0))} \quad (3.12)$$

Since both the true and the interpolated trajectories start from a same initial state ($\delta\vec{X}_0 = 0$) and end at the same final state, it must satisfy the following constraint derived from Eq. (3.11) :

$$\delta\vec{X}(t_f) = \Phi_d(t_f, t_0) \delta\vec{X}_0 + \Phi_d(t_f, t_0) \int_{t_0}^{t_f} \left[\Phi_d^{-1}(\tau, t_0) B \cdot \delta\vec{U}(\tau) \right] d\tau \quad (3.13)$$

$$= \int_{t_0}^{t_f} \left[\Phi_d(t_f, t_0) \Phi_d^{-1}(\tau, t_0) B \cdot \delta\vec{U}(\tau) \right] d\tau \quad (3.14)$$

$$= \int_{t_0}^{t_f} \left[\Phi_d(t_f, \tau) B \cdot \delta\vec{U}(\tau) \right] d\tau = 0 \quad (3.15)$$

In order to show that the STM propagated to the final time by the modeled dynamics is close to the STM computed from the true dynamics, the full differential equation of the state difference between two trajectories is investigated :

$$\delta\dot{\vec{X}}(t) = \dot{\vec{X}}_T(t) - \dot{\vec{X}}_I(t) \quad (3.16)$$

$$= \vec{F}(\vec{X}_T, t) + B \cdot \vec{U}_T(t) - \vec{F}(\vec{X}_I, t) - B \cdot \vec{U}_I(t) \quad (3.17)$$

$$= \vec{F}(\vec{X}_I + \delta\vec{X}, t) - \vec{F}(\vec{X}_I, t) + B \cdot (\vec{U}_T(t) - \vec{U}_I(t)) \quad (3.18)$$

$$= \frac{\partial\vec{F}}{\partial\vec{X}} \Big|_{\vec{X}_I} \cdot \delta\vec{X}(t) + \frac{1}{2!} \left(\frac{\partial^2\vec{F}}{\partial\vec{X}^2} \Big|_{\vec{X}_I} \cdot \delta\vec{X}(t) \cdot \delta\vec{X}(t) \right) + \dots + B \cdot \delta\vec{U}(t) \quad (3.19)$$

$$= \frac{\partial\vec{F}}{\partial\vec{X}} \Big|_{\vec{X}_I} \cdot \delta\vec{X}(t) + \frac{1}{2!} \left(\frac{\partial^2\vec{F}}{\partial\vec{X}^2} \Big|_{\vec{X}_I} \cdot \delta\vec{X}(t) \cdot \delta\vec{X}(t) \right) + \dots + B \cdot \epsilon \delta\vec{U}'(t) \quad (3.20)$$

in which ϵ physically means the maximum value of $\| \delta\vec{U}(t) \|$ and represents the fact that the order of norm value of the difference between the true and the modeled perturbing acceleration is relatively small in general compared to the known acceleration [36] :

$$\epsilon = \text{Max} \| \vec{U}_T - \vec{U}_I \| \ll \| \vec{F}(\vec{X}, t) \| \quad (3.21)$$

Using Moulton's method of analytic continuation, the solutions to this dynamic system of equations can be expanded into the power series of ϵ about the reference solution [37] :

$$\delta\vec{X}(t) = \delta\vec{X}^{(0)}(t) + \delta\vec{X}^{(1)}(t) \epsilon + \frac{1}{2!} \delta\vec{X}^{(2)}(t) \epsilon^2 + \dots \quad (3.22)$$

By denoting the known analytical solution when $\epsilon = 0$ as $\delta\vec{X}^{(0)}$, the solution at order 0 can be easily obtained as $\delta\vec{X}^{(0)}(t) = 0$ since $\delta\vec{U}(t) = 0$, which means the modeled perturbing acceleration is same as the true perturbing acceleration and therefore there is zero state deviation.

Upon substituting the general form of the solution (Eq. (3.22)) of $\delta\vec{X}(t)$ into the full equations of motion (Eq. (3.20)) and rearranging the terms as power series in ϵ and equating coefficients of corresponding powers of ϵ up to an order of 2, the following is found :

$$\epsilon^0 : \delta\dot{\vec{X}}^{(0)}(t) = \left[\frac{\partial\vec{F}}{\partial\vec{X}} \Big|_{\vec{X}_I} + \frac{1}{2!} \left(\frac{\partial^2\vec{F}}{\partial\vec{X}^2} \Big|_{\vec{X}_I} \cdot \delta\vec{X}^{(0)}(t) \right) \right] \cdot \delta\vec{X}^{(0)}(t) \quad (3.23)$$

$$\epsilon^1 : \delta\dot{\vec{X}}^{(1)}(t) = \left(\frac{\partial\vec{F}}{\partial\vec{X}} \Big|_{\vec{X}_I} + \frac{\partial^2\vec{F}}{\partial\vec{X}^2} \Big|_{\vec{X}_I} \cdot \delta\vec{X}^{(0)}(t) \right) \cdot \delta\vec{X}^{(1)}(t) + B \cdot \delta\vec{U}'(t) \quad (3.24)$$

$$\epsilon^2 : \delta\dot{\vec{X}}^{(2)}(t) = \frac{\partial\vec{F}}{\partial\vec{X}} \Big|_{\vec{X}_I} \cdot \delta\vec{X}^{(2)}(t) + \frac{\partial^2\vec{F}}{\partial\vec{X}^2} \Big|_{\vec{X}_I} \cdot \left(\delta\vec{X}^{(0)}(t) \cdot \delta\vec{X}^{(2)}(t) + \delta\vec{X}^{(1)}(t) \cdot \delta\vec{X}^{(1)}(t) \right) \quad (3.25)$$

By applying the fact that the initial conditions for all solutions are zero ($\delta\vec{X}^{(k)}(0) = 0, k \geq 0$) and the solution at order 0 is $\delta\vec{X}^{(0)}(t) = 0$, the solution to these equations can be expressed as :

$$\epsilon^0 : \delta\vec{X}^{(0)}(t, t_0) = 0 \quad (3.26)$$

$$\epsilon^1 : \delta\vec{X}^{(1)}(t, t_0) = \int_{t_0}^t \left[\Phi_d(t, \tau) B \cdot \delta\vec{U}'(\tau) \right] d\tau \quad (3.27)$$

$$\epsilon^2 : \delta\vec{X}^{(2)}(t, t_0) = \int_{t_0}^t \left[\Phi_d(t, \tau) \frac{\partial^2\vec{F}}{\partial\vec{X}^2} \Big|_{\vec{X}_I} \cdot \delta\vec{X}^{(1)}(\tau) \cdot \delta\vec{X}^{(1)}(\tau) \right] d\tau \quad (3.28)$$

With the previous constraint from Eq. (3.15), the solution at the final time can be obtained as :

$$\epsilon^0 : \delta\vec{X}^{(0)}(t_f, t_0) = 0 \quad (3.29)$$

$$\epsilon^1 : \delta\vec{X}^{(1)}(t_f, t_0) = \int_{t_0}^{t_f} \left[\Phi_d(t_f, \tau) B \cdot \delta\vec{U}'(\tau) \right] d\tau = \frac{1}{\epsilon} \int_{t_0}^{t_f} \left[\Phi_d(t_f, \tau) B \cdot \delta\vec{U}(\tau) \right] d\tau = 0 \quad (3.30)$$

$$\epsilon^2 : \delta\vec{X}^{(2)}(t_f, t_0) = \int_{t_0}^{t_f} \left[\Phi_d(t_f, \tau) \frac{\partial^2\vec{F}}{\partial\vec{X}^2} \Big|_{\vec{X}_I} \cdot \delta\vec{X}^{(1)}(\tau) \cdot \delta\vec{X}^{(1)}(\tau) \right] d\tau \neq 0 \quad (3.31)$$

It shows that the solution of state difference at order 1 is zero at the final time even though it varies along the trajectory. With these solutions at the final time, the following relationship can

be obtained :

$$\delta\vec{X}(t_f, t_0) = \frac{1}{2!}\delta\vec{X}^{(2)}(t_f, t_0) \epsilon^2 + \dots \quad (3.32)$$

$$\implies \vec{X}_T(t_f, t_0) - \vec{X}_I(t_f, t_0) = \frac{1}{2!}\delta\vec{X}^{(2)}(t_f, t_0) \epsilon^2 + \dots \quad (3.33)$$

$$\implies \Phi_T(t_f, t_0)(X_T(0) - X_0) - \Phi_I(t_f, t_0)(X_I(0) - X_0) = \frac{1}{2!}\delta\vec{X}^{(2)}(t_f, t_0) \epsilon^2 + \dots \quad (3.34)$$

$$\implies [\Phi_T(t_f, t_0) - \Phi_I(t_f, t_0)](X_T(0) - X_0) = \frac{1}{2!}\delta\vec{X}^{(2)}(t_f, t_0) \epsilon^2 + \dots \quad (3.35)$$

$$\implies \Phi_T(t_f, t_0) = \Phi_I(t_f, t_0) + H.O.T \quad (3.36)$$

in which $\Phi_T(t_f, t_0)$ and $\Phi_I(t_f, t_0)$ are the STM that maps deviations in the initial state from the initial time to the final time using the true dynamics or the modeled dynamics respectively. *H.O.T* means the high order terms involving ϵ^k with $k > 2$, which is neglected in the linear region.

This verifies that the STM is independent of the dynamics in the linear region as long as it connects the initial state to the final state at a given transfer time. Therefore, a reconstructed dynamics equation with the event representation facilitates the linear propagation of state uncertainty analytically. When the initial state uncertainty is small compared to the size of the orbit and the propagation time is less than a few orbital periods, the covariance matrix can be linearly propagated using the STM [4, p. 188] :

$$P_T(t_f) = \Phi_T(t_f, t_0) P_0 \Phi_T(t_f, t_0)^T \quad (3.37)$$

$$= \Phi_I(t_f, t_0) P_0 \Phi_I(t_f, t_0)^T + H.O.T \quad (3.38)$$

$$\simeq \Phi_I(t_f, t_0) P_0 \Phi_I(t_f, t_0)^T = P_I(t_f) \quad (3.39)$$

in which P is the covariance matrix and the subscripts T and I designate their related true and represented dynamics respectively. Since the STM propagated to the final time by modeled dynamics is proven to be close to the true STM, the covariance matrix at the final time can be computed by using the event representation.

3.1.2 Numerical study

Different orbital maneuver scenarios are simulated as space events in order to numerically verify the analytical study. To check the accuracy of uncertainty propagation using an event representation, the orbital state as well as the STM propagated by modeled dynamics using an event representation are compared with ones obtained by the true dynamics. Also, analytical prediction of the 3σ confidence boundaries with the event representation are compared with the true distributions obtained from Monte Carlo results. The essential TFCs are used to model unknown dynamics for an event, which is covered in the previous chapter.

All the simulations are performed on a low-earth orbiting (LEO) satellite and the initial condition is shown in Table D.1, with initial spherical uncertainty of $1m$ in position and $1 \times 10^{-2}m/s$ in velocity. Several different cases are tested with a low or high thrust maneuver event as well as

Table 3.1: Initial state of orbital elements

$a(km)$	e	$i(deg)$	$\Omega(deg)$	$\omega(deg)$	$\nu(deg)$
7500	0.1	20	20	20	180

no space event. As revealed in Table D.2, the magnitude of thrust acceleration is $10^{-2}m/s^2$ for the low thrust maneuver and $10m/s^2$ for the high thrust maneuver. Any thrust dispersion or restriction is ignored. The number and duration of an event as well as the observation gap are different for each case. A general 2-body dynamics model with respect to Earth-Centered Inertial

Table 3.2: Different space event cases (P : orbital period, 1.8 hr)

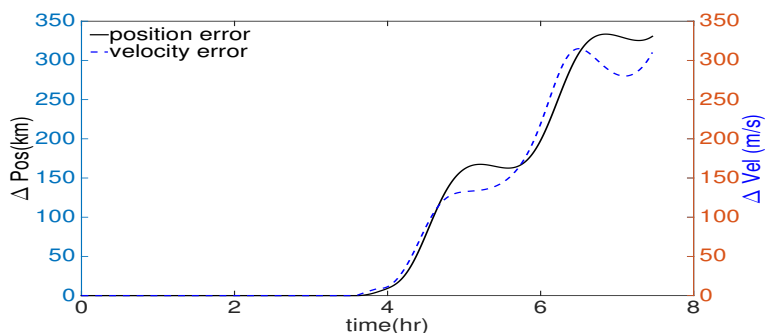
Case	Type/Magnitude of burn (m/s^2)	Duration (sec)	Observation gap (P)	ΔV (m/s)
1	Low single / 1×10^{-2}	1000	1	10
2	Low multiple (4) / 1×10^{-2}	4×1616	2	64.64
3	Low single / 1×10^{-2}	1000	4	10.00
4	High single / 1×10	20	1	200
5	High single / 1×10	20	2	200
6	No burn / 0	-	1	0

(ECI) position-velocity coordinate is considered as the known dynamics, and the orbital state and the STM are propagated by the Matlab built-in solver, ode45 that integrates a system of ordinary

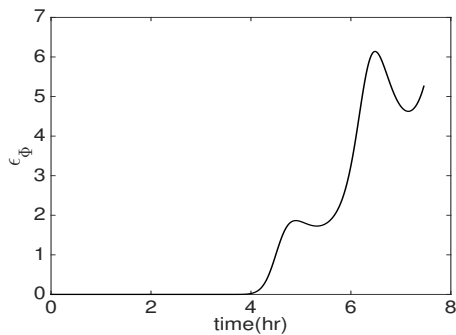
differential equations using explicit 4th and 5th Runge-Kutta formula [38]. For each scenario, the following steps are performed :

- (1) Integrate the reference orbit and its STM to the final time using the true dynamics of a given space event. Then, the initial covariance is propagated linearly across the unknown event using Eq. (3.37) and the covariance ellipses at the final time, Cov_{True} , are computed.
- (2) Compute the essential TFCs based on the initial and the final true states. Among three different ways of obtaining the essential TFCs [13], the numerically updated method is used in this simulation. With the computed essential TFCs, the initial orbit and STM as well as the covariance matrix are propagated forward to the final time and then the covariance ellipses at the final time, Cov_{Est} , are computed.
- (3) Propagate 10,000 Gaussian samples of initial state based on the initial covariance to the final time using the true dynamics of the space event. This Monte Carlo result of final state distribution, $\text{True}_{\text{Monte}}$, is regarded as truth.
- (4) Compute the state difference between the true and the estimated trajectory and compare those computed STMs and covariance ellipses from previous steps.

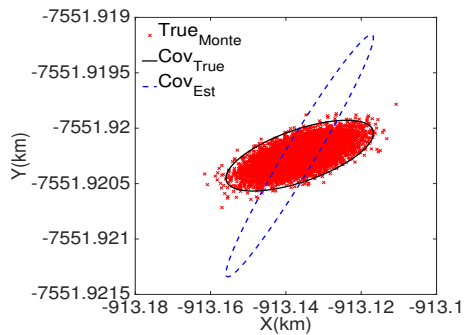
To show that it is necessary to compensate for an unknown event when estimating a post-event state from a pre-event state, the orbit is estimated without representing an unknown event for case 3 as an example. For this case without representing an unknown event, the essential TFCs are not computed and the initial orbit is propagated only with the known dynamics for the step 2 in the simulation process. The result is shown in Fig. 3.2. The first subplot, Fig. 3.2(a), exhibits the state difference between the true and the estimated orbits starts growing significantly as soon as the USE occurs. The STM and the covariance matrix propagated by the only known dynamics also become remarkably different from the true ones. Since both STM and the covariance matrix show very similar behavior, only a plot of STM difference is showed in Fig. 3.2(b). In order to decide how well estimated STMs (Φ_I) are close to true STMs (Φ_T), the following relative norm of



(a) State difference between true and interpolated trajectories



(b) Relative norm of STM difference



(c) Phase plot of X-Y at the final time

Figure 3.2: Uncertainty propagation without modeling the unknown event for case 3

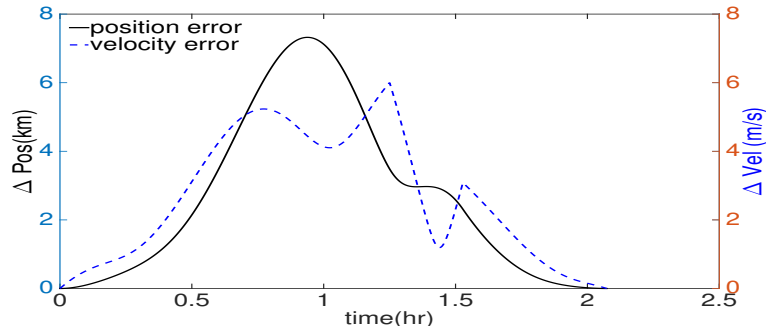
STM difference is defined and used :

$$\varepsilon_{\Phi} = \frac{\| I - \Phi_T^{-1}(t_f, t_0)\Phi_I(t_f, t_0) \|}{\| \Phi_T(t_f, t_0) \|}, \quad \varepsilon_{\Phi} = 0 \quad \text{when} \quad \Phi_T = \Phi_I \quad (3.40)$$

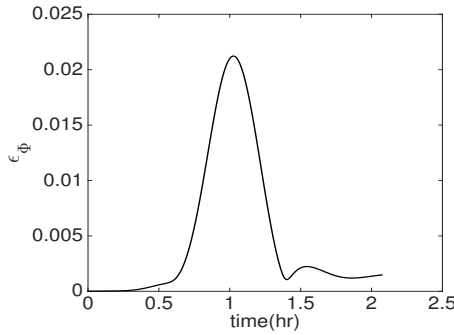
in which Φ_T is the STM obtained by using the true dynamics while Φ_I designates an estimated STM with represented dynamics. Without compensating the unknown event, the resulting estimated final state distribution does not match with the Monte Carlo result which is shown in Fig. 3.2(c). Also, it shows that the covariance ellipse computed from the true dynamics encloses the true distribution, which verifies that the non-linearity effect can be ignored in this simulation. Results are similar for different state phase plots, so only the phase plot of X-Y state and its covariance ellipse are shown in this paper for simplicity.

With representing each unknown event using the essential TFCs, Fig. 3.3-3.8 illustrate that the state deviations go close to zero and the relative norm value of STM difference between the one propagated with the event represented dynamics and the one with the true dynamics also goes close to zero as the time approaches the given final time. Note that this event representation approach with the essential TFCs does not recover the true trajectory or the true dynamics for an unknown event, instead it generates a dynamical trajectory that mimics the same secular behavior such that the orbit reaches the same final state as the true orbit trajectory. The resulting covariance ellipse with this event representation encloses the final state distribution obtained from the Monte Carlo simulation for each case, which are shown in the (c) subfigures of Fig. 3.3-3.8. Also, it is shown on these plots that the estimated covariance ellipse using the event representation lays on top of the ellipse generated by the true dynamics. Figure 3.8 shows uncertainty propagation with event representation of case 6 where there is no space event. In this figure, the computed TFC values are so small (order of 10^{-12}) that the reconstructed trajectory and STM are close to the true ones. It verifies that the proposed approach is still valid even with no event occurred in the truth.

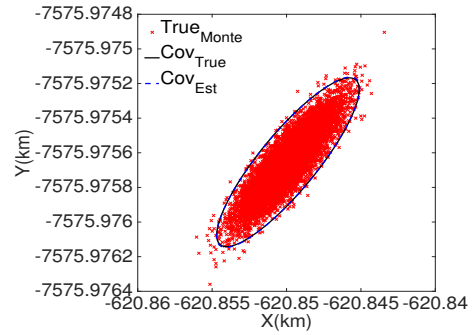
For the linearly propagated final covariance using event representation to be able to describe the true final state uncertainty, it must satisfy a necessary condition of covariance realism which can be checked by averaged uncertainty realism test [39][40]. Covariance realism can be evaluated



(a) State difference between true and interpolated trajectories

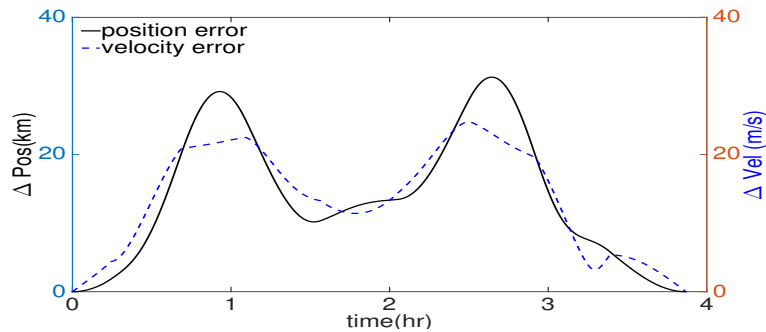


(b) Relative norm of STM difference

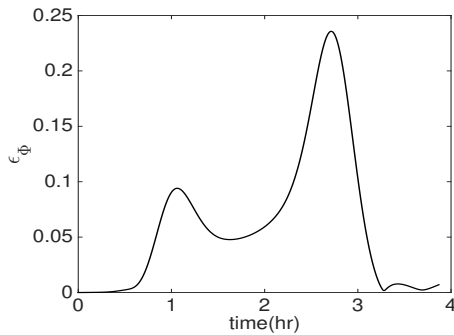


(c) Phase plot of X-Y at the final time

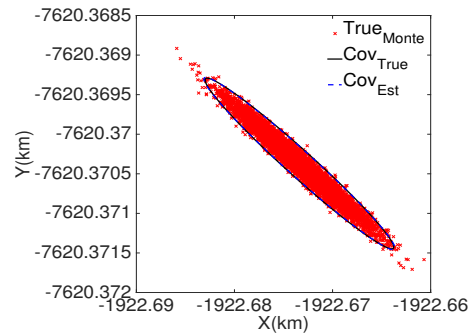
Figure 3.3: Uncertainty propagation with event representation for case 1



(a) State difference between true and interpolated trajectories

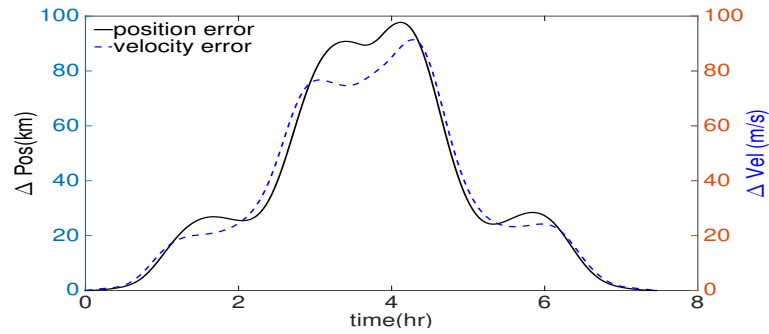


(b) Relative norm of STM difference

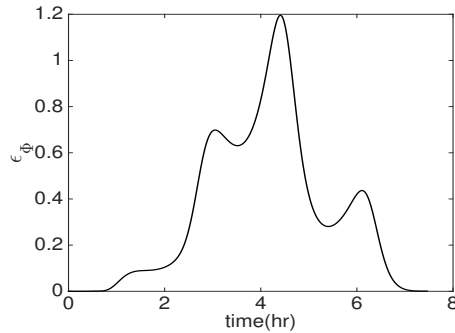


(c) Phase plot of X-Y at the final time

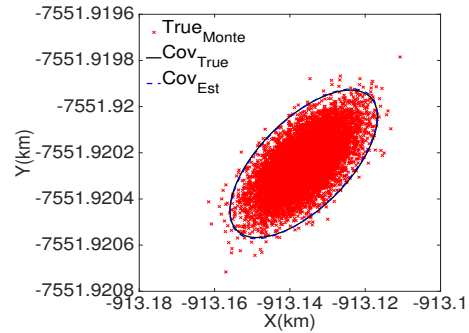
Figure 3.4: Uncertainty propagation with event representation for case 2



(a) State difference between true and interpolated trajectories

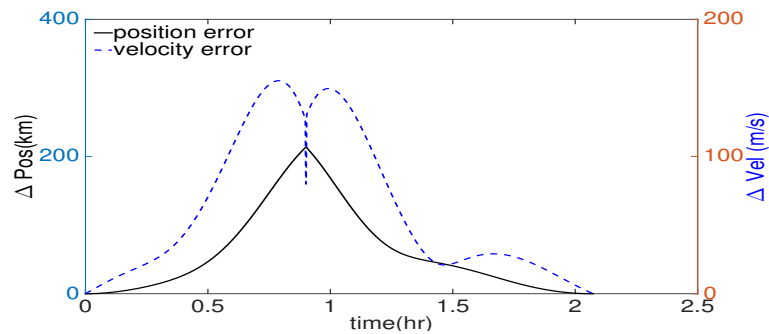


(b) Relative norm of STM difference

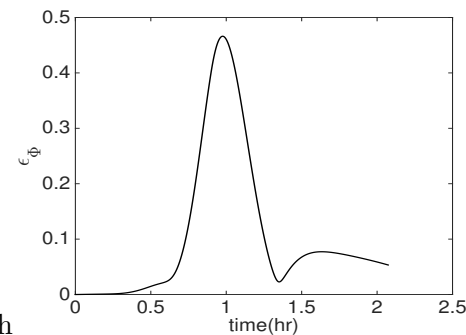


(c) Phase plot of X-Y at the final time

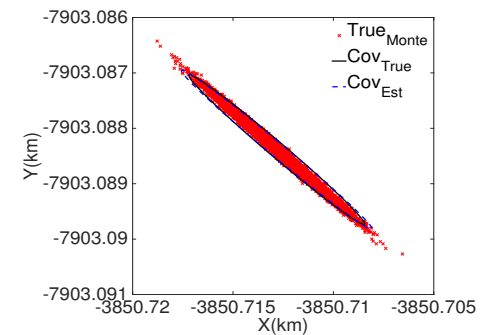
Figure 3.5: Uncertainty propagation with event representation for case 3



(a) State difference between true and interpolated trajectories

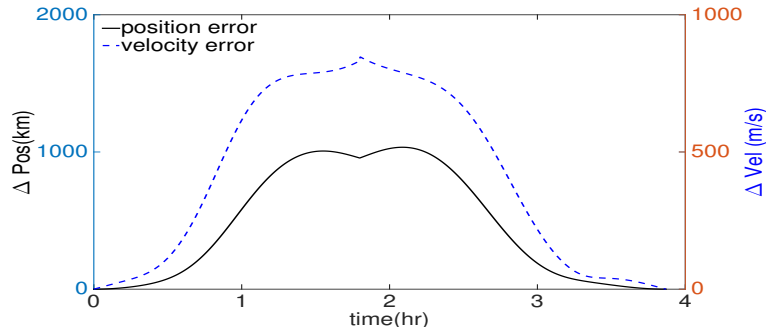


(b) Relative norm of STM difference

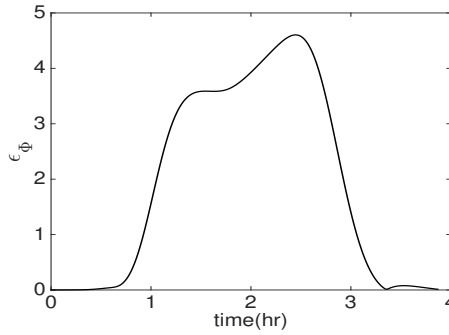


(c) Phase plot of X-Y at the final time

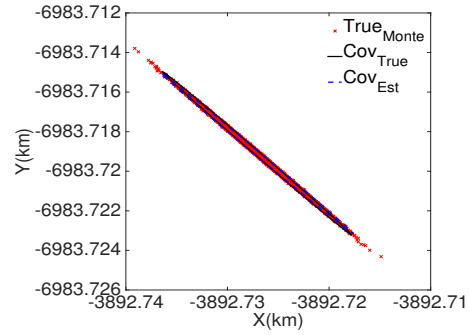
Figure 3.6: Uncertainty propagation with event representation for case 4



(a) State difference between true and interpolated trajectories

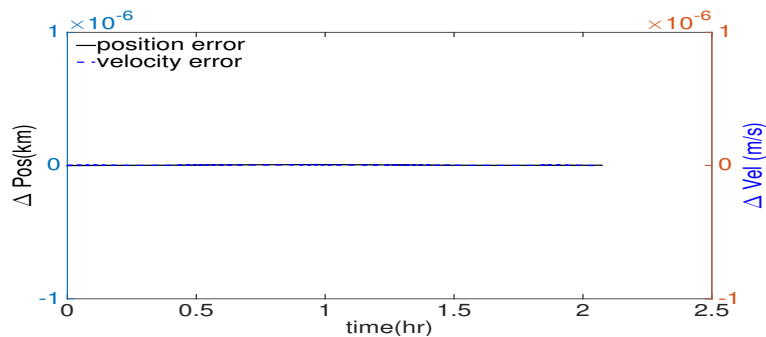


(b) Relative norm of STM difference

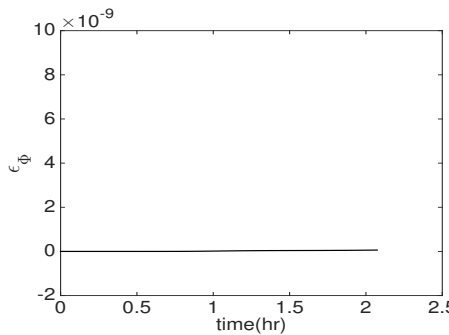


(c) Phase plot of X-Y at the final time

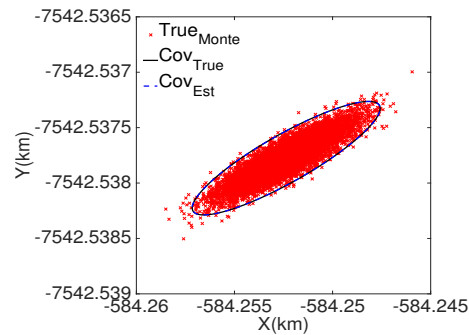
Figure 3.7: Uncertainty propagation with event representation for case 5



(a) State difference between true and interpolated trajectories



(b) Relative norm of STM difference



(c) Phase plot of X-Y at the final time

Figure 3.8: Uncertainty propagation with event representation for case 6

by computing the averaged uncertainty realism metric based on the Mahalanobis distance [41]. By assuming the orbital state uncertainty is Gaussian distribution, the Mahalanobis distance between estimated final state using event representation and truth final state ($\vec{X}_T(t_f)$) is defined as:

$$\mathcal{M}(\vec{X}_I(t_f); \vec{X}_T(t_f), P_I(t_f)) = (\vec{X}_I(t_f) - \vec{X}_T(t_f))^T P_I(t_f)^{-1} (\vec{X}_I(t_f) - \vec{X}_T(t_f)) \quad (3.41)$$

where $\vec{X}_I(t_f)$ is an estimated orbital state at the final time by using event representation and $P_I(t_f)$ is its corresponding covariance obtained by Eq. (3.39). Then, the averaged uncertainty realism metric can be computed by averaging over multiple Monte Carlo trials:

$$\bar{\mathcal{U}} \equiv \frac{1}{nk} \sum_{i=1}^k \mathcal{M}^i(\vec{X}_I(t_f); \vec{X}_T(t_f), P_I(t_f)) \quad (3.42)$$

in which \mathcal{M}^i is the Mahalanobis distance metric computed in the i -th Monte Carlo trial and n is the dimension of the state vector, 6. For the propagated covariance using event representation to be reliable, it is necessary that the value of the averaged uncertainty realism to be within the confidence interval. The two sided 99.9% confidence interval for this test, with $k = 10,000$ Monte Carlo trials, is [0.9811, 1.0191] [39]. The computed averaged uncertainty realism metric $\bar{\mathcal{U}}$ with different cases is shown in Table 3.3. This simulation result shows that the uncertainty realism established by the linearly propagated covariance matrix using the event representation passes the uncertainty realism test. Therefore, these numerical simulation results along with the analytical proof verify that the uncertainty propagation using the representation of a USE can be used for the linear propagation of state uncertainty information.

Table 3.3: Averaged uncertainty realism test result

	Case 1	Case 2	Case 3	Case 4	Case 5	Case 6
$\bar{\mathcal{U}}$	0.9894	1.0151	1.0008	1.0159	1.0135	1.0094
Within confidence interval?	Yes	Yes	Yes	Yes	Yes	Yes

*Two sided 99.9% confidence interval: [0.9811, 1.0191]

3.2 Orbit determination across unmodeled space events via event representation

Propagating an orbit uncertainty across a USE given only *a priori* information and post-event measurements is a challenging problem and has never been attempted before. A conventional method used at the time of encountering a USE is to initiate the batch filter over a post-event tracking arc with large initial uncertainties. To distinguish this batch filter from the modified batch filter in this chapter, we label it as a regular batch filter that estimates only post-event satellite position and velocity vectors. With the regular batch filter, the state covariance matrix is inflated to address the uncertainty in the post-event estimation and the accuracy of state estimate is low at this stage. Making use of the pre-event OD solution through the TFC event representation will improve the overall OD solutions, specially when there is no measurement available during a USE. In this chapter, a simple way to propagate an orbit uncertainty across a USE using the modified Batch filter with the event representation using the essential TFC set is introduced first. Then, different combinations of TFCs are used to modify the Batch filter in the following subchapter to investigate how different event representations with different TFC sets affect the OD solution across a USE.

3.2.1 Modified Batch filter with the essential TFC set

The problem is to propagate the satellite orbit state to a future time along with a suitable estimate of its confidence boundary. Given a set of post-event measurements of a satellite after an unknown space event, the regular batch processor can estimate the post-event satellite trajectory by reinitiating the filter over the post-event tracking arc with a largely inflated initial uncertainty. When there is accurate *a priori* information of pre-event orbital state, this regular batch filter is unable to incorporate the pre-event orbit information with the post-event measurement data. By modeling governing dynamics of an unknown event with the essential TFCs, the regular batch filter can be modified to estimate the orbit solution across unknown events when there is tracking

data only available after the USE. This modified batch filter with the essential TFCs is able to keep *a priori* information through an unknown event and then use it to improve the quality of the post-event OD solution. In order to show that the performance of the proposed batch filter with TFCs is superior to the regular batch filter, various OD simulations are performed with simulated tracking data and the results from both filters are compared.

To analyze the performance of the batch filter with the essential TFCs in a simple way, the two-body dynamics under the simple point-mass gravity field is assumed to be the only known dynamics that exist between a satellite and the Earth. When a satellite is exposed to a USE, the motion of the satellite can be described as Eq. (3.2). To model the event dynamics, the essential TFC set is used to represent the unknown perturbing accelerations [13] :

$$\vec{U} = \alpha_0^R \hat{r} + (\alpha_0^S + \alpha_1^S \cos E + \beta_1^S \sin E) \hat{s} + (\alpha_1^W \cos E + \beta_1^W \sin E) \hat{w} \quad (3.43)$$

$$= \begin{bmatrix} \hat{r} & \hat{s} & \hat{w} \end{bmatrix} \begin{bmatrix} 1 & 0 & 0 & 0 & 0 & 0 \\ 0 & 1 & \cos E & \sin E & 0 & 0 \\ 0 & 0 & 0 & 0 & \cos E & \sin E \end{bmatrix} \begin{bmatrix} \alpha_0^R & \alpha_0^S & \alpha_1^S & \beta_1^S & \alpha_1^W & \beta_1^W \end{bmatrix}^T \quad (3.44)$$

$$= T \cdot S \cdot c_{ess} \quad (3.45)$$

in which T is the transformation matrix ($\hat{r} = \frac{\vec{r}}{|\vec{r}|}$, $\hat{w} = \frac{\vec{r} \times \vec{v}}{|\vec{r} \times \vec{v}|}$, $\hat{s} = \hat{w} \times \hat{r}$) from the body frame (RSW) to the inertial frame (ECI), and S matrix generates the perturbing acceleration in the body frame from the essential TFCs.

The proposed batch filter directly append these essential TFCs to the state vector (the satellite position and velocity vectors) to estimate the perturbing thrust acceleration as well as the orbital state. The augmented state vector consists of time-dependent satellite position and velocity vectors and constant TFCs. By representing an unknown event with an essential TFC set, the

governing equations of motion can be rewritten as follows :

$$\dot{\vec{X}}(t) = \vec{F}(\vec{X}, t) + B \cdot \vec{U}(\vec{X}, t) \quad (3.46)$$

$$\frac{d}{dt} \begin{bmatrix} \vec{r} \\ \vec{v} \\ \vec{c}_{ess} \end{bmatrix} = \begin{bmatrix} \vec{v} \\ \dot{\vec{v}} \\ 0_{6 \times 1} \end{bmatrix} + \begin{bmatrix} 0_{3 \times 3} \\ I_{3 \times 3} \\ 0_{6 \times 3} \end{bmatrix} \cdot \vec{U}(\vec{X}, t) \quad (3.47)$$

in which $\vec{F}(\vec{X}, t)$ is the known dynamics and $\vec{U}(\vec{X}, t)$ is the represented unknown acceleration. Along with the augmented state and governing dynamics equations, the state Jacobian and measurement Jacobian matrices have to be modified to complete the batch algorithm with TFCs :

$$\begin{aligned} \frac{d\Phi_R(t, t_0)}{dt} &= \frac{\partial}{\partial \vec{X}_0} \left[\vec{F}(\vec{X}, t) + B \cdot \vec{U}(\vec{X}, t) \right] \\ &= \frac{\partial \vec{F}(\vec{X}, t)}{\partial \vec{X}} \cdot \frac{\partial \vec{X}(t)}{\partial \vec{X}_0} + B \cdot \frac{\partial U(\vec{X}, t)}{\partial \vec{X}} \cdot \frac{\partial \vec{X}(t)}{\partial \vec{X}_0} \\ &= \left[\frac{\partial \vec{F}(\vec{X}, t)}{\partial \vec{X}} + B \cdot \frac{\partial U(\vec{X}, t)}{\partial \vec{X}} \right] \cdot \Phi_R(t, t_0) \\ H = \tilde{H} \cdot \Phi_R(t, t_0) &= \frac{\partial G(\vec{X}, t)}{\partial \vec{X}} \cdot \Phi_R(t, t_0) \end{aligned} \quad (3.48)$$

$$(3.49)$$

in which $G(\vec{X}, t)$ is the measurement equation. This modification in the batch filter allows for periods of a USE to be fit through without having a precise model of the event. This modified batch filter estimates the essential TFCs as well as the initial orbital state by processing all the post-event tracking data in a single batch. It simply takes *a priori* information from the pre-event epoch, propagates orbit state and STM across the period of the unknown event according to the modeled dynamics with the event representation. After that, the filter compares a post-event observation with a computed measurement using the propagated state via the represented dynamics. Then, the filter adjusts the TFCs and the initial state until the event representation connects all the post-event measurement data with the *a priori* state. This process provides the least square solution that minimizes the sum of the squares of the difference between the predicted observation and the actual observation and the best estimate is determined by repeating this iteration until the estimation process has converged. A detailed flow chart for the modified Batch processor with

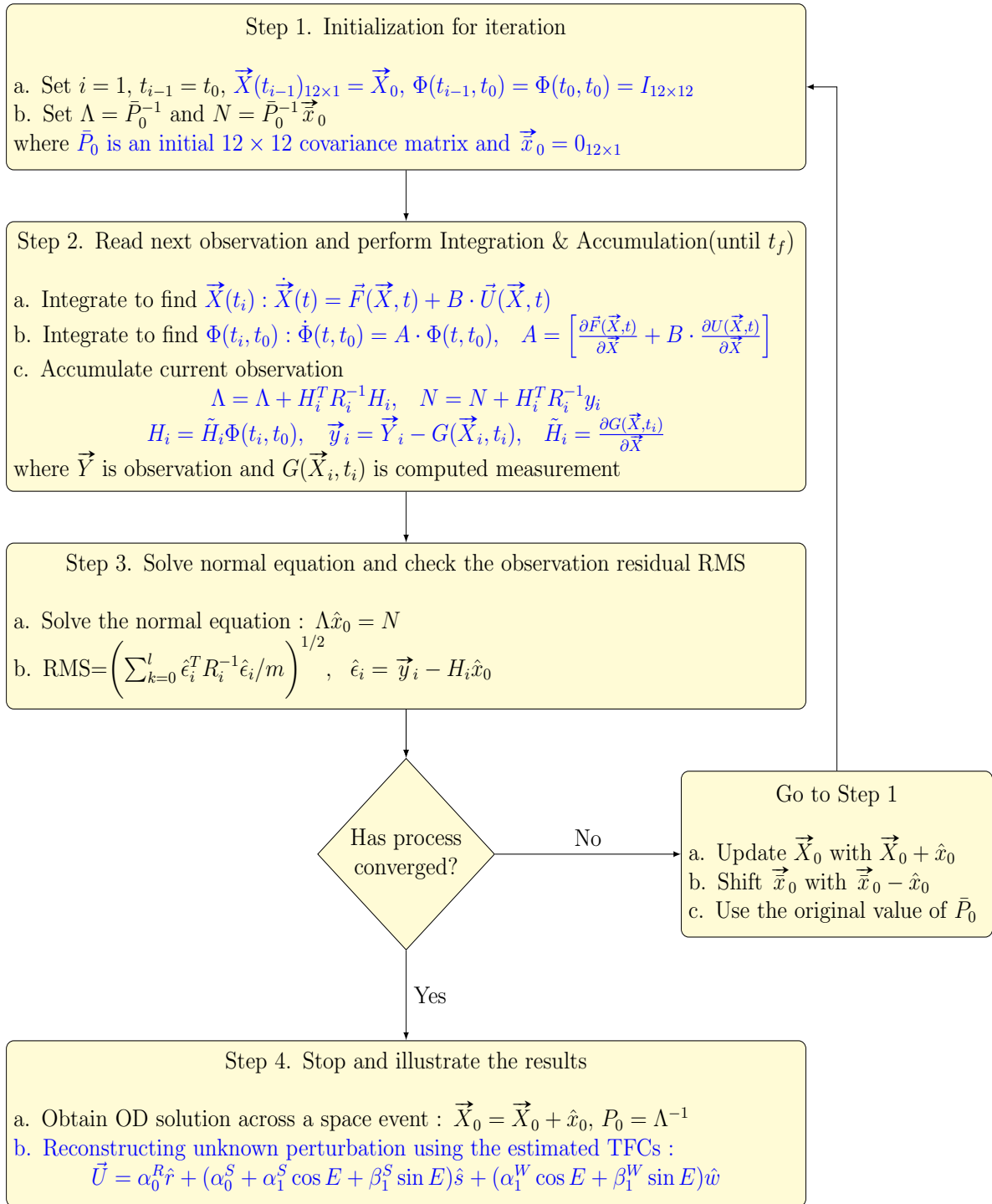


Figure 3.9: Flow chart for the modified Batch algorithm (blue : modified part)

TFCs is shown in Fig. 3.9, which is based on the general batch processing algorithm [4]. In this figure, all the modifications associated with the TFC event representation are shown in blue. To check the convergence, the root mean square (RMS) of observation residuals is computed [4]:

$$RMS = \left(\sum_{k=0}^l \hat{\epsilon}_i^T R_i^{-1} \hat{\epsilon}_i / m \right)^{1/2} \quad (3.50)$$

$m = l \times p$: the total number of observation

$R_i^{-1} = W$: weighting matrix

$$\hat{\epsilon}_i = \vec{y}_i - H_i \hat{x}_0 \quad (3.51)$$

where l, p are the number of observation data and the dimension of error vector respectively. When the RMS no longer changes, the best estimate of \hat{x}_0 is assumed to be converged. Once the process has converged, the filter illustrates the results using various graphical presentations including reconstruction of a control profile. The TFCs have a similar effect as adding a process noise term to compensate for the unknown dynamics in this filter and the contribution of adding TFCs on state uncertainty estimations is proved in Appendix B. Due to this, the modified batch filter provides better convergence performance and better post-event OD solution than the regular batch filter. It must be stressed again, however, that the TFC estimates that arise from this filter provide additional information not available if a process noise term were added instead.

3.2.1.1 Simulations using the essential TFC set

In order to validate the modified batch filter with the essential TFCs and to check the filter's performance, the same space event scenarios from chapter 3.1 are simulated. A relatively accurate *a priori* information ($\sigma_{position} = 1m$, $\sigma_{velocity} = 1 \times 10^{-2}m/s$) is obtained after filtering pre-event satellite tracking data (range and range-rate) from three different ground stations over three orbital periods. With the *a priori* information obtained from the pre-event tracking data, true orbit trajectories are compiled using the true event dynamics and post-event measurements are generated. The sensor measurement error is imitated by adding white Gaussian noises to the true sensor value. For the post-event observation, a single tracking station is used to not only simplify

the analysis, but also demonstrate the filter's capability. The station is assumed to be capable of tracking the satellite for an hour. The measurement type is range and range-rate data obtained at every minute after a certain observation gap. It is also assumed that there is no observation available during the USE in this simulation.

Without modeling an unknown event, it is difficult to correlate a post-event measurement arc to a pre-event orbital state. The standard batch filter is processed through the unknown event of case 1 without representing the event and the result is shown in Fig. D.1. This figure has two y-axes on both left and right sides to show their different magnitudes. The Y-axis label for state error appears on the left, and the Y-axis label for 3σ boundary appears on the right. The state estimation errors are too large to stay within 3σ uncertainty boundaries, which is caused by errors in the dynamical model. To deal with this situation, the regular batch filter is reinitiated just over the post-event tracking arc and the result is shown in Fig. 3.11(b). For all the cases, the

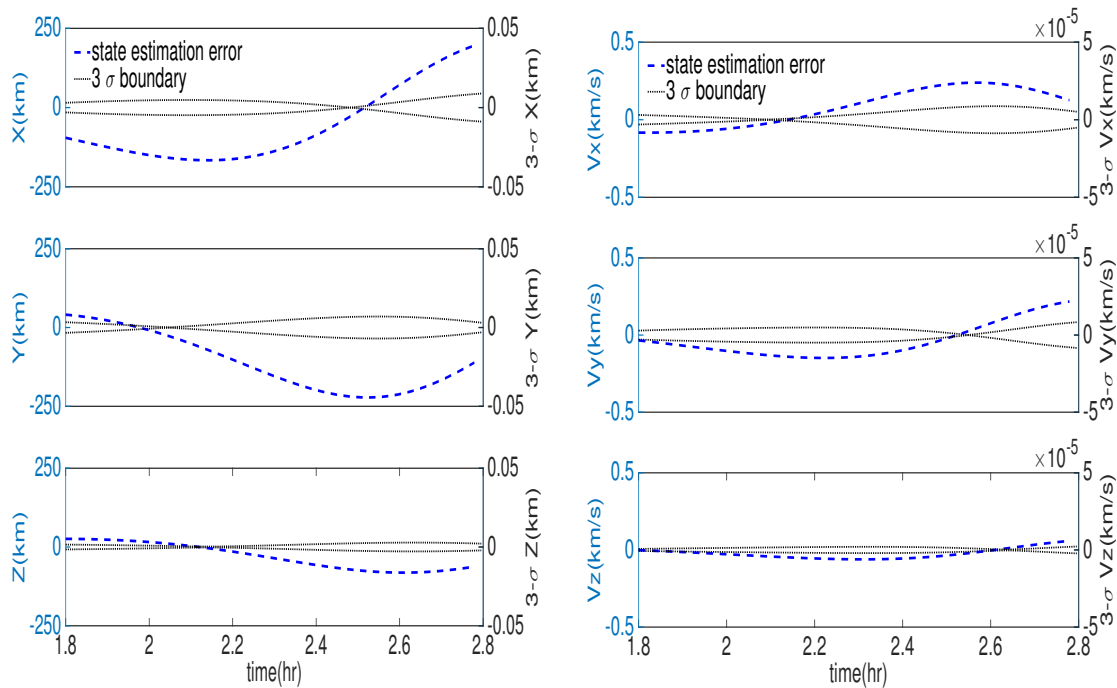
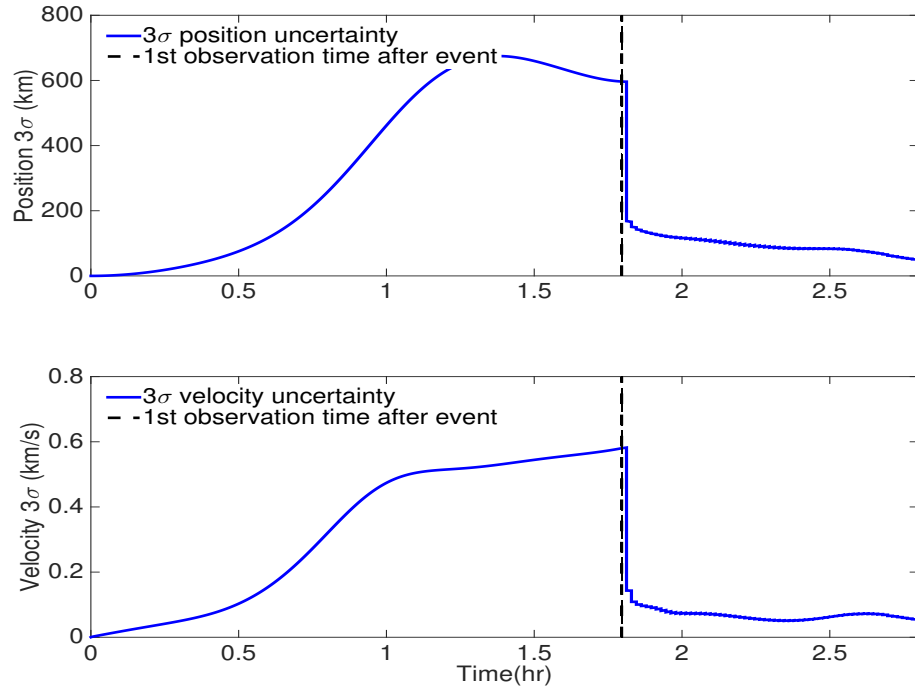
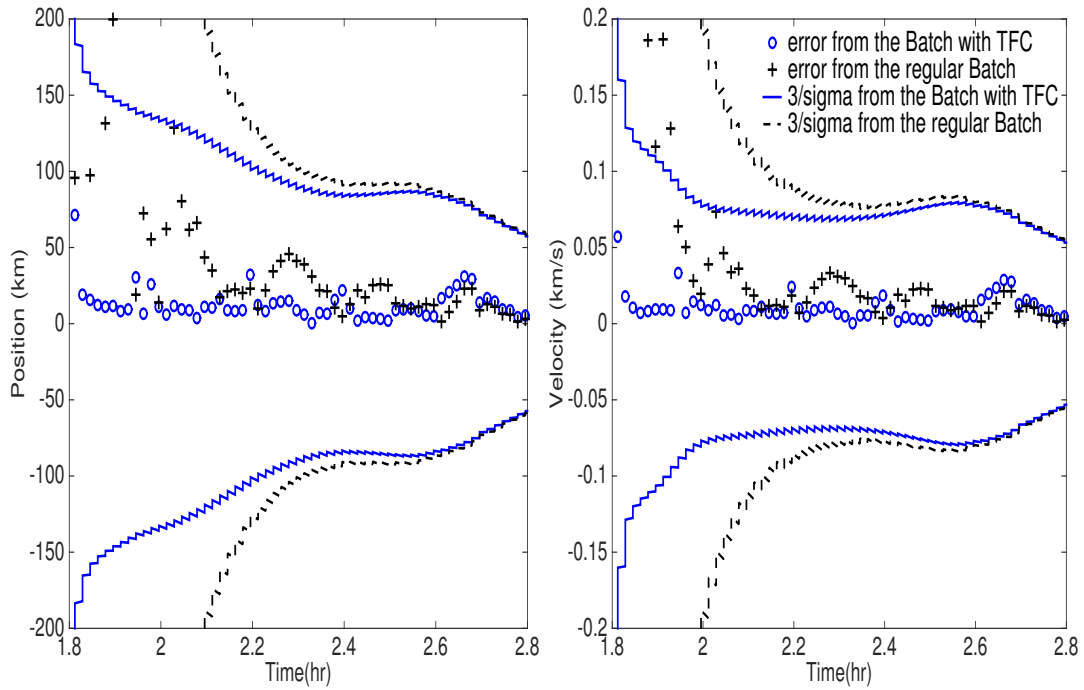
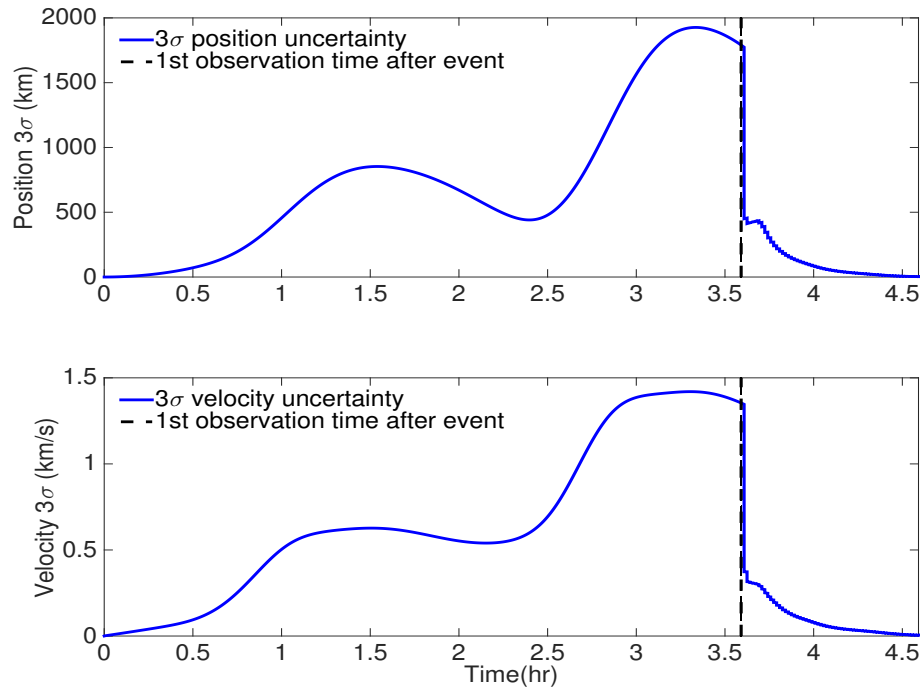
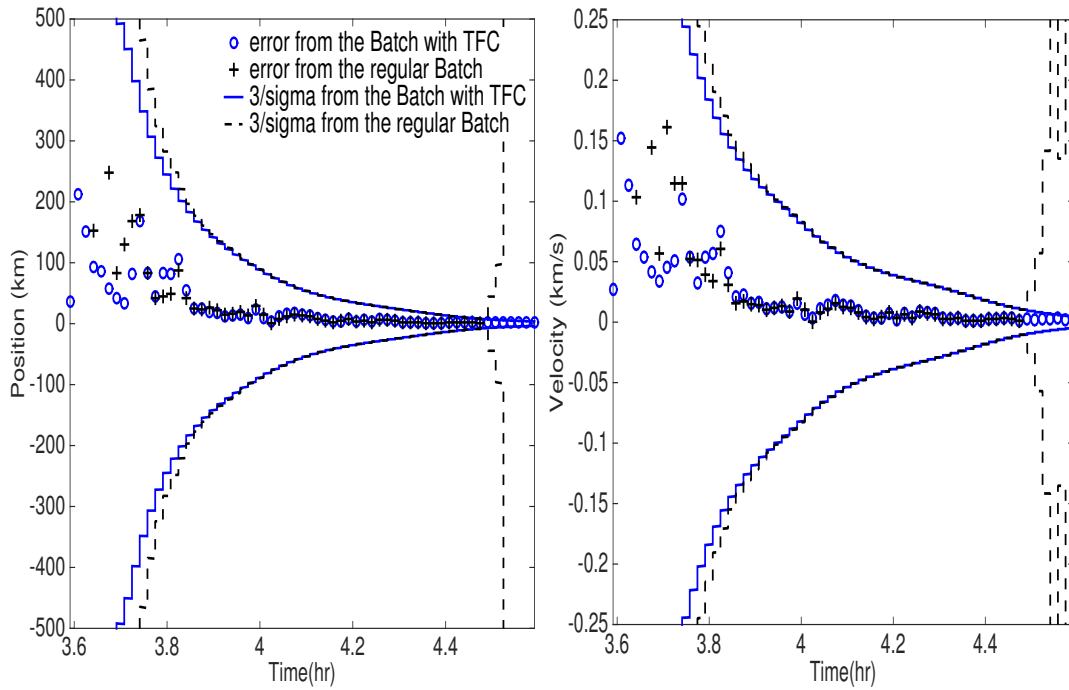


Figure 3.10: State estimation error & 3σ boundary without modeling an unknown event for case 1

regular batch filter is reinitiated over the post-event tracking data and the results are compared with OD solutions obtained from the proposed batch filter with the event representation. Four

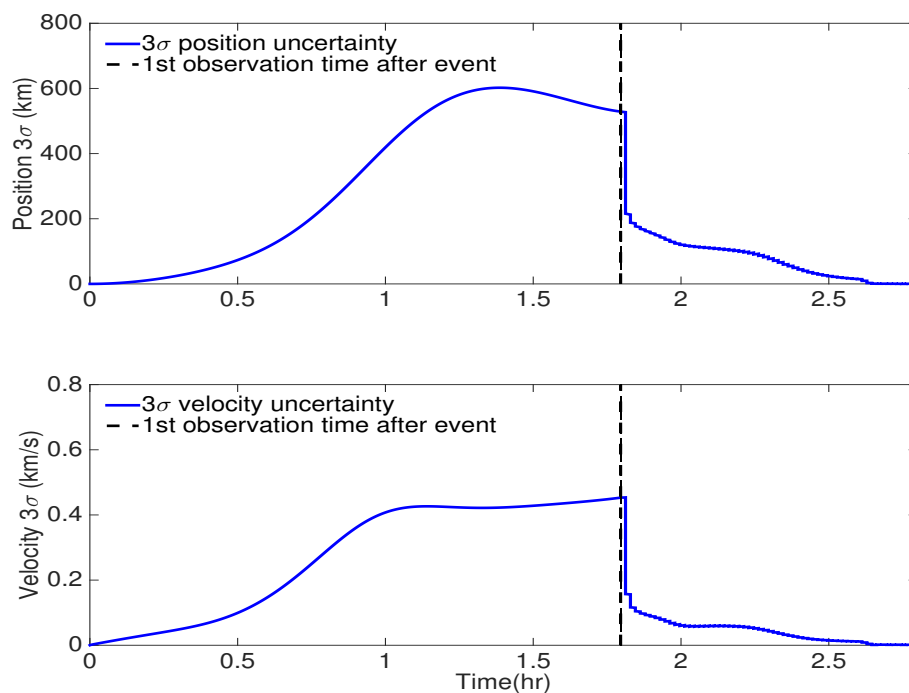
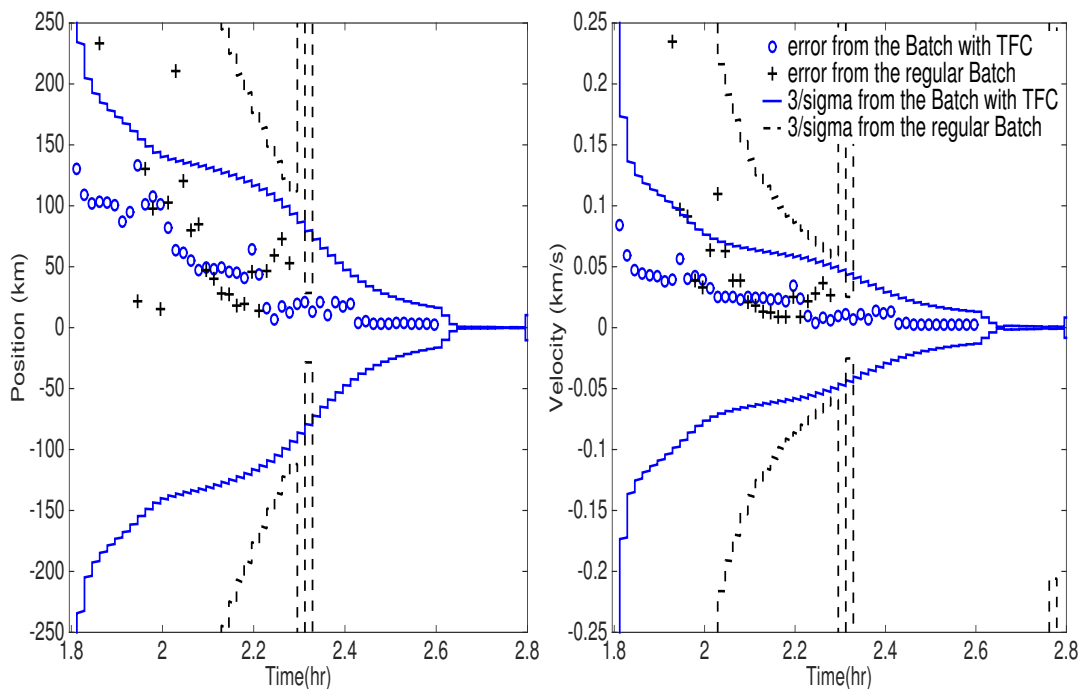
(a) Estimated 3σ state uncertainty from the modified batch filter with TFCs(b) Post-event state estimation error & 3σ uncertainty boundaryFigure 3.11: State estimation error with 3σ uncertainty boundary for case 1

(a) Estimated 3σ state uncertainty from the modified batch filter with TFCs(b) Post-event state estimation error & 3σ uncertainty boundaryFigure 3.12: State estimation error with 3σ uncertainty boundary for case 2

of the cases (1, 2, 4 and 6) are shown in Fig. 3.11-3.15. The first subplots, 3.11(a)-3.15(a), show the time history of estimated 3σ uncertainties obtained by the modified batch filter with TFCs by patching all the filter solutions per each measurement segment including the period across an unknown event. The black dotted vertical line indicates the first observation time after an unknown event. These subplots show that the uncertainty boundary grows until the filter processes the first post-event observation and is reduced after each post-event observation.

The second subplots, Fig. 3.11(b)-3.15(b), exhibit different OD solutions only for the post-event epoch by comparing the estimated 3σ state uncertainty boundaries and the state estimation errors resulting from a regular batch filter and the modified batch filter with TFCs. Note that these plots show the accumulated result of sixty OD solutions obtained with each of different measurement sets (one to sixty measurements). When a new measurement data comes in, both the modified batch filter with TFCs and the regular batch filter are reinitiated with the updated measurement set to newly estimate the initial state as well as the covariance (and the TFC values for the modified batch filter with TFCs). The *a priori* state before an unknown event is the initial state for the modified batch filter with TFCs while an expected state (computed by the previously known dynamics without modeling the event) at the first post-event measurement time is the initial state for the regular batch filter. Then, both updated initial states are propagated to the next measurement time and the OD solution is stored just for the segment between the current measurement time to the next measurement time. Therefore, Fig. 3.11(b)-3.15(b) should not be interpreted as a mapping of the state estimate or the covariance matrix from the initial time to the final measurement time. Instead, these plots show how the number of measurement data affects the filter performance at each measurement segment. This process is equivalent to the sequential algorithm and provides the same state estimate as the sequential filter with TFCs when the orbit estimates are mapped to the same measurement time. Only batch solutions are compared in this paper for simplicity's sake.

Both batch filters provide valid OD solutions that the actual state errors are well within the estimated 3σ standard deviation bounds. However, the state uncertainty volume and the estimation

(a) Estimated 3σ state uncertainty from the modified batch filter with TFCs(b) Post-event state estimation error & 3σ uncertainty boundaryFigure 3.13: State estimation error with 3σ uncertainty boundary for case 4

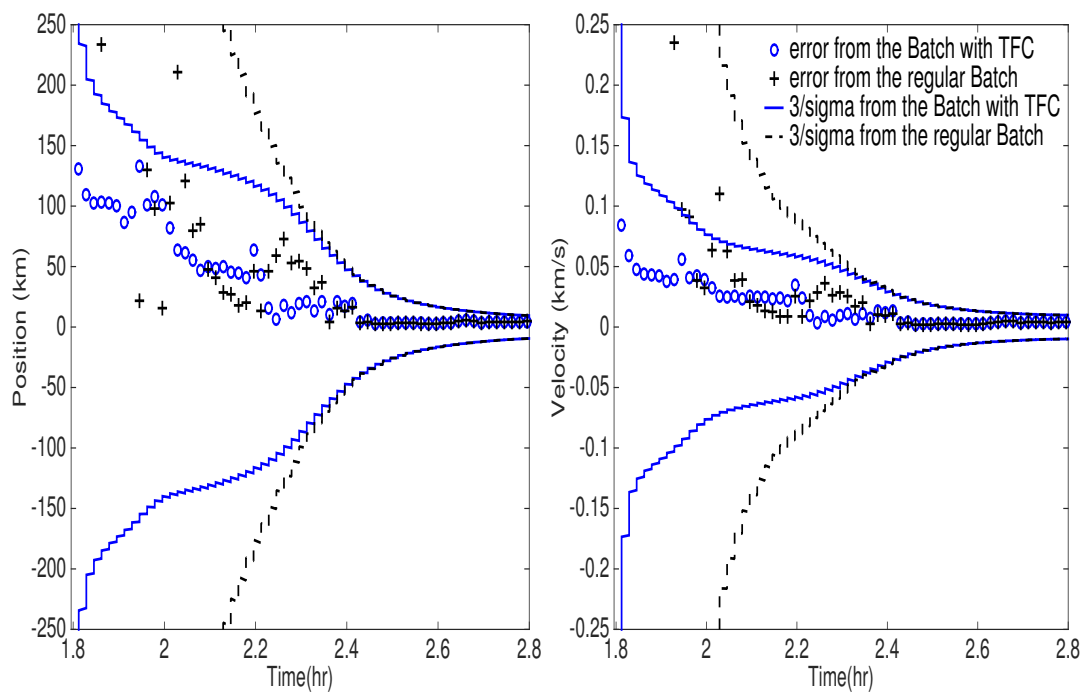
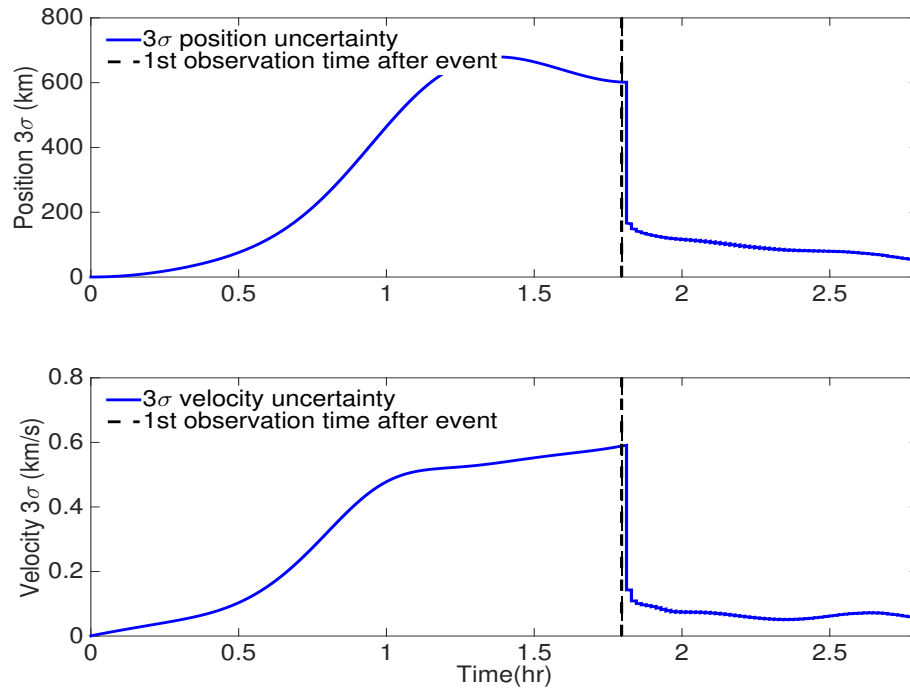
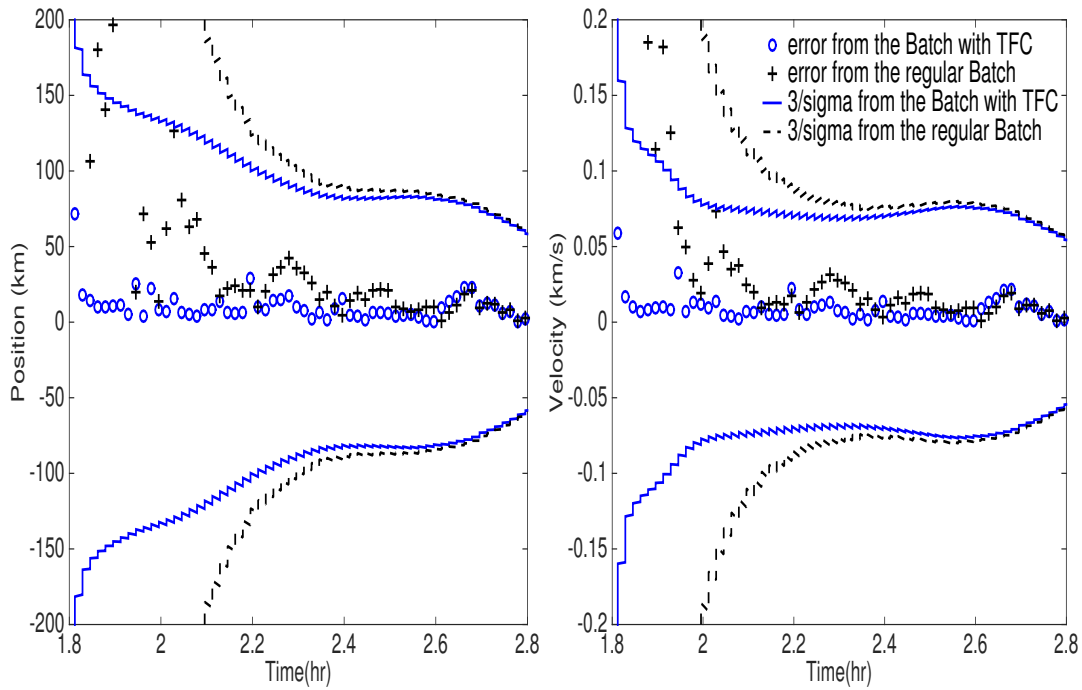


Figure 3.14: State estimation error with 3σ uncertainty boundary with IOD for case 4

(a) Estimated 3σ state uncertainty from the modified batch filter with TFCs(b) Post-event state estimation error & 3σ uncertainty boundaryFigure 3.15: State estimation error with 3σ uncertainty boundary for case 6

error using the modified batch filter with TFCs are significantly smaller than those with the regular batch filter at the early part of the post-event tracking arc. By representing the unknown event, the modified batch filter with TFCs takes advantage of having accurate *a priori* information and is able to improve the orbital state and the uncertainty solution with limited measurement data. It also demonstrated that the estimation accuracy of the modified batch filter with TFCs increases as the filter receives more measurement data to represent the unknown event more accurately. However, for the case 4 when there is a large ΔV maneuver ($\Delta V = 200m/s$), both batch filters start diverging at 30 minutes (for the regular batch), or 50 minutes (for the batch with TFCs) after the initial measurement. It is due to the fact that the initial estimates for the state or TFCs are not close to the true values and the batch filter performance is degraded over a longer time span, which is shown in Fig. 3.13(b). It is also shown in Fig. 3.12(b) for case 2 when there is a relatively large ΔV ($\Delta V = 64.64m/s$) due to multiple burns, the OD solution from the regular batch filter diverges at the end of the tracking arc. Note that the modified batch filter with TFCs starts to diverge (does not diverge for the case 2) at a later time than the regular batch filter, which gives another advantage of using the proposed filter with an event representation. An initial OD (IOD) can be used to update the initial state and TFCs with the first 30 measurements, which provides more reliable reference trajectory close to the truth and eliminates the divergence. The results of applying IOD to both batch filters are shown in Fig. 3.14 for case 4, and it reveals that both batch solutions have converged. Simulation result for case 5 is very similar to the case 4 result, therefore it is omitted to avoid repetition. For all the cases, both filters produce the OD solution that the estimated state remains within several km of the true state after processing the single tracking arc. Figure 3.15 shows that including the essential TFCs in the batch process for a case where there is no actual space event still provides better OD solution than a regular batch filter. This modified batch filter can still incorporate the pre-event orbit solution with post-event measurements even when there is no event occurred, and provides improved post-event OD solution.

Since the event representation allows us to keep the OD across an unknown event, the batch filter with the essential TFCs yields better OD solution at the beginning of the post-event tracking

arc. This preliminary orbit may be used to improve the accuracy of state by making further observations at some future time. Also, this filter shows more robustness to a large state deviation due to a large-scale ΔV event. Besides, it provides a representation of an unknown acceleration by computing a control profile with the estimated TFCs. The modeled perturbing acceleration components for different cases are compared with the true controlling accelerations in Fig. 3.16. This figure shows that the modeled and the true acceleration components are of the same order of magnitude when the observations are made near the actual event time. If the observation gap is too large compared to the actual event duration like case 3, 4 and 5, the modeled thrust acceleration is spread over the whole time span. However, the control effort can be computed by integrating the thrust acceleration components over the time interval, which still can be used to estimate the magnitude of perturbing acceleration. The ΔV computed from the event representation is compared with the true ΔV value for each case, which is shown in Table D.3. Note that the proposed approach

Table 3.4: Estimated Vs True ΔV in circumferential direction

Case	1	2	3	4	5	6
Estimated (m/s)	9.95	64.66	9.04	202.89	190.00	0.065
True (m/s)	10	64.64	10	200	200	0

still estimates TFC values when there is no actual space event, which is shown at Fig. 3.16(f). Their magnitudes are so small that their estimated ΔV is also small and the modified batch filter with TFCs still provide a valid OD solution. More detailed study with various cases will be conducted to examine this property of perturbation magnitude estimation in our future research.

So far, all simulation cases are processed with range and range-rate observation data to analyze the performance of the proposed approach in simple way. Although modern radar signal processing can provide both range and range-rate measurement, this measurement type is rarely available in Space Situational Awareness (SSA) data. To verify that our approach is also valid with other relevant measurement type, the same six cases are simulated with range, azimuth, elevation measurements, and the result for case 1 is shown in Fig. 3.17 as an example since other cases have shown similar results. With different measurement type and its corresponding noise level,

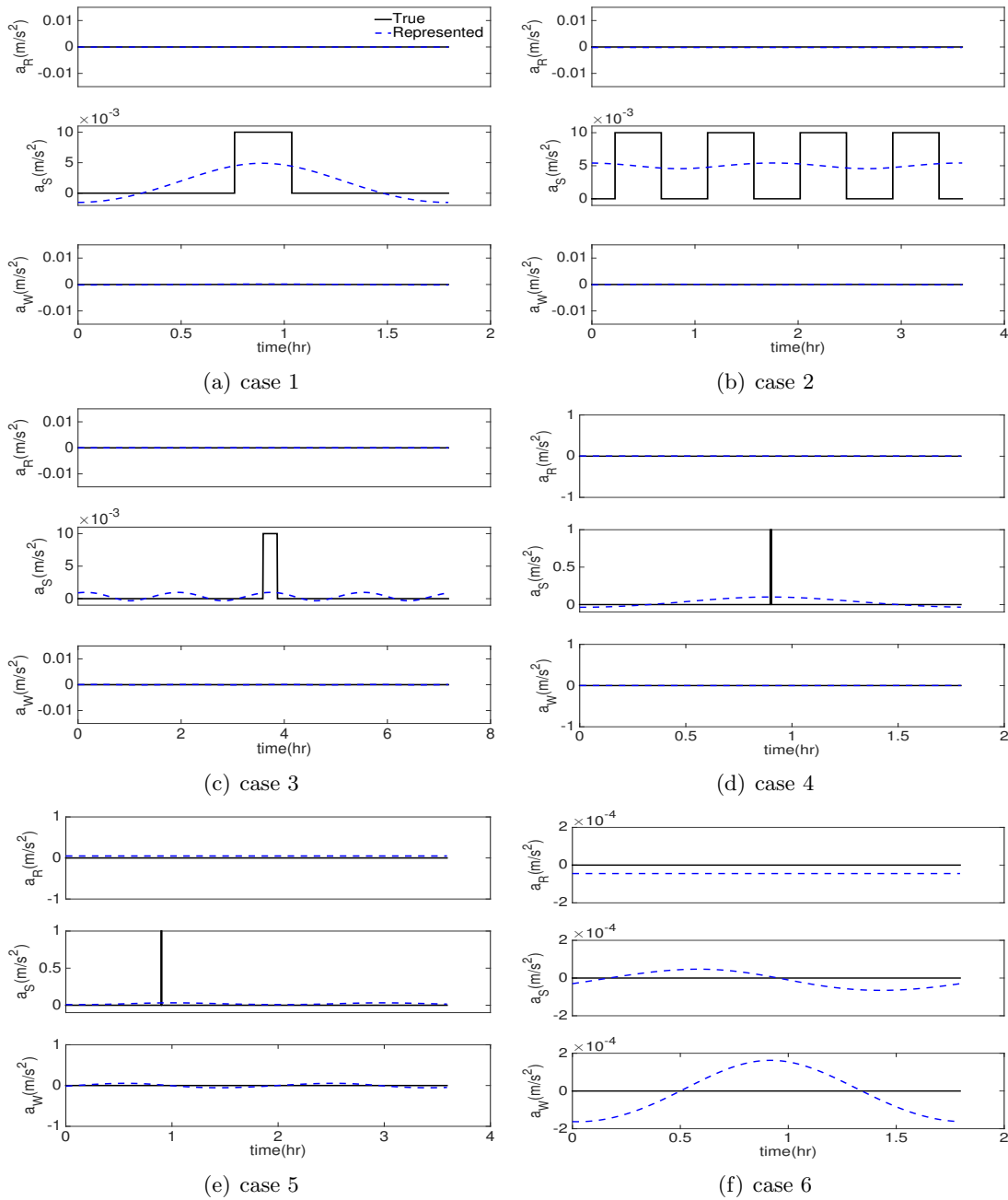


Figure 3.16: Represented vs True acceleration components in body frame

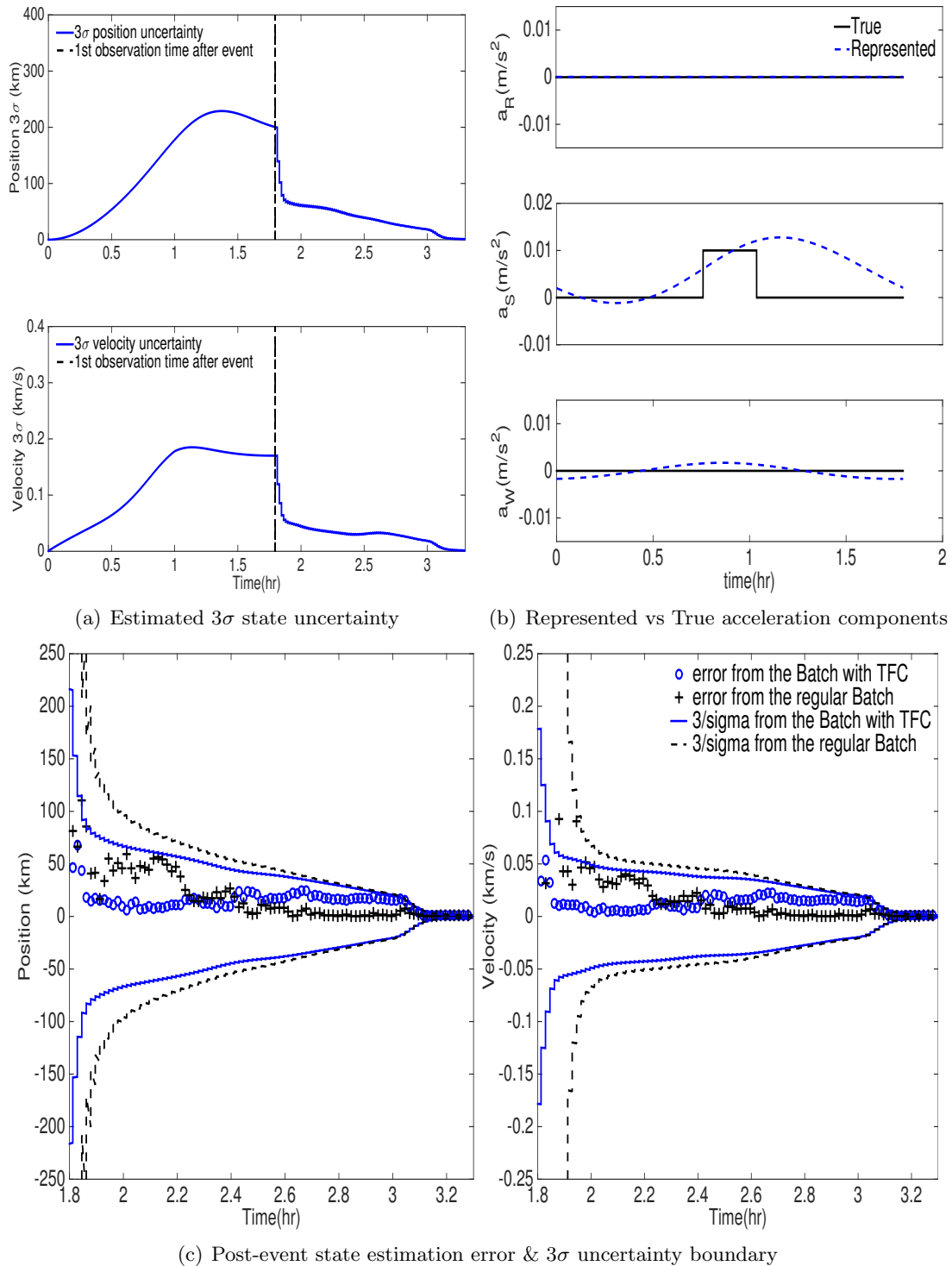


Figure 3.17: Batch result for case 1 with range, azimuth, elevation measurement

convergence rate of OD solution and its accuracy is little different but the proposed batch filter is still able to perform better than the regular batch filter. Also, Fig. 3.17(b) shows that the filter provides an equivalent performance of estimating the magnitude of an unknown acceleration. The amount of additional code required to process the proposed filter is very small. A big advantage of using this batch filter with TFCs is that there is no “tuning” required to estimate the thrust parameters prior to running the simulation since an initial guess for the thrust coefficients can be simply zeros with small initial uncertainty. Although the batch filter in this analysis is based on simple point-mass gravity for the Earth, modification to higher fidelity models is relatively straightforward using Eq. (3.48).

3.2.2 Modified Batch filter with different TFC sets

It is verified that the covariance propagation in the linear region is independent of represented dynamics by comparing propagated orbital states and STMs. Then, the previous chapter shows how to adapt this finding into a Batch formulation with the essential TFC set to obtain post-event OD solutions across USEs. However, it does not compare OD solutions obtained by using different dynamics representation. Therefore, it is useful to check whether different event representations using different combinations of TFCs do produce equivalent OD solutions across USEs.

It has been shown that different combinations of TFC can be used to represent perturbing acceleration and provide a required thrust profile to generate an apparent secular behavior [13]. In chapter 2, 6 efficient sets of 6 TFCs are selected to make a fast assessment of any perturbing

acceleration and able to produce an equivalent orbital transfer for an USE:

$$\begin{aligned}
\vec{c}_{ess1} &= \begin{bmatrix} \alpha_0^R & \alpha_0^S & \alpha_1^S & \beta_1^S & \alpha_1^W & \beta_1^W \end{bmatrix}^T \\
\vec{c}_{ess2} &= \begin{bmatrix} \alpha_0^R & \beta_1^R & \alpha_0^S & \beta_1^S & \alpha_1^W & \beta_1^W \end{bmatrix}^T \\
\vec{c}_{ess3} &= \begin{bmatrix} \alpha_0^R & \alpha_1^R & \alpha_0^S & \alpha_1^S & \alpha_1^W & \beta_1^W \end{bmatrix}^T \\
\vec{c}_{ess4} &= \begin{bmatrix} \alpha_0^R & \alpha_1^R & \beta_1^R & \alpha_0^S & \alpha_1^W & \beta_1^W \end{bmatrix}^T \\
\vec{c}_{ess5} &= \begin{bmatrix} \alpha_1^R & \alpha_0^S & \alpha_1^S & \beta_1^S & \alpha_1^W & \beta_1^W \end{bmatrix}^T \\
\vec{c}_{ess6} &= \begin{bmatrix} \alpha_1^R & \beta_1^R & \alpha_0^S & \beta_1^S & \alpha_1^W & \beta_1^W \end{bmatrix}^T
\end{aligned} \tag{3.52}$$

Like the full set of 14 TFCs (\vec{c}), these different combinations of 6 TFCs can represent unknown perturbations and provide an analytical solution of control profile to connect two separated states across unmodeled events. For example, an unknown perturbing acceleration can be represented by using the 6th essential TFC set (\vec{c}_{ess6}) :

$$\begin{aligned}
\vec{U} &= (\alpha_1^R \cos E + \beta_1^R \sin E) \hat{r} + (\alpha_0^S + \beta_1^S \sin E) \hat{s} \\
&+ (\alpha_1^W \cos E + \beta_1^W \sin E) \hat{w}
\end{aligned} \tag{3.53}$$

These different TFC sets generate the same secular behavior for a given unmodeled event as long as they tie two separate states together.

3.2.2.1 Simulation with different TFC sets

In order to compare OD solutions with different TFC sets, different types of unmodeled event cases are simulated. In this chapter, 4 different cases of USEs are analyzed with the modified filter, as is shown in Table 3.5. Different from the previous simulation cases, there are perturbations acting on different directions of a satellite. Cases 1-3 describe cases with an unknown acceleration acting on a single direction, while case 4 represents an example with a perturbation along a random direction. For all these cases, perturbing accelerations last for 1000 seconds and the actual magnitude of perturbing acceleration is 1×10^{-2} m/s² for case 1-3 and $3 \sim 6 \times 10^{-3}$ m/s² for case 4. The observation

Table 3.5: Different unmodeled event cases

case	direction	ΔV (m/s)
1	Radial (R)	10 (R)
2	circumferential (S)	10 (S)
3	normal (W)	10 (W)
4	Random	6(R) 9(S) 3(W)

gap across an unmodeled event is 1-orbital period ($\simeq 1.8$ hours) for all the cases and there is no measurement available during the event period. All simulations are performed on a low-earth orbiting (LEO) satellite and the pre-event orbit state is shown in Table 3.6. Two-body dynamics

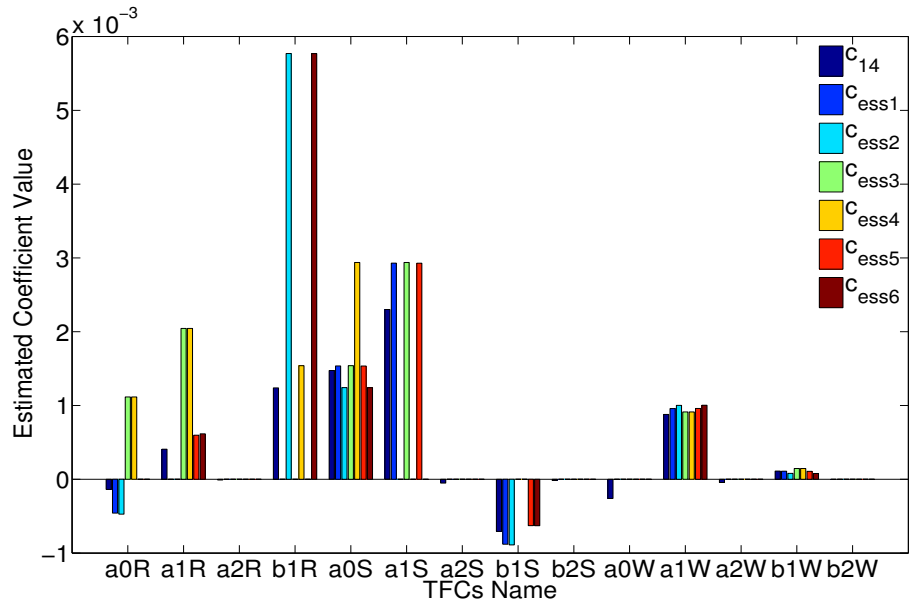
Table 3.6: Initial orbit state of LEO satellite

h_0 (km)	e	i (deg)	Ω (deg)	ω (deg)	ν (deg)
1122	0.1	20	20	20	0

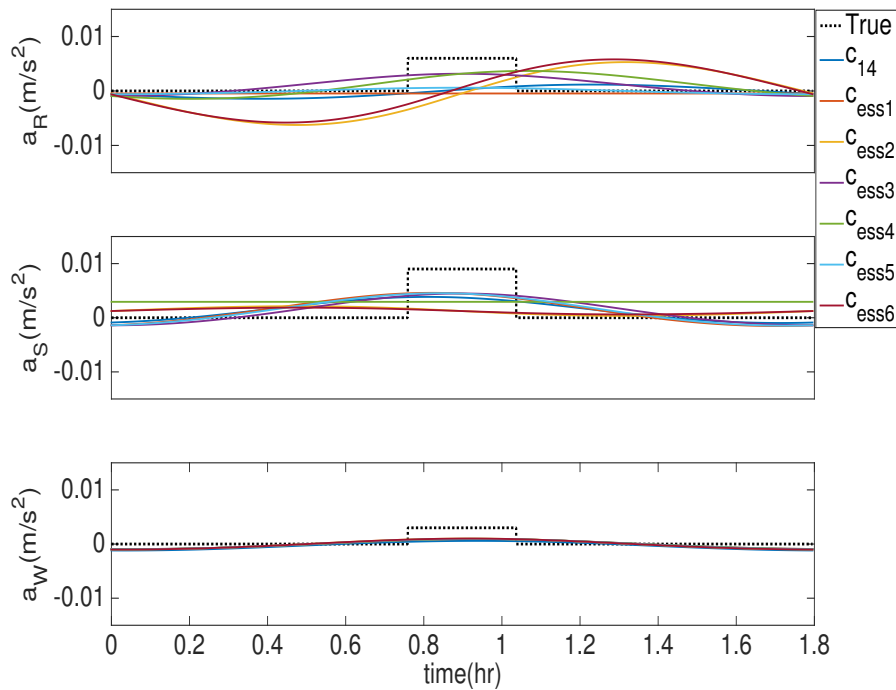
h_0 : altitude at perigee; Earth Radius : 6378.137 km

under the uniform gravity field is assumed to be the only known dynamics upon a satellite, which allows us to compare OD solution of the modified filter in a simple way. As a part of simulation, a measurement generating function produces a small number of post-event measurements (range and range-rate measurements from a single ground station) that are collected at every minute after unmodeled events. For an initial condition, a pre-event OD solution is obtained by processing a simulated pre-event tracking data for 3 orbital periods, which provides an OD result with spherical uncertainty of 1 m in position and 1×10^{-2} m/s in velocity. Given this pre-event OD solution and a set of post-event measurements, the modified batch filter with each different TFC set determines a post-event orbit as well as TFC values.

Simulation results are illustrated by two graphical presentations : one that compares the recovered control profile with each TFC set versus the true perturbation; the other that compares OD solutions from the modified filter to those from the regular batch filter. Simulation results and figures are very similar for different cases, so only the resulting figures for case 4, the most representative case, are shown to avoid repetition (simulation results for case 1 \sim 3 are shown in Appendix C). Figures. 3.18 shows the represented perturbing acceleration for case 4. In this figure,



(a) Estimated TFC values for different TFC sets



(b) Represented vs True acceleration components

Figure 3.18: Event representation for case 4

Table 3.7: True vs Estimated ΔV for different cases (m/s)

		True	14-TFC set	set 1	set 2	set 3	set 4	set 5	set 6
case 1	R	10	2.8897	4.7517	4.7497	15.1622	15.1622	3.9380	3.9677
	S	0	4.7950	5.9447	5.9401	0.3199	0.5045	4.2801	4.2744
	W	0	0.6268	0.7949	0.7966	0.7502	0.7502	0.8015	0.8033
case 2	R	0	5.6536	0.3328	26.2376	0.7409	7.0409	0.2760	26.2400
	S	10	12.2043	14.5362	8.8852	14.5363	20.9269	14.5340	8.8843
	W	0	0.9207	0.9505	1.1084	-0.0673	0.9410	0.9511	1.1093
case 3	R	0	0.1812	0.1904	0.8080	0.4190	0.4190	0.1578	0.8143
	S	0	0.3369	0.4133	0.0906	0.4022	0.6333	0.4324	0.1556
	W	10	10.3769	10.6291	10.6351	10.6360	10.6360	10.6292	10.6352
case 4	R	6	5.4243	2.9631	23.8513	9.2573	11.1981	2.4569	23.9105
	S	9	11.3491	13.6142	8.0233	13.1765	19.0002	13.3777	8.0180
	W	3	3.8708	3.9644	4.1319	3.8002	3.8002	3.9730	4.1407

the first subfigure displays estimated TFC values from the modified batch filter with 7 different TFC sets including the full set of 14 TFC. Since these 7 TFC sets have different configuration of TFCs on each direction (radial, circumferential, normal), their estimated values are different from each other. It is noticeable that some TFCs are more dominant than others, depending on the true perturbing direction. For case 4, the radial and circumferential components of TFC sets are more dominant than normal ones.

The second subfigure, Fig. 3.18(b), compares the reconstructed perturbing acceleration to the true perturbation. The shapes of the recovered control profile using 7 different TFC sets are different from each other as well as the true perturbing acceleration. However, it is shown that the magnitudes of reconstructed accelerations are found to be the same order of magnitudes as the true perturbations. This can be also shown by computing a control effort (ΔV) by integrating the thrust acceleration profile over the time interval, which is shown in Table. D.3. Even though the computed ΔV s do not exactly match with true values, it still can be used to bound the control effort necessary for linking two separate states across an unmodeled event. Note that using the full set of 14 TFCs does not exhibit any superior performance over other sets with 6 TFCs. In fact, the modified batch filter with the 14-TFC set does not produce more accurate OD estimation than others either, which is shown in Fig. 3.19-3.20. Also, none of those 6 TFC sets recovers the

true perturbation more accurately than others, considering the control shape and the expenditure (ΔV). Therefore, we can represent an unmodeled event with any TFC set, which still allows us to quantify the magnitude of an actual perturbation and to choose a preferred control figuration for a given event.

To examine the filter performance with different TFC sets, OD solutions from the modified batch filter over one-hour post-event tracking arc are compared. With an updated initial state and estimated TFC values from the modified filter, the pre-event orbit is propagated through an unmodeled event period using the represented dynamics with different TFC sets. For a comparison, state errors and covariance envelopes from the regular batch filter are also computed by applying the filter over the post-event tracking arc with an inflated covariance matrix. All the results on various cases are consistent with the others and simulation results of case 4 are shown in Fig. 3.19. Each subplot describes the errors of the state estimate from the modified filter with the 14-TFC set as \circ , those from the modified filter with each set of 6 essential TFCs as $+$, and ones with the regular batch filter without TFCs as \square . Different covariance boundaries obtained with those filters are shown with their respective colors (black for regular batch filter; blue for batch with 14 TFCs; others for batch with 6 TFCs). Figure. 3.19 shows that all post-event state errors are within their uncertainty boundaries and they are similar to each other. The modified filter with different TFC sets is able to deliver a valid post-event OD solution across unmodeled events. However, this figure does not reveal the advantage of using the modified batch filter with essential TFCs over the regular batch filter.

To investigate the benefit of applying the TFC representation approach, the accuracy of OD solutions is examined with different size of post-event tracking data duration (1 ~ 90 measurements in 1 ~ 90 minutes). When a new measurement data comes in, the modified batch filter with different TFC sets as well as the regular batch filter are reinitiated with a new measurement set and estimate post-event orbit solutions. Figure. 3.20 displays a collection of OD solutions estimated with different sizes of tracking data duration. State errors and their uncertainty boundaries are computed at their respective last measurement time of each tracking duration. Both subfigures show that state errors

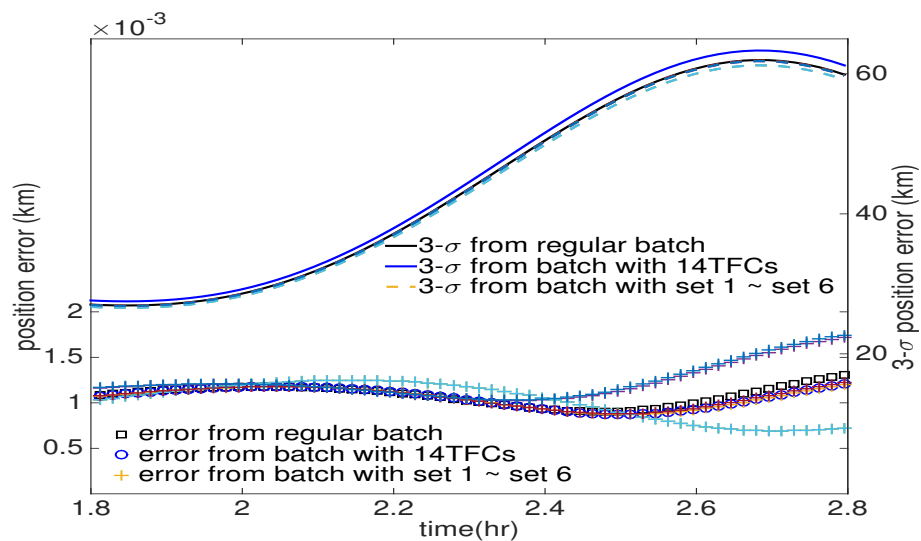
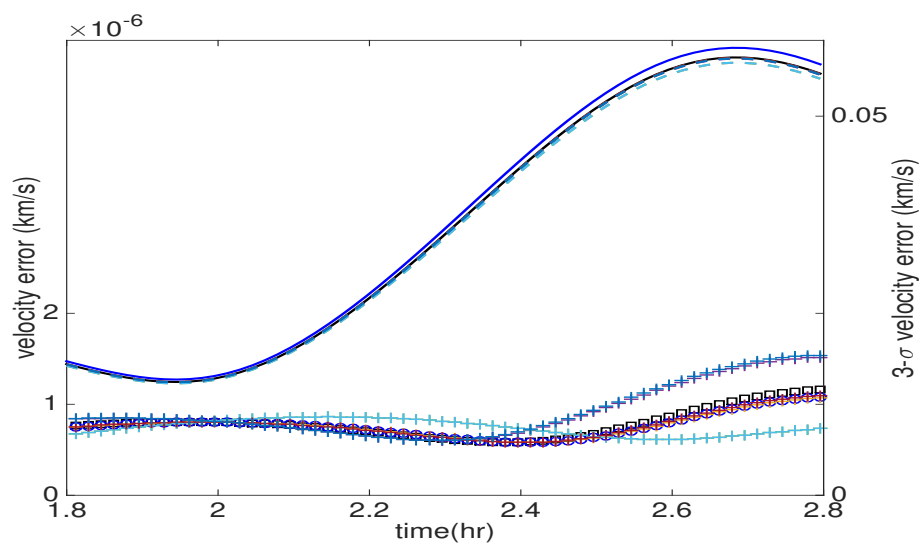
(a) Position error with 3σ uncertainty boundary(b) Velocity error with 3σ uncertainty boundary

Figure 3.19: Post-event OD solution from different batch filters for case 4 with one hour tracking data

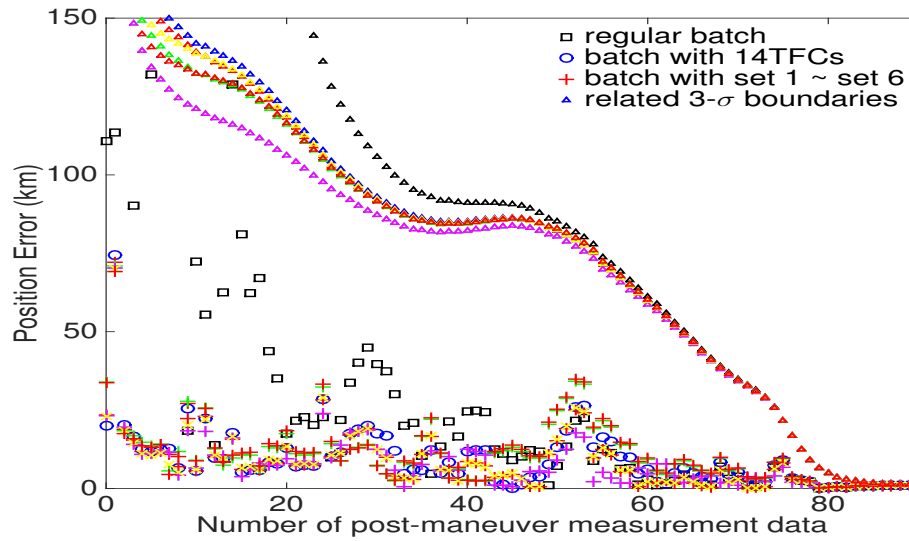
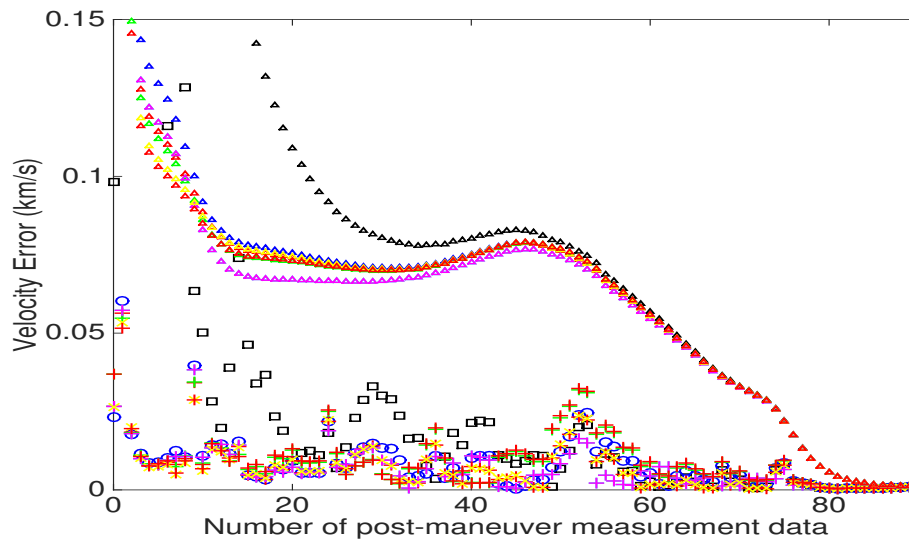
(a) Position error with 3σ uncertainty boundary(b) Velocity error with 3σ uncertainty boundary

Figure 3.20: OD solution with different sizes of tracking data for case 4

are well within their $3\text{-}\sigma$ uncertainty boundaries and each OD solution from the modified batch filter with different TFC sets is consistent with each other regardless of a size of measurement data. This validates that the covariance propagation in the linear region is independent of the represented dynamics, by showing that different event representations using different TFC sets produce similar OD solutions across unmodeled events. It is also found that the regular batch filter requires at least 3 range and range-rate measurements to achieve a converged OD solution. For the modified batch filter, dynamic representation with TFCs enables the filter to incorporate an accurate pre-event OD solution with the post-event measurement data and then provides a valid OD solution even with a single post-event measurement. Since the TFC representation of unknown dynamics allows us to maintain orbit solution across an unmodeled event, OD solutions from the modified batch filters exhibit more accurate state and smaller uncertainty boundaries at the early time of the post-event tracking. After processing the measurement data for one hour (60 measurements), OD solutions from the modified batch filters become equivalent to the one obtained with the regular batch filter. Note that the modified batch filter still has a benefit of providing a representation of an unmodeled event, which can be used for post-event analysis.

3.3 Summary

Propagation of orbit uncertainty based on the event representation is studied and its application in the satellite orbit determination (OD) across unknown and unmodeled space events (USEs) is evaluated. Analytical and numerical studies verify that the covariance propagation in the linear region is independent of the dynamics as long as they represent the same orbital change due to unknown perturbations. Therefore, an event representation can be used to take into account the presence of an unknown event in the computation of the state uncertainty across the period of an unknown event. To apply these characteristics to the OD processing in the presence of a USE, the event representation with thrust-Fourier-coefficient (TFC) is used since it is a very simple and effective way to represent a USE. Different TFC sets are used to represent unknown perturbations and a batch filter with TFCs is developed to perform OD across an unknown event. This filter is a

fully automated process that maintains OD across USEs and avoids the difficulty of manual tuning of thrust coefficients. Simulation results show that each TFC set provides different representation of the unknown perturbing acceleration, which yields varying magnitudes of delta velocity for a given event. However, OD solutions across unknown events using different TFC sets display equivalent performance over the post-event arc as long as those TFC sets are capable of generating the apparent secular motion caused by a given unknown event. The modified batch filter with any TFC set provides faster convergence, better orbit solution, and more flexibility with the initial guess than those in the regular batch filter. Once a USE is represented with any TFC set, the modified filter can incorporate the pre-event orbital state with the post-event tracking data. Therefore, the proposed batch filter provides more accurate post-event state and uncertainty estimation than a regular batch filter does at the early time of the post-event tracking. The proposed OD filter is particularly valuable for the case with no measurement available during a USE period and could allow ground station operators to obtain a valid orbit trajectory right after an unknown event. It also provides insight into the unknown accelerations leading to a given USE. With the estimated TFCs, it computes an estimate of controlling effort, which can be used to bound the control effort necessary for linking two separate states across a USE.

Chapter 4

Event Detection and Maneuvering Satellite Tracking Using Event Representation with 14 Thrust-Fourier-Coefficients

The space catalog has been growing dramatically in recent years and maintaining tracking of satellites is essential to enhance space situational awareness (SSA) capability in Earth orbit. The determination and prediction of the maneuvering satellite's orbit is complicated, specially when it is operated by uncooperative parties. In this chapter, a new event detection algorithm and a maneuvering satellite tracking method using the event representation with thrust-Fourier-coefficients (TFCs) are introduced. A perturbed satellite trajectory under an unknown and unmodeled space event (USE), transitioning between two arbitrary orbital states, can be represented as an equivalent orbital transfer that can be generated by the represented dynamics involving TFCs. This event representation technique with TFCs allows for the usage of existing pre-event orbit determination (OD) solutions to estimate the post-event orbit trajectory. Applying this technique to solve SSA related problems, the sequential filter is modified with TFCs so that it is able to blend incoming post-event observations with the predicted OD estimations to minimize the post-event OD solution errors. Therefore, the TFC event representation enables the modified OD filters to maintain tracking of maneuvering satellites as well as to detect a USE in the absence of a dynamical model of the event.

4.1 Event representation with 14 TFCs

In order to process OD across a USE, its unknown and unmodeled dynamics have to be represented in an OD process to compensate for its effect on a satellite. In this chapter, a mathematical model for unknown dynamics representation using TFCs is briefly reviewed. For a given orbital change across a USE, there are an infinite number of ways to connect the pre-event orbit state with the post-event orbit state using different control laws. Instead of using the essential TFC set, the 14-TFC set is used to represent a USE in more detail to solve SSA related problems in this chapter. It is shown in chapter 2 that there is a simple way to analytically obtain a unique solution for the 14-TFC set. This minimum norm solution of those 14 TFCs from Eq. (2.19) effectively represents an unknown perturbing acceleration :

$$\vec{C} = \overline{G}(\vec{\alpha})^T \cdot [\overline{G}(\vec{\alpha}) \cdot \overline{G}(\vec{\alpha})^T]^{-1} \cdot \left[\frac{\vec{\alpha}(t_f) - \vec{\alpha}(t_0)}{t_f - t_0} \right] \quad (4.1)$$

where $\overline{G}(\vec{\alpha})$ is a matrix form of the averaged Gauss equations while $\vec{\alpha}(t_f)$ and $\vec{\alpha}(t_0)$ are the post-event state and the pre-event state respectively. It computes 14 TFCs that control the secular motion of a satellite across a USE to reach the given post-event state at a given time. The implication of this result is that the perturbed motion of satellite under USEs can be represented on average as an equivalent maneuver involving 14 constant TFCs. In chapter 2, this TFC event representation is extended to non-averaged thrusting between Cartesian position and velocities to show that it is relevant to represent USEs that occurred over a fraction of an orbit period. With

the computed 14 TFCs from Eq. (4.1), the control profile for a USE can be represented as follows :

$$\begin{aligned} \vec{U} \simeq & (\alpha_0^R + \alpha_1^R \cos E + \beta_1^R \sin E + \alpha_2^R \cos 2E) \hat{r} \\ & + (\alpha_0^S + \alpha_1^S \cos E + \beta_1^S \sin E + \alpha_2^S \cos 2E + \beta_2^S \sin 2E) \hat{s} \end{aligned} \quad (4.2)$$

$$\begin{aligned} & + (\alpha_0^W + \alpha_1^W \cos E + \beta_1^W \sin E + \alpha_2^W \cos 2E + \beta_2^W \sin 2E) \hat{w} \\ = & \begin{bmatrix} \hat{r} & \hat{s} & \hat{w} \end{bmatrix} \begin{bmatrix} A1 & \text{zeros} & \text{zeros} \\ \text{zeros} & A2 & \text{zeros} \\ \text{zeros} & \text{zeros} & A3 \end{bmatrix} \vec{C} \end{aligned} \quad (4.3)$$

$$= T \cdot S \cdot \vec{C} \quad (4.4)$$

$$A1 = \begin{bmatrix} 1 & \cos E & \cos 2E & \sin E \end{bmatrix}$$

$$A2 = A3 = \begin{bmatrix} 1 & \cos E & \cos 2E & \sin E & \sin 2E \end{bmatrix}$$

in which T is the transformation matrix ($\hat{r} = \frac{\vec{r}}{|\vec{r}|}$, $\hat{w} = \frac{\vec{r} \times \vec{v}}{|\vec{r} \times \vec{v}|}$, $\hat{s} = \hat{w} \times \hat{r}$) from the body frame (RSW) to the inertial frame (ECI), and S matrix generates the perturbing acceleration in the body frame from the 14 TFCs. Figure 4.1 illustrates how the set of 14 TFCs represents unknown accelerations acting on a satellite. Any control law applied to a thrusting satellite over a finite time period can be

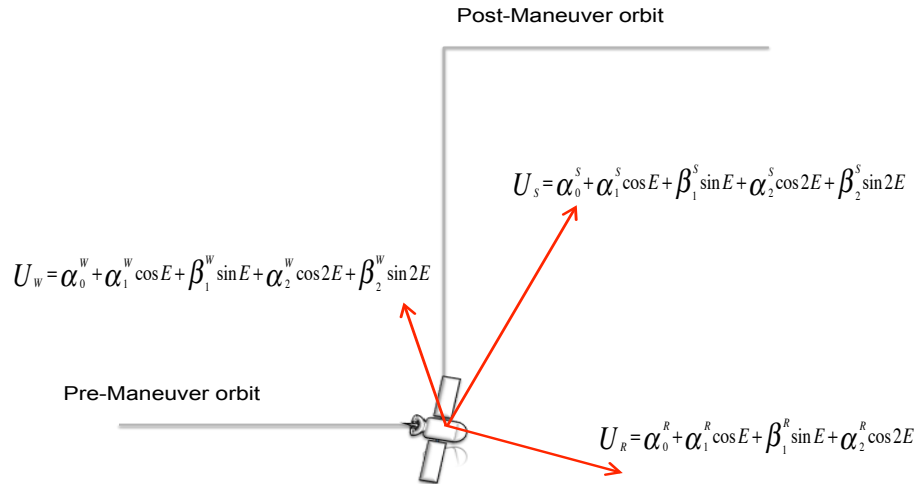


Figure 4.1: Event acceleration representation using 14 TFCs

rigorously represented with these 14 TFCs [13]. Although the event representation with 14 TFCs

does not recover the actual perturbing acceleration for a given USE, it provides a unique dynamics model that can generate an equivalent orbital change. Therefore, this event representation can be used to take into account the presence of an unknown acceleration in the tracking of a satellite across a USE.

4.2 Event detection with event representation using 14 TFCs

Detecting a USE is an important task for maintaining SSA of Earth orbiting satellites. Predicting the trajectory of a satellite across the period of a USE requires the detection of an event before it can be modeled in the orbit estimation. There are numerous techniques to detect an event that have appeared in the literature. Most of them are based on the consistency check between a referencing pre-event orbit and a filtered post-event orbit solution. An event is suspected when the difference of detection parameters, between estimated values from incoming data and known values from a reference orbit, exceeds their defined thresholds. Measurement residuals are primarily used in the data processing to check their consistency by searching for outliers beyond their nominal bounds [42],[43],[44]. For example, the Orbit Determination Tool Kit(ODTK) developed by the Analytical Graphics Inc. (AGI) uses a sequential filter to detect an event by analyzing rejected data from the filter that do not fit into the previous orbit [6]. If an individually observed measurement is very far away from its expected value, an event is suspected to happen. A sudden change in orbital energies or orbital elements of tracking data can also be used to detect an event. Patera [1] used the orbital energy to detect a space event based on the technique of a moving window curve fit as post-processing. Similarly, Swartz et al [29] presented an event detection method based on the Space Incident Flagging Technique (SIFT) by employing a polynomial-curve-fit technique to detect the change of the satellite's energy. With the orbital elements as detection parameters, Kececy et al. [45], Song et al. [46], and Lemmens & Krag [47] post-processed the two-line-element set (TLE) data to find any inconsistencies due to maneuvers. Also, Lee and Hwang [48] applied Interacting Multiple Model (IMM) estimation to detect an event by comparing a resulting change in the orbital elements. In a different way, Kececy and Jah [15] compared filter-smoother updates

through the position and velocity state to detect a single low thrust finite maneuver event by using the batch least-squares and extended Kalman filter (EKF). Recently, a new detection parameter was introduced to recognize spacecraft maneuvers by examining the optimal control distance metric generated by measurement residuals. It is similar to the traditional Mahalanobis distance approach that an event likely has occurred if the probability of the control distance is larger than its systemic uncertainty [41]. Holzinger et al. [8] presented a maneuver detection method for data-sparse environments by applying a control distance metric from an optimal control solution. Singh et al. [9] modified this control distance metric based detection scheme with a minimum-fuel cost function. Lately, Lubey and Scheeres [10] adapted these approaches to detect an event and to reconstruct its unmodeled dynamics using optimal control policies.

A new event detection approach proposed in this paper is based on the event representation method using Thrust-Fourier-Coefficients (TFCs), which uses these TFCs as event detection parameters. The TFC event representation method represents a satellite's motion under an unknown event, transitioning between two arbitrary orbital states, as an equivalent orbit maneuver connecting those two states by applying the Fourier series representation of perturbing accelerations. The previous study has shown that this event representation method using TFCs rigorously provides a unique control law between measurement points that can generate the given secular behavior of a satellite due to an unknown event [13]. Therefore, the new approach utilizes given pre-event information in conjunction with incoming measurement data to detect acceleration changes on a spacecraft due to unknown maneuvers. Note that the measurement data can be collected during or after maneuvers. Fourier series representations of thrust accelerations were used by Hudson and Scheeres who applied averaging techniques to perturbing motions of a spacecraft and represented the secular motion of a spacecraft with 14 TFCs [11]. Ko and Scheeres adapted this approach to represent an event transitioning between two arbitrary orbital states using the TFCs that account for unknown perturbing accelerations [13]. Applying this approach, a sequential filter is modified with an event representation method using TFCs. The modified filter, labeled as ' KF_{TFC} ', directly estimates unknown accelerations in terms of TFCs and plays a main role in our proposed

event detection algorithm. The proposed approach distinguishes itself from other event detection approaches in that it detects event onset and termination time explicitly based on estimated TFCs. This algorithm may be applied to a wide variety of event detection problems, ranging from an impulsive burn maneuver to a continuous low-thrust maneuver.

4.2.1 Event detection algorithm using the modified sequential filter

Maintaining OD across an unmodeled event requires the compensation of unknown dynamics, which is in need of an event detection process established without having event information. Generally, it is not necessary to precisely reconstruct unknown dynamics in order to detect an unmodeled event. Since the 14-TFC set, represented as \vec{C} , can rigorously represent a finite basis of unknown thrust accelerations, it can be used to detect a change-point of accelerations acting on a satellite. By representing the acceleration of an unmodeled event using Eq. (4.2), the governing equations of motion can be rewritten with 14 constant TFCs:

$$\frac{d}{dt} \begin{bmatrix} \vec{X} \\ \vec{C} \end{bmatrix} = \begin{bmatrix} \vec{F}(\vec{X}) \\ 0_{14 \times 1} \end{bmatrix} + \begin{bmatrix} B \\ 0_{14 \times 3} \end{bmatrix} \cdot \vec{U} \quad (4.5)$$

where \vec{F} and B are from Eq. (3.2). By defining the generalized state vector $\vec{Z} = \begin{bmatrix} \vec{X} \\ \vec{C} \end{bmatrix}$, Eq. (4.5) can be linearized by expanding about a reference state vector denoted by \vec{Z}^* :

$$\dot{\vec{Z}}(t) = \dot{\vec{Z}}^*(t) + \left[\frac{\partial \dot{\vec{Z}}(t)}{\partial \vec{Z}(t)} \right]^* (\vec{Z}(t) - \vec{Z}^*(t)) + \text{higher order terms} \quad (4.6)$$

where * indicates that the quantity is evaluated on the reference trajectory with zero TFCs ($\vec{C}^* = \vec{0}$). By ignoring higher order terms and defining $\vec{z}(t) = \vec{Z}(t) - \vec{Z}^*(t) = \begin{bmatrix} \vec{X} - \vec{X}^* \\ \vec{C} - \vec{C}^* \end{bmatrix} = \begin{bmatrix} \vec{x} \\ \vec{c} \end{bmatrix}$,

Eq. (4.6) can be written as:

$$\dot{\vec{z}} = \left[\frac{\partial \dot{\vec{Z}}(t)}{\partial \vec{Z}(t)} \right]^* \vec{z} \quad (4.7)$$

$$= \begin{bmatrix} \frac{\partial(\vec{F}(\vec{X})+B\cdot\vec{U})}{\partial \vec{X}} & \frac{\partial(\vec{F}(\vec{X})+B\cdot\vec{U})}{\partial \vec{C}} \end{bmatrix}^* \begin{bmatrix} \vec{x} \\ \vec{c} \end{bmatrix} \quad (4.8)$$

$$= A(t) \vec{z} \quad (4.9)$$

The linearized measurement model for observation also can be expressed with the generalized state:

$$\vec{Y} = \vec{G}(\vec{Z}, t) + \vec{\epsilon} = \vec{G}(\vec{Z}^*, t) + \left[\frac{\partial \vec{G}}{\partial \vec{Z}} \right]^* (\vec{Z}(t) - \vec{Z}^*(t)) + \text{higher order terms} + \vec{\epsilon} \quad (4.10)$$

$$\vec{y} = \left[\frac{\partial \vec{G}}{\partial \vec{X}} \quad \frac{\partial \vec{G}}{\partial \vec{C}} \right]^* \begin{bmatrix} \vec{x} \\ \vec{c} \end{bmatrix} + \vec{\epsilon} = \begin{bmatrix} \tilde{H}_x & \tilde{H}_c \end{bmatrix} \begin{bmatrix} \vec{x} \\ \vec{c} \end{bmatrix} + \vec{\epsilon} \quad (4.11)$$

$$= \tilde{H} \vec{z} + \vec{\epsilon}, \quad E[\vec{\epsilon}] = 0, \quad E[\vec{\epsilon} \vec{\epsilon}^T] = R \quad (4.12)$$

in which \vec{y} is an observation deviation vector while the observation error, $\vec{\epsilon}$, is random with zero mean and specified covariance of R for each measurement type. With Eq. (4.8) and (4.12), the linear estimation problem using 14 TFCs is defined and the sequential filter can be set up to estimate the TFCs as well as the state:

$$\dot{\vec{z}} = A(t) \vec{z} \quad (4.13)$$

$$\vec{y} = \tilde{H} \vec{z} + \vec{\epsilon} \quad (4.14)$$

Detailed description of how to implement the sequential filter with TFCs is not included in this paper since it follows the standard flow of the sequential filter which is well explained in [4].

The modified sequential filter, KF_{TFC} , estimates unknown accelerations in terms of TFCs and the orbital state jointly. If there is no measurement data available during an unmodeled event, KF_{TFC} propagates a pre-event OD solution across the period of an unmodeled event according to modeled dynamics with the event representation. Then, the propagated state is compared with incoming measurements and the filter adjusts TFCs to connect the post-event measurement data

with a given *a priori* state. Without measurements during a USE, KF_{TFC} is unable to detect event onset or termination time. Instead, it assumes that an event starts at the last pre-event measurement time and ends at the first post-event measurement time. However, it can still examine whether there is an unmodeled event or not during the measurement gap by checking the magnitude of estimated TFCs. An event is declared when a weighted norm of estimated TFCs from the OD filter exceeds a pre-defined nominal threshold, which will be explained in the following chapter. In the modified sequential filter, the 14 TFC set serves as an added process noise term to compensate for an unmodeled event which also has been shown with the modified batch filter in [49].

With measurement data available during an unmodeled event, KF_{TFC} may be used to detect event onset and termination time more precisely. To recognize a change-point of unknown acceleration, the filter needs to estimate TFCs at each measurement update and requires an initialization of TFCs to zeros at the beginning of each time update. This modification with KF_{TFC} allows us to perform OD estimation similar to an extended Kalman filter (EKF). To distinguish it from KF_{TFC} , we label it as ' EKF_{TFC} '. With these two filters, an event detection algorithm is developed to estimate unmodeled eventing time and accelerations. This new event detection algorithm should have the following four essential functions: (1) estimation of unknown acceleration in terms of TFCs; (2) estimation of orbital state along with the estimated TFCs; (3) detection of event onset and termination time; and (4) representation of unknown acceleration across the estimated event period. The proposed algorithm processes the following steps:

- (1) Run EKF_{TFC} over all the pre-event tracking arc to obtain nominal values of 14 TFCs as well as a pre-event OD solution
- (2) Estimate TFCs at each measurement interval by processing EKF_{TFC} forwards in time with a pre-event OD solution as an initial state
- (3) Inspect magnitudes of the estimated TFCs to identify event onset time
- (4) Record the time when a generalized norm of estimated 14 TFCs exceeds a nominal threshold (from step 1) as an output for subsequent analysis

- (5) Keep processing measurement data until measurement residuals return to a nominal (non-event) condition
- (6) Initialize EKF_{TFC} using the last filter updated orbital state and covariance
- (7) Run EKF_{TFC} backwards in time with estimating TFCs over each measurement interval
- (8) Inspect magnitudes of the estimated TFCs to identify event termination time and do the same as step 4
- (9) Run KF_{TFC} forwards in time with an estimated eventing time based on the results from step 4 and 8, which provides a unique 14 TFCs set that forces the orbit to fit through all measurement data over the estimated eventing period
- (10) Represent an unmodeled event with the result from step 4, 8, and 9 using Eq. (4.2)

The process from step 2 to 8 can be iterated to improve the estimation of event termination time since the backward EKF_{TFC} in step 6 may start with less accurate initial information using the last updated post-event OD solution. Note that this process is still valid for the case when no measurement data is available during maneuvers. In this case, the estimated TFC values will exceed their nominal values at the first post-maneuver measurement time in step 3 that can be considered as the maneuver termination time. In step 8, the estimated TFC values from the backward EKF_{TFC} will exceed their nominal values at the last pre-maneuver measurement time that can be regarded as the maneuver onset time. It means that this algorithm regards the relatively large measurement gap, in where an unknown maneuver is suspected to occur, as the maneuvering period.

To identify the event onset or the termination time in step 3 and 8, one has to determine whether the estimated 14 TFC values over each measurement interval are due to a systematic uncertainty or a result of an unmodeled event. It can be checked, using the Chi-Square test (χ_n^2 test) based change-point detection scheme [50]. A change-point of unknown accelerations is declared

if

$$\Gamma > \lambda = \chi_n^2(3\sigma) \quad (4.15)$$

$$\Gamma = \vec{C}^T P_{cc}^{-1} \vec{C} \quad (4.16)$$

where σ is the level of confidence and λ is the threshold value of nominal TFCs that is determined using a result from step 1. P_{cc} is the covariance of estimated TFCs (\vec{C}) from the filter. This detection test relies on the assumption that individual TFCs are Gaussian distributed and independent. The λ is from upper bounds of nominal TFCs due to systematic uncertainties, and it can be adjusted to enforce the level of confidence. The test provides an output of possible event onset or termination time when the filtered TFC estimate exceeds a defined threshold. Outliers due to noisy data can be rejected by comparing them between each adjacent measurement segment. If a change-point is due to an outlier, the estimated TFCs will come back to their nominal values at the following measurement update time since there is no perturbing acceleration to account for. It indicates that the satellite stays in its predicted orbit trajectory. If the satellite is in a perturbed orbit, the norm values of estimated TFCs will stay above the threshold for a certain period, which allows us to detect a USE.

4.2.2 Simulations and results

In order to validate the proposed event detection algorithm with the event representation using 14 TFCs, different simulated USE cases are studied. All the simulations are performed on a low-earth orbiting (LEO) satellite, and its initial state is shown in Table D.1. There are

Table 4.1: Initial state of LEO satellite

$h_0(km)$	e	$i(deg)$	$\Omega(deg)$	$\omega(deg)$	$\nu(deg)$
1885	0.1	20	20	20	180

h_0 : altitude at apogee; Earth radius : 6378.137km[7]

two possible kinds of perturbing acceleration for a USE[46]. One is an impulsive or a discrete perturbation like any collision with other space object, structural breakup, or an explosion. The

other is a relatively small continuous perturbation such as a low thrust malfunction or significant environmental change. To check the performance of the proposed algorithm over these different perturbations, 6 different USE cases are simulated. Also, the proposed algorithm is processed with different types of simulated measurement data to check its capability, which is shown in Table D.2. The ΔV is $10m/s$ for both impulsive and discrete burns. During these events, measurement data is

Table 4.2: Simulation cases with different USEs

Case	Type	Duration of Burn V (min)	Measurement available during event?	Measurement type
1	impulsive burn	-	Yes	range, range-rate
2	impulsive burn	-	No (observation gap : 1hr)	range, range-rate
3	discrete burn	30	Yes	range, range-rate
4	discrete burn	30	Yes	range, Az, El
5	discrete burn	30	Yes	RA, Dec
6	structural deployment	continuous	Yes	range, range-rate

Az : Azimuth, EL : Elevation, RA : Right Ascension, Dec : Declination

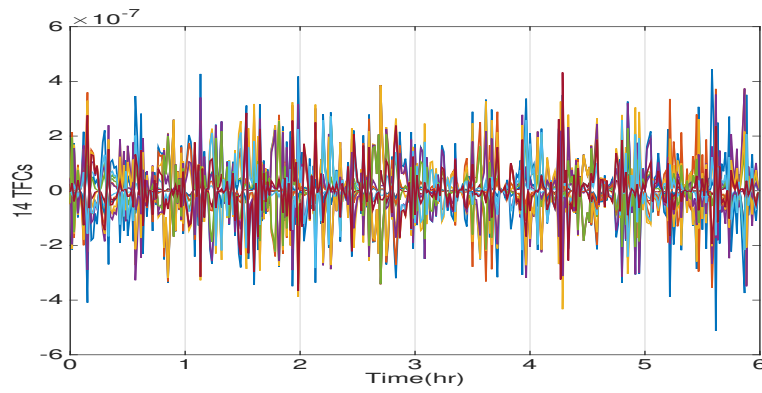
available except for case 2 where there is no available measurement for an hour when an impulsive burn occurs in the middle. The sensor measurement error is imitated by adding white Gaussian noises to the true sensor value, and Matlab is used to implement the algorithm.

Case 1 ~ 2 demonstrate a situation where a satellite performs an impulsive high-thrust maneuver. These two cases are also compared to see how the data sparse environment (no measurement available during the maneuver) affects the performance of the algorithm by checking the accuracy post-event OD solutions and their represented dynamics. Also, case 1 is tested with 2 outliers (at $t = 1$ hour and $t = 2$ hours) in measurement data to check the outlier rejection capability. Case 3 ~ 5 is simulated to compare its performance over a discrete burn maneuver by processing 3 different measurement types. Case 6 is simulating a situation, in which the atmospheric drag is mis-modeled after an unknown structural deployment occurs. This non-gravitational dynamics mis-modeling may be interpreted as a continuous low-thrust maneuver and case 6 is tested to check the versatility of the algorithm on low-thrust maneuver detection. A general 2-body dynamics model with respect to Earth-Centered Inertial (ECI) position-velocity coordinate is considered as

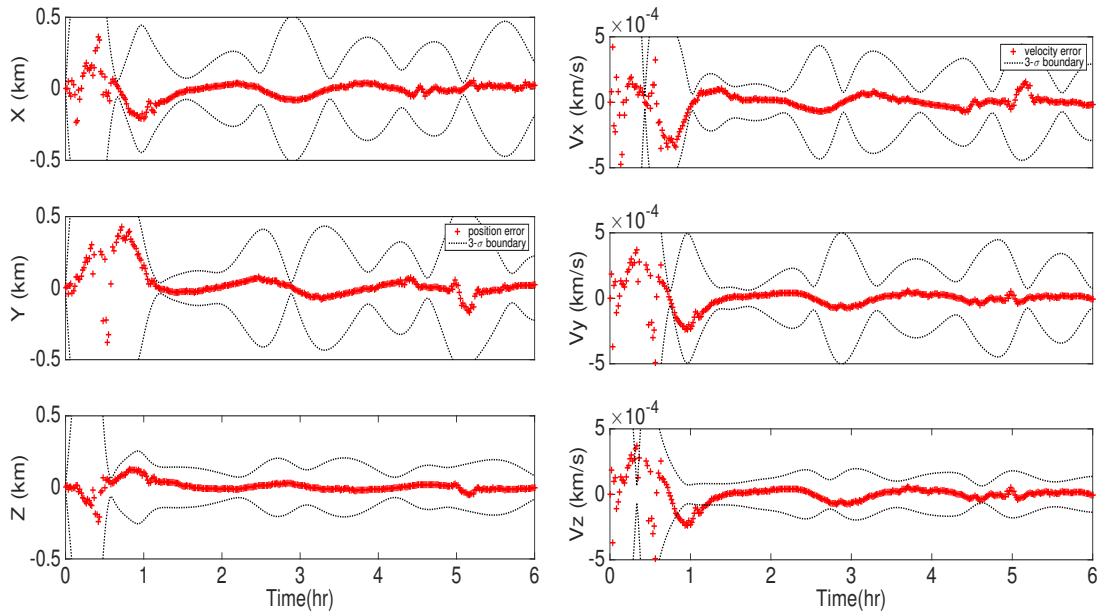
the known dynamics for all the cases except case 6 where J2 and the atmospheric drag acceleration are also included in the known dynamics. Although the simulation is based on simple point-mass gravity for the Earth to analyze the performance of the proposed algorithm in simple way, modification to a full force model is relatively straightforward by defining the known dynamics with higher fidelity models. Once the known dynamics is specified, the proposed algorithm using the TFC event representation is able to account for unmodeled perturbing accelerations, which is fairly shown in case 6.

To initiate the algorithm, it is necessary to obtain an initial condition and a pre-event OD solution. This can be done by processing pre-event tracking data with EKF_{TFC} , explained in step 1 in the previous subchapter. Figure 4.2 displays the result from the step 1 for case 1. The modified filter still estimates TFC values when no actual event has occurred during an observation period, which is shown at Fig. 4.2(a). Since there is no perturbation to be compensated for, these TFCs estimates are due to the sensor measurement errors which have a Gaussian distribution. Their magnitudes are so small that the modified filter with TFCs still provides a valid OD solution that the actual state errors are well within the estimated 3σ standard deviation boundaries obtained by the filter. The estimated TFC values are used to compute the threshold value of nominal TFCs for the change-point detection of thrust acceleration. The result also verifies that any incoming measurement data may be processed with the modified single sequential filter without regard to whether an actual event has occurred or not. The TFC set works as a process noise term to compensate for arbitrary modeling errors or maneuver events by inflating the covariance of the state.

With a pre-event OD solution, EKF_{TFC} runs forwards and backwards in time to estimate the TFCs at each measurement interval. Then, their generalized norm values are computed using Eq. (4.16), which is shown in Fig. 4.3 for case 1. In both subfigures, there is a change-point where Γ , a generalized norm value of TFCs, increases significantly and goes beyond the threshold, λ . From Fig. 4.3(a), an event is predicted to begin at three hours after the initial time. In this figure, the outliers can be easily recognized by comparing their subsequent estimated TFC values.

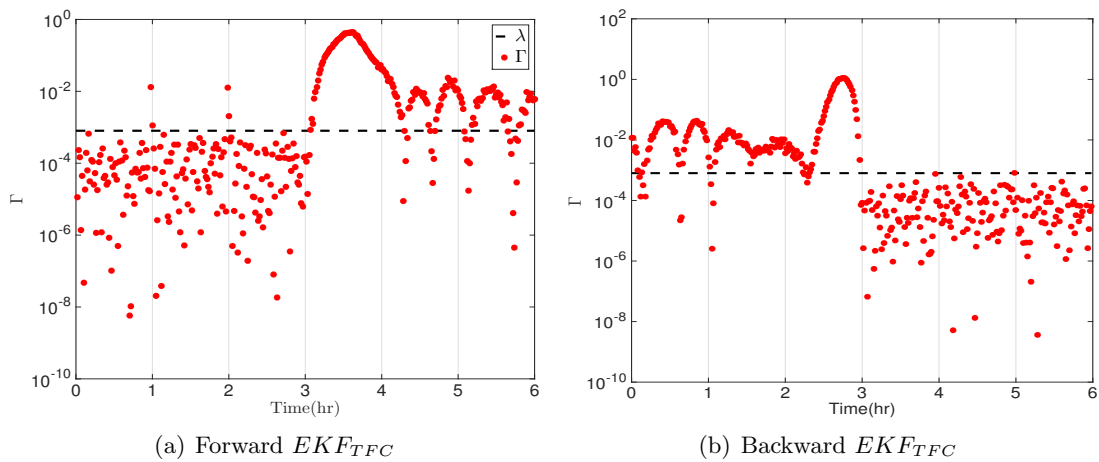


(a) Time history of estimated 14 TFCs



(b) Position errors with 3σ uncertainty boundaries (c) Velocity errors with 3σ uncertainty boundaries

Figure 4.2: EKF_{TFC} results with pre-event tracking data in step 1 for case 1

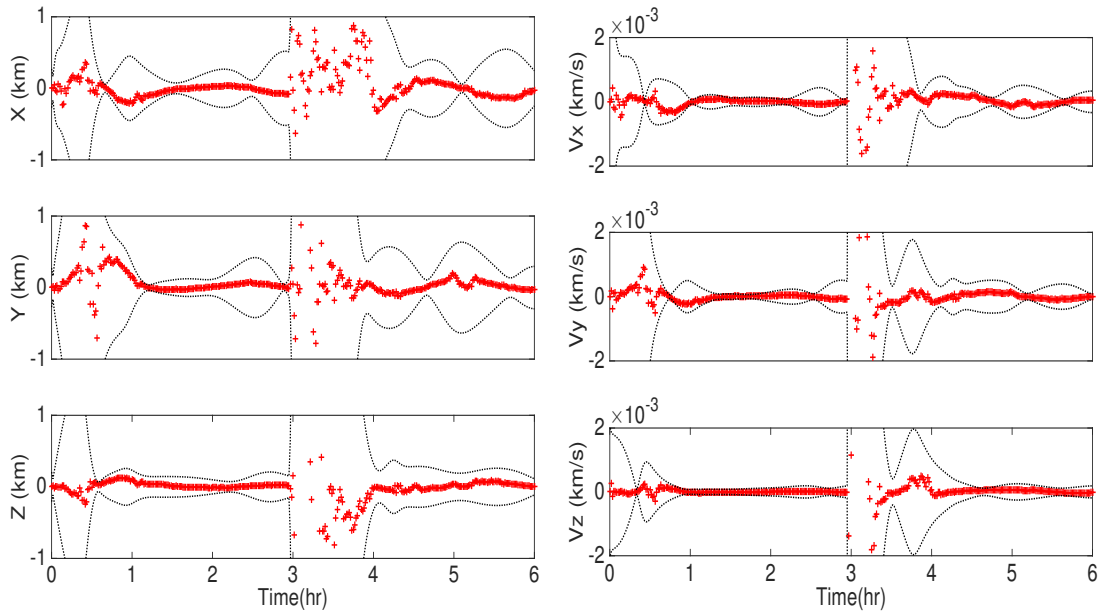


(a) Forward EKF_{TFC}

(b) Backward EKF_{TFC}

Figure 4.3: Generalized norm value of TFCs from EKF_{TFC} in step 2-8 for case 1

The two isolated TFC jumps (at $t = 1$, $t = 2$ hr) indicate that the satellite stays in its previous orbit plane and therefore there is no perturbing thrust to be compensated for. This shows that this algorithm is able to separate outliers from measurement data. From Fig. 4.3(b), the event is suspected to stop right before time passes three hours, which illustrates the event termination time appears before the onset time. It may be caused by a detection delay of the algorithm for a USE with a relatively short thrusting time. If a measurement interval is longer than an actual eventing time, the perturbing effect of a USE becomes apparent at the following measurements after the event. For case 1 with impulsive burn, we can extrapolate the event has a burn time shorter than the measurement interval, 1 minute, which may be interpreted as an impulsive burn. Having an estimated event time, the modified sequential filter, KF_{TFC} , runs forwards in time and provides a unique TFC set as well as post-event OD solutions. As shown in Fig. 4.4, the state estimation errors resulting from the filter are within the estimated 3σ state uncertainty boundaries. Besides



(a) Position errors with 3σ uncertainty boundaries (b) Velocity errors with 3σ uncertainty boundaries

Figure 4.4: OD solution with estimated perturbation in step 9 for case 1

estimating an event period and providing post-event OD solutions, the proposed algorithm also delivers a representation of an unmodeled event. Using the estimated TFC set from step 9 for case

1, the event with an impulsive thrusting can be represented as Fig. 4.5(a) where the represented control profile is compared with the true thrust acceleration.

If there is no available measurement data across an unmodeled event, such as case 2, it is difficult to determine an event time with a relatively large measurement interval. However, the proposed detection algorithm is able to detect the presence of an unmodeled event by checking estimated TFC values over the measurement gap. We have checked the performance of the algorithm with longer observation gaps (1 and 2 orbital period). The result showed that it still could detect the existence of a USE and provides a valid post-event OD solution across the longer observation gaps. There is no special limit about the observation interval to detect a USE using the TFC event representation, but the non-linearity effect could be an issue when propagating the orbit information across the large measurement gap since this approach is valid in linear region. The reason of choosing 1-hour measurement gap instead of 1 or 2 orbital period is to show that the TFC event representation is able to account for non-averaging thrusting over a fraction of an orbit period. The final result of processing the algorithm for case 2 is shown in Fig. 4.5(b)-4.6, where the representation of unknown acceleration and the OD solutions are examined. Figure 4.5(a) and 4.5(b) also illustrate that the algorithm may yield different representations for the same event while providing valid post-event OD solutions. It is due to the fact that the estimated event onset and termination times are based on available measurement data, which is different for each case.

Detection of an event with discrete burn is tested with different types of measurement data, and the results of applying the detection algorithm to those measurements for case 3-5 are shown in Fig. 4.7-4.11. Figure 4.7 shows the OD solution by processing range and range-rate data to estimate the event time and the thrust profile for case 3. Due to inaccuracy of those estimations, some of the state estimations are out of 3σ boundaries. This can be improved by iterating the process as described in the previous chapter. Figure 4.8 shows how the OD solutions have improved after two iterations for case 3. The state errors become smaller and the fit accuracy is improved. It is mainly because the filter detects the event termination time better with an improved post-event OD solution after each iteration. Figure 4.9 compares the event representations for both cases.

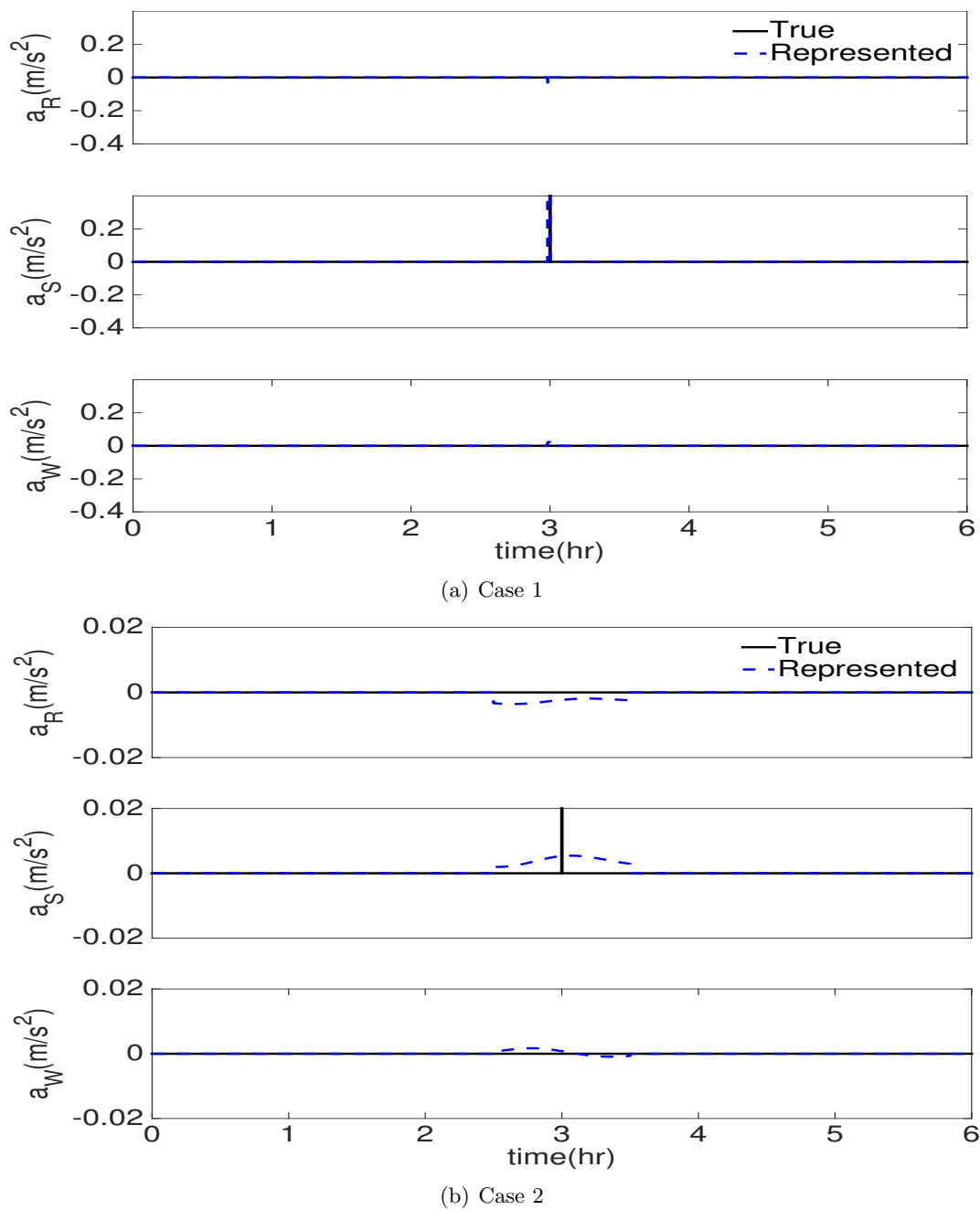
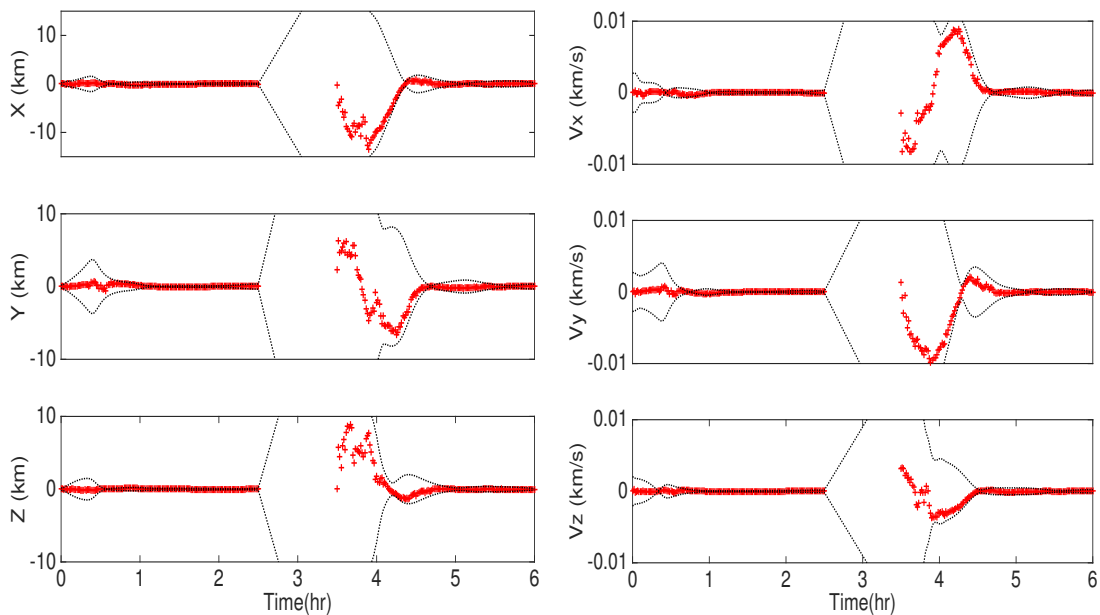
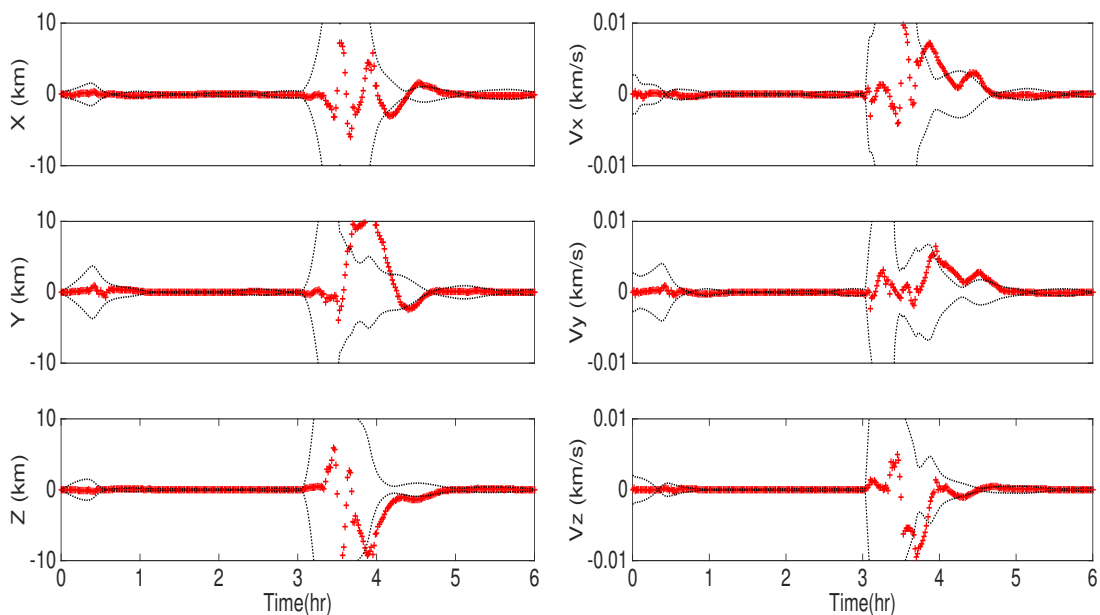


Figure 4.5: Unknown acceleration representation with estimated TFCs in step 10



(a) Position errors with 3σ uncertainty boundaries (b) Velocity errors with 3σ uncertainty boundaries

Figure 4.6: OD solution with estimated perturbation for case 2



(a) Position errors with 3σ uncertainty boundaries (b) Velocity errors with 3σ uncertainty boundaries

Figure 4.7: OD solution with estimated perturbation for case 3

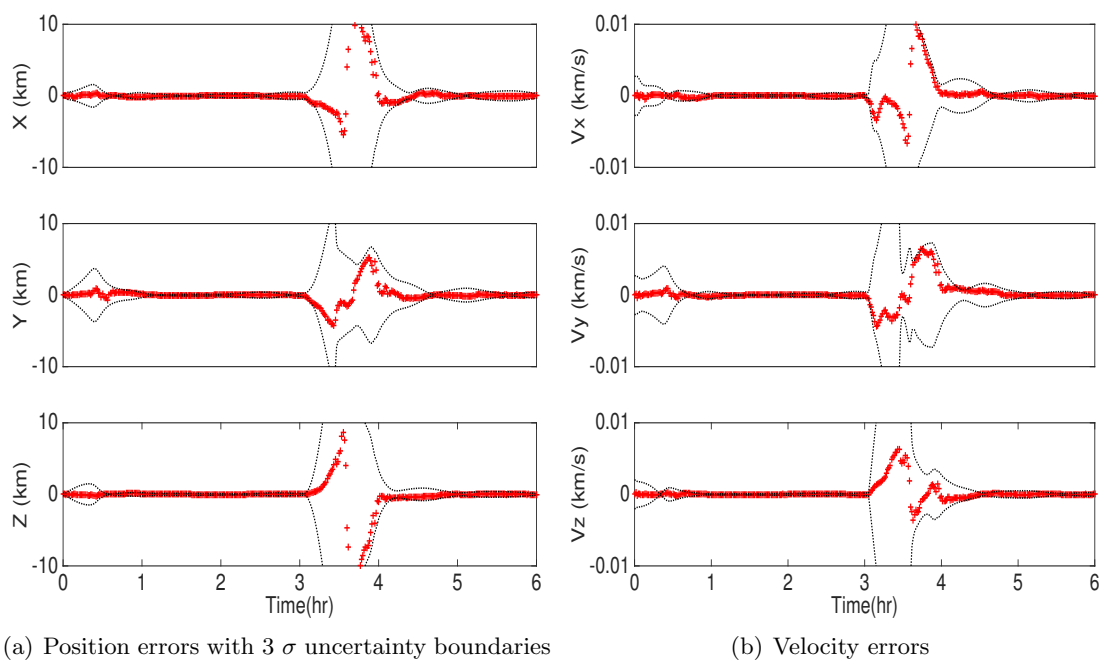
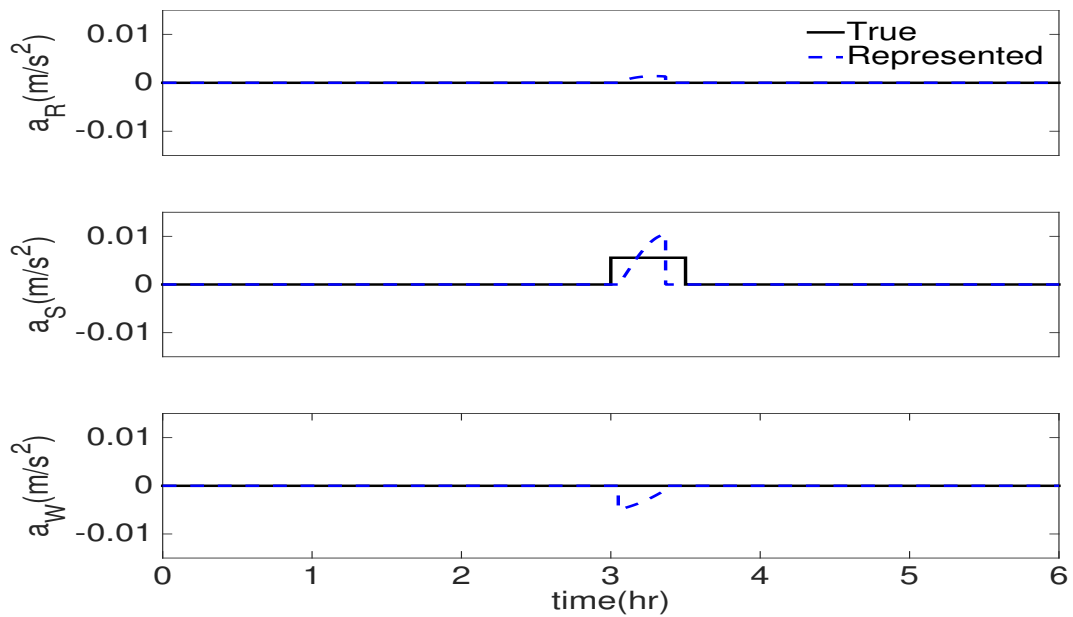
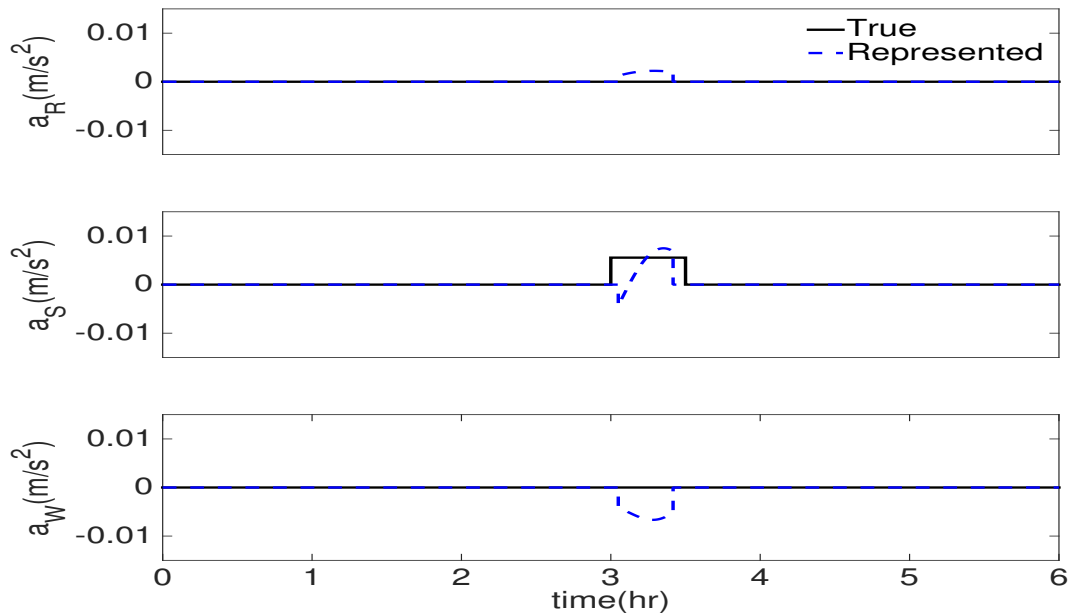


Figure 4.8: OD solution with estimated perturbation for case 3 after two iterations

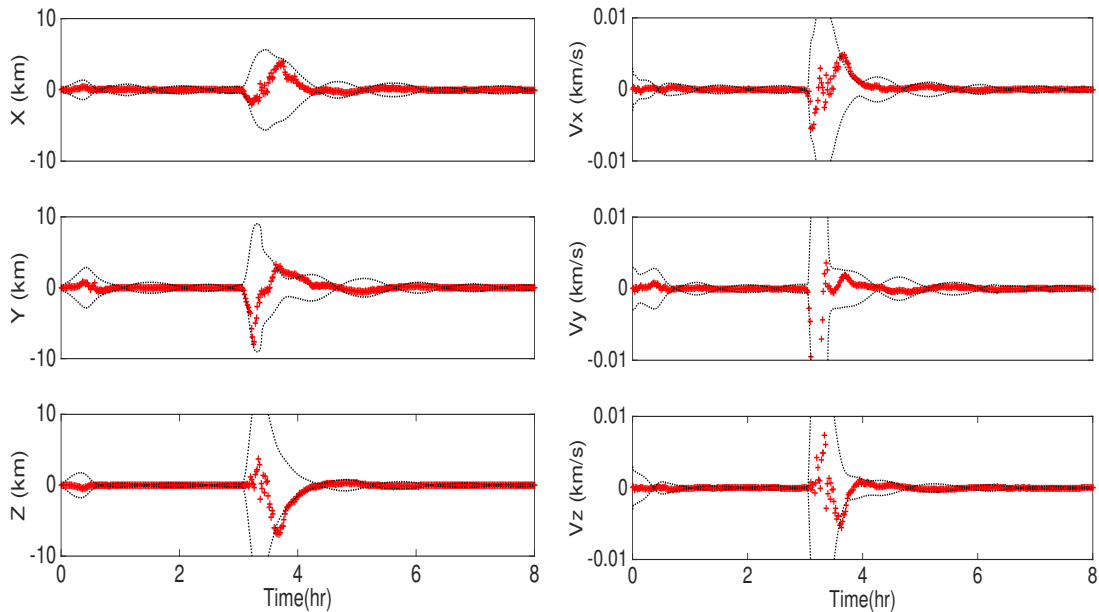
(a) First estimation with 3σ uncertainty boundaries

(b) Estimation after 2nd iteration

Figure 4.9: unmodeled event representation for case 3

Although they are similar to each other, the estimated event termination time is found to be closer to the true value after two iterations if the circumferential components are examined closely.

For case 4 and 5, the detection algorithm is processed with different angle measurements. Figures 4.10-4.12 display post-processing OD solutions and event representations. The result

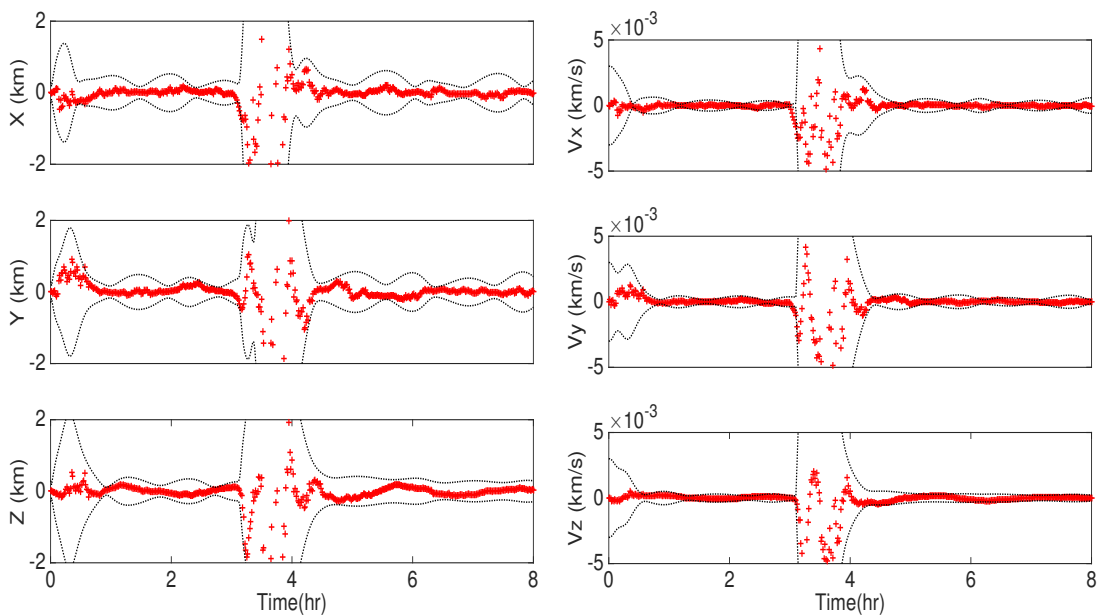


(a) Position errors with 3σ uncertainty boundaries (b) Velocity errors with 3σ uncertainty boundaries

Figure 4.10: OD solution with estimated perturbation for case 4

verifies that the angle measurement data also can be used to detect an unmodeled event and to provide valid OD solutions. Note that it takes a longer time for OD solutions to be converged after a USE since angle measurements usually do not contribute much to a high accuracy OD solution. Also, there is a delay of detecting an event onset time when using angle measurements only (case 5), which is shown in Fig. 4.12(b). However, they can still be used in the event detection algorithm when range data is unavailable.

For the mis-modeled drag case, it is assumed that a structural deployment causes a change in the cross-sectional area of a satellite. Without compensating this change, the mis-modeled atmospheric drag makes the filter diverge after the deployment. This event may be interpreted as a continuous unknown low-thrust maneuver. Different from the previous cases, there is no event



(a) Position errors with 3σ uncertainty boundaries (b) Velocity errors with 3σ uncertainty boundaries

Figure 4.11: OD solution with estimated perturbation for case 5

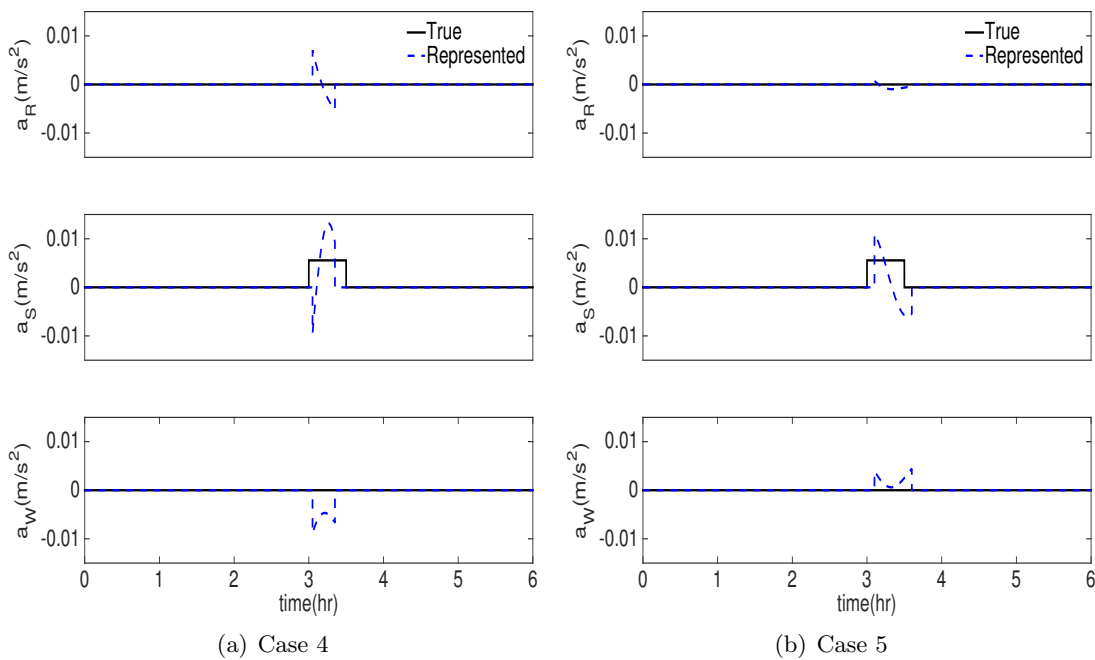


Figure 4.12: unmodeled event representation

termination time for this case. It causes the measurement residuals and TFCs to increase in time after the deployment, which are shown in Fig. 4.13. Since the measurement residual does not return

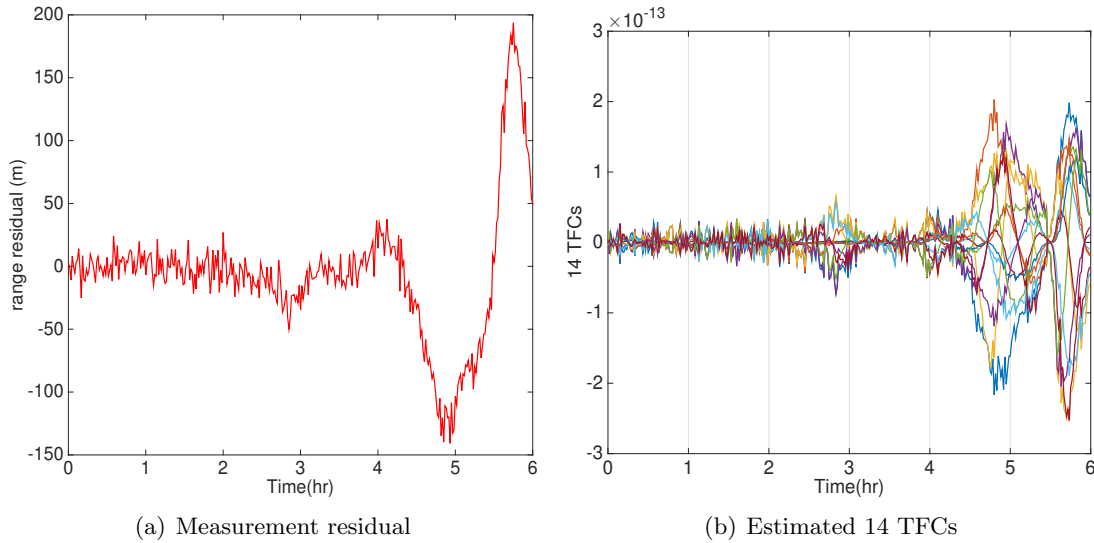


Figure 4.13: Measurement residuals and TFC estimates from forward EKF_{TFC} for case 6

to a nominal boundary, step 5-8 of the algorithm cannot be processed, which means that the event termination time cannot be identified. However, the detection algorithm can still detect a change-point of unknown acceleration after the structural deployment, which is regarded as the event onset time. With the estimated event onset time, the algorithm assumes the last measurement time as the event termination time. It is based on the fact that precise detection of event termination time is not as critical as that of event onset time [51]. Once the estimated event begins, the state covariance matrix is inflated so that the filter is able to accept the subsequent measurement data and to provide valid post-event OD solutions.

For case 6, the structural deployment happens at about two hours after the initial time. The algorithm estimates that the event begins after two and one-half hours. There is a detection delay around one-half hour, which is due to the fact that the accumulated effect of mis-modeling drag does not show up immediately in the estimation process. This may be found in the measurement residual plot in Fig. 4.13(a) as well as the drag representation plot in Fig. 4.14. The represented control profile is different from the true mis-modeled drag; however, it still helps one to estimate the

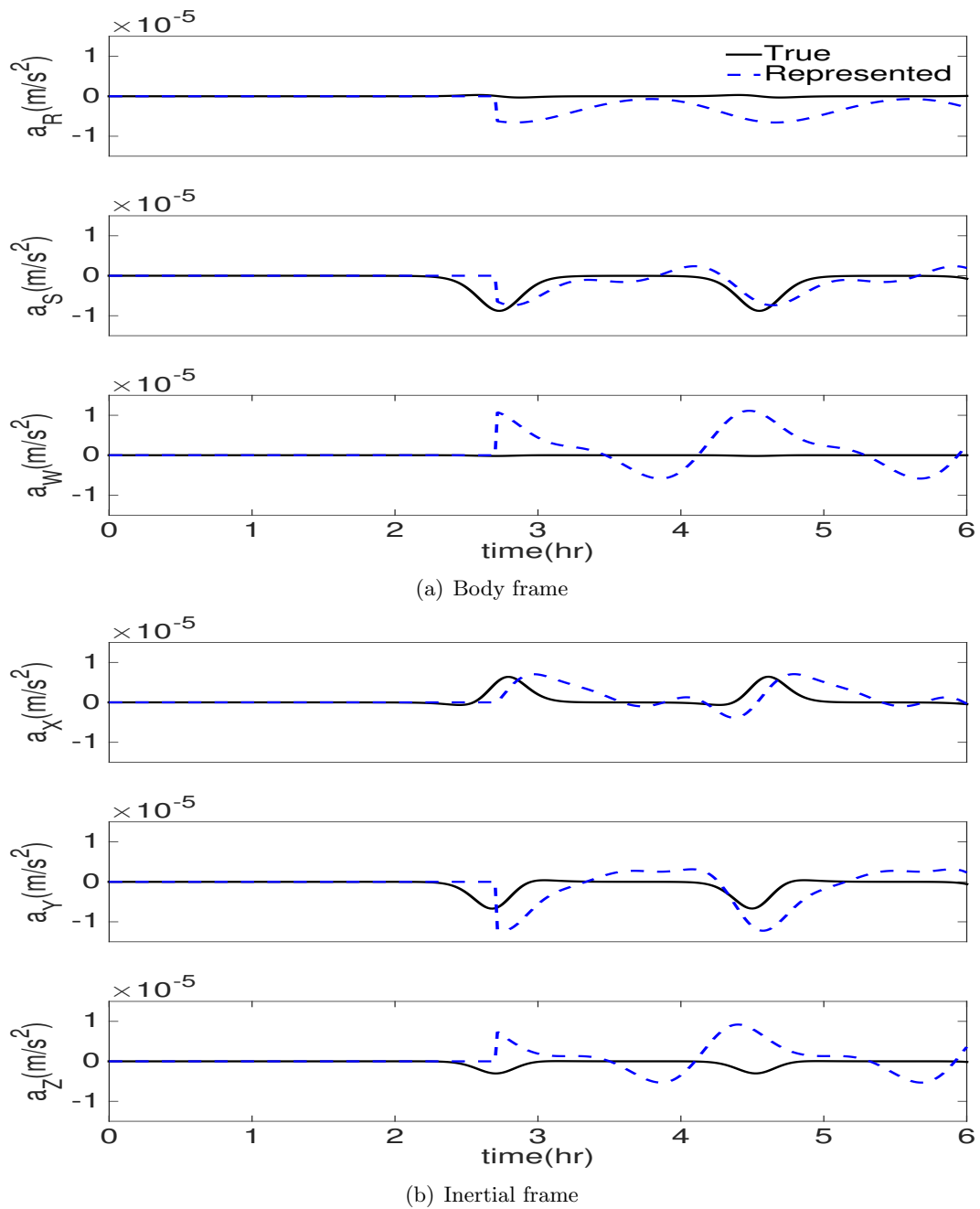
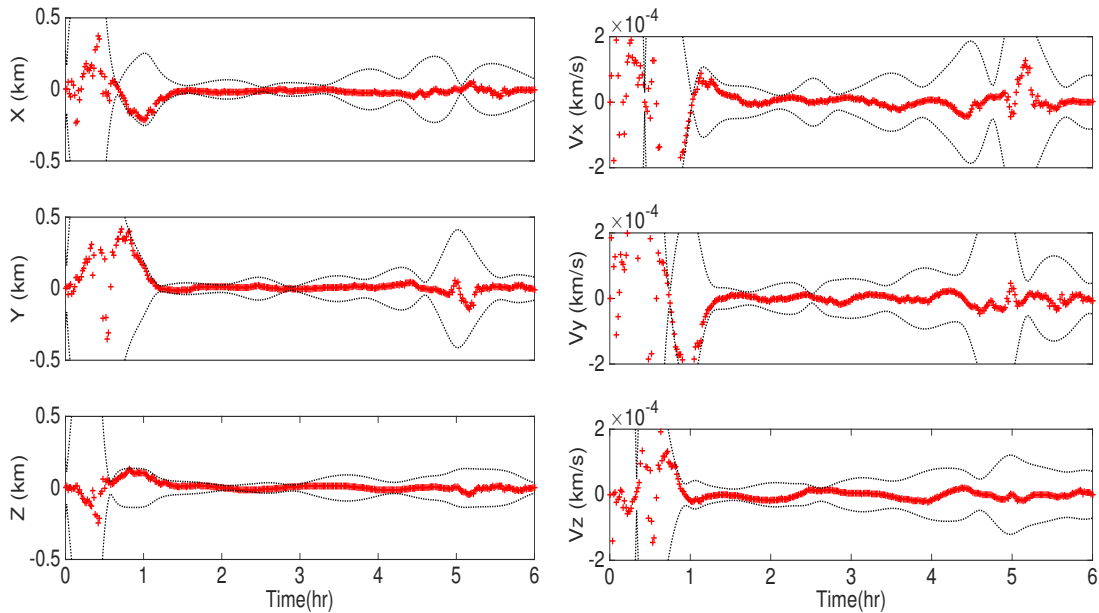


Figure 4.14: Un-modeled drag representation for case 6

magnitude degree of perturbing acceleration. Note that the proposed event detection algorithm is not designed to recover the true perturbing acceleration. Instead, it aims to track a satellite under unknown acceleration by representing an event rigorously and to provide more accurate post-event OD solutions. With the estimated event period and the represented acceleration, the OD solution across the period of mis-modeling of drag is obtained and shown in Fig. 4.15. The state errors



(a) Position errors with 3σ uncertainty boundaries (b) Velocity errors with 3σ uncertainty boundaries

Figure 4.15: OD solution with estimated perturbation for case 6

from the algorithm throughout the mis-modeling period after the deployment stay within their uncertainty boundaries. From all the simulated cases, the proposed event detection algorithm, utilizing the event representation technique, shows consistent performance and versatility. The proposed algorithm is able to detect different event types and to provide valid OD solutions by processing different measurement data.

4.3 Tracking a maneuvering satellite with event representation using TFCs

Maneuvering satellite tracking has been an important task in order to maintain SSA of Earth orbiting satellites. However, it becomes difficult especially when a maneuver is related to

an unknown perturbing event. Any unknown change of force model is regarded as an unknown maneuver, which can be caused by unplanned/non-cooperative maneuver, structural deployment, or collision with space debris. Without compensating for unknown perturbations acting on orbiting satellites, incoming data after an unknown maneuver will be rejected and a satellite can be lost. To deal with this situation, there are three possible ways to recover a post-maneuver orbit trajectory: re-initiation of OD process, maneuver reconstruction, and filtering-through approach [52][53][54]. The first approach is to re-initiate an OD filter over the post-maneuver tracking arc with a largely inflated initial uncertainty. It disregards the pre-maneuver orbit solution and estimates an initial orbit for the post-maneuver orbit trajectory. The maneuver reconstruction approach is a post-processing to determine the maneuver time period and the magnitude of thrust accelerations by using both pre-maneuver and post-maneuver orbits. It involves more computations and difficulty of tuning the thrusting parameters, but provides more accurate post-maneuver OD solutions. The filtering-through approach is to fit the post-maneuver observation into the existing pre-maneuver orbit trajectory by compensating the thrusting acceleration. This real-time tracking approach assumes that the data association has been done and the maneuvering target is identified as the same tracked target[54]. Then, it forces the OD filter to process incoming observation data in real-time to estimate post-maneuver orbits by adapting its dynamics and state covariance. In this section, an emphasis is placed on the filtering-through approach using the TFC event representation method.

A number of different techniques for the filtering-through approach have been developed to track aircraft and missile in aeronautics society, which can be transformed into maneuvering spacecraft tracking [54][55][56]. These techniques available for the real-time maneuvering target tracking can be classified into three groups: single-model based adaptive Kalman filtering, multiple-model algorithms, and decision-based adaptive filtering [53][51]. The simple approach is to use a single-model based Kalman filter to estimate the state of a satellite, but in the presence of unknown and unmodeled acceleration, its performance is seriously degraded [57][58][59]. To account for an unknown perturbation in real-time, adaptive filtering algorithm was developed to track maneuvering

targets[60]. This approach allows the unknown acceleration to be estimated from measurements without making decision. However, its performance degrades during the non-maneuvering period since the filter tries to compensate for noise-induced errors [53]. The multiple model approach arranges a bank of Kalman filters in parallel, where each filter matches a particular maneuvering dynamics model [61][62]. It is based on the assumption that the types of possible maneuvers are finite. Among the various algorithms have been developed for this approach, the interacting multiple model (IMM) algorithm [62], and the adaptive IMM (AIMM) algorithm [63] have shown to be efficient and effective ones. These algorithms have been modified to track a maneuvering spacecraft and they are successful at performing real-time OD across the maneuvering period [48][64]. Although this approach has been a favorite option, it has disadvantages of having the complex algorithm and heavy computational load.

The decision-based adaptive filtering developed so far falls into three categories: equivalent noise, input detection and estimation (IDE), and switching model approach [51]. The equivalent noise approach assumes that unknown dynamics can be sufficiently modeled by a white or colored process noise [65]. The popular technique for this approach is to adjust the noise level, by increasing the process noise magnitude, to account for the effect of a maneuver on state estimation [66]. Adaptive Kalman filtering with the noise identification [67] or with the gain adaption [68] are included in this approach. It appears that this approach is relatively simple but encounters a difficult problem of finding equivalent noise level and related noise statistics in real time. In addition, this approach does not provide any dynamical information about the magnitude of the unknown accelerations. The IDE approach is to detect a maneuver and to estimate an unknown acceleration input explicitly from the available measurement data [51]. Using the estimated control input, the satellite state is estimated directly without having a maneuver model. Main examples of this approach are the input estimation (IE) technique [69], the modified input estimation (MIE) technique [70], the enhanced Input Estimation (EIE) technique [71], and the generalized input estimation (GIE) technique [72]. These algorithms apply some simplifying assumptions that require unknown maneuvers to be constant acceleration input, to have a certain maneuver duration, or to

have a known maneuver onset time. These assumptions are quite restrictive in real satellite tracking applications under unknown maneuvers. If these assumptions made do not correspond to the actual nature of the unknown maneuver, filter performance may be degraded. The switching model approach describes the motion of a satellite with a non-maneuvering model and a maneuvering model [51]. Upon receiving measurement data, the algorithm decides which dynamics model to use in real time. The variable state dimension (VSD) algorithm [73], the enhanced VSD algorithm [74], and the two-stage filtering [75] can be included in this approach. To track a maneuvering satellite with this approach, a nonlinear VSD estimator with a single unscented Kalman filter (UKF) using two state models has been developed [76]. The performance of this approach heavily depends on good maneuver detection, but often it is difficult to detect maneuver termination time. Also, it will be challenging to apply this approach to a low-thrust maneuver case due to a delay of maneuver detection and a difficulty of finding an appropriate maneuver model.

The tracking technique proposed in this chapter falls into the single-model based adaptive Kalman filtering. It distinguishes itself from other methods in that it does not rely on any assumption about a maneuver. This method does not rely on a statistical description of an unknown maneuver as a random process. Instead, it utilizes the event representation technique with TFCs to explicitly estimate an unknown control acceleration. It has shown that any maneuver performed by a satellite transitioning between two arbitrary orbital states can be represented as an equivalent maneuver connecting those two states using TFCs. Applying this TFC event representation, the extended Kalman filter (EKF) is modified to track a maneuvering satellite in real-time. This algorithm estimates the state and the control input jointly without requiring any *a priori* information of a maneuver. It detects a maneuver and inflates the TFC uncertainty level, which allows the EKF filters through unknown maneuvering period by accepting incoming observation data with added state uncertainty, while continuing to estimate the orbit in real-time.

4.3.1 Modified extended Kalman filter with 14 TFCs

Tracking a maneuvering satellite using 14 TFCs consists of a modified EKF with a TFC covariance inflation. In the modified EKF, the state vector is expanded to include the 14 TFCs, $\vec{Z} = \begin{bmatrix} \vec{X} \\ \vec{C} \end{bmatrix}$, in order to estimate the perturbing thrust acceleration as well as the orbital state in real time. Representing the unknown dynamics with the 14 TFCs, the motion of a maneuvering spacecraft can be rewritten with the generalized state vector:

$$\frac{d}{dt} \vec{Z} = \begin{bmatrix} \vec{F}(\vec{Z}) \\ 0_{14 \times 1} \end{bmatrix} + \begin{bmatrix} B \\ 0_{14 \times 3} \end{bmatrix} \cdot \vec{U}(t) \quad (4.17)$$

where \vec{F} and B are from Eq. (3.2). Along with the augmented state and represented dynamics, the state transition matrix (STM) $\Phi(t, t_0)$ is defined and partitioned as:

$$\Phi(t, t_0) = \frac{\partial \vec{Z}(t)}{\partial \vec{Z}(t_0)} = \begin{bmatrix} \Phi_{xx}(t, t_0) & \Phi_{xc}(t, t_0) \\ \Phi_{cx}(t, t_0) & \Phi_{cc}(t, t_0) \end{bmatrix} \quad (4.18)$$

Then, the differential equation for STM can be expressed using Eq. 4.9:

$$\dot{\Phi}(t, t_0) = A(t)\Phi(t, t_0) \quad (4.19)$$

$$\begin{bmatrix} \dot{\Phi}_{xx}(t, t_0) & \dot{\Phi}_{xc}(t, t_0) \\ \dot{\Phi}_{cx}(t, t_0) & \dot{\Phi}_{cc}(t, t_0) \end{bmatrix} = \begin{bmatrix} \frac{\partial(\vec{F}(\vec{X}(t))+B \cdot \vec{U}(t))}{\partial \vec{X}(t)} & \frac{\partial(\vec{F}(\vec{X}(t))+B \cdot \vec{U}(t))}{\partial \vec{C}} \\ 0 & 0 \end{bmatrix} \begin{bmatrix} \Phi_{xx}(t, t_0) & \Phi_{xc}(t, t_0) \\ \Phi_{cx}(t, t_0) & \Phi_{cc}(t, t_0) \end{bmatrix} \quad (4.20)$$

From Eq. 4.20, the following property can be easily obtained:

$$\dot{\Phi}_{cx}(t, t_0) = 0, \quad \dot{\Phi}_{cc}(t, t_0) = 0 \quad (4.21)$$

$$\Phi_{cx}(t, t_0) = \Phi_{cx}(t_0, t_0) = 0, \quad \Phi_{cc}(t, t_0) = \Phi_{cc}(t_0, t_0) = I \quad (4.22)$$

To examine the contribution of TFCs on the state uncertainty estimation, the covariance matrix, P_Z , can be propagated forward from an initial time to a current time by using the partitioned STM. At the initial time, it is assumed that there is no correlation between the state and TFCs

($P_{xc_0} = P_{cx_0} = 0$):

$$P_Z = \Phi(t, t_0)P_{Z_0}\Phi^T(t, t_0) \quad (4.23)$$

$$\begin{bmatrix} P_{xx} & P_{xc} \\ P_{cx} & P_{cc} \end{bmatrix} = \begin{bmatrix} \Phi_{xx}(t, t_0) & \Phi_{xc}(t, t_0) \\ 0 & I \end{bmatrix} \begin{bmatrix} P_{xx_0} & 0 \\ 0 & P_{cc_0} \end{bmatrix} \begin{bmatrix} \Phi_{xx}(t, t_0) & \Phi_{xc}(t, t_0) \\ 0 & I \end{bmatrix}^T \quad (4.24)$$

From Eq. (4.24), the partitioned covariance matrix can be expressed as:

$$P_{xx} = \Phi_{xx}(t, t_0)P_{xx_0}\Phi_{xx}^T(t, t_0) + \Phi_{xc}(t, t_0)P_{cc_0}\Phi_{xc}^T(t, t_0) \quad (4.25)$$

$$P_{xc} = \Phi_{xc}(t, t_0)P_{cc_0} \quad (4.26)$$

$$P_{cx} = P_{cc_0}\Phi_{xc}^T(t, t_0) \quad (4.27)$$

$$P_{cc} = P_{cc_0} \quad (4.28)$$

where P_{xx} is the error covariance matrix related to a position and velocity state. The second term in Eq. (4.25) is a positive definite and compensates for the error due to unmodeled perturbing acceleration via P_{cc_0} . When there is a USE, this term automatically inflates the state covariance and represents the contributed uncertainty from unmodeled dynamics.

The modified EKF initializes the 14 TFCs to zeros with nominal TFC covariance matrix, P_{cc_0} , at the initial time:

$$P_{cc_0} = \lambda I_{14 \times 14} \quad (4.29)$$

where λ is the norm value of nominal 14 TFCs that is obtained by running this filter over the pre-maneuver tracking arc when getting an initial reference trajectory. The computed norm value, λ , can also be used as a threshold value to determine a maneuver onset and a termination time, which is already shown in the previous chapter. The modified EKF operates in its normal mode in the absence of any maneuvers and the 14 TFCs works as a process noise to account for any systematic error such as a measurement error. The estimated values of 14 TFCs are so small that these nominal TFCs do not alter the reference trajectory significantly. When there is an unmodeled event, the filter recognizes it by detecting any measurement residual exceeding a threshold number of

standard deviations from the mean residual for that object. Upon detecting this maneuver onset, the modified EKF adjusts 14 TFCs to avoid filter divergence and to compensate for unknown dynamics by increasing the covariance of the 14 TFCs in Eq. (4.25). Instead of using nominal covariance of 14 TFCs, the filter applies the inflated covariance:

$$P_{cc_k} = \gamma P_{cc_k} \quad (4.30)$$

where P_{cc_k} is the covariance matrix of the 14 TFCs at the current observation time ($t = t_k$) and γ is a scale up factor, 2. If P_{cc_k} is too small, the estimated state covariance can become too small and the estimation process can diverge. If P_{cc_k} is chosen too large, the covariance bound is raised to an unnecessarily large value, which permits larger errors in the estimate of solution. Therefore, the filter keeps increasing P_{cc_k} until measurement residuals fall within desired uncertainty boundaries, and then this iteration process terminates immediately after that.

Using an adequate P_{cc_k} from Eq. (4.30), the updated TFC values provide a sufficient thrust acceleration to bring the estimated orbit trajectory close to the true perturbed orbit. In other words, the estimated TFCs successfully account for the unknown acceleration. Then, the process proceeds to the next observation time ($t = t_{k+1}$) and the reference orbit is updated. The filter reinitializes the 14 TFCs to zeros to process next measurement data. At this stage, the problem is that the filter diverges if the covariance of 14 TFCs is reinitialized to the nominal covariance matrix, P_{cc_0} . This divergence occurs because using P_{cc_0} does not inflate the state covariance sufficiently to account for the uncertainty contributed by TFCs estimation after the covariance inflation for a USE. To avoid this problem, the modified EKF uses the mean covariance matrix for P_{cc} at reinitialization:

$$P_{cc_{k+1}} = \frac{P_{cc_k} + P_{cc_0}}{2} \quad (4.31)$$

Even when there is no actual maneuver, this procedure is still valid since P_{cc_k} would be similar to P_{cc_0} and therefore $P_{cc_{k+1}} \simeq (P_{cc_0} + P_{cc_0})/2 = P_{cc_0}$. In this way, the proposed filter achieves a good tracking performance during the non-maneuvering period as well as the maneuvering period,

without detecting a maneuver termination time explicitly. The flow chart for the modified EKF associated with the TFC event representation is shown in Fig. 4.16, which is based on the general EKF algorithm[4]. This process does not require for the filter to have any *a priori* knowledge of a maneuver. Therefore, the modified EKF can be applied to a wide variety of maneuvering satellite tracking problems, ranging from an impulsive burn to a continuous low-thrust maneuver.

4.3.2 Simulations and results using 14 TFCs

In order to validate the modified EKF with 14 TFCs and to check the filters performance, the same space event scenarios from chapter 4.2 are simulated. Assume there is a fairly accurate

Table 4.3: Simulation cases with different maneuvers

Case	Type	Duration of Burn V (min)	Measurement available during event?	Measurement type
1	impulsive burn	-	Yes	range, range-rate
2	impulsive burn	-	No (observation gap : 1hr)	range, range-rate
3	discrete burn	30	Yes	range, range-rate
4	discrete burn	30	Yes	range, Az, El
5	discrete burn	30	Yes	RA, Dec
6	structural deployment	continuous	Yes	range, range-rate

Az : Azimuth, EL : Elevation, RA : Right Ascension, Dec : Declination

a priori orbit information available with pre-maneuver tracking data. The modified EKF utilizes the *a priori* orbit solution in conjunction with incoming measurement data to maintain tracking of a maneuvering satellite. It is also assumed that the track association has been done and the maneuvering satellite is identified as the same tracked satellite. Figure 4.17 shows OD solutions and estimated TFC values from the modified EKF for case 1. The state errors and uncertainty boundaries decrease until an impulsive burn occurs at $t = 3$ hr. Then, the filter increases TFCs to account for the perturbing acceleration, which inflates the uncertainty boundaries to accept the measurement data during the maneuver. The TFCs estimation with an inflated TFC covariance forces measurement residuals fall within 3σ boundaries (30m for range, 3m/s for range-rate), which is shown in Fig. 4.18. As a result, the state estimation errors are within their estimated 3σ state

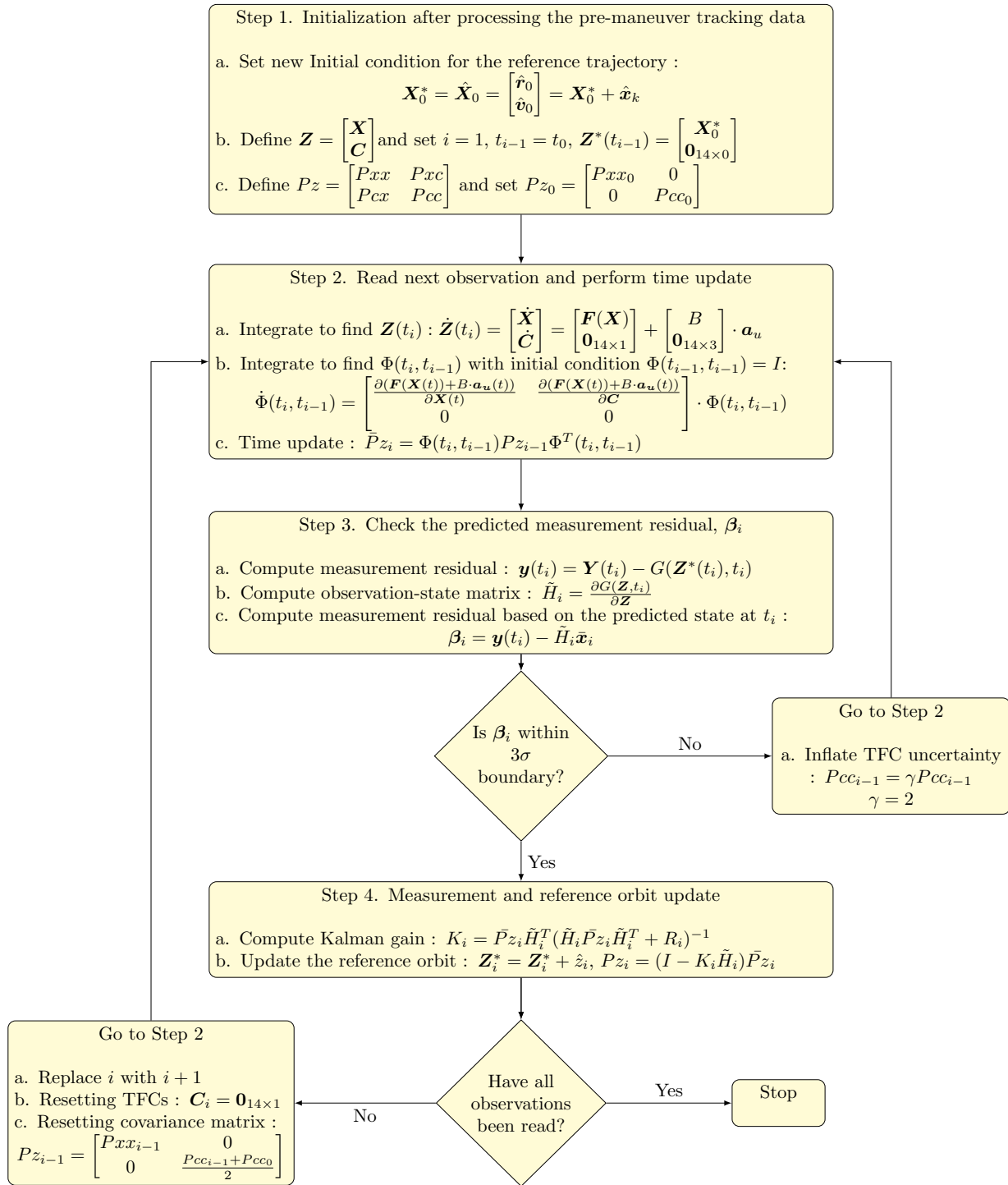


Figure 4.16: Flow chart for the modified EKF

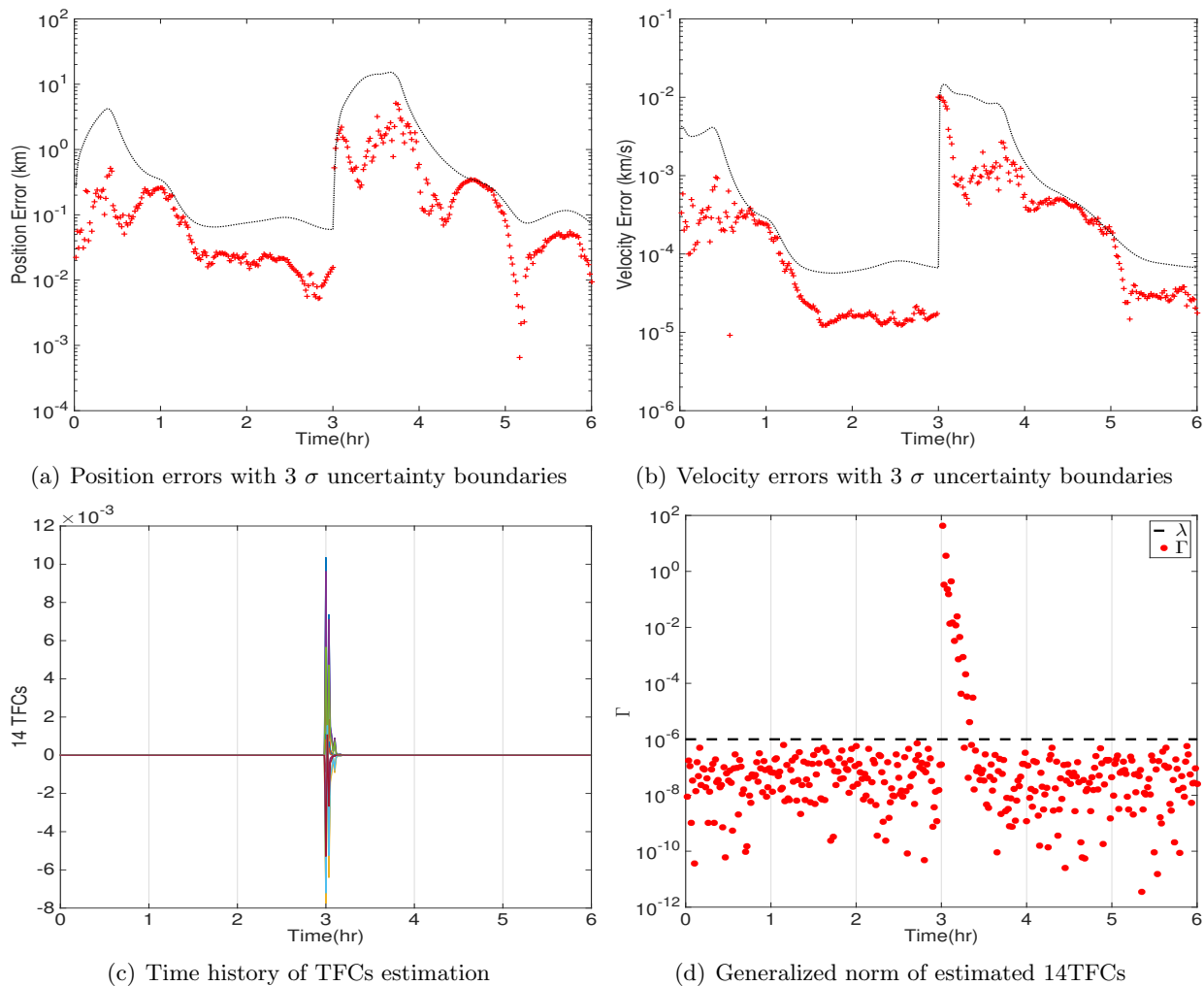


Figure 4.17: OD solution from the modified EKF for case 1

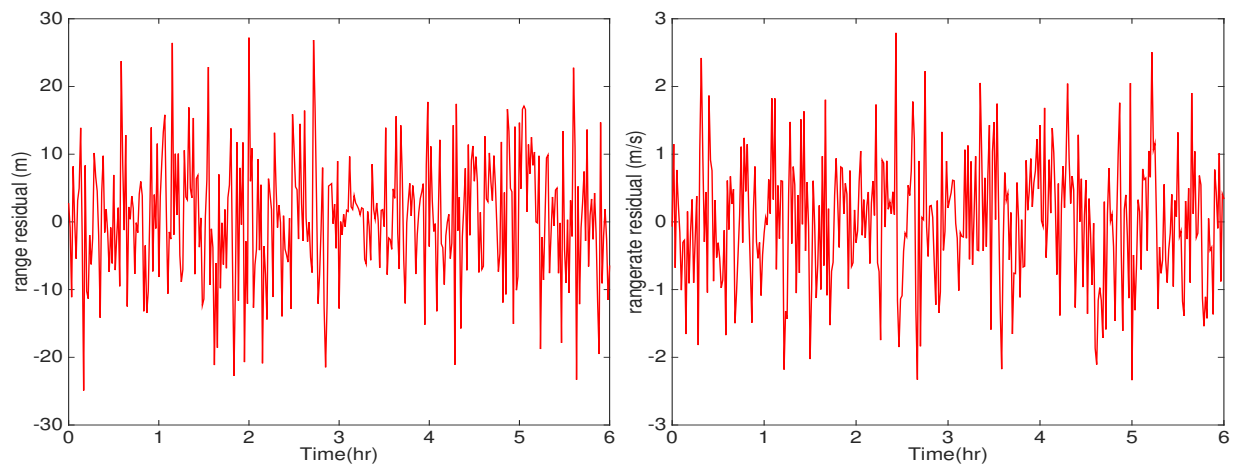


Figure 4.18: Measurement residuals from the modified EKF for case 1

uncertainty boundaries and the filter is able to maintain tracking of a satellite under an impulsive burn. From Fig. 4.17(c)-4.17(d), a maneuver onset time can be easily detected by checking the TFCs estimation or a generalized norm value of 14 TFCs, Γ . There is a change-point where those values increase significantly and go beyond their thresholds. The maneuver is estimated to begin at three hours after the beginning of the simulation. It is also noticeable in Fig. 4.17(d) that the inflated TFCs falls back to the nominal threshold (λ) at $t = 3.2\text{hr}$, which indicates that the maneuver has terminated. This allows us to estimate the duration of an unmodeled event. Note that the estimation of maneuver termination time from the filter is not accurate mainly due to its inherent difficulty and a delay of detection. However, timely detection of a maneuver termination time is usually not as important as timely detection of maneuver onset time during the tracking. This is because tracking a non-maneuvering satellite assuming it is maneuvering still provides an acceptable state estimation with a related uncertainty boundary [51].

When there is no measurement data available during the maneuver like case 2, the modified EKF can still maintain tracking of a maneuvering satellite across a relatively large measurement interval, which is shown in Fig. 4.19. The TFC covariance inflation increases the state uncertainties, which allows the modified filter to process the post-maneuver measurements and to estimate the post-maneuver orbit. The estimated TFCs from the filter are able to generate a sufficient thrust acceleration to connect the pre-maneuver orbit with the estimated post-maneuver trajectory. Figure 4.20-4.22 show that the modified filter can successfully process OD across a maneuver with 30 minutes continuous burn for case 3-5. The position errors are substantially less than ten kilometers where unknown accelerations do occur, and all state errors are within their estimated 3σ uncertainty boundaries. In Fig. 4.20(c)-4.21(c), there are two big jumps in TFCs estimation, which is different from the impulsive burn case that has a single jump. From these figures, it is difficult to determine the maneuver onset and the termination time. In this case, checking a generalized norm value is more useful to estimate the maneuver onset and the termination time since it is easier to distinguish those change-points. From Fig. 4.20(d)-4.21(d), the satellite is estimated to perform the maneuver for about 45-55 minutes while the actual burn time is 30 minutes. This maneuvering

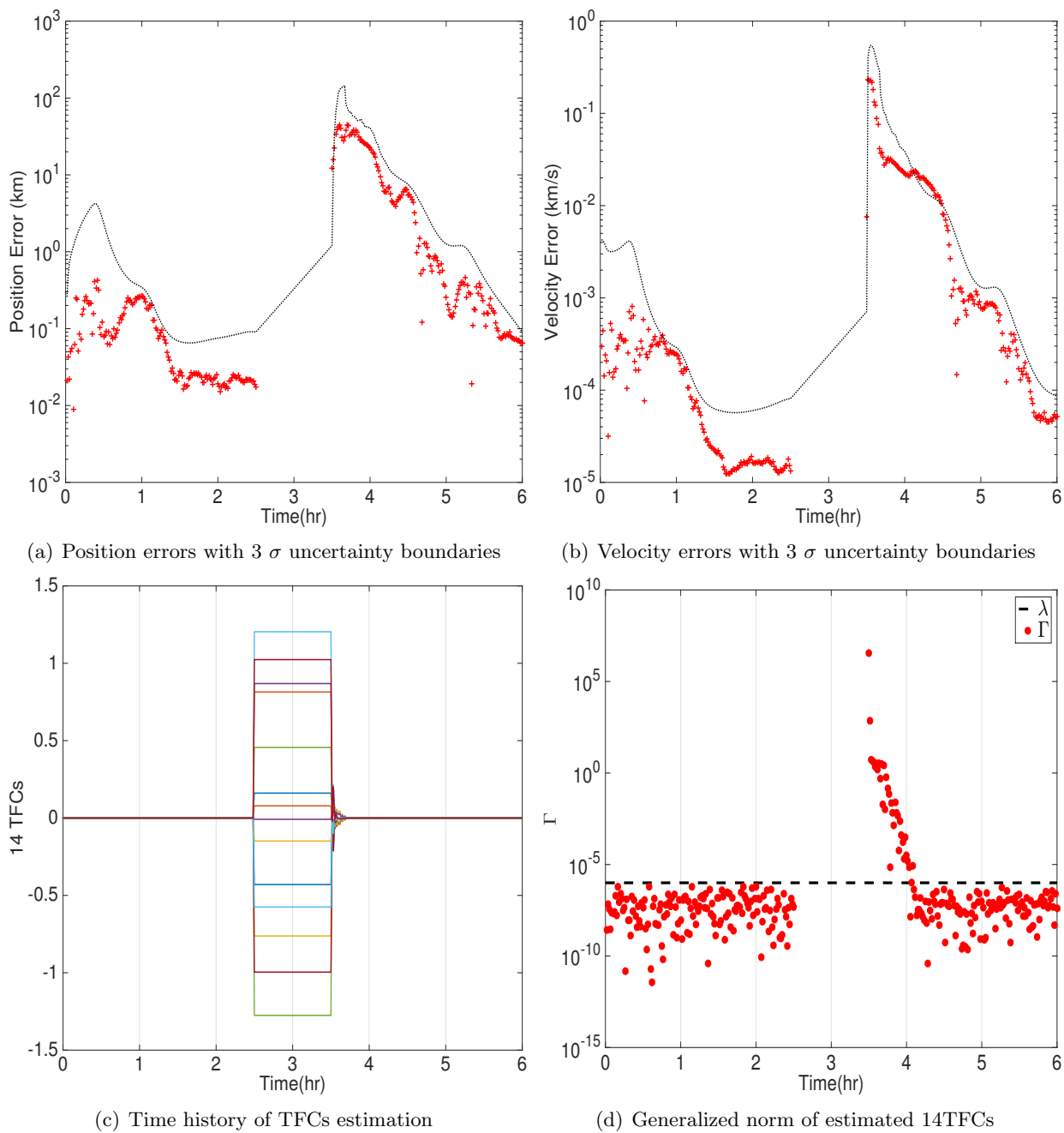


Figure 4.19: OD solution from the modified EKF for case 2

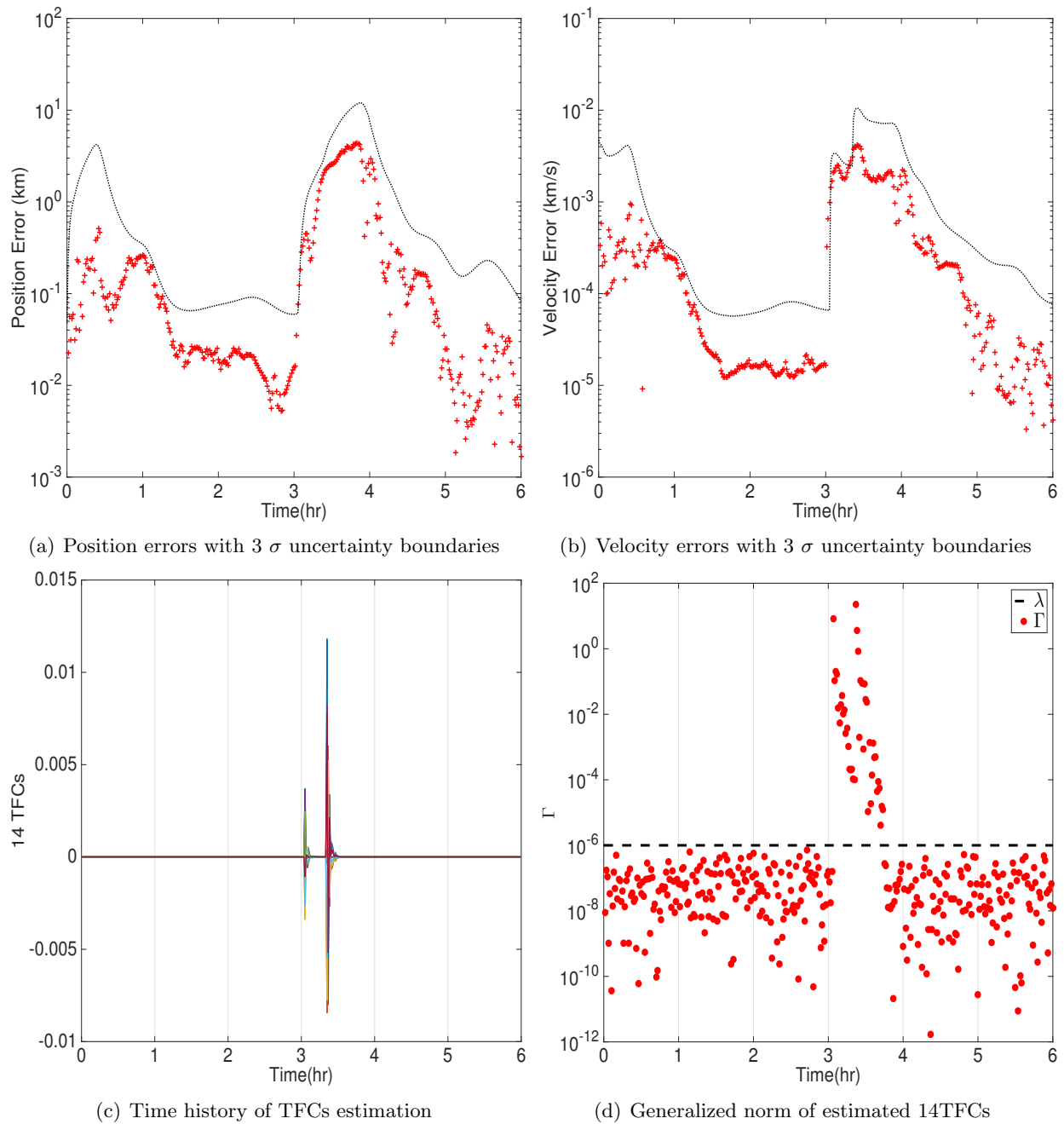


Figure 4.20: OD solution from the modified EKF for case 3

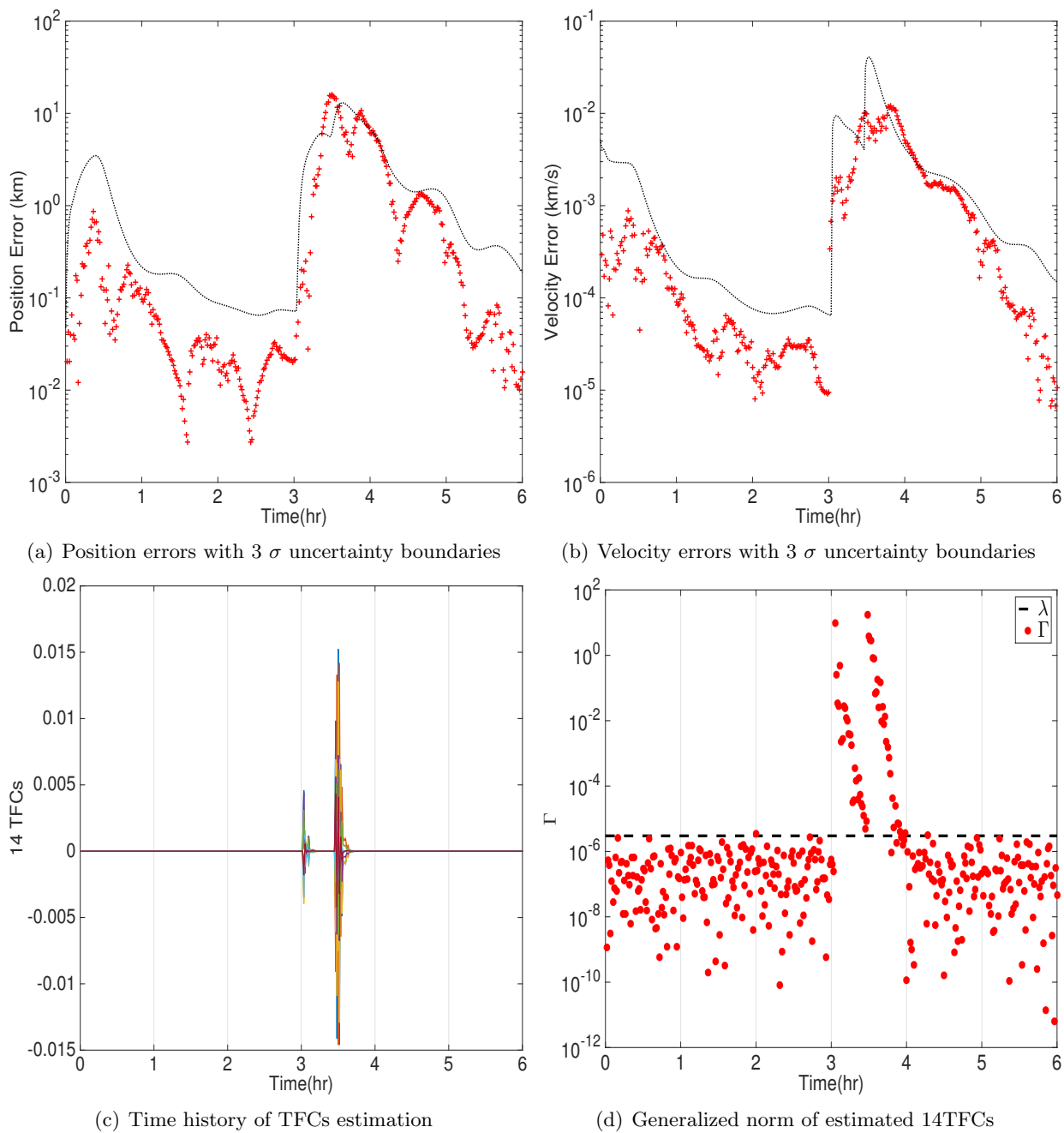


Figure 4.21: OD solution from the modified EKF for case 4

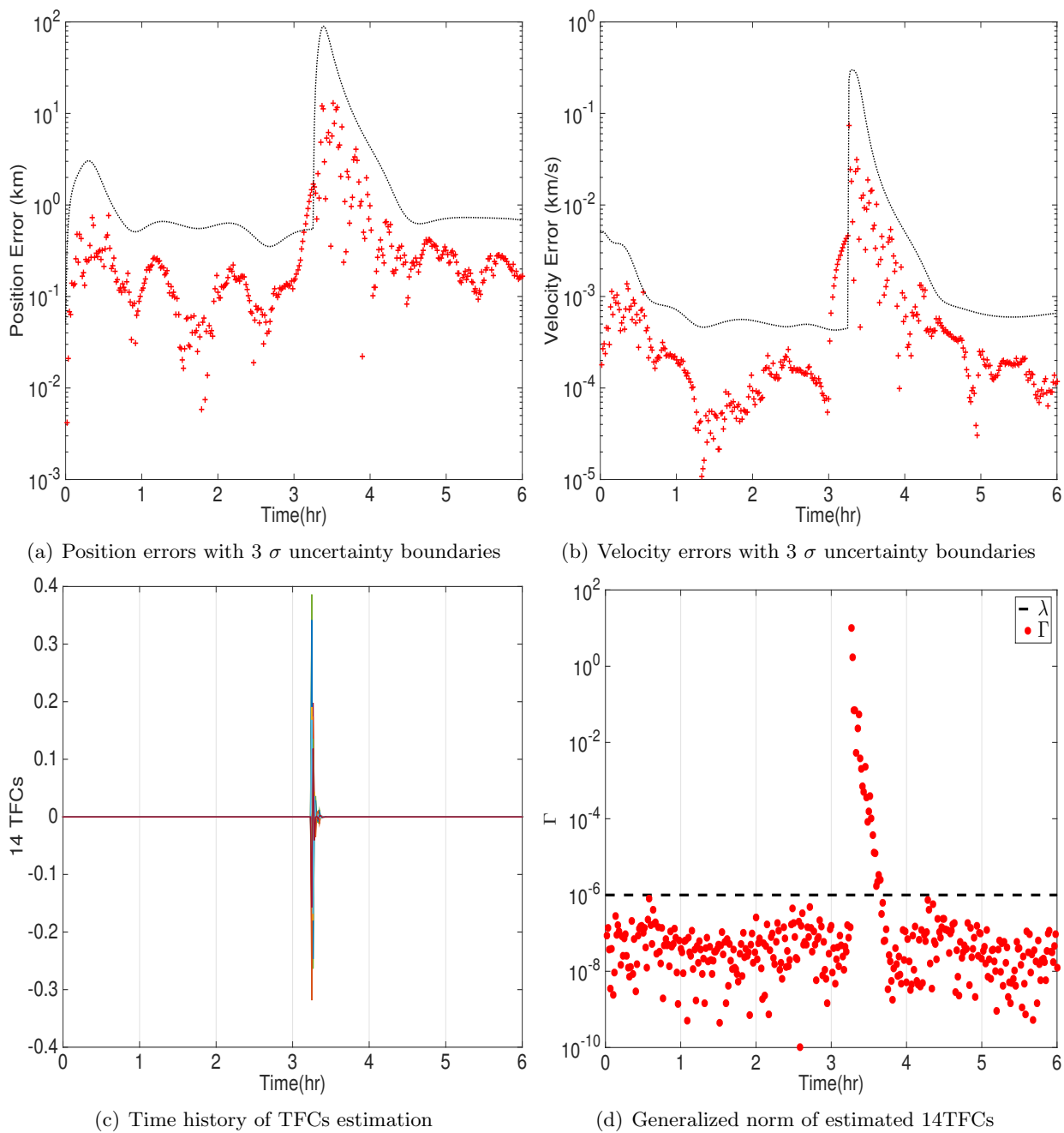


Figure 4.22: OD solution from the modified EKF for case 5

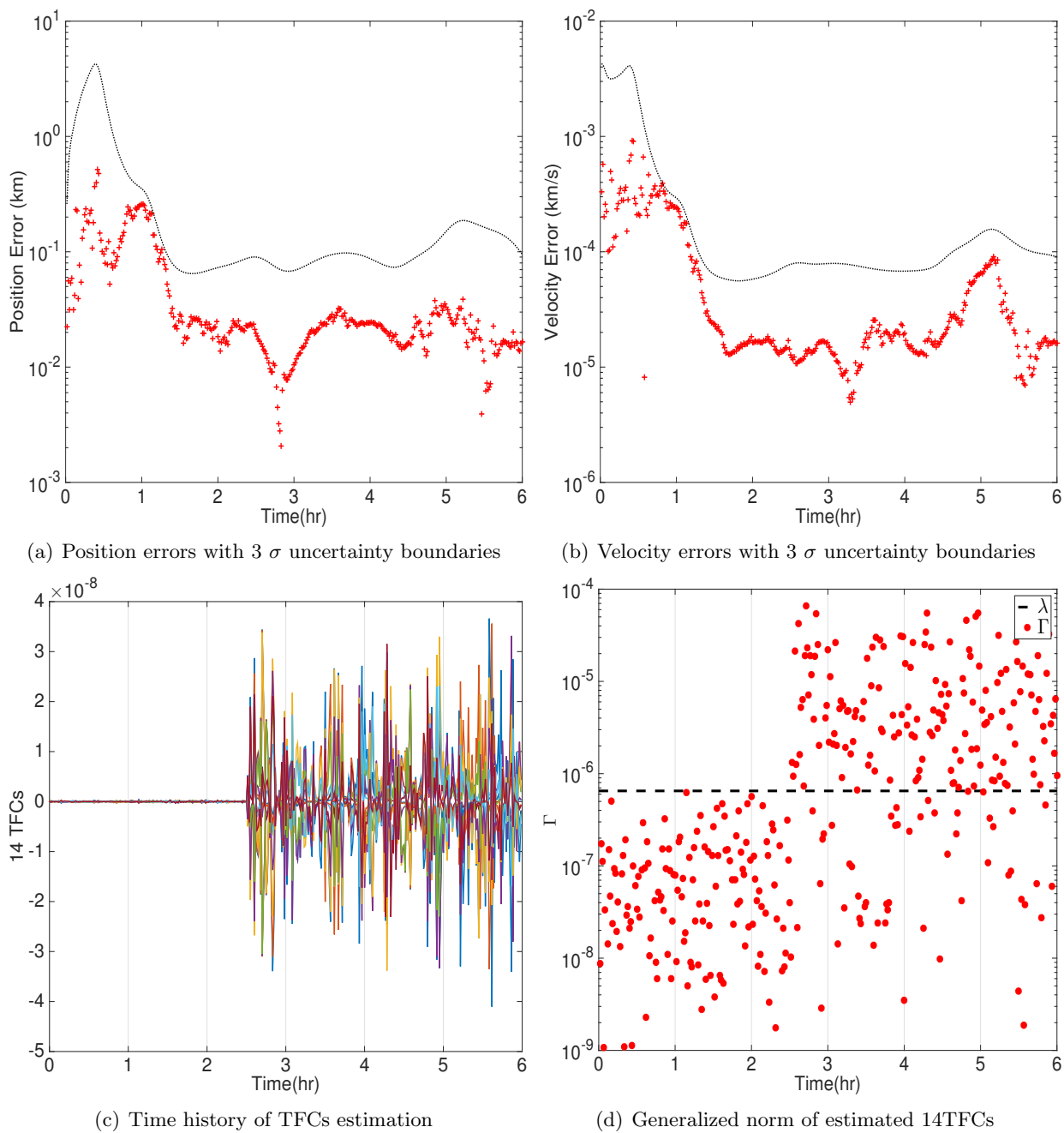


Figure 4.23: OD solution from the modified EKF for case 6

time estimation can be improved by using the proposed event detection algorithm introduced in the previous chapter. As a post-processing, it will provide more accurate estimation of the maneuver termination time. Nevertheless, the modified EKF is still able to maintain real-time tracking of a satellite while providing a valid OD solution during the maneuver and after the maneuver.

When there are only angle measurements available like case 5, there is a delay of detecting the maneuver onset time since the right ascension (RA) and declination (Dec) angle measurement data generally do not yield high accuracy OD estimations. This detection delay affects the performance of the modified EKF, which is shown in Fig. 4.22. In this figure, the satellite position and velocity errors are out of their estimated 3σ uncertainty boundaries at the beginning of the maneuver due to the detection delay. However, with more data coming in, the filter is able to keep tracking of a maneuvering satellite using angle measurement only.

Figure 4.23 shows that the filter detects continuous perturbing accelerations consistently. Once the estimated maneuver begins, the state covariance matrix is inflated so that the filter is able to accept the subsequent measurement data and to provide valid OD solutions. Different from the previous cases, there is no maneuver termination time for case 6, which explains why those inflated TFCs do not decrease back to the nominal values in Fig. 4.23(c) and 4.23(d). The structural deployment begins at two hour after the initial time, but the algorithm estimates that the maneuver begins after $t = 2.5\text{hr}$. There is a detection delay of around 30 minutes, which is due to the fact that the accumulated effect of low-thrust burn does not show up immediately in the estimation process. From all the simulated cases, the proposed maneuver tracking algorithm shows consistent performance of providing valid OD solutions across unknown maneuvers and continues tracking of satellites. Aside from successfully tracking a satellite, the proposed algorithm also provides a direct estimate of the unknown maneuvering period.

4.3.3 Simulations and results using the essential TFC set

The advantage of tracking a satellite with the essential TFC set is able to represent a space event with less computational requirements. Like the 14-TFC set, the EKF can be modified with

the essential TFC set to track a maneuvering satellites. In order to check the performance of the modified EKF with the essential TFC set, the same space event scenarios from chapter 4.2 (Table D.2) are simulated. For all the cases, OD solutions with using the essential TFC set show consistent and similar results as those obtained by using 14 TFC set. To avoid repetition, the resulting figures for case 1, 3, and 6 are only shown in this subchapter. These results yield a high confidence in the ability of the modified EKF to maintain tracking of a maneuvering satellite. It demonstrates the effectiveness of the filter in tracking satellites with various maneuvers. This OD filter, incorporating a simple EKF and the event representation technique using the essential TFC set, provides the same performance of tracking a maneuvering satellite as the modified EKF with 14-TFC set does. It proves that once an unknown thrust acceleration is represented by any valid TFC set, the represented dynamics can be utilized to track a maneuvering satellite.

4.4 Summary

The event representation method using TFCs is applied to detect a USE and to maintain tracking of a maneuvering satellite by continuing the orbit solution arc. First, detecting unmodeled events based on the event representation method using TFCs is studied. By including 14 TFCs as an appended state, the sequential filter is modified to detect a change-point of unknown accelerations. With this modified filter, an event detection algorithm is implemented to estimate both the event onset and the termination time as well as unknown accelerations. It is a knowledge-free event detection scheme that does not require any information about an unmodeled event. The simulation study proves that the proposed detection algorithm is able to detect various types of events by incorporating the pre-event orbital state with incoming observation data.

Second, real-time tracking of maneuvering satellites based on the event representation technique using TFCs is studied. An extended Kalman filter (EKF) is modified with TFCs and its tracking performance is tested by applying it over different satellite maneuver cases. The simulation result shows that the modified EKF is able to maintain tracking of a satellite by providing valid orbit solutions across unknown maneuvers. This EKF has three main advantages. First,

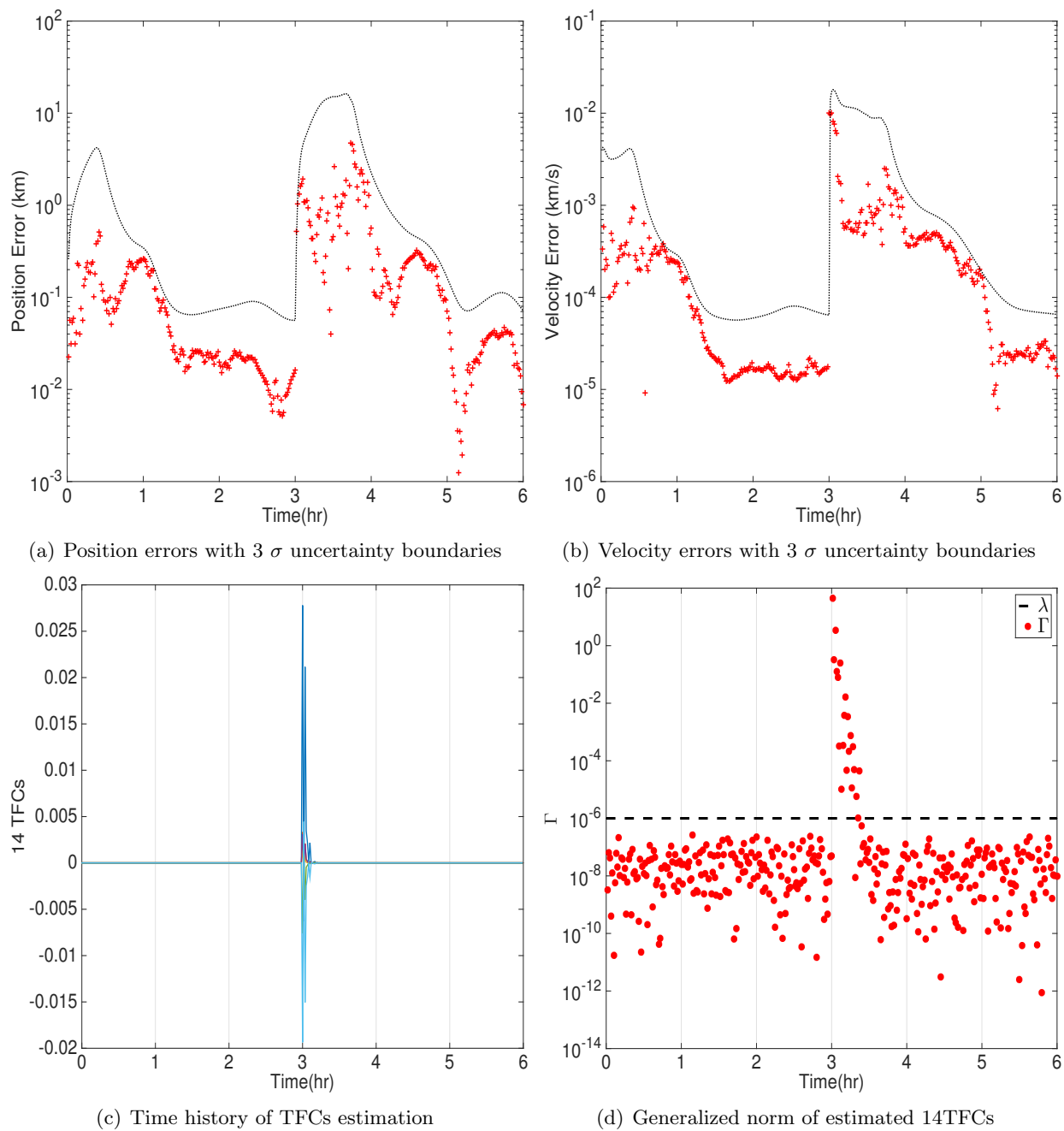


Figure 4.24: OD solution from the modified EKF with the essential TFC set for case 1

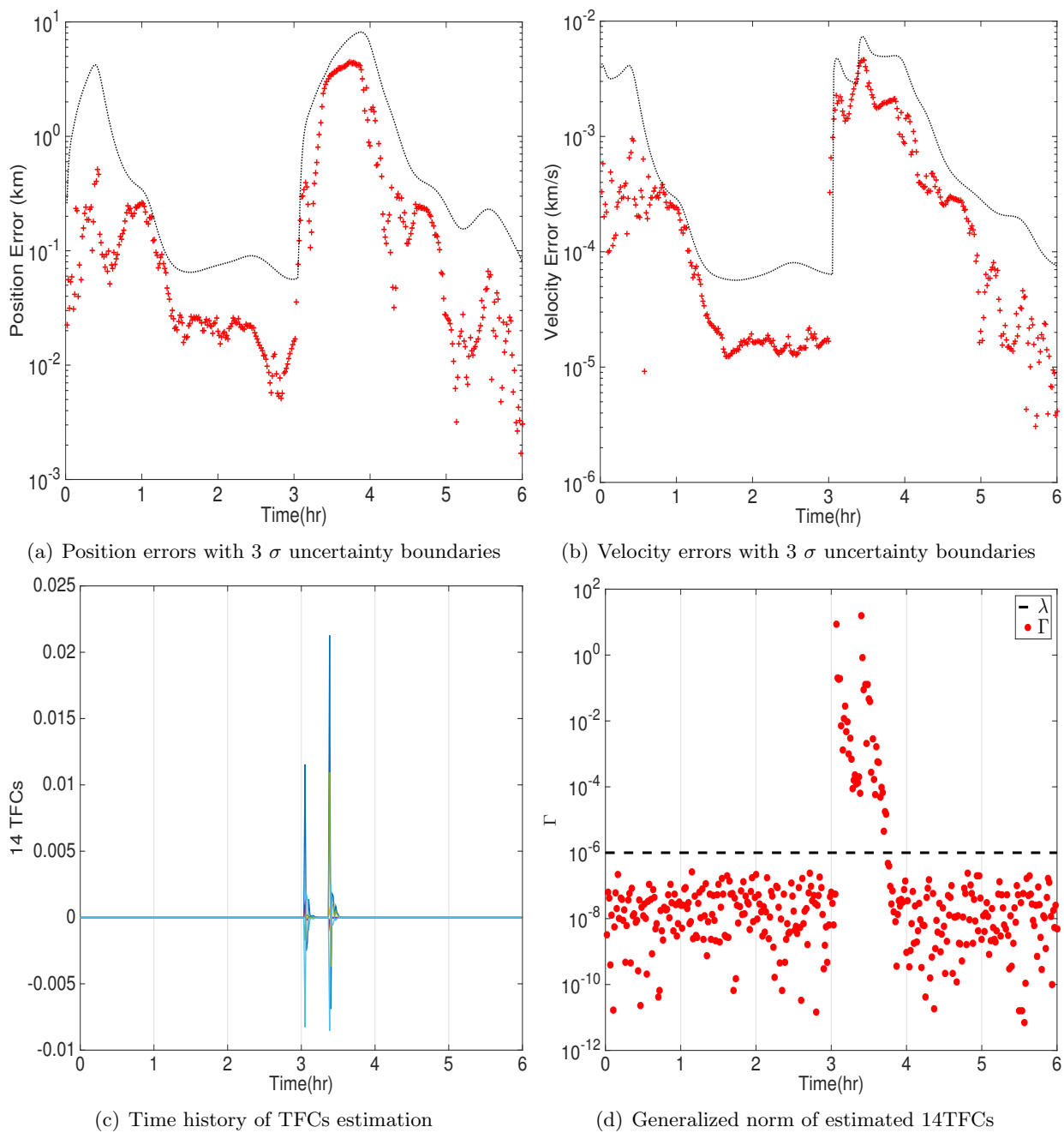


Figure 4.25: OD solution from the modified EKF with the essential TFC set for case 3

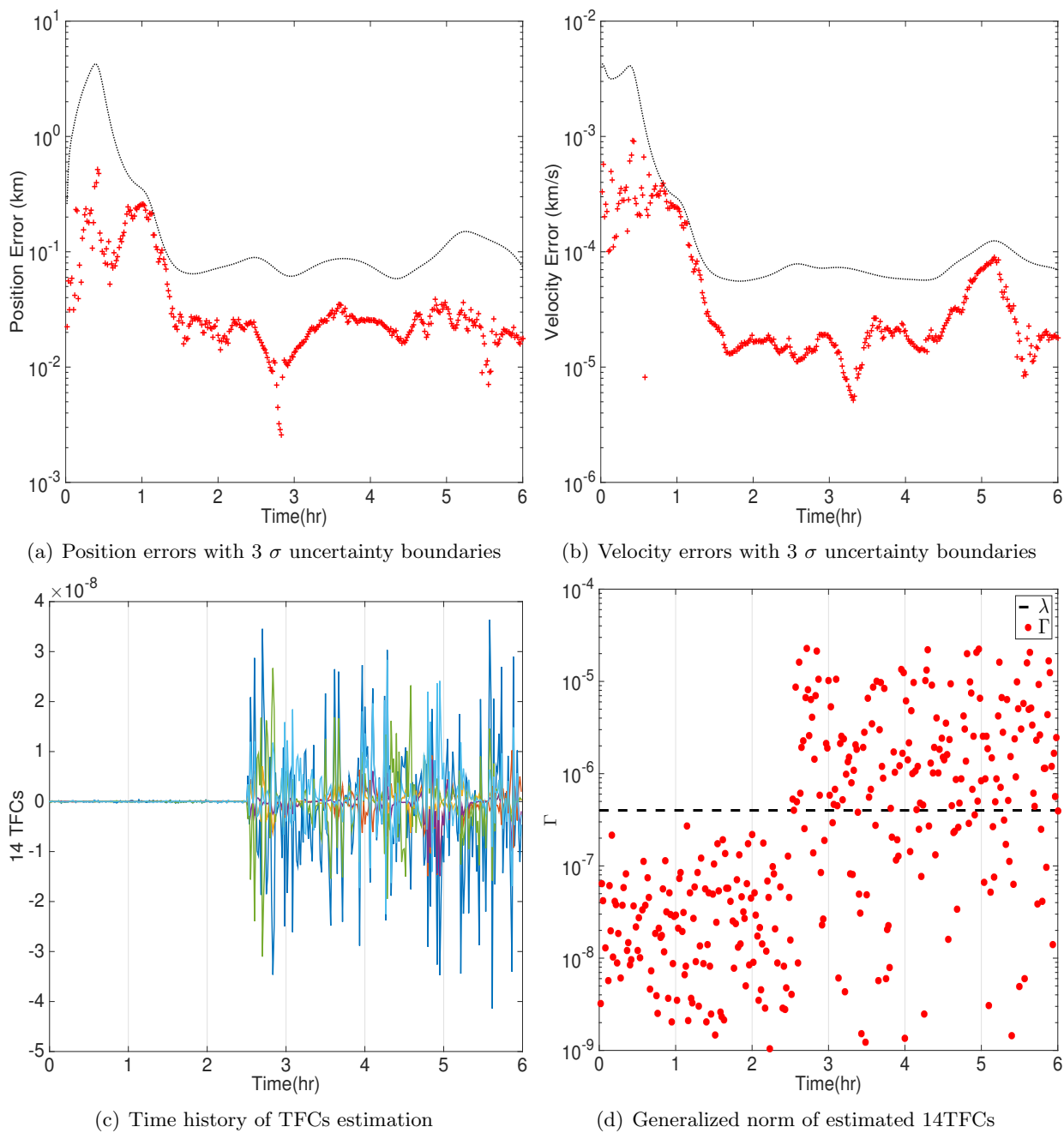


Figure 4.26: OD solution from the modified EKF with the essential TFC set for case 6

unlike other methods, no pre-defined model of unknown accelerations is required. Second, it is a fully automated process that is also simple to implement. Third, it is able to track a wide range of operating satellites as they undergo maneuvers, ranging from an impulsive burn to a continuous low-thrust burn. In addition, the filter also enables us to estimate unknown maneuver onset and termination time directly from observation data. Incorporation of such a capability could play an essential role in analyzing a mission task as well as future behaviors of a satellite.

Chapter 5

Conclusion and Future Works

5.1 Conclusion

This dissertation presents characteristics and applications of the event representation technique using the thrust-Fourier-coefficients (TFCs). First, a new way of representing an unknown and unmodeled space event (USE) with TFCs was described. Second, we analyzed the uncertainty propagation with an event representation across USEs. Our study demonstrated that orbit determination (OD) process could be maintained across the period of a USE by applying an event representation method. Then, the event representation technique with TFCs was applied to solve space situational awareness (SSA) problems and simulation studies were performed to verify our approach.

Chapter 2 analyzed time rates of change in mean orbital elements due to the TFCs and studied the secular behaviors of the orbit controlled by different TFC sets. Then, a computation algorithm was developed to represent any change in orbit state across a USE as an equivalent maneuver using TFCs. Numerical studies showed that a selected set of 6 TFCs as well as the 14-TFC set could represent a USE by providing a unique control law to dynamically interpolate states across an unknown event. The efficiency of represented control laws using different TFC set was verified with simulation studies of targeting problems. The results showed that the TFC event representation method generically provided the fundamental elements of perturbing accelerations with no restriction on the USE type.

Chapter 3 was devoted to investigate the applicability of the event representation technique to

orbit uncertainty propagation. Analytic study proves that the propagated state transition matrix (STM) mapping from an initial to a final state is quasi-independent of event dynamics based on the condition that a satellite moves from a given initial state to the same final state at a given time. Applying this fundamental finding, numerical simulations verified that the dynamics representation interpolating two disparate orbit states could be used to linearly propagate the orbit uncertainty information via STM. With this property, the Batch filter was modified with the TFC event representation to estimate the orbital state and its uncertainty across USEs. Case studies with simulated tracking data showed that, given limited tracking data, the modified Batch filter provided more accurate post-event OD solution than regular batch filter. The TFC event representation technique enabled the filter to make use of the previous orbit information to improve the accuracy of post-event orbit solution.

In chapter 4, new OD algorithms to detect a USE and to maintain tracking of a maneuvering satellite were developed by utilizing the TFC event representation technique. The sequential filter was modified by appending the 14 TFCs as solve-for states. Using this modified sequential filter, the event detection algorithm was implemented by processing observation data both forwards and backwards in time to detect event onset and termination time, respectively. Along with the estimated event time period, the detection algorithm provided more accurate post-event orbit solutions. A case study of detecting USEs with different types of simulated measurement data verified the validity of the algorithm. Since the TFC event representation method generates an equivalent thrust profile for a USE, it also can be applied to continue tracking of a satellite across unknown events. This application is demonstrated by modifying the extended Kalman filter (EKF) with TFCs. The modified EKF was capable of filtering through in real time and maintaining an OD solution in the presence of USEs by applying a single represented dynamics model. This EKF filter has the advantage of not confronting the difficulty of selecting parameters and distinguishes itself from other approaches in that it does not rely on any assumption about a USE or multiple dynamics models for a given event.

5.2 Future Works

Modifying common OD program with the TFC event representation: The event representation technique using TFCs can be adapted into commonly used OD software programs such as STK/ODTK, TRACE, GEODYN, GTDS, GOA etc [78]. Regardless of whether these programs use a Batch processor or a sequential processor, implementing this method with existing OD filters can be easily done by appending TFCs and the represented dynamics to the pre-built OD algorithms. This modified dynamical model using TFCs analytically describes the forces acting on the satellite including unknown perturbations due to USEs. Along with the augmented state and represented dynamics, the state Jacobian as well as the measurement Jacobian matrices have to be modified to complete the modification in the process. To check its feasibility, the least square filter available in Orbit Determination Toolbox (ODTBX) has been modified with the event representation technique using 6 TFCs in ([79]). We chose to use the ODTBX¹ least square filter because it is a pre-built MATLAB based software package that can be modified easily. Post-event OD solutions using this modified ODTBX with TFCs for different USE cases are shown in the Appendix D. It demonstrates the flexibility and relevance of adapting the TFC event representation technique into existing OD software programs. The difficulty of this future work is to get an access to OD software algorithms to apply those modifications since many of them are not open to the public. Utilization of these modified OD software programs to process actual tracking data could be included as a part of this future work.

Event representation with higher order TFCs: Additional possible application of the method is to include higher order terms of TFCs to accurately represent a USE. Any physical control law can be represented in terms of an infinite sum of sine and cosine functions of Fourier series, and our study has shown that the 14 zero-, first-, and second-order TFC terms is able to provide a basis of the true perturbing acceleration for USE. The represented dynamics using these 14 TFCs take the form of periodic control laws that generate the given secular motion of a

¹ Available at: <http://opensource.gsfc.nasa.gov/projects/ODTBX/>.

satellite under a USE. This event representation can be improved by exploiting higher-order Fourier coefficients that can modify the shape and frequency of the unknown control law without altering the average dynamics. However, the direct approximation of these higher order Fourier coefficients is not straightforward and has not yet solved. Since constant 14 TFCs govern the mean motion of a perturbed satellite orbit, they can be fixed with the averaged solution from (2.30) to represent the given secular effect of a USE. Then, the higher order TFCs could be numerically estimated to match the short term behavior of a satellite under a USE. With these estimates of the higher order TFCs, the true perturbing dynamics could be represented more accurately. Examining its computational complexities in more detail could be studied in this work.

Solving guidance problem with thrust restriction: The event representation using different essential candidate sets of TFCs can be developed to solve guidance problems of changing a certain orbital element of a satellite with limited thrusting capability. The TFC event representation provides a control law to interpolate dynamically between states of a required orbital transfer. Using the represented controlling acceleration components, the actual control inputs for a satellite, such as magnitude and direction of thrust acceleration, can be computed. This control input is a function of time and TFCs, and provides a satellite with a continuous stream of control commands that describe the desired magnitude and direction of thrust. Different from other guidance laws, such as Lambert guidance [80], or proportional guidance [81], this guidance law using TFCs will make a satellite arrive at the desired final position with a desired final velocity since we are controlling 6-dimensional orbital space with 6 TFCs. This method will be useful for rendezvous or docking missions. In addition, the event representation using different combinations of TFCs provides different shapes of possible control laws, which gives an advantage in terms of finding feasible solutions that satisfy any restriction on control laws. Possible constraints like a limit on the amplitude of adjustable thrust, thrust dispersions, and a limit on thrust direction should be considered for this work. This application permits mission designers to optimize a control law across different realization types with considering any control requirement.

Bibliography

- [1] Patera, R., "Space Event Detection Method," *Journal of Spacecraft and Rockets*, Vol. 45, No. 3, 2008, pp. 554–559. doi: 10.2514/1.30348
- [2] National Research Council, *Continuing Kepler's Quest: Assessing Air Force Space Command's Astrodynamics Standards*, Washington, DC: The National Academies Press, 2012.
- [3] Woodburn, J., Carrico, J., and Wright, J. R., "Estimation of Instantaneous Maneuvers Using a Fixed Interval Smoother," Proceedings of the AAS/AIAA Astrodynamics Specialist Conference, AAS 03-518, Vol. 116, AAS, 2004. pp. 243–260.
- [4] Tapley, B. D., Schutz, B. E., and Born, G. H., *Statistical Orbit Determination*, Elsevier Academic Press, San Diego, CA, 2010.
- [5] Wright, J. R., *Orbit Determination Tool Kit Theorems & Algorithms*, Analytical Graphics, Inc., 2006.
- [6] Hujsak, R. S., Woodburn, J. W., and Seago, J. H., "The Orbit Determination Tool Kit (ODTK) - Version 5," Proceedings of the AAS/AIAA Space Flight Mechanics Meeting, AAS 07-125, Vol. 127, AAS, San Diego, CA, 2007. pp. 381–400.
- [7] Vallado, D. A., *Fundamentals of Astrodynamics and Applications*, 3rd ed., Microcosm Press, El Segundo, CA, 2007, pp. 139–140, 788–790.
- [8] Holzinger, M. J., Scheeres, D. J., and Alfriend, K. T., "Object Correlation, Maneuver Detection, and Characterization using Control Distance Metrics," *Journal of Guidance, Control, and Dynamics*, Vol. 35, No. 4, 2012, pp. 1312–1325. doi: 10.2514/1.53245
- [9] Singh, N., Horwood, J. T., and Poore, A. B., "Space Object Maneuver Detection via a Joint Optimal Control and Multiple Hypothesis Tracking Approach," Proceedings of the 22nd AAS/AIAA Space Flight Mechanics Meeting, AAS 12-159, Vol. 143, AAS, 2012. pp. 843–862.
- [10] Lubey, D. P., and Scheeres, D. J., "Identifying and Estimating Mismodeled Dynamics via Optimal Control Policies and Distance Metrics," *Journal of Guidance, Control, and Dynamics*, Vol. 37, No. 5, 2014. pp. 1512–1523. doi: 10.2514/1.G000369
- [11] Hudson, J. S., and Scheeres, D. J., "Reduction of Low-Thrust Continuous Controls for Trajectory Dynamics," *Journal of Guidance, Control, and Dynamics*, Vol. 32, No. 3, 2009, pp. 780–787. doi: 10.2514/1.40619

- [12] Hudson, J. S., and Scheeres, D. J., "Orbital Targeting Using Reduced Eccentric Anomaly Low-Thrust Coefficients," *Journal of Guidance, Control, and Dynamics*, Vol. 34, No. 3, 2011, pp. 820–831. doi: 10.2514/1.51336
- [13] Ko, H. C., and Scheeres, D. J., "Essential Thrust-Fourier-Coefficient Set of Averaged Gauss Equations for Orbital Mechanics," *Journal of Guidance, Control, and Dynamics*, Vol. 37, No. 4, 2014, pp. 1236–1249. doi: 10.2514/1.62407
- [14] Shoemaker, J., "Space Situational Awareness and Mission Protection," *DARPA Tech 2005*, August 9-11 2005.
- [15] Kelecyc, T., and Jah, M., Detection and Orbit Determination of a Satellite Executing Low Thrust Maneuvers, *Acta Astronautica*, Vol. 66, No. 5, 2010, pp. 798–809. doi:10.1016/j.actaastro.2009.08.029
- [16] Baird, M. A., "Maintaining Space Situational Awareness and Taking It to the Next Level," *Air and Space Power Journal*, Vol. 27, No. 5, 2013, pp 50–72.
- [17] Kluever, C. A., "Low-Thrust Orbit Transfer Guidance Using an Inverse Dynamics Approach," *Journal of Guidance, Control, and Dynamics*, Vol. 18, No. 1, 1995, pp. 187–189.
- [18] Kluever, C. A. and Oleson, S. R., "Direct Approach for Computing Near-Optimal Low-Thrust Earth-Orbit Transfers," *Journal of Spacecraft and Rockets*, Vol. 35, No. 4, 1998, pp. 509–515.
- [19] Kluever, C. A., and Shaughnessy, D., "Trajectory-Tracking Guidance Law for Low-Thrust Earth-Orbit Transfers," *Journal of Guidance, Control, and Dynamics*, Vol. 23, No. 4, 2000, pp. 754–756.
- [20] Ferrier, C., and Epenoy, R., "Optimal Control for Engines with Electro-Ionic Propulsion Under Constraint of Eclipse," *Acta Astronautica*, Vol. 48, No. 4, 2001, pp. 181–192.
- [21] Petropoulos, A. E., "Some Analytic Integrals of the Averaged Variational Equations for a Thrusting Spacecraft," Interplanetary Network Progress Report 42-150, Jet Propulsion Lab., California Inst. of Technology, Pasadena, CA, Aug. 2002, pp. 1–29.
- [22] Bonnard, B., Caillaud, J. B., and Dujol, R., "Averaging and Optimal Control of Elliptic Keplerian Orbits with Low Propulsion," *Systems and Control Letters*, Vol. 55, 2006, pp. 755–760.
- [23] Gao, Y., "Near-Optimal Very Low-Thrust Earth-Orbit Transfers and Guidance Schemes," *Journal of Guidance, Control, and Dynamics*, Vol. 30, No. 2, 2007, pp. 529-539.
- [24] Gao, Y., "Low-Thrust Nonlinear Guidance by Tracking Mean Orbital Elements," *Journal of Guidance, Control, and Dynamics*, Vol. 31, No. 4, 2008, pp. 1103–1110.
- [25] Brouwer, D., and Clemence, G. M., *Methods of Celestial Mechanics*, Academic Press, New York, 1961, Chaps. XI.
- [26] Haberman, R., *Applied Partial Differential Equations with Fourier Series and Boundary Value Problems*, 4th ed., Pearson Prentice-Hall, Upper Saddle River, NJ, 2004, pp. 89–92.
- [27] Kalman, R. E., "On the General Theory of Control Systems," *Proceedings of the First IFAC Moscow Congress*, 1960, pp. 481–493.

- [28] Whittaker, E. T. and Robinson, G., *The Calculus of Observations*, London: Blackie, 1924, pp. 36–40.
- [29] Swartz, R. L., Coggi, J., and McNeill, J., “A Swift SIFT for Satellite Event Detection,” AIAA 2010-7527, 2010 AIAA/AAS Astrodynamics Specialist Conference, Toronto, Ontario Canada, August 2010. doi: 10.2514/6.2010-7527
- [30] Johnson, T., “TDRS-3 Orbit Determination Across Unknown Maneuvers,” Madrid: 4th International Conference on Astrodynamical Tools and Techniques, May 2010.
- [31] Leondes, C. T., “Theory and Applications of Kalman Filtering,” No. AGARD-OGRAPH-139. Advisory Group for Aerospace Research and Development NEUILLY-SUR-SEINE (FRANCE), 1970.
- [32] Tapley, B. D., and Ingram, D. S., “Estimating Unmodeled Acceleration During Orbit Determination,” First Annual Meeting of the AAS Division of Dynamical Astronomy, Austin, Texas, January, 1970.
- [33] Myers, K. A., and Tapley, B. D., “Dynamical Model Compensation for Near-Earth Satellite Orbit Determination,” *AIAA Journal*, Vol. 13, No. 3, 1975, pp. 343–349.
- [34] Scheeres, D. J., and Holzinger, M. J., “The Control Distance Metric and Constraints on Maneuvering Satellites,” Information Fusion (FUSION), 2012 15th International Conference on, July 2012, pp. 2035–2042.
- [35] Gelb, A., *Applied optimal estimation*, The M.I.T. Press, Cambridge, MA, 1974, pp. 57–67.
- [36] Scheeres, D. J., *Orbital Motion in Strongly Perturbed Environments*, Springer-Praxis Publishing, New York, NY, 2012, pp. 158–161.
- [37] Moulton, F. R., *Differential Equations*, The Macmillan Company, New York, NY, 1930, pp. 39–57.
- [38] Press, W. H., Teukolsky, S. A., Vetterling, W. T., and Flannery, S. A., *Numerical Recipes: The Art of Scientific Computing*, 3rd ed., Cambridge University Press, New York, NY, 2007, pp. 907–915.
- [39] Horwood, J. T., Aristoff, J. M., Singh, N., Poore, A. B., and Hejduk, M. D., “Beyond Covariance Realism: A New Metric for Uncertainty Realism,” In SPIE Defense+ Security, International Society for Optics and Photonics, June 2014, pp. 90920F 1–14. doi: 10.1117/12.2054268
- [40] Markley, F. L., and Carpenter, J. R., “Generalized Linear Covariance Analysis,” *Journal of the Astronautical Sciences*, Vol. 57, Jan–Jun 2009, pp. 233–260.
- [41] Mahalanobis, P. C., “On the Generalized Distance in Statistics,” In Proceedings of the National Institute of Science of India, Vol. 2, No. 1, April 1936, pp. 49–55.
- [42] Willsky, A. S., and Jones, H. L., “A Generalized Likelihood Ratio Approach to the Detection and Estimation of Jumps in Linear Systems,” *IEEE Transactions on Automatic Control*, February 1976. pp. 108–112. doi: 10.1109/TAC.1976.1101146

- [43] Bar-Shalom, Y., and Birmiwal, K., “Variable Dimension Filter for Maneuvering Target Tracking,” *IEEE Transactions on Aerospace and Electronic Systems* Vol.18, No. 5, 1982. pp. 621–629. doi: 10.1109/TAES.1982.309274
- [44] Basseville, M., and Benveniste, A., “Design and Comparative Study of Some Sequential Jump Detection Algorithms for Digital Signals,” *IEEE Transactions on Acoustics, Speech, and Signal Processing*, Vol. 31, No. 3, 1983, pp. 521–535. doi: 10.1109/TASSP. 1983.1164131
- [45] Kelecyc, T., Hall, D., Hamada, K., and Stocker, M. D., “Spacecraft Maneuver Detection Using Two-Line Element (TLE) Data,” Proceedings of the Advanced Maui Optical and Space Surveillance Technologies Conference, Maui, HI, September 12–15, 2007.
- [46] Song, W., Wang, R., and Wang, J., “A Simple and Valid Analysis Method for Orbit Anomaly Detection,” *Advances in Space Research*, Vol. 49, No. 2, 2012, pp. 386–391.
- [47] Lemmens, S., and Krag, H., “Two-Line-Elements-Based Maneuver Detection Methods for Satellites in Low Earth Orbit.” *Journal of Guidance, Control, and Dynamics*, Vol. 37, No. 3, 2014, pp. 860–868. doi: 10.2514/1.61300
- [48] Lee, S., and Hwang, I., “Interacting Multiple Model Estimation for Spacecraft Maneuver Detection and Characterization,” In Proceedings of the AIAA Guidance, Navigation, and Control Conference, Kissimmee, Florida, January, 2015.
- [49] Ko, H. C., and Scheeres, D. J., (2014), “Event Representation Based Orbit Determination Across Unknown Space Events,” *Journal of Guidance, Control, and Dynamics*, (2015), accessed May 20, 2015. doi: <http://arc.aiaa.org/doi/abs/10.2514/1.G001050>
- [50] Nikulin, M. S., “Chi-Squared Test for Normality”. In: Proceedings of the International Vilnius Conference on Probability Theory and Mathematical Statistics, Vol. 2, pp. 119–122.
- [51] Li, X. R., and Jilkov, V. P., “A Survey of Maneuvering Target Tracking – Part IV: Decision-Based Methods, Proceedings of SPIE Conference on Signal and Data Processing of Small Targets, Vol. 4728-60, Orlando, Florida, April 2002.
- [52] Abbot, R. I., and Wallace, R. I., “Decision Support in Space Situational Awareness,” *Lincoln Laboratory Journal*, Vol. 16, No. 2, (2007), pp. 297–335.
- [53] Cloutier, J. R., Lin, C. F., and Yang, C., “Maneuvering Target Tracking via Smoothing and Filtering Through Measurement Concatenation,” *Journal of Guidance, Control, and Dynamics*, Vol.16, No. 2, 1993, pp. 377–384.
- [54] Goff, G. M., Black, J. T., and Beck, J. A., “Tracking Maneuvering Spacecraft with Filter-through Approaches Using Interacting Multiple Models,” *Acta Astronautica* 114 (2015), pp. 152–163. doi:10.1016/j.actaastro.2015.05.009
- [55] Spingarn, K., and Weidemann, H. L., “Linear Regression Filtering and Prediction for Tracking Maneuvering Aircraft Vehicles,” *IEEE Trans. on Aerospace and Electronics System*, Vol. AES-8, 1972, pp. 800-810.
- [56] Yun, J, and Ryoo, C. K., “Missile Guidance Law Estimation Using Modified Interactive Multiple Model Filter,” *Journal of Guidance, Control, and Dynamics*, Vol. 37, No. 2, 2014, pp. 484–496, doi:10.2514/1.61327.

- [57] Schlee, F. H., Standish, C. J., and Toda, N. F., "Divergence in the Kalman Filter," *AIAA Journal*, Vol. 5, No. 6, 1967, pp. 1114–1120.
- [58] Tarn, T. J., and Zaborsky, J., "A Practical Non-Diverging Filter," *AIAA Journal*, Vol. 8, No. 6, 1970, 1127–1133.
- [59] Jazwinski, A. H., *Stochastic Processes and Filter Theory*, Academic Press, New York, NY, 1970, Chapter 8.
- [60] Hampton, R. L. T., and Cooke, J. R., "Unsupervised Tracking of Maneuvering Vehicles," *IEEE Trans. on Aerospace Electronic Systems*, Vol. AES-2, 1973, pp. 197–207.
- [61] Maybeck, P. S., and Hentz, K. P., "Investigation of Moving-Bank Multiple Model Adaptive Algorithms," *Journal of Guidance, Control, and Dynamics*, Vol. 10, No.1, 1987, pp. 90–96.
- [62] Blom, H. A. P., and Bar-Shalom, Y., "The Interacting Multiple Model Algorithm for Systems with Jump-linear Smoothing Application," *IEEE Trans. on Automatic Control*, Vol. AC-33, No. 8, 1988, pp. 780-783.
- [63] Munir, A., and Atherton, D. P., "Adaptive Interacting Multiple Model Algorithm for Tracking a Maneuvering Target," *IEE Proc. of Radar, Sonar, and Navigation*, Vol. 142, No. 1, 1995, pp. 11–17.
- [64] Goff, G. M., Black, J. T., and Beck, J. A., "Orbit Estimation of a Continuously Thrusting Spacecraft Using Variable Dimension Filters." *Journal of Guidance, Control, and Dynamics* In press (2015), doi: 10.2514/1.G001091
- [65] Singer, R. A., "Estimating Optimal Tracking Filter Performance for Manned Maneuvering Target," *IEEE Trans. on Aerospace Electronic Systems*, Vol. AES-6, No. 4, 1970, pp. 473-483.
- [66] Jazwinski, A. H., "Adaptive filtering," *Automatica* Vol. 5, No. 4, 1969, pp. 475–485.
- [67] Chen, G., and Chui, C. K., "A Modified Adaptive Kalman Filter for Real-Time Applications," *IEEE Trans. on Aerospace Electronic Systems*, Vol. AES-27, No.1, 1991, pp. 149-154.
- [68] Belanger, P. R., "Estimation of Noise Covariance Matrices for a Linear Time-Varying Stochastic Process," *Automatica*, Vol. 10, No. 3, 1974, pp. 267–275.
- [69] Chan, Y. T., Hu, G. C., and Plant. J. B., "A Kalman Filter Based Tracking Scheme with Input Estimation," *IEEE Trans. on Aerospace and Electronics System*, Vol. AES-15, No. 2, 1979, pp. 237-244.
- [70] Whang, I. H., Lee, J., and Sung. T., "Modified Input Estimation Technique Using Pseudoresidual," *IEEE Trans. on Aerospace and Electronics System*, Vol. AES-30, No. 1, 1994, pp. 220-228.
- [71] Bogler, P. L., "Tracking a Maneuvering Target using Input Estimation," *IEEE Trans. on Aerospace and Electronics System*, Vol. AES-23, No. 3, 1987, pp. 298-310.
- [72] Lee, H., and Tahk, M. J., "Generalized Input-Estimation Technique for Tracking Maneuvering Targets," *IEEE Trans. on Aerospace and Electronics System*, Vol. AES-35, No. 4, 1999. pp. 1388–1402.

- [73] Bar-Shalom, Y., and Birmiwal, K., "Variable Dimension Filter for Maneuvering Target Tracking," *IEEE Trans. on Aerospace and Electronics System*, Vol. AES-18, No. 5, 1982, pp. 621-629.
- [74] Cloutier, J. R., Lin, C. F., and Yang, C., "Enhanced Variable Dimension Filter for Maneuvering Target Tracking," *IEEE Trans. on Aerospace and Electronics System*, Vol. AES-29, No. 3, 1993, pp. 786-797.
- [75] Friedland, B., "Treatment of Bias in Recursive Filtering," *IEEE Trans. on Automatic Control*, Vol. AC-14, No. 4, 1969, pp. 359-367.
- [76] Hu, X., Hu, X., and Huang, Y., "A Nonlinear Variable Dimension Estimator for Maneuvering Spacecraft Tracking via the Unscented Kalman Filter," *IEEE International Conference on Information and Automation*, 2008, pp. 226-231
- [77] Ko, H. C., and Scheeres, D. J., "Maneuver Detection with Event Representation using Thrust-Fourier-Coefficients," 2015 AAS/AIAA Astrodynamics Specialist Conference, No. 15-631, AAS/AIAA, August 2015.
- [78] Vetter, J. R., "Fifty Years of Orbit Determination," *Johns Hopkins APL technical digest*, Vol. 27, No. 3, 2007, pp. 239-252.
- [79] Ko, H. C., and Scheeres, D. J., "Spacecraft Orbit Anomaly Representation Using Thrust-Fourier-Coefficients with Orbit Determination Toolbox," Proceedings of the Advanced Maui Optical and Space Surveillance Technologies Conference, Maui, Hawaii, September, 2014, p. 63.
- [80] Avanzini, G., "A Simple Lambert Algorithm," *Journal of Guidance, Control, and Dynamics*, Vol. 31, No. 6, 2008, pp. 1587-1594.
- [81] Adler, F. P., "Missile Guidance by Three-Dimensional Proportional Navigation," *Journal of Applied Physics*, Vol. 27, No. 5, 1956, pp. 500-507.
- [82] Graybill, F. A., "An Introduction to Linear Statistical Models," McGraw-Hill, New York, NY, 1961.

Appendix A

Computation of \mathcal{G}_{ess} Matrix for Non-averaged Solution

A full expression of \mathcal{G}_{ess} matrix (Eq. 2.32) for the non-averaged solution is derived.

$$\mathcal{G}_{ess} = \frac{1}{n} \int_0^E G(\alpha, \tau)_{ess} (1 - e \cos E) dE$$

$$= \begin{bmatrix} \mathcal{G}_{1,1} & \mathcal{G}_{1,5} & \mathcal{G}_{1,6} & \mathcal{G}_{1,8} & 0 & 0 \\ \mathcal{G}_{2,1} & \mathcal{G}_{2,5} & \mathcal{G}_{2,6} & \mathcal{G}_{2,8} & 0 & 0 \\ 0 & 0 & 0 & 0 & \mathcal{G}_{3,11} & \mathcal{G}_{3,13} \\ 0 & 0 & 0 & 0 & \mathcal{G}_{4,11} & \mathcal{G}_{4,13} \\ \mathcal{G}_{5,1} & \mathcal{G}_{5,5} & \mathcal{G}_{5,6} & \mathcal{G}_{5,8} & \mathcal{G}_{5,11} & \mathcal{G}_{5,13} \\ \mathcal{G}_{6,1} & \mathcal{G}_{6,5} & \mathcal{G}_{6,6} & \mathcal{G}_{6,8} & 0 & 0 \end{bmatrix} \quad (\text{A.1})$$

$$\mathcal{G}_{1,1} = \frac{2}{n^2} e (1 - \cos E)$$

$$\mathcal{G}_{1,5} = \frac{2}{n^2} \sqrt{1 - e^2} E$$

$$\mathcal{G}_{1,6} = \frac{2}{n^2} \sqrt{1 - e^2} \sin E$$

$$\mathcal{G}_{1,8} = \frac{2}{n^2} \sqrt{1 - e^2} (1 - \cos E)$$

$$\mathcal{G}_{2,1} = \frac{a^2}{\mu} (1 - e^2) (1 - \cos E)$$

$$\mathcal{G}_{2,5} = \frac{a^2}{\mu} \sqrt{1 - e^2} \left(2 \sin E - \frac{3}{2} e E - \frac{e \sin 2E}{4} \right)$$

$$\mathcal{G}_{2,6} = \frac{a^2}{\mu} \sqrt{1 - e^2} \left(E + \frac{\sin E}{2} - \frac{7}{4} e \sin E - \frac{e \sin 3E}{12} \right)$$

$$\mathcal{G}_{2,8} = \frac{a^2}{\mu} \sqrt{1 - e^2} \left(\frac{(1 - \cos 2E)}{2} - \frac{5e(1 - \cos E)}{4} - \frac{e(1 - \cos 3E)}{12} \right)$$

$$\begin{aligned}
\mathcal{G}_{3,11} &= \frac{a^2}{\mu} \frac{1}{\sqrt{1-e^2}} \left(-\frac{3}{2}e \cos w \sin E + \frac{1}{2}(1+e^2) \cos w \left(E + \frac{\sin 2E}{2} \right) - \frac{1}{2}\sqrt{1-e^2} \sin w \frac{1-\cos 2E}{2} \right) \\
&\quad + \frac{a^2}{\mu} \frac{1}{\sqrt{1-e^2}} \left(-\frac{1}{4}e \cos w \left(\sin E + \frac{\sin 3E}{3} \right) + \frac{1}{4}e\sqrt{1-e^2} \sin w \left(\frac{1-\cos 3E}{3} + 1 - \cos E \right) \right) \\
\mathcal{G}_{3,13} &= \frac{a^2}{\mu} \frac{1}{\sqrt{1-e^2}} \left(-\frac{3}{2}e \cos w (1 - \cos E) + \frac{1}{2}(1+e^2) \cos w \frac{1-\cos 2E}{2} - \frac{1}{2}\sqrt{1-e^2} \sin w \left(E - \frac{\sin 2E}{2} \right) \right) \\
&\quad + \frac{a^2}{\mu} \frac{1}{\sqrt{1-e^2}} \left(-\frac{1}{4}e \cos w \left(\frac{1-\cos 3E}{3} + 1 - \cos E \right) + \frac{1}{4}e\sqrt{1-e^2} \sin w \left(\sin E - \frac{\sin 3E}{3} \right) \right) \\
\mathcal{G}_{4,11} &= \frac{a^2}{\mu} \frac{\csc i}{\sqrt{1-e^2}} \sqrt{1-e^2} \cos w \left(\frac{1-\cos 2E}{4} - \frac{e}{4} \left(\frac{1-\cos 3E}{3} + 1 - \cos E \right) \right) \\
&\quad + \frac{a^2}{\mu} \frac{\csc i}{\sqrt{1-e^2}} \sin w \left(\frac{1+e^2}{2} \left(E + \frac{\sin 2E}{2} \right) - \frac{3e}{2} \sin E - \frac{e}{4} \left(\sin E + \frac{\sin 3E}{3} \right) \right) \\
\mathcal{G}_{4,13} &= \frac{a^2}{\mu} \frac{\csc i}{\sqrt{1-e^2}} \sqrt{1-e^2} \cos w \left(\frac{1}{2} \left(E - \frac{\sin 2E}{2} \right) - \frac{e}{4} \left(\sin E - \frac{\sin 3E}{3} \right) \right) \\
&\quad + \frac{a^2}{\mu} \frac{\csc i}{\sqrt{1-e^2}} \sin w \left(\frac{1+e^2}{2} \frac{1-\cos 2E}{2} - \frac{3e}{2} (1 - \cos E) - \frac{e}{4} \left(\frac{1-\cos 3E}{3} + \cos E - 1 \right) \right) \\
\mathcal{G}_{5,1} &= -\frac{a^2 \sqrt{1-e^2}}{\mu e} (\sin E - eE) \\
\mathcal{G}_{5,5} &= \frac{a^2}{\mu e} \left((2-e^2)(1-\cos E) - \frac{e(1-\cos 2E)}{2} \right) \\
\mathcal{G}_{5,6} &= \frac{a^2}{\mu e} \left(\frac{2-e^2}{2} \frac{1-\cos 2E}{2} - \frac{e(1-\cos 3E)}{4 \cdot 3} \right) \\
\mathcal{G}_{5,8} &= \frac{a^2}{\mu e} \left(\frac{2-e^2}{2} \left(E - \frac{\sin 2E}{2} \right) - \frac{e}{4} \left(\sin E - \frac{\sin 3E}{3} \right) \right) \\
\mathcal{G}_{5,11} &= -\cos i \mathcal{G}_{4,11} \\
\mathcal{G}_{5,13} &= -\cos i \mathcal{G}_{4,13} \\
\mathcal{G}_{6,1} &= -\frac{a^2}{\mu} \left(3E - \frac{1+3e^2}{e} \sin E + e^2 \frac{\sin 2E}{2} \right) \\
\mathcal{G}_{6,5} &= -\frac{a^2}{\mu} \sqrt{1-e^2} \left(\frac{2-e^2}{e} (1-\cos E) - \frac{1-\cos 2E}{4} \right) \\
\mathcal{G}_{6,6} &= -\frac{a^2}{\mu} \sqrt{1-e^2} \left(\frac{2-e^2}{e} \frac{1-\cos 2E}{4} - \frac{1}{4} \left(\frac{1-\cos 3E}{3} + 1 - \cos E \right) \right) \\
\mathcal{G}_{6,8} &= -\frac{a^2}{\mu} \sqrt{1-e^2} \left(\frac{2-e^2}{2e} \left(E - \frac{\sin 2E}{2} \right) - \frac{1}{4} \left(\sin E - \frac{\sin 3E}{3} \right) \right)
\end{aligned}$$

Appendix B

Contribution of Adding TFCs on State Uncertainty Estimation

The state vector is expanded to include the essential TFC set (\vec{C}) in order to estimate the perturbing thrust acceleration, \vec{U} , as well as the orbital state. Modeling the unknown dynamics using the essential TFC set, the governing equations of motion can be rewritten with the augmented state:

$$\frac{d}{dt} \begin{bmatrix} \vec{X} \\ \vec{C} \end{bmatrix} = \begin{bmatrix} \vec{F}(\vec{X}) \\ 0_{6 \times 1} \end{bmatrix} + \begin{bmatrix} B \\ 0_{6 \times 3} \end{bmatrix} \cdot \vec{U} \quad (\text{B.1})$$

where F and B are from Eq. (3.2). By defining the generalized state vector $\vec{Z} = \begin{bmatrix} \vec{X} \\ \vec{C} \end{bmatrix}$, Eq. (B.1) can be linearized by expanding about a reference state vector denoted by \vec{Z}^* :

$$\dot{\vec{Z}}(t) = \dot{\vec{Z}}^*(t) + \left[\frac{\partial \dot{\vec{Z}}(t)}{\partial \vec{Z}(t)} \right]^* (\vec{Z}(t) - \vec{Z}^*(t)) + \text{higher order terms} \quad (\text{B.2})$$

where * indicates that the quantity is evaluated on the reference trajectory with zero TFCs ($\vec{C}^* = \vec{0}$). By ignoring higher order terms and defining $\vec{z}(t) = \vec{Z}(t) - \vec{Z}^*(t) = \begin{bmatrix} \vec{X} - \vec{X}^* \\ \vec{C} - \vec{C}^* \end{bmatrix} = \begin{bmatrix} \vec{x} \\ \vec{c} \end{bmatrix}$,

Eq. (B.2) can be written as:

$$\dot{\vec{z}} = \left[\frac{\partial \dot{\vec{Z}}(t)}{\partial \vec{Z}(t)} \right]^* \vec{z} = A(t) \vec{z} \quad (\text{B.3})$$

$$\begin{bmatrix} \dot{\vec{x}} \\ \dot{\vec{c}} \end{bmatrix} = \begin{bmatrix} \frac{\partial(\vec{F}(\vec{X})+B \cdot \vec{U})}{\partial \vec{X}} & \frac{\partial(\vec{F}(\vec{X})+B \cdot \vec{U})}{\partial \vec{C}} \\ 0 & 0 \end{bmatrix} \begin{bmatrix} \vec{x} \\ \vec{c} \end{bmatrix} \quad (\text{B.4})$$

The measurement model for observation and the error property can be expressed as;

$$\vec{Y} = G(\vec{Z}, t) + \vec{\epsilon} = G(\vec{Z}^*, t) + \left[\frac{\partial G}{\partial \vec{Z}} \right]^* (\vec{Z}(t) - \vec{Z}^*(t)) + \text{higher order terms} + \vec{\epsilon} \quad (\text{B.5})$$

$$\vec{y} = H\vec{z} + \vec{\epsilon} \quad (\text{B.6})$$

$$= \begin{bmatrix} \frac{\partial G}{\partial \vec{X}} & \frac{\partial G}{\partial \vec{C}} \end{bmatrix} \begin{bmatrix} \vec{x} \\ \vec{c} \end{bmatrix} + \vec{\epsilon} = \begin{bmatrix} H_x & H_c \end{bmatrix} \begin{bmatrix} \vec{x} \\ \vec{c} \end{bmatrix} + \vec{\epsilon} \quad (\text{B.7})$$

$$E[\vec{\epsilon}] = 0, \quad E[\vec{\epsilon}\vec{\epsilon}^T] = R \quad (\text{B.8})$$

in which $\vec{\epsilon}$ is observation errors. The *a priori* estimates of initial state (\bar{x}, \bar{c}) and their associate statistical properties are given as;

$$\bar{x} = \vec{x} + \vec{\eta}, \quad E[\vec{\eta}] = 0, \quad E[\vec{\eta}\vec{\eta}^T] = \bar{P}_{xx} \quad (\text{B.9})$$

$$\bar{c} = \vec{c} + \vec{\xi}, \quad E[\vec{\xi}] = 0, \quad E[\vec{\xi}\vec{\xi}^T] = \bar{P}_{cc} \quad (\text{B.10})$$

$$E[\vec{\eta}\vec{\epsilon}^T] = E[\vec{\xi}\vec{\epsilon}^T] = 0, \quad E[\vec{\eta}\vec{\xi}^T] = \bar{P}_{xc}, \quad E[\vec{\xi}\vec{\eta}^T] = \bar{P}_{cx} \quad (\text{B.11})$$

At the initial time, it is assumed that there is no correlation between the state and TFCs ($\bar{P}_{xc} = \bar{P}_{cx} = \vec{0}$). To exploit the contribution of TFCs on the state uncertainty, one can modify the measure equation as:

$$\vec{y}_A = H_A\vec{z} + \vec{\epsilon}_A \quad (\text{B.12})$$

$$\begin{bmatrix} y \\ \bar{x} \\ \bar{c} \end{bmatrix} = \begin{bmatrix} H_x & H_c \\ I & 0 \\ 0 & I \end{bmatrix} \begin{bmatrix} \vec{x} \\ \vec{c} \end{bmatrix} + \begin{bmatrix} \vec{\epsilon} \\ \vec{\eta} \\ \vec{\xi} \end{bmatrix} \quad (\text{B.13})$$

$$E[\vec{\epsilon}_A] = \begin{bmatrix} E[\vec{\epsilon}] \\ E[\vec{\eta}] \\ E[\vec{\xi}] \end{bmatrix} = \vec{0}, \quad E[\vec{\epsilon}_A\vec{\epsilon}_A^T] = R_A = \begin{bmatrix} R & 0 & 0 \\ 0 & \bar{P}_{xx} & 0 \\ 0 & 0 & \bar{P}_{cc} \end{bmatrix} \quad (\text{B.14})$$

To obtain the weighted least square solution of z , the performance index to be minimized is

defined as:

$$J = \frac{1}{2} \vec{\epsilon}_A^T W_A \vec{\epsilon}_A \quad (\text{B.15})$$

$$= \frac{1}{2} (\vec{y}_A - H_A \vec{z})^T W_A (\vec{y}_A - H_A \vec{z}) \quad (\text{B.16})$$

with the weighting matrix, W_A , is expressed as:

$$W_A = R_A^{-1} = \begin{bmatrix} R^{-1} & 0 & 0 \\ 0 & \bar{P}_{xx}^{-1} & 0 \\ 0 & 0 & \bar{P}_{cc}^{-1} \end{bmatrix} \quad (\text{B.17})$$

where \bar{P}_{xx} is the *a priori* error covariance matrix related to the original position and velocity state ($= \bar{P}_x$). To obtain a minimum of Eq. (B.16), the following necessary condition has to be satisfied:

$$\frac{\partial J}{\partial \vec{z}} = -(\vec{y}_A - H_A \vec{z})^T W_A H_A = 0 \quad (\text{B.18})$$

From this equation, the least square solution of \vec{z} can be obtained:

$$H_A^T W_A (\vec{y}_A - H_A \vec{z}) = 0 \quad (\text{B.19})$$

$$\vec{z} = (H_A^T W_A H_A)^{-1} H_A^T W_A \vec{y}_A \quad (\text{B.20})$$

where $(H_A^T W_A H_A)^{-1}$ is the definition of the covariance matrix:

$$P_A = (H_A^T W_A H_A)^{-1} = \Lambda^{-1} \quad (\text{B.21})$$

in which the inverse of the covariance matrix is defined as the information matrix (Λ). By breaking

up the covariance matrix, the partitioned information matrix can be expressed as:

$$P_A = \begin{bmatrix} P_{xx} & P_{xc} \\ P_{cx} & P_{cc} \end{bmatrix} = (H_A^T W_A H_A)^{-1} \quad (\text{B.22})$$

$$\Lambda = \begin{bmatrix} \Lambda_{xx} & \Lambda_{xc} \\ \Lambda_{cx} & \Lambda_{cc} \end{bmatrix} = \begin{bmatrix} H_x^T & 1 & 0 \\ H_c^T & 0 & 1 \end{bmatrix} \begin{bmatrix} R^{-1} & 0 & 0 \\ 0 & \bar{W}_{xx} & 0 \\ 0 & 0 & \bar{W}_{cc} \end{bmatrix} \begin{bmatrix} H_x & H_c \\ I & 0 \\ 0 & I \end{bmatrix} \quad (\text{B.23})$$

$$\Lambda_{xx} = H_x^T R^{-1} H_x + \bar{W}_{xx} \quad (\text{B.24})$$

$$\Lambda_{xc} = H_x^T R^{-1} H_c \quad (\text{B.25})$$

$$\Lambda_{cx} = H_c^T R^{-1} H_x = \Lambda_{xc}^T \quad (\text{B.26})$$

$$\Lambda_{cc} = H_c^T R^{-1} H_c + \bar{W}_{cc} \quad (\text{B.27})$$

Using the definition of information matrix, the partitioned covariance matrix can be expressed as:

$$P_{xx} = (\Lambda_{xx} - \Lambda_{xc} \Lambda_{cc}^{-1} \Lambda_{cx})^{-1} \quad (\text{B.28})$$

$$P_{xc} = -(\Lambda_{xx} - \Lambda_{xc} \Lambda_{cc}^{-1} \Lambda_{cx})^{-1} \Lambda_{xc} \Lambda_{cc}^{-1} \quad (\text{B.29})$$

$$P_{cx} = -(\Lambda_{cc} - \Lambda_{cx} \Lambda_{xx}^{-1} \Lambda_{xc})^{-1} \Lambda_{cx} \Lambda_{xx}^{-1} \quad (\text{B.30})$$

$$P_{cc} = (\Lambda_{cc} - \Lambda_{cx} \Lambda_{xx}^{-1} \Lambda_{xc})^{-1} \quad (\text{B.31})$$

Using the Schur Identity [82] and Eq. (B.31), Eq. (B.28) can be rewritten as:

$$P_{xx} = (\Lambda_{xx} - \Lambda_{xc} \Lambda_{cc}^{-1} \Lambda_{cx})^{-1} \quad (\text{B.32})$$

$$= \Lambda_{xx}^{-1} + \Lambda_{xx}^{-1} \Lambda_{xc} (\Lambda_{cc} - \Lambda_{cx} \Lambda_{xx}^{-1} \Lambda_{xc})^{-1} \Lambda_{cx} \Lambda_{xx}^{-1} \quad (\text{B.33})$$

$$= \Lambda_{xx}^{-1} + \Lambda_{xx}^{-1} \Lambda_{xc} P_{cc} \Lambda_{cx} \Lambda_{xx}^{-1} \quad (\text{B.34})$$

The first term on the right-hand side of the equation, Λ_{xx}^{-1} , can be rewritten using Eq. (B.24), which is the definition of the covariance P_x associated with estimating the state vector only, neglecting errors in TFCs:

$$\Lambda_{xx}^{-1} = (H_x^T R^{-1} H_x + \bar{W}_{xx})^{-1} = P_x \quad (\text{B.35})$$

where $P_x = (H_x^T R^{-1} H_x + \overline{W}_{xx})^{-1} = ((H_x^T R^{-1} H_x + \overline{W}_{xx})^{-1})^T = P_x^T$. With this equations , the uncertainty of position and velocity including the contribution from TFCs can be described as:

$$P_{xx} = P_x + P_x \Lambda_{xc} P_{cc} \Lambda_{cx} P_x \quad (\text{B.36})$$

$$= P_x + P_x \Lambda_{xc} P_{cc} (P_x \Lambda_{xc})^T \quad (\text{B.37})$$

where the second term is positive definite and compensates the error due to unmodeled event dynamics. This term automatically inflates the state covariance and represents the contributed uncertainty from unmodeled dynamics of a USE. Note that $-P_x \Lambda_{xc}$ is same as the sensitivity matrix ($S_{xc} = -P_x H_x^T R^{-1} H_c$) defined in [4, p. 395]:

$$P_{xx} = P_x + P_x \Lambda_{xc} P_{cc} (P_x \Lambda_{xc})^T \quad (\text{B.38})$$

$$= P_x + (-P_x H_x^T R^{-1} H_c) P_{cc} (-P_x H_x^T R^{-1} H_c)^T \quad (\text{B.39})$$

$$= P_x + S_{xc} P_{cc} S_{xc}^T \quad (\text{B.40})$$

in which the sensitivity matrix maps effects of TFC error into the state uncertainty estimate.

Appendix C

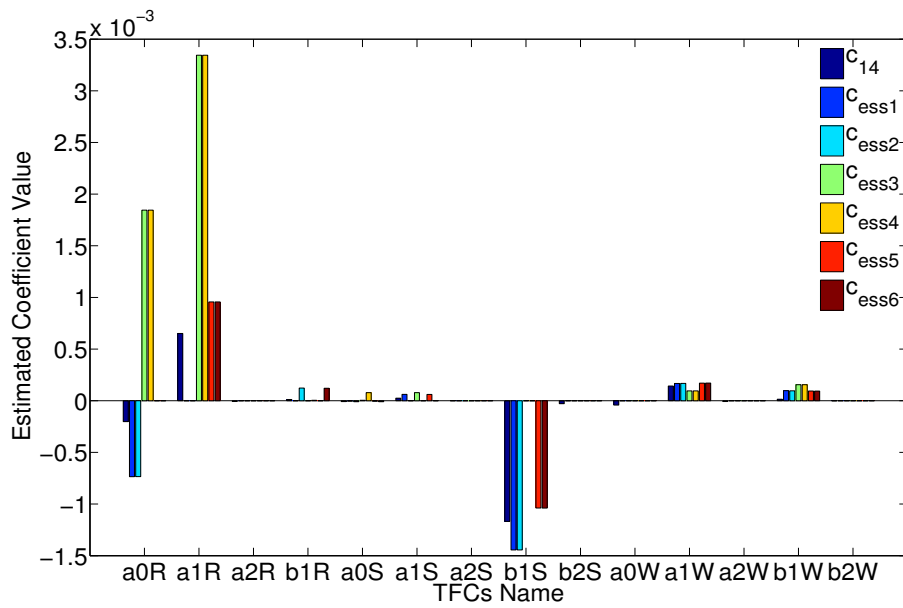
Orbit Determination Across Unmodeled Space Events via Event Representation Using Different TFC Sets

In chapter 3.2.2, four different types of unmodeled event cases are processed with the modified Batch filter using different TFC sets and the result for case 4 is only shown to avoid repetition. Simulation results for case 1 ~ 3 are shown in this Appendix. Cases 1-3 describe cases with perturbations acting on a single direction, while case 4 represents a USE with an unknown acceleration acting on a random direction. For each case, the first subfigure displays estimated TFC values from

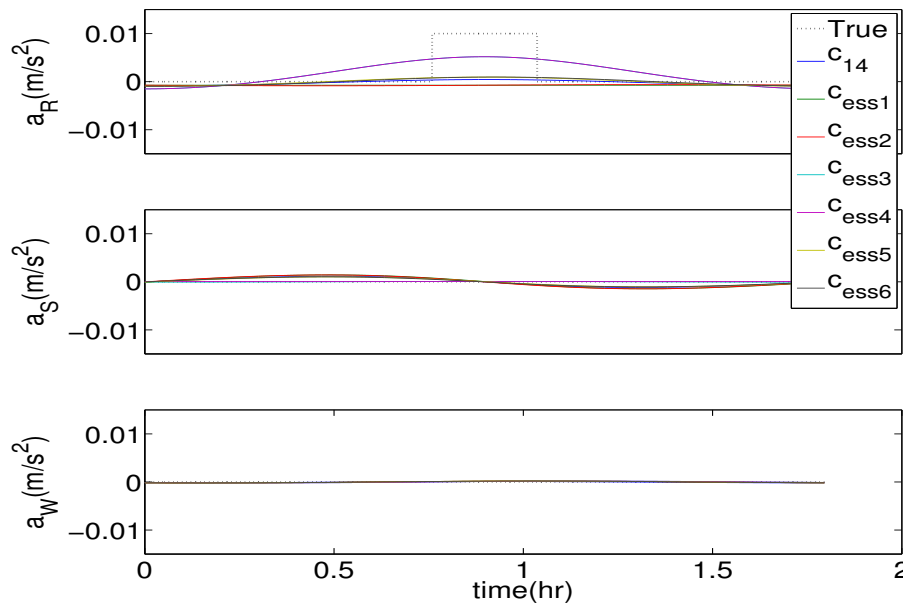
Table C.1: Different unmodeled event cases

case	direction	ΔV (m/s)
1	Radial (R)	10 (R)
2	circumferential (S)	10 (S)
3	normal (W)	10 (W)
4	Random	6(R) 9(S) 3(W)

the modified Batch filter with 7 different TFC sets including the full set of 14 TFC. The second subfigure compares the reconstructed perturbing acceleration to the true perturbation. Next two subplots describe the errors of the state estimate from the modified Batch filter with the 14-TFC set as \circ , those from the modified filter with each set of 6 TFCs as $+$, and ones with the regular Batch filter without TFCs as \square . Different covariance boundaries obtained with those filters are shown with their respective colors (black for regular batch filter; blue for batch with 14 TFCs; others for batch with 6 TFCs). The result shows that event representations using different combinations of TFCs produce equivalent OD solutions across USEs, which validates our approach.



(a) Estimated TFC values for different TFC sets



(b) Represented vs True acceleration components

Figure C.1: Event representation for case 1

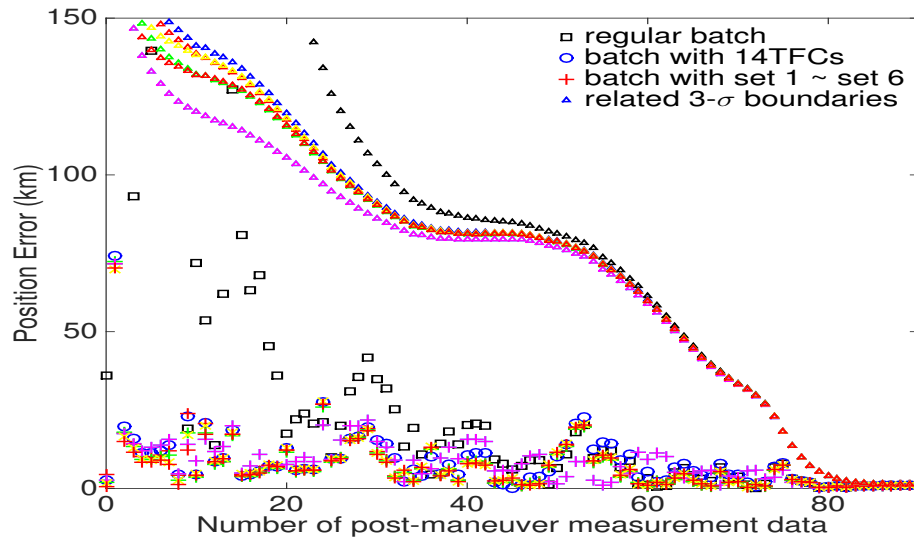
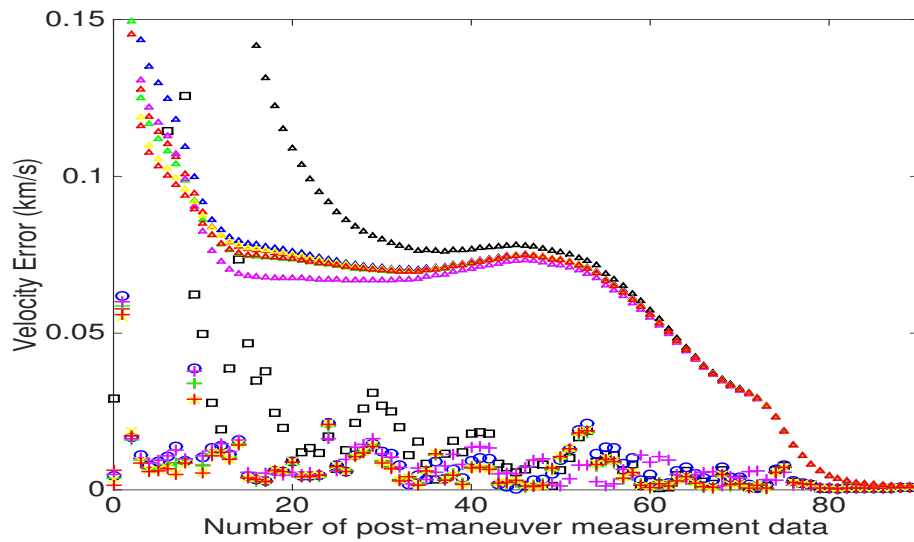
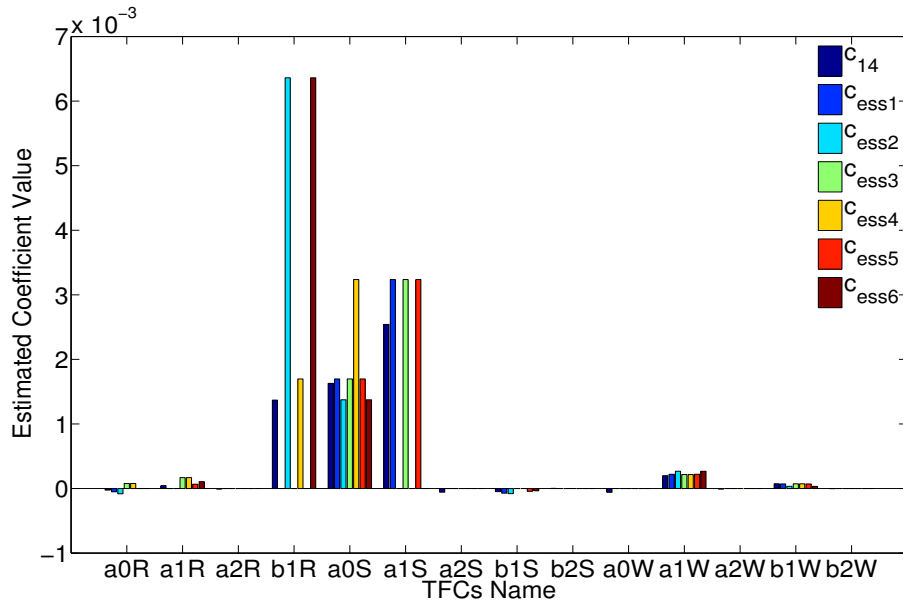
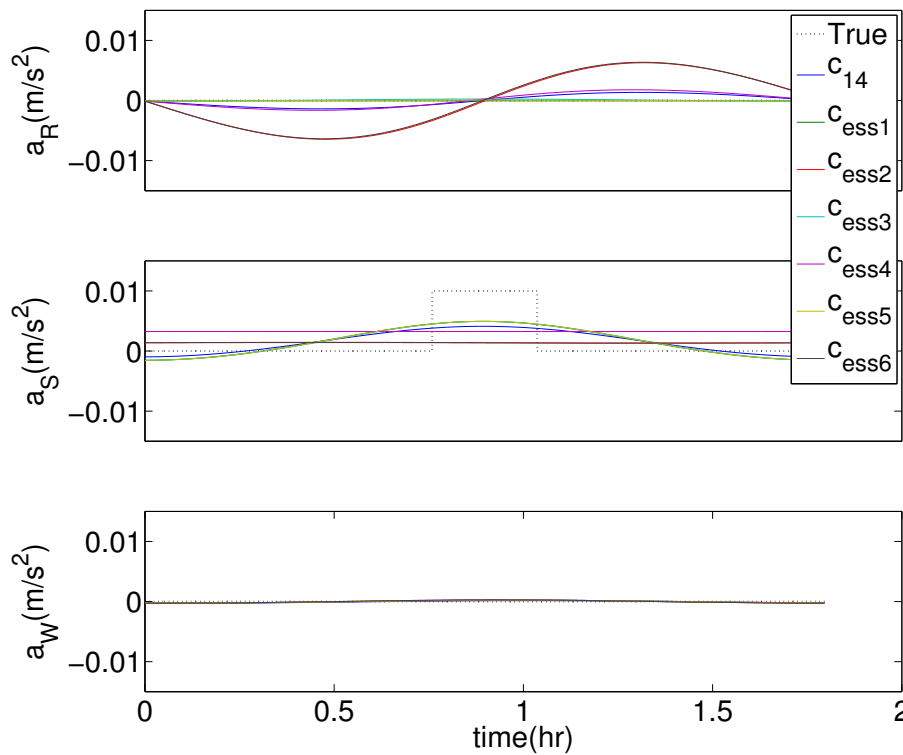
(a) Position error with 3σ uncertainty boundary(b) Velocity error with 3σ uncertainty boundary

Figure C.2: OD solution with different sizes of tracking data for case 1

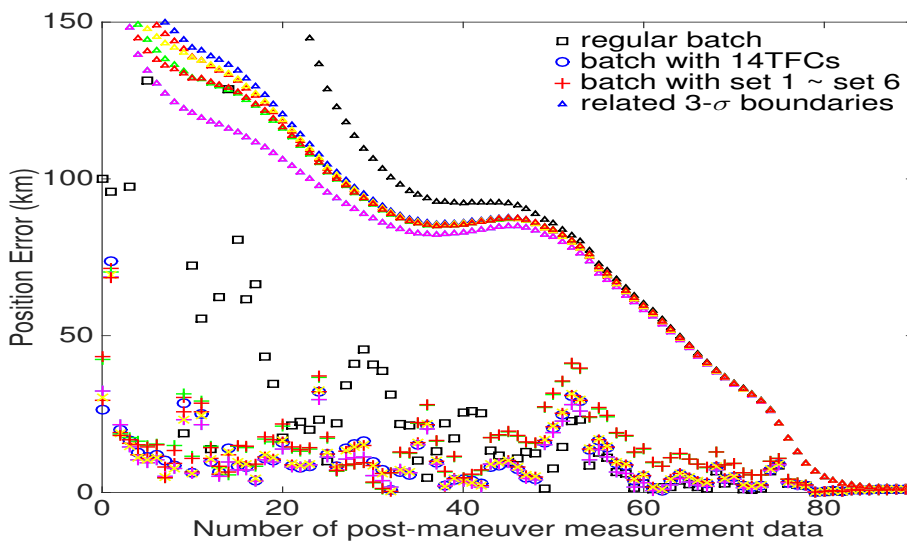


(a) Estimated TFC values for different TFC sets

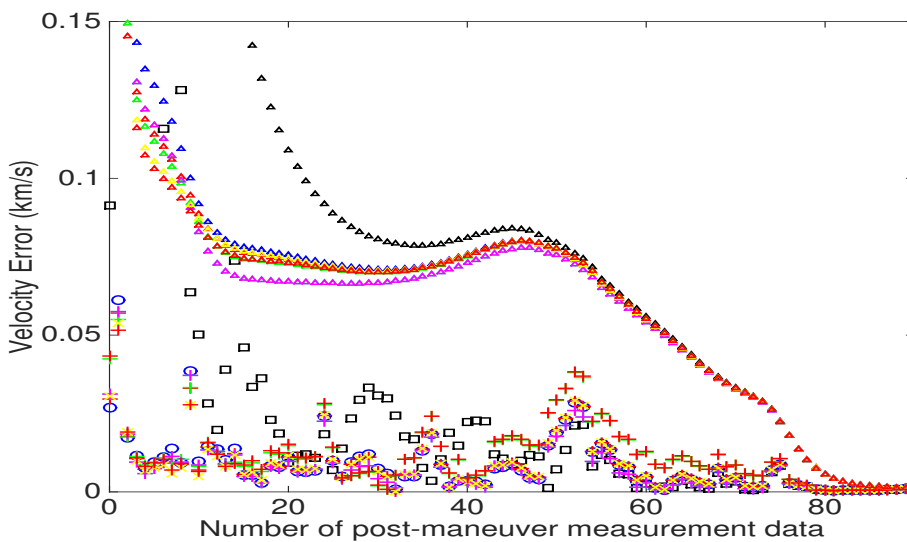


(b) Represented vs True acceleration components

Figure C.3: Event representation for case 2

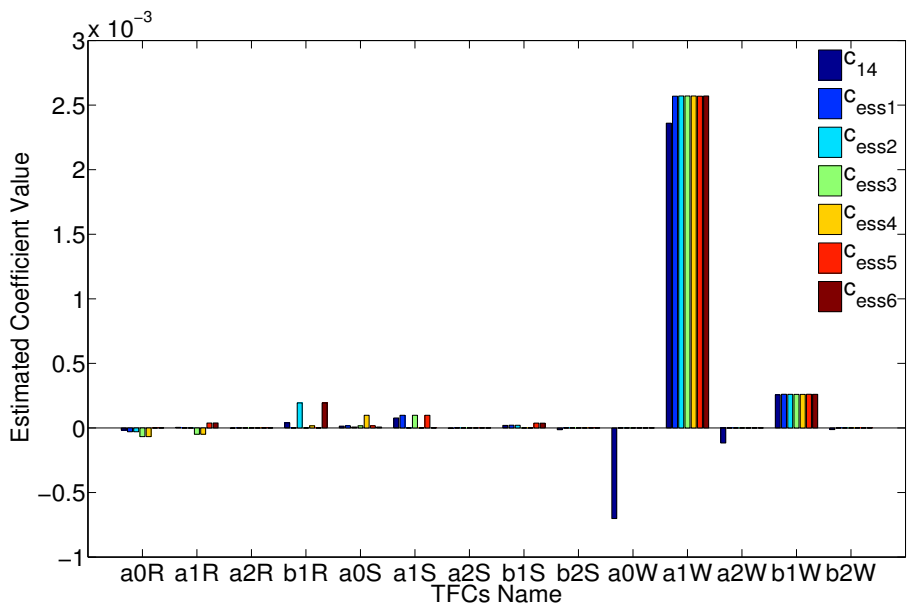


(a) Position error with 3σ uncertainty boundary

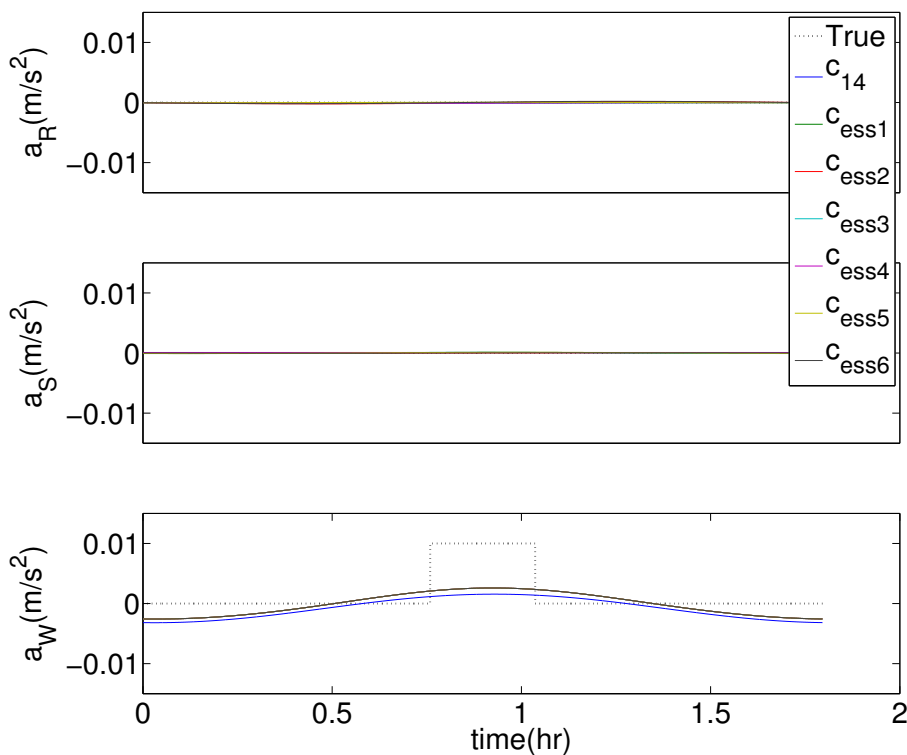


(b) Velocity error with 3σ uncertainty boundary

Figure C.4: OD solution with different sizes of tracking data for case 2

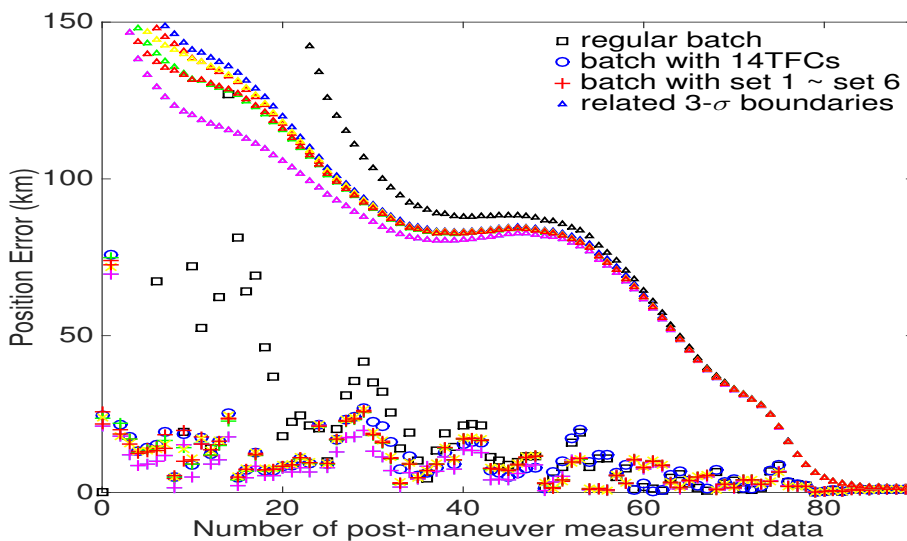


(a) Estimated TFC values for different TFC sets

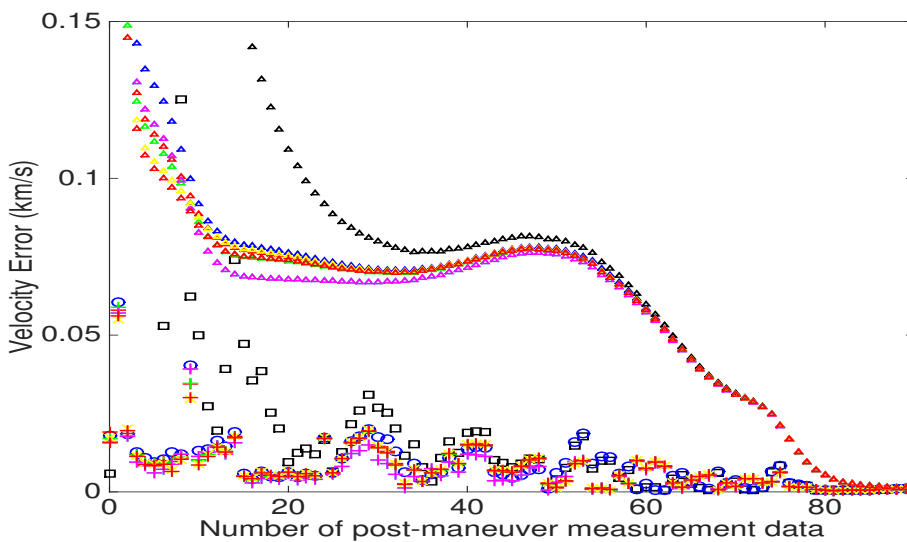


(b) Represented vs True acceleration components

Figure C.5: Event representation for case 3



(a) Position error with 3σ uncertainty boundary



(b) Velocity error with 3σ uncertainty boundary

Figure C.6: OD solution with different sizes of tracking data for case 3

Appendix D

Simulation Result of Modifying Orbit Determination Toolbox (ODTBX) with the TFC event representation

In order to validate the modified ODTBX with the TFC event representation, several simulated USE cases are analyzed with the filter. All the simulations are performed on a low-earth orbiting (LEO) satellite and a typical initial condition is chosen as Table D.1. To check the perfor-

Table D.1: Initial state of LEO satellite

$h_0(km)$	e	$i(deg)$	$\Omega(deg)$	$\omega(deg)$	$\nu(deg)$
1350	0.05	101	80	30	0

h_0 : altitude at perigee

mance of the modified filter in a simple way, 6 different cases of USE are tested with the modified filter, which are shown in Table D.2. Case 1-3 are for the continuous low thrust malfunction cases

Table D.2: Perturbations for different USE cases

case	type	ΔV (m/s)	Direction
1	Continuous	100	Along-track
2	Continuous	100	Radial
3	Continuous	100	Cross-track
4	Impulsive	10	Along-track
5	Impulsive	10	Radial
6	Impulsive	10	Cross-track

on each direction. Each malfunction starts at 5 minutes after the last pre-event measurement and ends at 5 minutes before the first post-event measurement. Case 4-6 are for the USEs related to an impulsive ΔV burn on each direction. Suppose all ground stations lose tracking of a satellite

as soon as this impulsive event happens. After one orbital period (1.88 hour) following the event, they are able to take measurements every 1 minute for next 3 hours.

To start the algorithm, the filter needs an initial state estimate, an associated initial state covariance, and an initial TFC estimate. Preliminary OD was performed to obtain the initial data by filtering a pre-event satellite tracking data (range and range-rate for 3 orbital periods). As a result, a relatively accurate a priori information ($\sigma_{position} = 1m$, $\sigma_{velocity} = 1cm/s$) was obtained and used as a priori information in our simulations. For the initial guess for TFCs, the modified filter can simply start with zeros without tuning those coefficients. With a priori information and the true event dynamics, the measurement generating function built in ODTBX produces post-event measurements. For the post-event observation, 3 ground tracking stations are selected from the ground station list in ODTBX and are used to generate range and range-rate data from true position and velocity vectors at every minute. The sensor measurement error ($10m$, $1 \times 10^{-2}m/sec$) is imitated by adding white Gaussian noises to the truth and it is assumed that there is no observation available during the unknown space event.

To compare how an unmodified least square filter perform over a USE, the original least square filter in ODTBX is processed through the unknown event of case 1 without representing the event and the result is shown in Fig. D.1. Without modeling the USE, the filter delivers

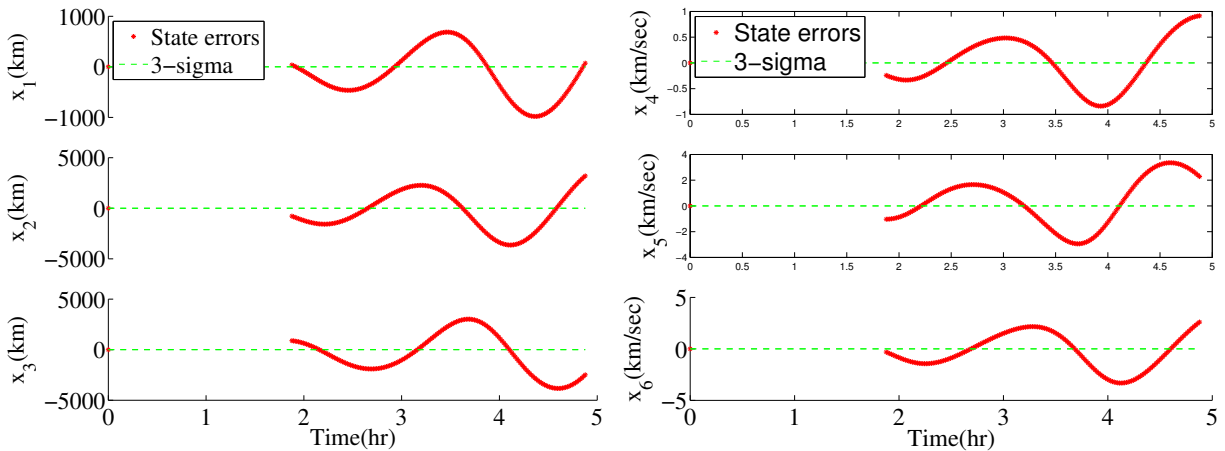


Figure D.1: OD result (state errors) with the unmodified filter on case 1

large state estimation errors that stay outside of the 3 sigma uncertainty boundaries which are relatively too small. It shows that the original ODTBX fails to maintain OD across a USE without compensating the perturbing effect. By modifying the ODTBX with the TFC event representation, OD was performed on the same case and the result is shown in Fig. D.2. The figure describes the error of the state estimate from the true trajectory as a red line and 3 sigma covariance boundary of the estimate as a green line. The modified filter successfully process all the measurements with a priori information, and the state errors as well as the measurement errors are within uncertainty boundaries. All the results on various cases are consistent with the expected behavior that the estimated state values are within confidence intervals and the filter provides a converged solution with the TFC event representation. For the impulsive perturbation case, Fig. D.3 illustrates the OD solution with the modified filter on case 6.

The performance of the modified ODTBX is also validated through use of 30 Monte Carlo simulations. The linearly propagated covariance results are compared to confidence intervals associated with the Monte Carlo analysis available in ODTBX. Each Monte Carlo run in ODTBX generates random deviations from the reference as initial conditions, and then it integrates each deviated case and uses this as truth for measurement generation and estimation in OD simulation [40]. Each run delivers the time series of estimation errors and residuals for each case. Figure. D.4 shows the results of 30 Monte Carlo runs on case 1, where red dots are individual actual errors while blue line indicates the mean error of ensembles from 30 Monte Carlo runs. In each subfigure, cyan bands show 1-3 sigma confidence intervals of the ensemble standard deviations and the green line displays mean value of 3 sigma uncertainty boundaries from 30 OD solutions. These uncertainty boundaries from the Monte Carlo runs with the modified filter enclose state and measurement errors. Thus, it confirms that the OD solutions from the modified filter are consistent and the modified least square filter is able to maintain OD across an unknown space event. Utilizing a priori information and an event representation of a USE, the modified filter is able to provide valid orbit states and uncertainty information without measurement data during the event. This OD solution can be used to improve the accuracy of orbit state right after a USE by making further observation after

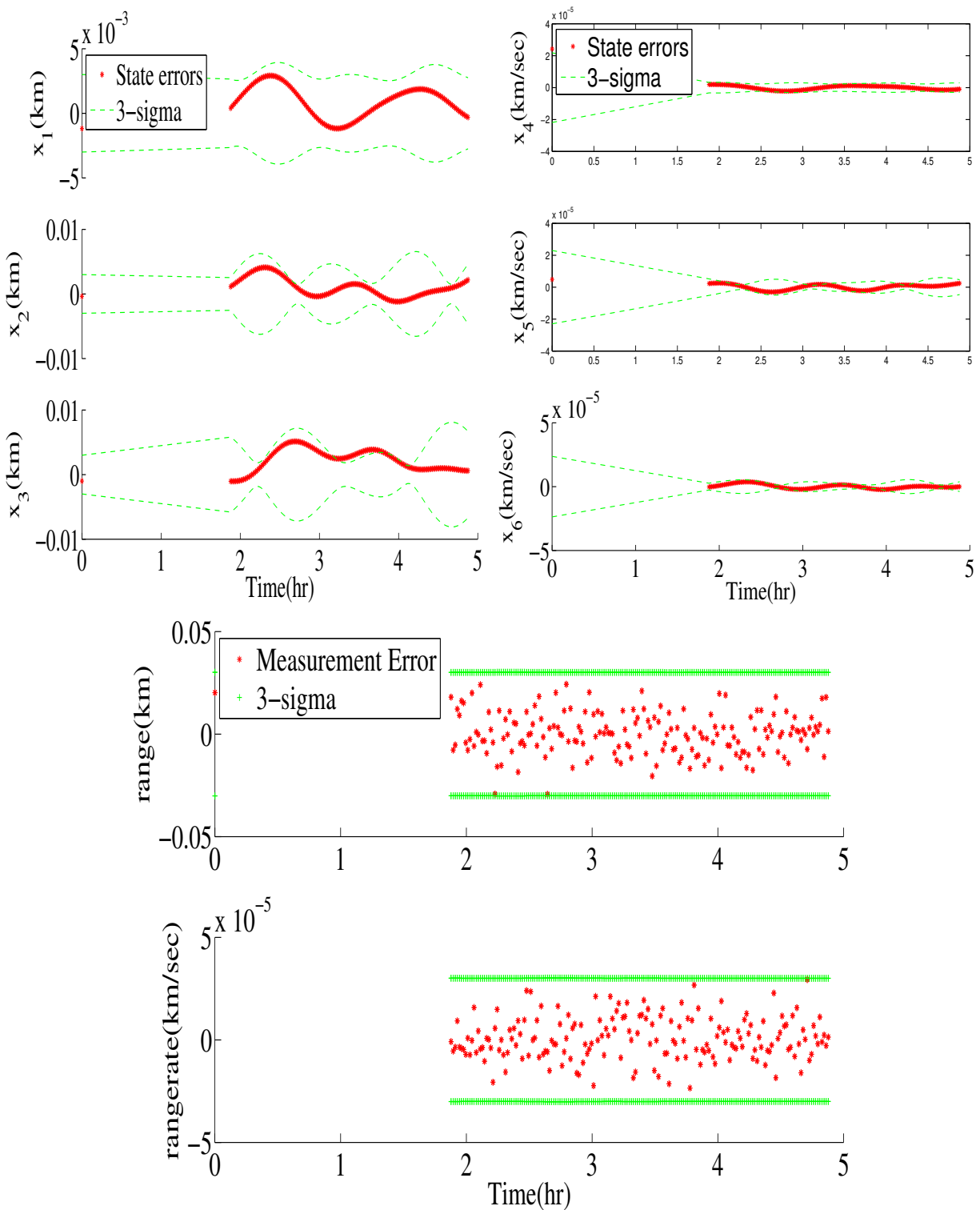


Figure D.2: OD result (state, measurement errors) with modified filter on case 1

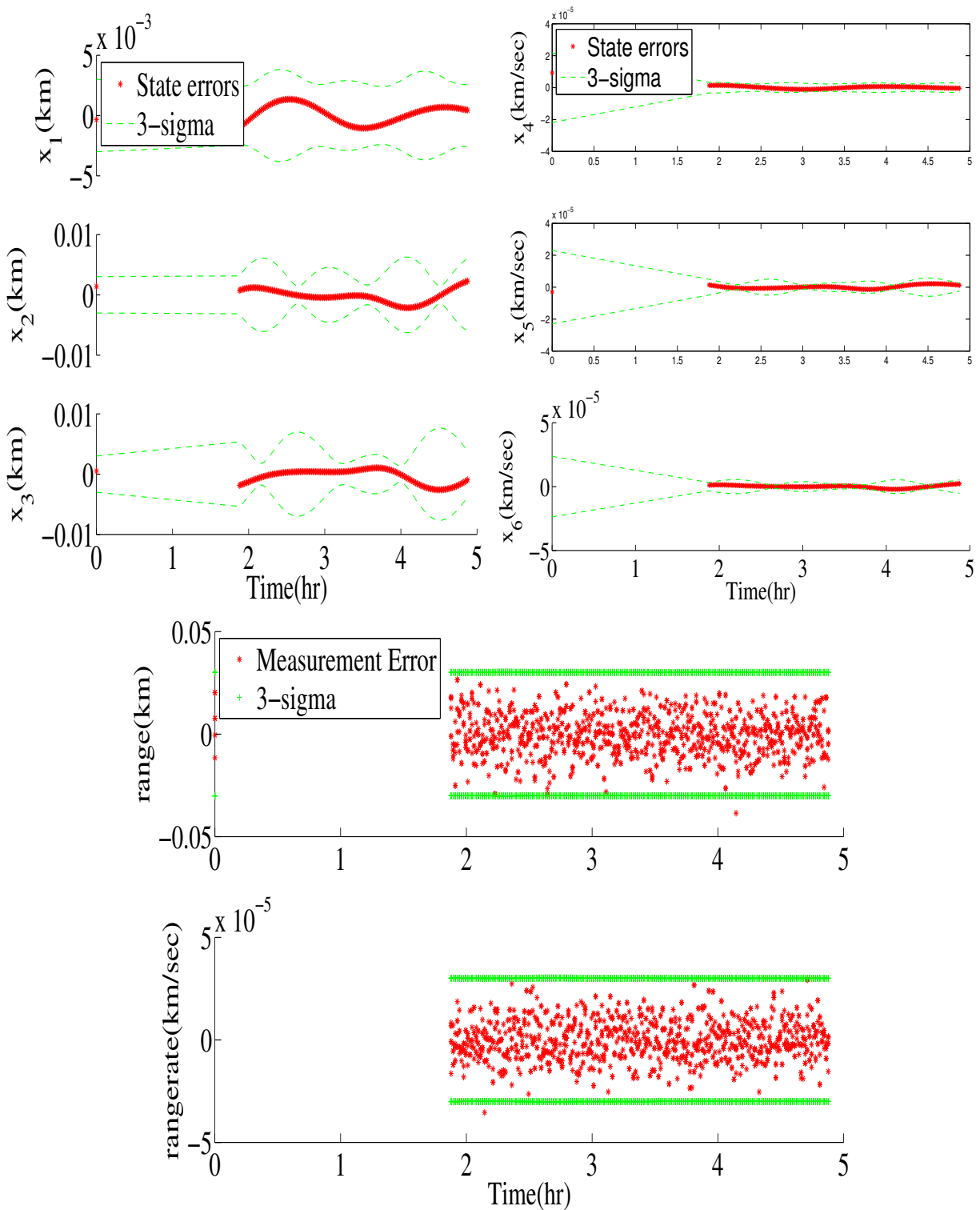


Figure D.3: OD result (state, measurement errors) with modified filter on case 6

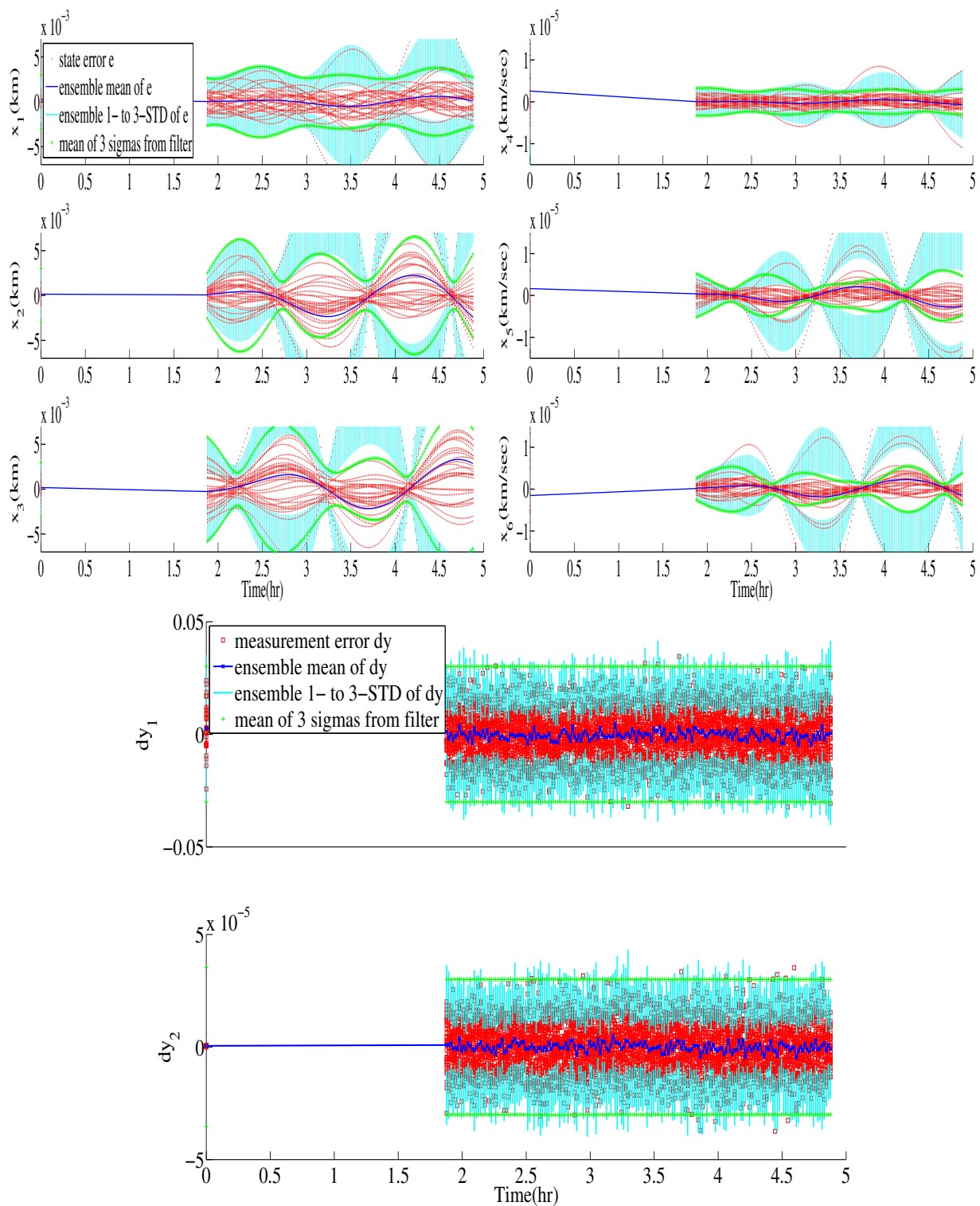


Figure D.4: OD results from 30 Monte Carlo runs on case 1

the event.

The modified filter also provides a representation of an unknown acceleration by constructing a control profile with TFCs. Figure. D.5 compares the reconstructed perturbing acceleration components to the true ones for the case 1, 3 and 4. For those USEs associated with continuous perturbations, the reconstructed accelerations are found to be the same order of magnitude as the true perturbations. For the impulsive cases, the modeled thrust acceleration is spread over the whole period of a USE, therefore the shape of the recovered control profile is different from the true one. Although this filter does not recover the actual perturbing acceleration precisely for a USE, yet it provides insight into the control effort for the unknown event. The control effort (ΔV) can be estimated by integrating the thrust acceleration profile over the time interval, which still can be used to quantify the magnitude of an actual perturbation. The represented perturbing acceleration components for different cases are shown in Table. D.3. Even though the computed ΔV s do not

Table D.3: Estimated ΔV from the filter

Direction	Continuous			Impulsive		
	case 1	case 2	case 3	case 4	case 5	case 6
Along-track	<u>99.2</u>	22.3	0	<u>10.3</u>	0.1	0
Radial	4.2	<u>50</u>	0.1	4.92	<u>24.9</u>	0
Cross-track	0	0	<u>50.1</u>	0	0	<u>12.1</u>

* True ΔV : 100m/s for continuous, 10m/s for impulsive

exactly match with true values, it still provides an estimate of controlling effort, which can be used to bound the control effort necessary for linking two separate states across an unknown event.

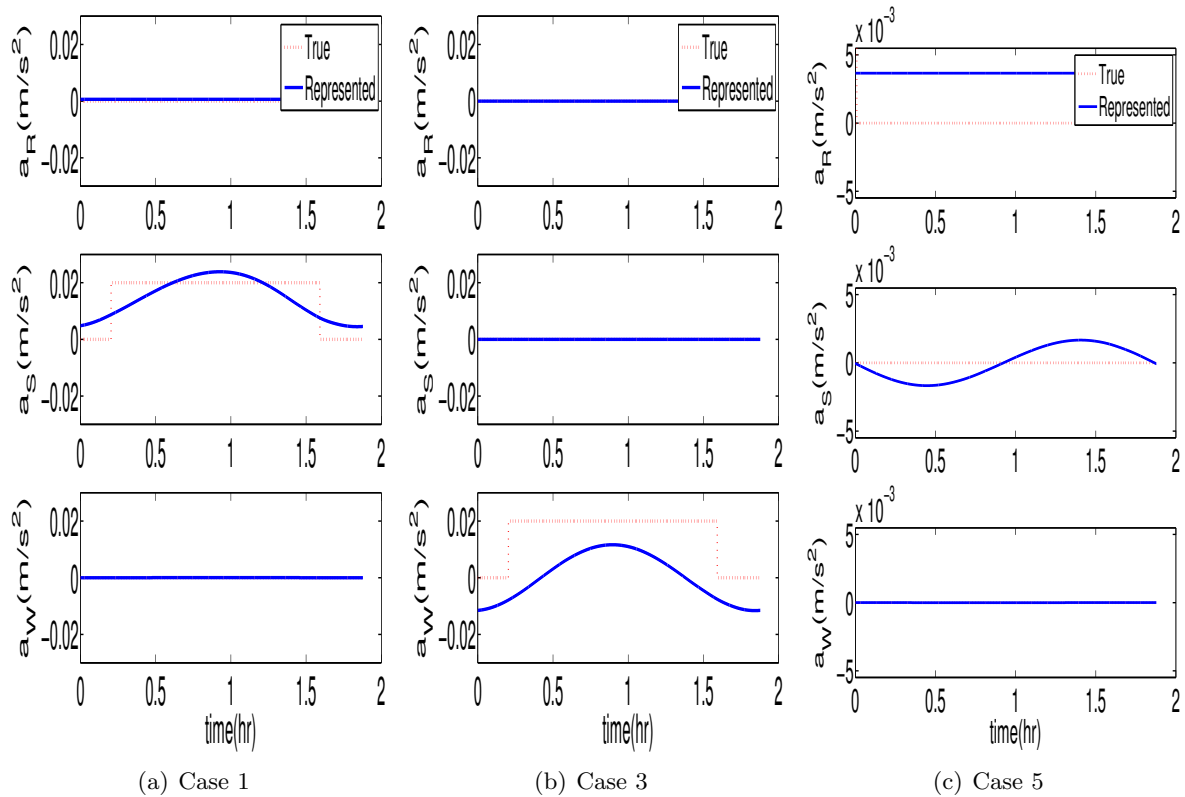


Figure D.5: Represented vs True acceleration components in body frame